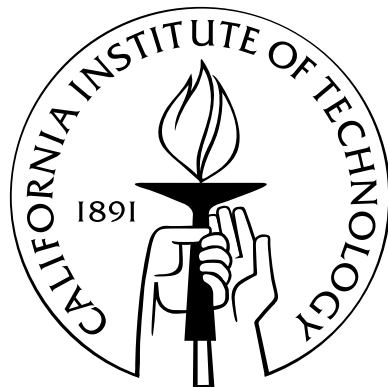


**Transition between Regular Reflection and Mach Reflection
in the Dual-Solution Domain**

Thesis by
Christopher A. Mouton

In Partial Fulfillment of the Requirements
for the Degree of
Doctor of Philosophy



California Institute of Technology
Pasadena, California

2007
(Defended December 1, 2006)

© 2007

Christopher A. Mouton

All Rights Reserved

To my parents, Jean-Claude and Birgit Mouton

Acknowledgements

I am sincerely grateful to my advisor, Dr. Hans Hornung, without whom none of this would have been possible. He has given me so much room to grow and to explore my interest in gas dynamics. His encouragement and guidance in all aspects of this work have been invaluable to me, and are something I will never forget.

I am truly indebted to Bahram Valiferdowsi for his extensive help in the design, manufacture, and repair of the Ludwieg tube facility. Without his expertise none of the experiments presented in this thesis would have been possible. The work of John Korte of NASA Langley Research Center on designing both the original Mach 2.3 as well as the Mach 4.0 is greatly appreciated.

Nicolas Ponchaut has been an invaluable friend throughout my studies and research. He has always been willing to assist me in my work, to criticize my math skills, to push me to code more efficiently, and to discuss the many problems facing the world. He is truly one of the smartest people I have met in my life, and I look up to him for that.

I would also like to thank the National Defense Science and Engineering Grant for funding the first three years of my studies at Caltech. I also thank Dr. John Schmissieux from the Air Force Office of Scientific Research for providing the funding and the trust to pursue this study of Mach reflection.

A special thanks to Jeff Bergthorson, Jim Karnesky, Amy Lam, Stuart Laurence, Daniel Lieberman, David Miller, Florian Pintgen, and Dr. Joseph Shepherd for giving me advice or helping me with various tasks related to my experiments. Thanks to Julian Cummings, Ralf Deiterding, and James Quirk for their help on the computational aspects of my work. Thanks also to Joe Haggerty, Ali Kiani, Bradley St. John, and Ricardo Paniagua for their work constructing many of the components of the Ludwieg tube facility.

Very importantly, I would like to thank my friends and family. The biggest thanks goes to my parents, Jean-Claude and Birgit, for their love and constant support. I also thank

my sister, Tina, for providing me a place to stay and unwind in Las Vegas, and for being available to listen to my problems. Special thanks to Valentine, Alfred, Brad, Abby, Amy, and Paul, whose support and encouragement throughout my time at Caltech is something I will always cherish. Thanks also to Damien for being an amazing friend and a perfect business partner.

I greatly appreciate the inspiration and guidance of my previous professors and teachers: Dr. David Goldstein, Jack McAleer, and Dr. Armando Galindo.

I also acknowledge the members of my committee: Dr. Hans Hornung, Dr. Joseph Shepherd, Dr. Dale Pullin, Dr. Paul Dimotakis, and Dr. Beverly McKeon for their suggestions and for their time.

璐，你的爱和支持伴随我度过了最后两个月的学习，对此我深深感激.

Abstract

A study of the shock-reflection domain for steady flow is presented. Conditions defining boundaries between different possible shock-reflection solutions are given, and where possible, simple analytic expressions for these conditions are presented. A new, more accurate estimate of the steady-state Mach stem height is derived based on geometric considerations of the flow. In particular, the location of the sonic throat through which the subsonic convergent flow behind the Mach stem is accelerated to divergent supersonic flow is considered. Comparisons with previous computational and experimental work show that the theory presented in this thesis more accurately predicts the Mach stem height than previous theories. The Mach stem height theory is generalized to allow for a moving triple point. Based on this moving triple point theory, a Mach stem growth rate theory is developed. This theory agrees well with computational and experimental results. Numerical computations of the effects of water vapor disturbances are also presented. These disturbances are shown to be sufficient to cause transition from regular reflection to Mach reflection in the dual-solution domain. These disturbances are also modeled as a simple energy deposition on one of the wedges, and an estimate for the minimum energy required to cause transition is derived.

Experimental results using an asymmetric wedge configuration in the Ludwieg tube facility at the California institute of Technology are presented. A Mach 4.0 nozzle was designed and built for the Ludwieg tube facility. This Mach number is sufficient to provide a large dual-solution domain, while being small enough not to require preheating of the test gas. The test time of the facility is 100 ms, which requires the use of high-speed cinematography and a fast motor to rotate one of the two wedges. Hysteresis in the transition between regular to Mach reflection was successfully demonstrated in the Ludwieg tube facility. The experiments show that regular reflection could be maintained up to a shock angle approximately halfway between the von Neumann condition and the detachment condition.

Energy deposition studies were performed using an Nd:YAG laser. Triggering transition

in this manner is found to depend on the location of the energy deposition. This finding is consistent with the numerical work presented in this thesis. Experiments were also performed to measure the Mach stem height and its growth rate. These results are compared with the theoretical estimates presented in this thesis. Excellent agreement between the steady-state Mach stem height and the theoretical estimates is seen. Comparisons of Mach stem growth rate with theoretical estimates show significant differences, but do show good agreement regarding the time required to reach the steady-state height.

Contents

Acknowledgements	v
Abstract	vii
1 Introduction	1
1.1 Outline and Contributions	6
2 Shock Reflection Domain	9
2.1 General Compressible Flow Equations	9
2.2 Possible Shock Reflections	11
2.2.1 Regular Reflection	11
2.2.2 Regular Reflection with Subsonic Downstream Flow	12
2.2.3 Mach Reflection	12
2.2.4 Mach Reflection with Subsonic Downstream Flow	13
2.2.5 Mach Reflection with a Forward-Facing Reflected Shock	14
2.2.6 Inverted Mach Reflection	14
2.2.7 Von Neumann Reflection	15
2.3 Domain Boundaries	17
2.3.1 Mach Wave Condition	17
2.3.2 Sonic Incident Shock Condition	17
2.3.3 Detachment Condition	18
2.3.4 Von Neumann Condition	22
2.3.5 Sonic Reflected Shock Condition	26
2.3.6 Normal Reflected Shock Condition	29
2.3.7 Sonic Forward-Facing Reflected Shock Condition	31
2.3.8 Sonic Condition	35

2.3.9	Complete Reflection Domain	37
3	Mach Stem Height Prediction	41
3.1	Problem Setup	42
3.2	Mass and Momentum Balance	42
3.3	Geometric Solution	52
3.4	Generalized Geometric Solution	54
3.5	Numerical Calculations	56
3.6	Mach Stem Height Results	58
3.7	Moving Triple Point Analysis	59
3.8	Mach Stem Height Variation	62
3.9	Three-Dimensional Mach Stem Growth	68
4	Dense Gas Disturbances	73
4.1	High Density Gas Region	73
4.1.1	Evolution of High Density Gas Region	74
4.1.2	Mechanism of Transition	85
4.1.3	Three-Dimensional Results	85
4.2	Energy Deposition	94
4.2.1	Minimum Energy Requirement	94
5	Asymmetric Oblique Shocks	105
5.1	Symmetric Analogy	109
6	Experimental Setup	111
6.1	Ludwieg Tube	111
6.1.1	Governing Equations	113
6.2	Mach 4 Nozzle	113
6.3	Dump Tank	117
6.4	Upstream Diaphragm Station	119
6.5	Adjustable Wedge Model	122
6.5.1	Motor and Gear Box	122
6.6	High Speed Schlieren Photography	124

7 Experimental Hysteresis	125
8 Experimental Transition	131
8.1 Energy Deposition Location	134
8.2 Tunnel Disturbances	134
9 Experimental Mach Stem Heights	139
9.1 Experimental Mach Stem Growth	140
10 Conclusions and Future Work	143
A Mach Reflection Domain	147
B Alternative Plots	152
C Mach 4 Nozzle Design	156
D Double Wedge Model	174
D.1 Adjustable Wedge Model	174
D.2 Fixed Wedge Model	183
Bibliography	189

List of Figures

1.1	Pseudosteady regular reflection and Mach reflection.	2
1.2	Steady regular reflection and Mach reflection.	2
1.3	Steady von Neumann reflection.	3
2.1	Basic flow parameters for a wedge with an attached shock.	10
2.2	Regular reflection with supersonic downstream flow.	11
2.3	Regular reflection with subsonic downstream flow.	12
2.4	Mach reflection.	13
2.5	Mach reflection with subsonic downstream flow.	14
2.6	Mach reflection with a forward-facing reflected shock.	15
2.7	Inverted Mach reflection.	16
2.8	Von Neumann reflection.	16
2.9	Flow over a zero-degree wedge producing a Mach wave.	17
2.10	Shock reflection domain, for $\gamma = 1.4$, considering only the Mach wave condition. .	18
2.11	Shock reflection domain, for $\gamma = 1.4$ considering only the sonic incident shock condition.	19
2.12	Flow over a wedge producing an incident and reflected shock.	19
2.13	Example of the detachment condition for $M = 4$ and $\gamma = 1.4$	20
2.14	Shock reflection domain, for $\gamma = 1.4$ considering only the detachment condition. .	22
2.15	Flow over a wedge producing a triple point at the von Neumann condition. .	23
2.16	Example of the von Neumann condition for $M = 4$ and $\gamma = 1.4$	23
2.17	Shock reflection domain, for $\gamma = 1.4$ considering only the von Neumann condition.	27
2.18	Flow over a wedge producing sonic flow behind the reflected shock. That is to say, $M_2 = 1$	27

2.19	Example of the sonic reflected shock condition for $M = 2.5$ and $\gamma = 1.4$	28
2.20	Shock reflection domain, for $\gamma = 1.4$ considering only the sonic reflected shock condition.	29
2.21	Flow over a wedge producing a reflected shock that is perpendicular to the flow behind the incident shock.	30
2.22	Example of the normal reflected shock condition for $M = 1.6$ and $\gamma = 1.4$	30
2.23	Shock reflection domain, for $\gamma = 1.4$ considering only the normal reflected shock condition.	32
2.24	Flow over a wedge producing sonic flow behind the forward-facing reflected shock.	32
2.25	Example of the sonic forward-facing reflected shock condition for $M = 1.45$ and $\gamma = 1.4$	33
2.26	Shock reflection domain, for $\gamma = 1.4$ considering only the sonic forward-facing reflected shock condition.	35
2.27	The shock reflection domain, for $\gamma = 1.4$ considering only the sonic condition.	37
2.28	Complete shock reflection domain for $\gamma = 1.4$	38
2.29	Detailed shock reflection domain for $\gamma = 1.4$, showing the region between Mach 2 and Mach 2.5.	39
3.1	Flow setup used by Azevedo to predict Mach stem height.	43
3.2	Triple point with a Mach stem that is not perpendicular to the flow.	50
3.3	Flow setup, allowing for a sonic throat downstream of the leading characteristic, used to predict the Mach stem height.	54
3.4	Representative mesh refinement for the calculation of the Mach stem height using Amrita.	57
3.5	Enlarged region of a representative mesh refinement for the calculation of the Mach stem height using Amrita.	57
3.6	Comparison of current Mach stem height calculations with current computational results and with previous computation, experimental, and analytic results.	58
3.7	Flow setup, allowing for a moving triple point, used to calculate the Mach stem height growth.	59

3.8	Moving triple point with a Mach stem that is not perpendicular to the flow..	60
3.9	Shock polar illustrating the effects of a moving Mach stem.	62
3.10	A very small Mach stem with a finite angle slipline.	64
3.11	Mach stem velocity as a function of Mach stem height	66
3.12	Theoretical and numerical results for the height of the Mach stem as a function of time with a wedge angle of 23°	67
3.13	Theoretical and numerical results for the height of the Mach stem as a function of time with a wedge angle of 25°	67
3.14	A quasi-schlieren image showing a comparison between the theoretical shock structure and an Euler computation.	68
3.15	Three-dimensional growth of a Mach stem.	69
3.16	Growth of a Mach stem considering a Mach stem with an initial finite width.	70
3.17	Numerical and theoretical growth of Mach stem height and growth in the spanwise direction at $a_\infty t/w=0.11$	71
3.18	Numerical and theoretical growth of Mach stem height and growth in the spanwise direction at $a_\infty t/w=0.39$	71
3.19	Numerical and theoretical growth of Mach stem height and growth in the spanwise direction at $a_\infty t/w=0.79$	72
4.1	Flow setup used for the Amrita simulations of dense gas disturbances.	75
4.2	Quasi-schlieren image showing a dense region of gas inserted upstream of the incident shock.	76
4.3	Quasi-schlieren image showing a dense region of gas after it has passed through the incident shock.	77
4.4	Quasi-schlieren image showing the bow shock of a dense region of gas impacting the wedge.	78
4.5	Quasi-schlieren image showing the reflected bow shock, the disturbed bow shock and the recompression shock.	79
4.6	Quasi-schlieren image showing the impact shock generated by the impact of the dense region of gas on the wedge.	80
4.7	Quasi-schlieren image showing the impact shock influencing the leading oblique shock.	81

4.8	Quasi-schlieren image showing the impact shock after it has passed over the reflection point.	82
4.9	Quasi-schlieren image showing the creation of a Mach stem due to the particle impact on the wedge.	83
4.10	Quasi-schlieren image showing the growing Mach stem created as a result of the dense region of gas impacting the wedge.	84
4.11	Quasi-schlieren image showing a dense region of gas impacting a wedge where transition from regular reflection to Mach reflection does not occur.	86
4.12	Quasi-schlieren image showing a dense region of gas impacting a wedge where transition from regular reflection to Mach reflection does occur.	87
4.13	Three-dimensional computations of 55 lumps of dense gas placed upstream of the incident shock.	89
4.14	Three-dimensional computations after 55 lumps of dense gas pass through the incident shock.	90
4.15	Three-dimensional computations of the transition from regular reflection to Mach reflection as a result of 55 lumps of dense gas disturbing the flow. . . .	91
4.16	Three-dimensional computations where portions of the Mach stem have reached the steady-state height.	92
4.17	Three-dimensional computations where the entire Mach stem has reached the steady-state height.	93
4.18	Initial density, pressure, and velocity profiles for the Euler solver based on Sedov's equations with $\nu = 2$ and $\gamma = 1.4$	98
4.19	Combination of Sedov's exact solution for strong shocks with Euler computations for weaker shocks.	99
4.20	Flow setup considering energy deposition along the wedge surface showing the blast wave just reaching the point of reflection.	100
4.21	A lower bound on the energy required for the blast wave to reach the point of reflection for the cylindrical case.	102
4.22	A lower bound on the energy required for the blast wave to reach the point of reflection for the spherical case.	103
4.23	Comparison of theoretical estimates and computational results for the energy required to cause transition from regular reflection to Mach reflection.	104

5.1	Flow setup with asymmetric wedges.	106
5.2	Example shock polar at the detachment condition with asymmetric wedges. .	107
5.3	Detachment condition for asymmetric wedges.	107
5.4	Example shock polar at the von Neumann condition with asymmetric wedges.	108
5.5	Von Neumann condition for asymmetric wedges.	108
5.6	Dual-solution domain for $M = 4$ for asymmetric wedges.	109
5.7	Equivalence curves between symmetric and asymmetric wedge configurations.	110
6.1	Overview drawing of the Ludwieg tube laboratory.	112
6.2	Composite schlieren image of the Mach waves generated in the Ludwieg tube nozzle by thin transverse strips of adhesive tape attached to the top and bottom walls.	113
6.3	Distribution of Mach number along the centerline of the Ludwieg tube nozzle from measurements of the Mach wave angles.	114
6.4	Mach 4.0 nozzle contour designed by J. J. Korte of NASA Langley Research Center.	115
6.5	Start-up process of the Mach 4 nozzle computed using Amrita.	116
6.6	Experimental flow at approximately 50 ms into the test time showing unstart. .	117
6.7	Simulation showing the unstart of the nozzle, 51.8 ms after diaphragm rupture, as a result of the reflected shock from the end of the dump tank.	117
6.8	Quasi-schlieren x - t diagram of the nozzle unstart with the downstream diaphragm.	118
6.9	Simulation showing undisturbed flow in the test section, 51.7 ms after diaphragm rupture.	119
6.10	Dump tank with modifications including the addition of a baffle and a tube extension.	120
6.11	Simulation showing the starting of the nozzle, 2.7 ms after the rupturing of the diaphragm located just upstream of the converging section of the nozzle. .	120
6.12	Simulation showing the correctly started flow 50.1 ms after the rupturing of the diaphragm located just upstream of the converging section of the nozzle. .	120
6.13	Quasi-schlieren x - t diagram of the nozzle successfully starting with the upstream diaphragm.	121

6.14	Wedge assembly consisting of a wedge, a connecting rod, a support structure, a motor, and a gearhead. The wedge rotates about the rod that runs through the wedge and the two vertical supports.	123
7.1	Demonstration of the hysteresis phenomenon in the Ludwieg tube. The initial wedge angles are set so that only regular reflection is possible.	126
7.2	Demonstration of the hysteresis phenomenon in the Ludwieg tube. The conditions are within the dual solution domain, just below the point where transition to Mach reflection will occur due to tunnel disturbances.	126
7.3	Demonstration of the hysteresis phenomenon in the Ludwieg tube. Transition to Mach reflection is just beginning to occur due to tunnel disturbances. . . .	127
7.4	Demonstration of the hysteresis phenomenon in the Ludwieg tube. The upper wedge angle is relatively large, and a large Mach stem exists.	127
7.5	Demonstration of the hysteresis phenomenon in the Ludwieg tube. The upper wedge angle is relatively large, and a large Mach stem exists.	128
7.6	Demonstration of the hysteresis phenomenon in the Ludwieg tube. Return to regular reflection as the von Neumann condition is approached.	129
8.1	Initial shock configuration below the von Neumann condition. Only regular reflection is possible.	132
8.2	Shock configuration before laser energy is deposited onto the lower wedge. Both regular reflection and Mach reflection are possible.	132
8.3	Blast wave resulting from the deposition of energy on the lower wedge using a laser.	133
8.4	The leading shock is disturbed in the region of the reflection due to the laser energy, which was previously deposited. Transition to Mach reflection will immediately follow.	133
8.5	Energy deposition points on the lower wedge.	135
8.6	Effect of wedge rotation speed on tripping due to natural tunnel disturbances.	136
8.7	Tunnel disturbances, such as dust, are capable of tripping the flow from regular reflection to Mach reflection.	137

9.1	Comparison of current experimental Mach stem height results against theoretical estimates, previous experimental results, and current computational work done using Amrita.	140
9.2	Comparison of current experimental Mach stem growth rates with theoretical estimates.	141
A.1	Complete shock reflection domain, for $\gamma = 1.4$, note that in the small region between the sonic and detachment condition RR is replaced by RRs. The symbol + refers to supersonic conditions and the symbol – refers to subsonic conditions.	148
A.2	Complete shock reflection domain, for $\gamma = 1.4$, note that in the small region between the sonic and detachment condition RR is replaced by RRs.	149
A.3	Complete shock reflection domain, for $\gamma = 5/3$, note that in the small region between the sonic and detachment condition RR is replaced by RRs.	150
A.4	Complete shock reflection domain, for $\gamma = 2$, note that in the small region between the sonic and detachment condition RR is replaced by RRs.	151
B.1	Detachment condition for asymmetric wedges.	153
B.2	Von Neumann condition for asymmetric wedges.	154
B.3	Dual solution domain for M=4 for asymmetric wedges.	155
C.1	Mach 4.0 nozzle assembly drawing of the various primary components and their relationships to each other.	165
C.2	Mach 4 nozzle (part 1) drawing.	166
C.3	Test section (part 6) drawing.	167
C.4	Window housing (part 9) drawing.	168
C.5	Window clamp (part 10) drawing.	169
C.6	Test section flange (part 11) drawing.	170
C.7	Window blank (part 12) drawing.	171
C.8	Injector flange (part 14) drawing.	172
C.9	Injector block (part 15) drawing.	173
D.1	Adjustable wedge model assembly drawing of the various primary components and their relationships to each other.	175

D.2	Bearing mount (part 1) drawing.	176
D.3	Window cap (part 6) drawing.	177
D.4	Motor mount (part 9) drawing.	178
D.5	Rocket (part 10) drawing.	179
D.6	Moving wedge (part 11) drawing.	180
D.7	Rocker housing (part 16) drawing.	181
D.8	Rocker housing lid (part 17) drawing.	182
D.9	Fixed wedge model assembly drawing of the various primary components and their relationships to each other.	184
D.10	Fixed wedge (part 1) drawing.	185
D.11	Vertical support (part 2) drawing.	186
D.12	Window cap (part 4) drawing.	187

List of Tables

8.1	Summary of transition for various energy deposition locations.	134
9.1	Mach stem heights measured at various upper wedge angles.	139
C.1	Mach 4 nozzle contour (in inches) by J. J. Korte.	156
C.2	Primary components of the Mach 4 nozzle.	164
D.1	Primary components of the adjustable wedge model.	174
D.2	Primary components of the fixed wedge model.	183

Chapter 1

Introduction

When a shock wave propagates over a solid wedge, the flow generated by the shock impinges on the wedge thus generating a second reflected shock, which ensures that the velocity of the flow is parallel to the wedge surface. Viewed in the frame of the reflection point, this flow is locally steady, and the configuration is referred to as a pseudosteady flow. When the angle between the wedge and the primary shock is sufficiently large, a single reflected shock is not able to turn the flow to a direction parallel to the wall and transition to Mach reflection occurs. These are illustrated in Figure 1.1

Much of the research in the field of Mach reflection has been done in this pseudosteady configuration. The concern of this thesis, however is the transition between regular and Mach reflection in steady flow. If a wedge is placed into a steady supersonic flow in such a way that its oblique attached shock impinges on a flat wall parallel to the free stream, the shock turns the flow toward the wall and a reflected shock is required to turn the flow back to a direction parallel to the wall. When the shock angle exceeds a certain value, the deflection achievable by a single reflected shock is insufficient to turn the flow back to a direction parallel to the wall and transition to Mach reflection is observed. Both regular reflection and Mach reflection in steady flow are illustrated in Figure 1.2.

The fundamental question regarding regular reflection and Mach reflection, is at which flow conditions they occur.

Most steady flow studies of shock reflection have considered a wedge placed above a planar surface. In experiments, the planar surface is most often replaced by a plane of symmetry in order to remove boundary layer effects. In his 1943 report, von Neumann [1] also considered this problem. He did so by first considering regular reflection, where the incident shock reflects directly off the planar surface. He notes that the purpose of the

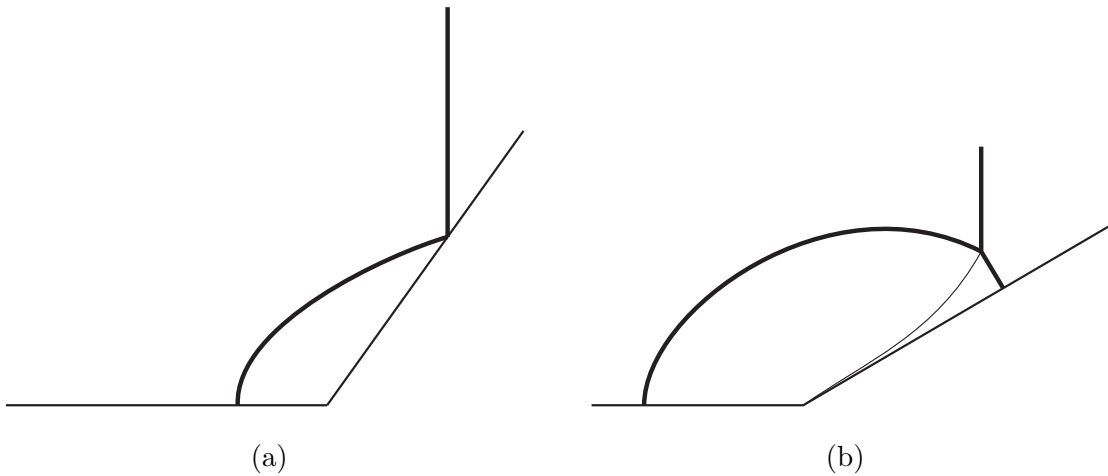


Figure 1.1: Pseudosteady regular reflection (a) and Mach reflection (b). The primary shock is traveling from left to right over the wedge.

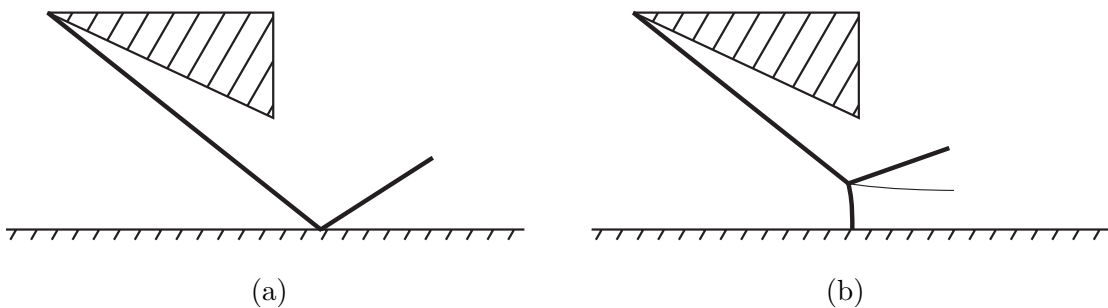


Figure 1.2: Steady regular reflection (a) and Mach reflection (b). The free-stream flow is from left to right.

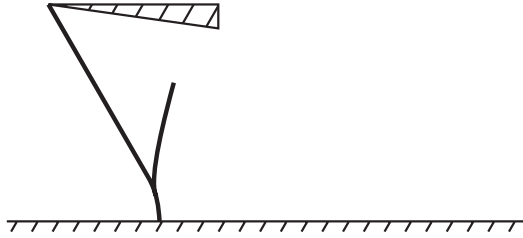


Figure 1.3: Steady von Neumann reflection. The free-stream flow is from left to right.

reflected shock is to turn the flow from behind the incident shock back to its initial angle. However, he considers the fact that the reflected shock has a maximum turning angle, and therefore a reflection directly off the planar surface (regular reflection) may not always be possible. Based on this maximum turning angle, he defines what he calls the extreme condition, which would later come to be known as the detachment condition. Simply put, the detachment condition is the largest incident shock angle for which the oblique reflected shock can turn the flow back to its original angle.

Von Neumann [1] in his analysis of Mach reflection considers the pseudosteady case. He defines Mach reflection as the configuration in which the incident shock does not reflect off the planar surface, but rather reflects from a triple point above the planar surface. In addition to the reflected shock from this triple point there is an additional shock, the Mach stem, which lies between the triple point and the planar surface. Also, a slipline originates from this triple point because of the different flow conditions behind the reflected shock and behind the Mach stem; even though the pressures behind both are the same.

In addition, von Neumann [1] postulates the possibility for what he calls quasi-stationary Mach reflection, which in the case of steady flow is simply Mach reflection. The condition for quasi-stationary Mach reflection is that the pressure behind the reflected shock is equal to the pressure obtained behind a stationary normal shock. This condition would later be renamed the von Neumann condition. For low Mach numbers von Neumann calculated that Mach reflection was not possible, although something resembling Mach reflection existed in experiments. He called this type of reflection extraordinary Mach reflection, which would later be renamed von Neumann reflection. Von Neumann reflection is illustrated in Figure 1.3.

The conclusion of von Neumann [1] is that in the parameter range where Mach reflection is possible, transition will in practice occur at the quasi-stationary Mach reflection condition,

i.e., the von Neumann condition. He also concluded that when Mach reflection is not possible, transition to extraordinary Mach reflection, i.e., von Neumann reflection, will occur at the detachment condition.

Although von Neumann's work [1] was a definitive step in the understanding of shock reflection phenomena, it missed some of the subtleties involved. In particular, the difference between the transition conditions for steady and pseudosteady flows were not recognized.

Later in 1975, Henderson and Lozzi [2] proposed a mechanical equilibrium condition. This condition states that the pressure behind the reflection must be continuous as the flow transitions from regular reflection to Mach reflection. This condition therefore corresponds to the von Neumann condition. Experiments in 1977 by Hornung and Kychakoff [3] observed that in steady flow at high Mach number transition occurs at the von Neumann angle.

In 1979, the distinction between the transition criteria for steady flows and those for pseudosteady flows was pointed out by Hornung, Oeretel, and Sandeman [4]. They argue that the von Neumann condition should be used for steady flows and the sonic condition for pseudosteady flows. For practical purposes the sonic and detachment conditions are almost indistinguishable, and different papers state the transition criteria as either the detachment condition or sonic condition. A single condition encompassing both the von Neumann condition for steady flows and the sonic condition for pseudosteady flows was referred to as the information condition. The condition states that in order for a Mach stem to exist, it is necessary that information about a length scale can reach the region near the reflection point in order to scale the Mach stem length.

In steady flow, any disturbance in the flow that is strong enough to set up a small Mach reflection would open an information path from the boundary conditions to the reflection point. This is because once the Mach stem is set up, the flow behind the Mach stem is subsonic, and a permanent information path is established. The original paper proposed that start-up disturbances were the cause of the initial transition, but later experiments showed that basic tunnel disturbances, such as dust or unsteadiness of the free stream, could also open such an information path. This also implies that without any disturbances, regular reflection is possible at shock angles greater than that at the von Neumann condition. This means that in steady flow, between the von Neumann condition and the detachment condition there is a region where both regular reflection and Mach reflection are possible, which is referred to as the dual-solution domain. The existence of

the dual-solution domain suggested the possibility of hysteresis in transition between the two reflection configurations. However, experiments by Hornung et al. did not observe regular reflection past the von Neumann condition. In the pseudosteady case, information about a length scale can reach the reflection point only if the flow behind the regular reflection is subsonic; therefore, in the pseudosteady case transition to Mach reflection occurs at the sonic condition, which is very near the detachment condition.

In 1979, Henderson and Lozzi [5] attempted to obtain regular reflection above the von Neumann condition, without success. Experiments by Hornung and Robinson in 1982 [6], further strengthened the argument that in steady flow transition occurs at the von Neumann condition.

In pseudosteady flows, accurate predictions of Mach stem height exist; however, until 1989, similar predictions of Mach stem height in steady flows did not exist. In 1982, the experiments of Hornung and Robinson [6] provided data on the Mach stem height in steady flow for various flow parameters. In 1989, Azevedo [7] published analytical predictions of the Mach stem height as part of his dissertation. The theory presented by Azevedo offered a simple solution for the Mach stem height that, however, underpredicted experimental values.

Using direct simulation Monte Carlo computations, Ivanov, Gimelshein, and Beylich [8] were able to demonstrate that there is indeed a hysteresis phenomenon between the von Neumann and detachment condition, as predicted by Hornung, Oeretel, and Sandeman [4]. No noise was added in the computations done by Ivanov and Gimelshein, and the transition from regular reflection to Mach reflection was seen to occur at the detachment condition. In their computations, they also examined transition in the opposite direction and found that transition from Mach reflection to regular reflection occurred within the dual solution domain, at neither the detachment nor von Neumann condition. In the same year, Chpoun et al. [9] confirmed the hysteresis phenomenon experimentally. A more detailed experimental study by Ivanov et al. [10] also demonstrated hysteresis with regular reflection up to the vicinity of the detachment condition.

Further experimental confirmation of the possibility of regular reflection existing in the dual solution domain was given by Sudani et al. in 2002 [11]. In this paper, Sudani et al. also show that various small disturbances can trip the flow from regular reflection to Mach reflection in the dual solution domain. Their findings, as well as those of Chpoun et al.

[9] and Ivanov et al. [12], explain why in most previous experiments transition occurred at the von Neumann condition and not inside the dual-solution domain. In particular, these authors showed that even small flow disturbances, such a tunnel dust, can cause transition from regular reflection to Mach reflection.

Some researchers, including Yan et al. [13], have suggested that using energy deposition to trip from Mach reflection to regular reflection within the dual-solution domain is possible. Both the experiments and the computations were done within the dual-solution domain with fixed wedge positions and an initial Mach reflection. In experiments, they were not able to transition from Mach reflection to regular reflection. They were only able to temporarily decrease the size of the Mach stem. In numerical experiments, they successfully transitioned from Mach reflection to regular reflection. This transition may however have been due to insufficient refinement, and the Mach stem simply decreases to a size smaller than a cell size and therefore effectively disappears.

1.1 Outline and Contributions

In this section an outline of the subsequent sections is presented, followed by an overview of the new contributions made by each section. Detailed substantiation of these claims are left to the respective sections.

First, a detailed shock analysis determining the domain boundaries of shock reflection in steady flow is presented. In particular, where possible, analytic solutions for boundaries between different solutions are presented and limiting values for these boundaries are given.

A new method for estimating the steady-state size of a Mach stem is presented based on the flow parameters and the flow geometry. These results are compared with previous theories, experiments and computations, as well as with current experiments and computations. This analysis of Mach stem height is expanded to allow for a moving triple point. In particular, the analysis shows that for a given triple point speed, there exists a single corresponding Mach stem height. A theory for the Mach stem growth rate is then developed based on this analysis. The growth rate of the Mach stem is compared with current experiments and computations.

A detailed look at the effects of disturbances on the possibility of tripping the flow between regular reflection and Mach reflection in the dual-solution domain is presented. It

is observed that the shock created as a result of the impact of dense particles on the wedge can cause transition from regular reflection to Mach reflection. Because of this result, the simplified case of direct energy deposition on the wedge is considered. A simple estimate of the lower bound of the required energy for transition to occur is presented. This estimate is compared with computational work on the minimum energy required for transition from regular reflection to Mach reflection to occur.

Most of the work in this thesis focuses on the case the reflection is generated by two wedges with a symmetry plane between them. However, for experimental simplicity, the experiments conducted as part of this thesis were performed with one fixed wedge and one movable wedge. Therefore, a simple method by which to compare symmetric and asymmetric results is presented.

The experimental setup for the hysteresis and the energy deposition experiments is presented. First, the hysteresis phenomenon is confirmed to exist in the Ludwieg tube facility. Since the Ludwieg tube facility has a short test time, only 100 ms, the effect of wedge rotation speed on the transition from regular reflection to Mach reflection is studied. The transition from regular reflection to Mach reflection due to deposition of energy on one of the wedges is also examined. This transition due to energy deposition leads to a rapid growth of the Mach stem from its initial regular reflection condition to the steady-state Mach stem height. This growth is compared with numerical and theoretical predictions.

The main contributions of this thesis are presented below:

- A more accurate prediction for the steady-state Mach stem height is given. The prediction model is based on gas-dynamical and geometric flow considerations, and focuses on determining the location of the sonic throat formed behind the Mach stem. This sonic throat is allowed to occur anywhere downstream of the leading characteristic of the aft wedge expansion.
- A prediction for the Mach stem growth rate from regular reflection to the steady-state Mach stem height is presented. This is the first theory of the growth rate of a Mach stem, and shows that Mach stems smaller than their steady-state size will grow until they reach their steady-state height.
- Numerical experiments show that small flow disturbances, such as dust particles or energy deposition, can cause transition from regular reflection to Mach reflection

inside the dual-solution domain. For the case of a dense particle, the importance of the impact shock, created when the particle impacts one of the wedges, is observed.

- Experiments show that using the newly constructed Mach 4.0 nozzle and the existing Ludwieg tube, hysteresis between regular reflection and Mach reflection can be observed. Regular reflection was maintained approximately halfway into the dual-solution domain. It is experimentally shown that the faster the shock configuration enters the dual-solution domain the further into the dual-solution domain regular reflection can be maintained.
- Experiments show that depositing energy onto one of the wedges can cause transition from regular reflection to Mach reflection. The importance of the deposition location is observed and is qualitatively consistent with the numerical and theoretical work of this thesis.
- Both the steady-state Mach stem height and Mach stem growth rate were measured experimentally. Excellent agreement between the Mach stem height theory, developed in the thesis, and experimental measurements is seen. The time to reach the steady-state Mach stem height agrees well with the theory developed in this thesis, although significant differences on the time-history of the Mach stem exist.

Chapter 2

Shock Reflection Domain

2.1 General Compressible Flow Equations

Throughout this thesis the medium is assumed to be a perfect gas. The reason for presenting yet another discussion of shock reflection domains is that a number of analytical solutions have been found that have not previously been given. Many compressible flow equations will be used that may be found, e.g., in NACA Report 1135 [14]. The pressure ratio across an oblique shock, ξ , is a function of the incoming Mach number, M_x , the shock angle, α , and the ratio of specific heats, γ . M_x refers to the Mach number in region x ; the free-stream Mach number is denoted M_∞ . Note that regardless of which way the shock is inclined the shock angle is always taken to be positive. These basic parameters are shown in Figure 2.1. Specifically, the pressure ratio is

$$\xi(M_x, \gamma, \alpha) = \frac{2\gamma M_x^2 \sin^2 \alpha - (\gamma - 1)}{\gamma + 1}. \quad (2.1)$$

Similarly, the flow deflection, θ , and Mach number, M , behind an oblique shock are also functions of M_x , γ , and α , and are given by

$$\theta(M_x, \gamma, \alpha) = \cot^{-1} \left[\left(\frac{(\gamma + 1) M_x^2}{2(M_x^2 \sin^2 \alpha - 1)} - 1 \right) \tan \alpha \right], \quad (2.2)$$

and

$$M(M_x, \gamma, \alpha) = \sqrt{\frac{(\gamma + 1)^2 M_x^4 \sin^2 \alpha - 4(M_x^2 \sin^2 \alpha - 1)(\gamma M_x^2 \sin^2 \alpha + 1)}{[2\gamma M_x^2 \sin^2 \alpha - (\gamma - 1)][(\gamma - 1) M_x^2 \sin^2 \alpha + 2]}}. \quad (2.3)$$

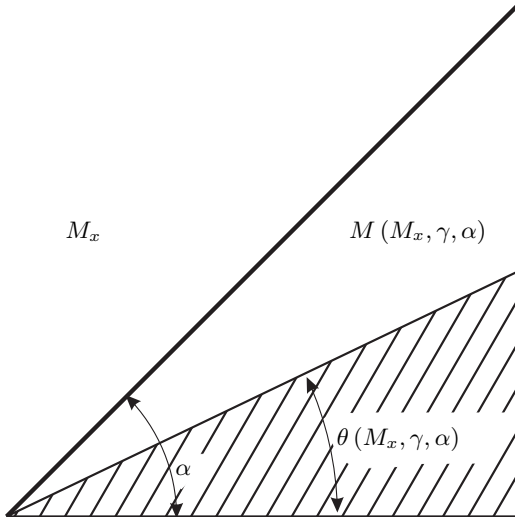


Figure 2.1: Basic flow parameters. M_x is the incoming Mach number, θ is the flow deflection angle, α is the shock angle, and $M(M_x, \gamma, \alpha)$ is the flow Mach number behind the oblique shock.

Setting the right-hand side of Equation 2.3 equal to unity produces a special shock angle value, α^* ,

$$\alpha^*(M_x, \gamma) = \sin^{-1} \sqrt{\frac{\gamma - 3 + M_x^2(\gamma + 1) + \sqrt{(\gamma + 1)[(M_x^2 - 3)^2 + \gamma(M_x^2 + 1)^2]}}{4\gamma M_x^2}}. \quad (2.4)$$

Another special value of the shock angle occurs when the flow deflection angle is maximum. This condition is found by setting the derivative of Equation 2.2 with respect to α equal to zero, i.e., $\frac{\partial M(M_x, \gamma, \alpha)}{\partial \alpha} = 0$. The shock angle for maximum deflection, $\alpha^{\theta_{\max}}$, is given by

$$\alpha^{\theta_{\max}}(M_x, \gamma) = \sin^{-1} \sqrt{(\gamma + 1) \frac{M_x^2 - \frac{4}{\gamma+1} + \sqrt{M_x^4 + 8\frac{\gamma-1}{\gamma+1}M_x^2 + \frac{16}{\gamma+1}}}{4\gamma M_x^2}}. \quad (2.5)$$

A final special value of the shock angle is simply the Mach angle, α^μ , which is given by

$$\alpha^\mu(M_x) = \sin^{-1} \frac{1}{M_x}. \quad (2.6)$$

This corresponds to a wave of zero strength.

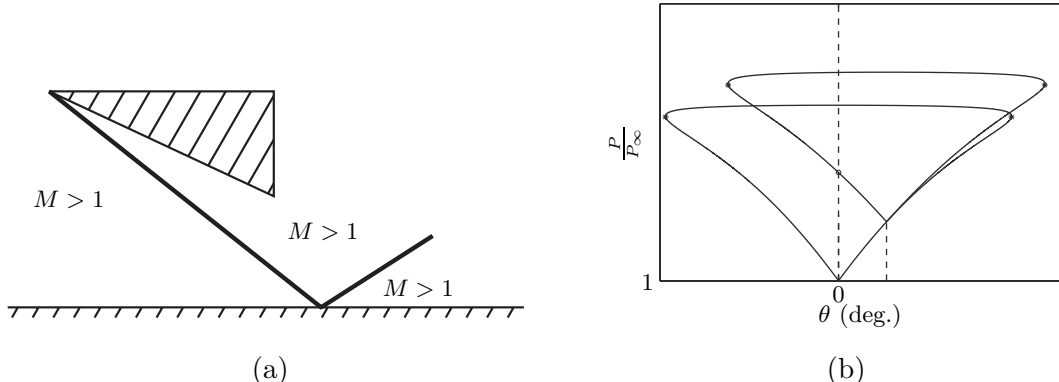


Figure 2.2: Regular reflection with supersonic downstream flow. Part (a) shows an example of regular reflection with supersonic flow downstream of the reflected shock. For simplicity the expansion wave originating from the downstream corner of the wedge is not shown. Part (b) shows an example shock polar diagram demonstrating regular reflection.

2.2 Possible Shock Reflections

There are several possible shock reflections. These are regular reflection with supersonic downstream flow (RR), regular reflection with subsonic downstream flow (RRs), Mach reflection with supersonic flow downstream of the reflected shock (MR), Mach reflection with subsonic flow downstream of the reflected shock (MRs), Mach reflection with a forward facing reflected shock (MRf), inverted Mach reflection (IMR), and von Neumann reflection (vNR).

2.2.1 Regular Reflection

The simplest configuration possible is regular reflection with supersonic flow downstream of the reflected shock. An example of regular reflection is shown in Figure 2.2(a). In this case, the reflected shock turns the flow by the exact same amount as the incoming shock, i.e., the reflected shock turns the flow by the wedge angle so that the flow is again parallel to the free-stream flow. The reflected shock, in this case, is sufficiently weak that the flow behind it remains supersonic. Figure 2.2(b) shows an example shock polar with regular reflection. The point where the reflected shock polar intersects the zero deflection line is denoted with a circle.

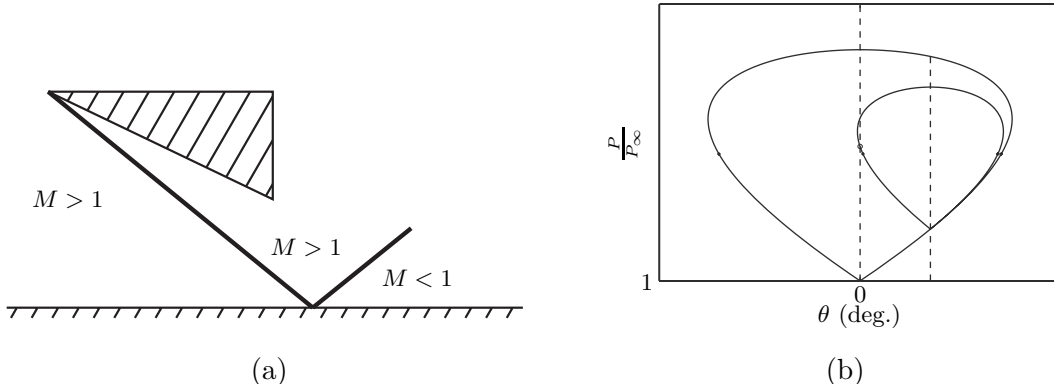


Figure 2.3: Regular reflection with subsonic downstream flow. Part (a) shows an example of regular reflection with subsonic flow downstream of the reflected shock. For simplicity the expansion wave originating from the downstream corner of the wedge is not shown. Part (b) shows an example shock polar diagram demonstrating regular reflection with subsonic flow downstream of the reflected shock. The reflected shock polar only crosses the zero deflection line above the sonic point.

2.2.2 Regular Reflection with Subsonic Downstream Flow

This case is identical to the regular reflection case, except that the flow downstream of the reflected shock is subsonic. An example of regular reflection with subsonic downstream flow is shown in Figure 2.3(a). As in the previous case, the reflected shock turns the flow by the exact same amount as the incoming shock, i.e., the reflected shock turns the flow by the wedge angle so that it is again parallel to the free-stream flow. The reflected shock is strong enough to cause the flow downstream of it to be subsonic. Since the shock angle for maximum flow deflection and sonic condition are very close, this condition can only exist for a narrow range of shock angles at any given Mach number. Figure 2.3(b) shows a shock polar with subsonic flow downstream of the reflected shock. We see in the figure that the reflected shock polar crosses the zero deflection line above the sonic point (denoted by an asterisk); therefore, the flow downstream of the reflected shock will be subsonic.

2.2.3 Mach Reflection

This case is also known as direct Mach reflection. Mach reflection exists when a reflected shock is unable to turn the flow by the required amount, i.e., the maximum flow turning angle at the given Mach number is less than the wedge angle. The Mach stem is inclined slightly downstream so that the flow behind the triple point is angled slightly downward.

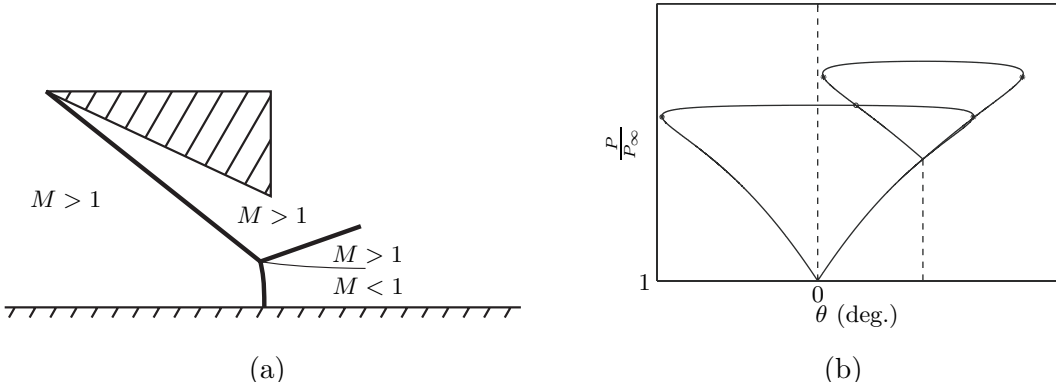


Figure 2.4: Mach reflection. Part (a) shows an example of Mach reflection. For simplicity the expansion wave originating from the downstream corner of the wedge is not shown. Part (b) shows an example shock polar diagram demonstrating Mach reflection. At the triple point the Mach stem has the properties of the flow given at the intersection of the two shock polars, which is denoted by a circle.

This means that the reflected shock needs to turn the flow by an angle that may be smaller than the wedge angle. This is illustrated in Figure 2.4(a). The flow behind the reflected shock and the flow behind the Mach stem must have the same flow angle and pressure. Figure 2.4(b) shows a shock polar for Mach reflection. The circle indicates the intersection of the reflected shock polar and the incident shock polar, giving pressure and flow angle behind the reflected shock and behind the Mach stem at the triple point. Further from the triple point, the Mach stem has the properties given by the points along the incident shock polar between the circle and the zero deflection line.

2.2.4 Mach Reflection with Subsonic Downstream Flow

This case is almost identical to the Mach reflection case except the flow behind the reflected shock is subsonic. Mach reflection with subsonic downstream flow, like Mach reflection, exists when a reflected shock is unable to turn the flow by the required amount, i.e., the maximum flow turning angle at the given Mach number is less than the wedge angle. The Mach stem is inclined slightly downstream (with concave upstream curvature) so that the flow behind the triple point is angled slightly downward. This means that the reflected shock no longer needs to turn the flow by the wedge angle but is strong enough to produce subsonic downstream flow. This is illustrated in Figure 2.5(a). The flow behind the reflected shock and the flow behind the Mach stem must have the same flow angle and the same pressure.

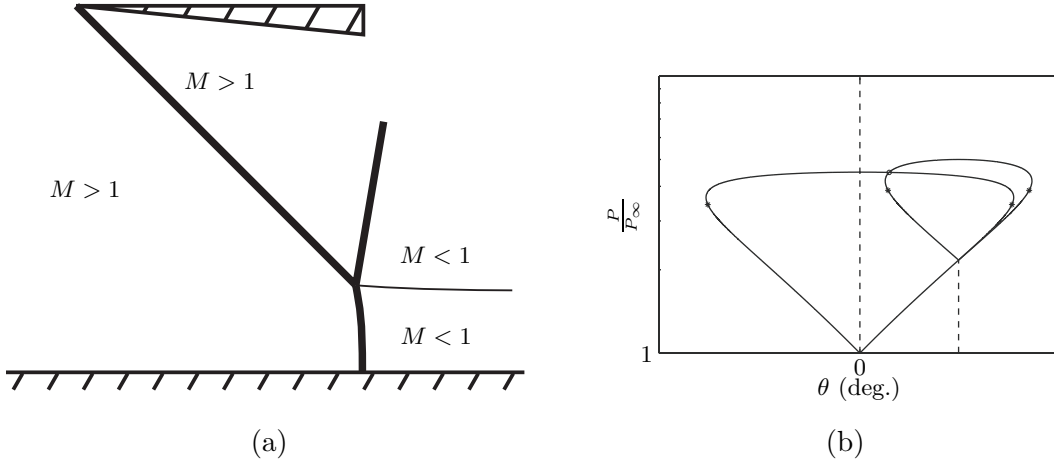


Figure 2.5: Mach reflection with subsonic downstream flow. Part (a) shows an example of Mach reflection with subsonic flow downstream of the reflected shock. For simplicity the expansion wave originating from the downstream corner of the wedge is not shown. Part (b) shows an example shock polar diagram demonstrating Mach reflection with subsonic flow downstream of the reflected shock. At the triple point the Mach stem has the properties of the flow given at the intersection of the two shock polars, which is denoted by a circle.

Figure 2.5(b) shows the reflected shock polar.

2.2.5 Mach Reflection with a Forward-Facing Reflected Shock

It is possible for Mach reflection to exist with a forward facing reflected shock, i.e., the reflected shock is inclined upstream at the triple point (convex upstream curvature). This condition can only exist if the flow downstream of the reflected shock is subsonic. This is necessary in order to allow the reflected shock to curve and become perpendicular to the wedge at the wedge surface, see Figure 2.6(a). The flow behind the reflected shock and the flow behind the Mach stem must have the same flow angle and the same pressure. Figure 2.6(b) shows the reflected shock polar with the reflected shock intersecting the incident shock to the right of the initial deflection angle. The fact that the intersection, illustrated by the circle, occurs to the right of the initial deflection angle means that the reflected shock is forward facing.

2.2.6 Inverted Mach Reflection

In certain cases, it is possible for the Mach stem to be inclined upstream so that the flow behind the triple point is inclined upward. The flow downstream of the reflected shock is also subsonic in this case. This is necessary in order to allow downstream disturbances

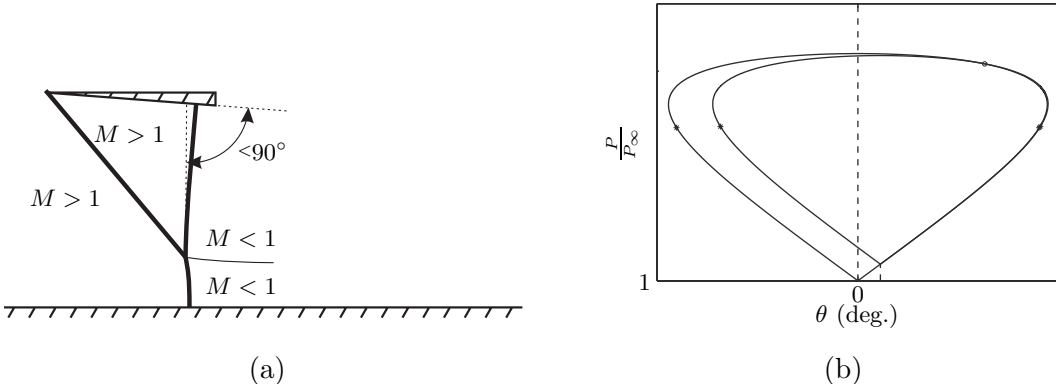


Figure 2.6: Mach reflection with a forward-facing reflected shock. Part (a) shows an example of Mach reflection with a forward facing reflected shock. The flow downstream of the reflected shock is subsonic. For simplicity the expansion wave originating from the downstream corner of the wedge is not shown. Part (b) shows an example shock polar where the reflected shock polar intersects the incident shock polar to the right of the initial deflection angle.

to influence the shock configuration. Inverted Mach reflection can only exist when regular reflection is also possible, since in inverted Mach reflection the reflected shock has to turn the flow by more than the wedge angle, see Figure 2.7(a). The flow behind the reflected shock and the flow behind the Mach stem must have the same flow angle and the same pressure. Figure 2.7(b) shows the shock polar and a circle indicates the intersection of the incident and the reflected shock polars. This intersection occurs to the left of the zero deflection line; hence, the Mach reflection will be inverted.

2.2.7 Von Neumann Reflection

The most complicated type of reflection is von Neumann reflection. This occurs when the reflected shock polar never intersects the incident shock polar, as shown in Figure 2.8(b). A simplified schematic of von Neumann reflection is shown in Figure 2.8(a). Because the details of von Neumann reflection are outside the scope of this thesis, readers are referred to the recent work by Skews and Ashworth [15], who present experimental verification of the details of von Neumann reflection. Their experimental work appears to confirm the existence of a series of supersonic patches and shocks behind the intersection of the incident and the reflected shocks as suggested by Tesdall and Hunter [16].

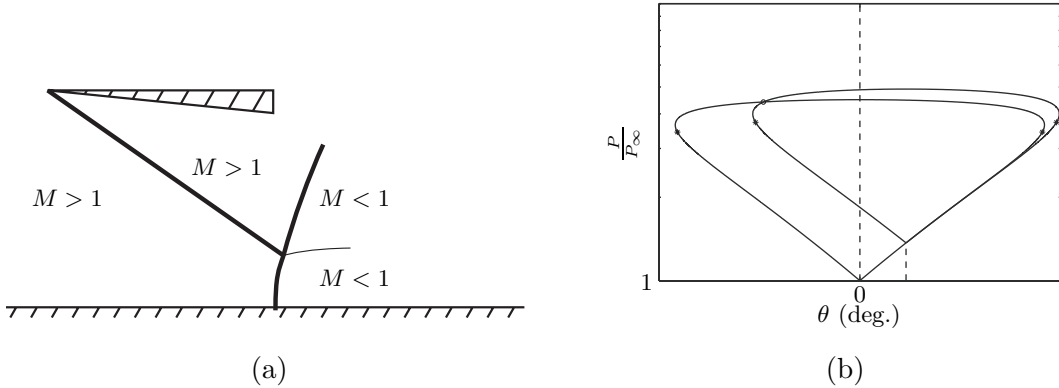


Figure 2.7: Inverted Mach reflection. Part (a) shows an example of inverted Mach reflection where the flow downstream of the triple point is inclined upward. The flow downstream of the reflected shock is subsonic. For simplicity the expansion wave originating from the downstream corner of the wedge is not shown. Part (b) shows an example shock polar in the case of inverted Mach reflection. The intersection between the incident and the reflected shock polars occurs to the left of the zero deflection line.

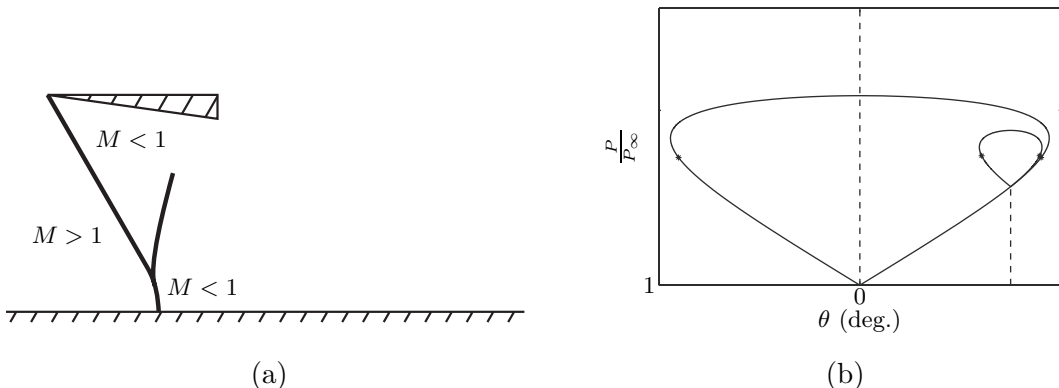


Figure 2.8: Von Neumann reflection. Part (a) shows an example of von Neumann reflection. There is no true Mach stem, since the incident shock simply curves and becomes perpendicular to the surface. Because of the lack of a true Mach stem, a triple point is not clearly defined. For simplicity the expansion wave originating from the downstream corner of the wedge is not shown. Part (b) shows an example shock polar in the case of von Neumann reflection. In this case the incident and the reflected shock polars do not intersect and there is no triple point solution.

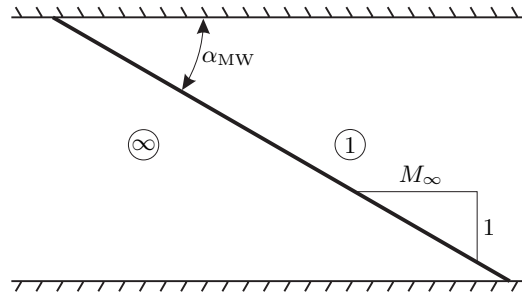


Figure 2.9: Flow over a zero-degree wedge producing a Mach wave. The flow in region 1 is therefore identical to the free-stream flow.

2.3 Domain Boundaries

2.3.1 Mach Wave Condition

For any given free-stream Mach number, M_∞ , a minimum shock angle exists. This angle is the Mach wave angle, α_{MW} , and is given simply by

$$\alpha_{MW} = \alpha^\mu(M_\infty). \quad (2.7)$$

This defines the lower boundary of the Mach reflection domain, since no incident shock can exist with a shock angle less than α_{MW} . A Mach wave produces a zero-flow deflection angle. A representative Mach wave is shown in Figure 2.9. An example of the shock reflection domain considering only the Mach reflection condition is shown in Figure 2.10.

2.3.2 Sonic Incident Shock Condition

If the incident shock is strong (i.e., if the flow behind the incident shock is subsonic), a reflected shock is not possible; therefore, no shock reflection can occur. This sets the upper boundary for the reflection domain since no incident shock with a higher angle can produce a shock reflection. This boundary is defined by the flow behind the incident shock being sonic. Specifically, the relation for the leading shock angle at this condition, α_{SIS} , is given by

$$\alpha_{SIS} = \alpha^*(M_\infty, \gamma). \quad (2.8)$$

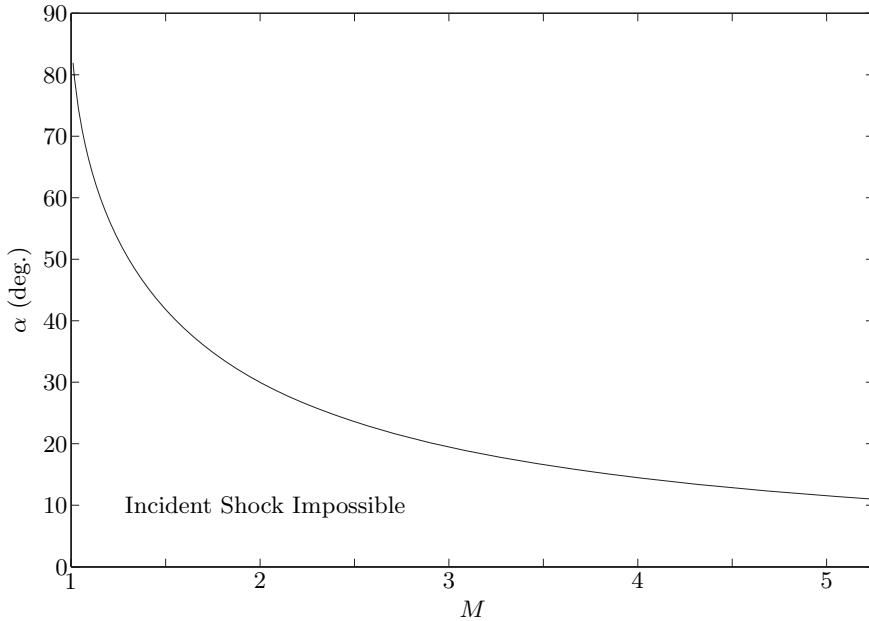


Figure 2.10: Shock reflection domain, for $\gamma = 1.4$, considering only the Mach wave condition.

In the limit of M_∞ going to ∞ , this relationship becomes

$$\lim_{M_\infty \rightarrow \infty} \alpha_{SIS} = \sin^{-1} \sqrt{\frac{\gamma + 1}{2\gamma}}. \quad (2.9)$$

The reflection domain, for $\gamma = 1.4$, considering only the sonic incident shock condition, is shown in Figure 2.11. No shock reflection is possible for shock reflection above α_{SIS} .

2.3.3 Detachment Condition

The detachment condition for a given Mach number is defined as the incident shock angle at which the maximum flow turning angle by the reflected shock equals the flow turning angle of the incident shock. For a shock angle larger than that at the detachment condition regular reflection is not possible. This is illustrated by the example in Figure 2.12. An example of the shock polar diagram for the detachment condition is shown in Figure 2.13. To find the incident shock angle at the detachment condition, α_D , the flow turning angle of the incident shock and the maximum flow deflection angle of the reflected shock must be

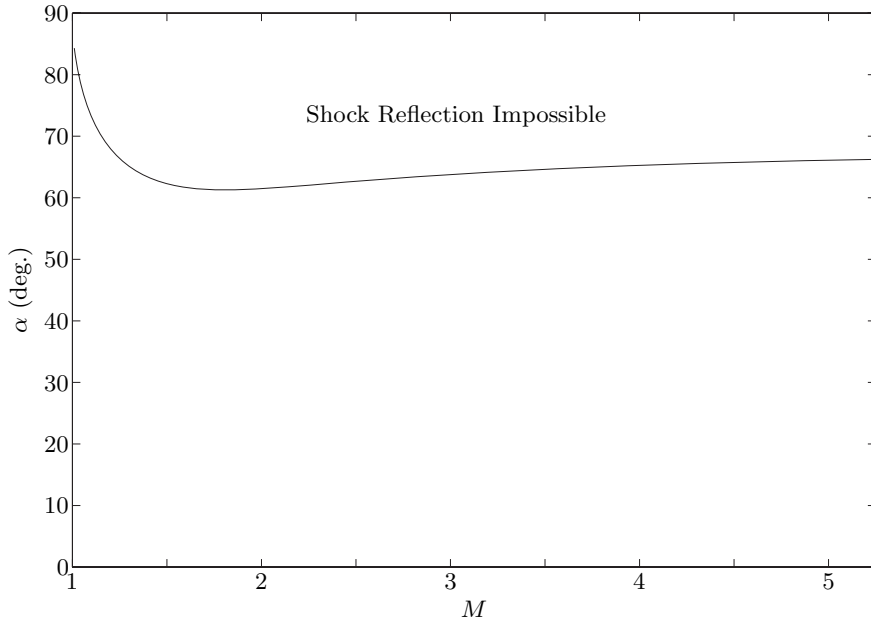


Figure 2.11: Shock reflection domain, for $\gamma = 1.4$ considering only the sonic incident shock condition.

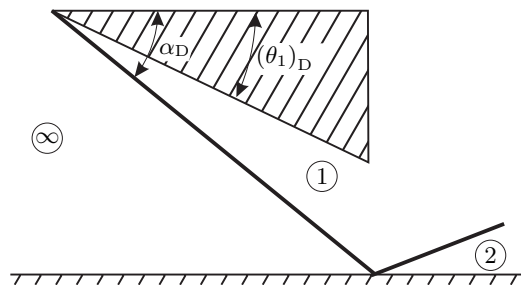


Figure 2.12: Flow over a wedge producing an incident and reflected shock. The wedge angle is equal to the maximum deflection angle of the reflected shock given the flow Mach number in region 1.

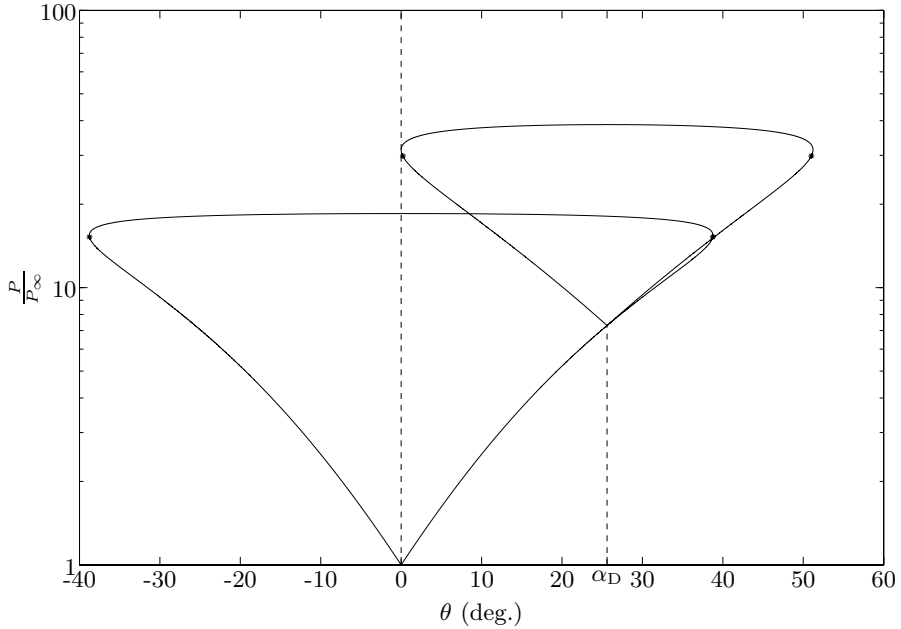


Figure 2.13: Example of the detachment condition for $M = 4$ and $\gamma = 1.4$. Note that the maximum deflection of the reflected shock corresponds to $\theta = 0$. The * denotes the sonic points of the shock loci.

the same. The Mach number behind the leading oblique shock at this condition is

$$(M_1)_D = M(M_\infty, \gamma, \alpha_D). \quad (2.10)$$

Therefore the following must be satisfied,

$$\theta(M_\infty, \gamma, \alpha_D) = \theta\left((M_1)_D, \gamma, \alpha^{\theta_{\max}}((M_1)_D, \gamma)\right). \quad (2.11)$$

Solving Equation 2.11 for α_D produces a fifth-order polynomial in $\sin^2 \alpha_D$,

$$D_0 + D_1 \sin^2 \alpha_D + D_2 \sin^4 \alpha_D + D_3 \sin^6 \alpha_D + D_4 \sin^8 \alpha_D + D_5 \sin^{10} \alpha_D = 0, \quad (2.12)$$

where

$$D_0 = -16 \quad (2.13)$$

$$\begin{aligned} D_1 &= 32M_\infty^2 - 4M_\infty^4 - 48M_\infty^2\gamma - 16M_\infty^4\gamma + 16\gamma^2 - 16M_\infty^4\gamma^2 \\ &\quad + 16M_\infty^2\gamma^3 + 4M_\infty^4\gamma^4 \end{aligned} \quad (2.14)$$

$$\begin{aligned} D_2 &= -16M_\infty^4 + 4M_\infty^6 - M_\infty^8 + 104M_\infty^4\gamma + 16M_\infty^6\gamma - 4M_\infty^8\gamma \\ &\quad - 64M_\infty^2\gamma^2 - 32M_\infty^4\gamma^2 + 8M_\infty^6\gamma^2 - 6M_\infty^8\gamma^2 - 56M_\infty^4\gamma^3 \\ &\quad - 16M_\infty^6\gamma^3 - 4M_\infty^8\gamma^3 - 12M_\infty^6\gamma^4 - M_\infty^8\gamma^4 \end{aligned} \quad (2.15)$$

$$\begin{aligned} D_3 &= M_\infty^8 - 64M_\infty^6\gamma + 4M_\infty^8\gamma + 96M_\infty^4\gamma^2 + 64M_\infty^6\gamma^2 + 14M_\infty^8\gamma^2 \\ &\quad + 64M_\infty^6\gamma^3 + 20M_\infty^8\gamma^3 + 9M_\infty^8\gamma^4 \end{aligned} \quad (2.16)$$

$$D_4 = 8M_\infty^8\gamma - 64M_\infty^6\gamma^2 - 32M_\infty^8\gamma^2 - 24M_\infty^8\gamma^3 \quad (2.17)$$

$$D_5 = 16M_\infty^8\gamma^2 \quad (2.18)$$

Note that there is only one physical solution to this equation, i.e., only one solution for $\sin^2 \alpha_D$ real and bounded between zero and one, for all Mach numbers greater than unity.

In the limit of M_∞ going to ∞ , the polynomial from Equation 2.12 becomes

$$\begin{aligned} \lim_{M_\infty \rightarrow \infty} & \left(-(\gamma+1)^4 \sin^4 \alpha_D + (\gamma+1)^2 (9\gamma^2 + 2\gamma + 1) \sin^6 \alpha_D \right. \\ & \left. - 8(3\gamma^3 + 4\gamma^2 - \gamma) \sin^8 \alpha_D + 16\gamma^2 \sin^{10} \alpha_D \right) = 0 \end{aligned} \quad (2.19)$$

Excluding the case where $\sin^2 \alpha_D = 0$, there are three solutions for $\sin^2 \alpha_D$. The only physical solution is

$$\lim_{M_\infty \rightarrow \infty} \alpha_D = \sin^{-1} \sqrt{\frac{1}{6\gamma} \left(3\gamma^2 + 4\gamma - 1 - \sqrt{9\gamma^4 + 36\gamma^3 - 2\gamma^2 - 44\gamma + 1} \cos \zeta_D \right)}, \quad (2.20)$$

where

$$\zeta_D = \frac{\pi}{3} + \frac{1}{3} \tan^{-1} \frac{12\sqrt{3\gamma(\gamma-1)^{-1}(\gamma+1)^5(27\gamma^2+36\gamma+1)}}{27\gamma^4 - 162\gamma^2 - 152\gamma - 1}. \quad (2.21)$$

An example of the reflection domain, considering only the detachment condition, is shown in Figure 2.14. For shock angles greater than the detachment angle regular reflection is not possible.

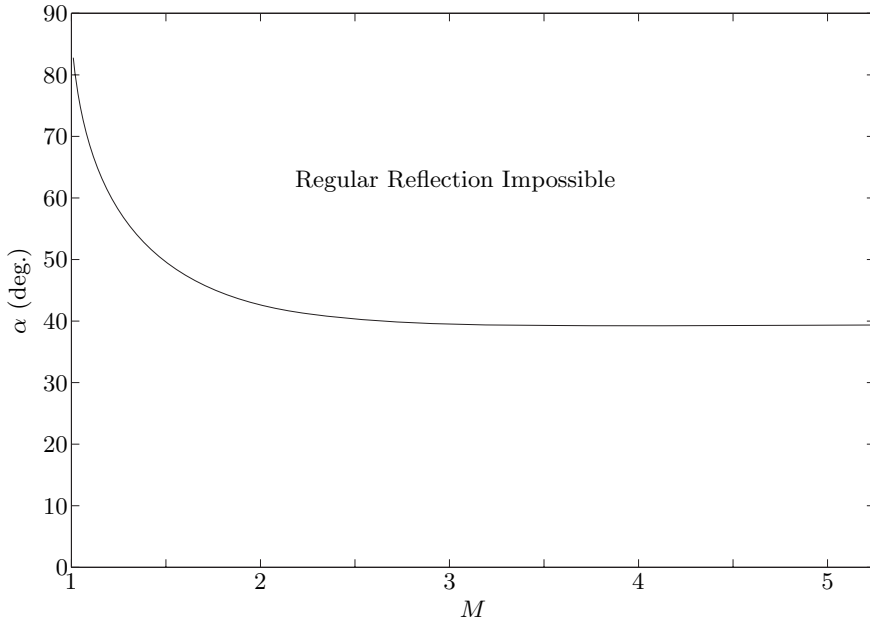


Figure 2.14: Shock reflection domain, for $\gamma = 1.4$ considering only the detachment condition.

2.3.4 Von Neumann Condition

The von Neumann condition is defined as the incident shock angle, α_{vN} , where the total pressure rise across both the incident and reflected shock equals that of a single normal shock. In addition, the flow turning angle of the incident shock equals that of the reflected shock. For shock angles above α_{vN} , inverted Mach reflection is impossible since the reflected shock polar intersects the incident shock polar to the right of the zero-deflection line. Similarly, for shock angles below α_{vN} , direct Mach reflection is impossible since the reflected shock polar intersects the incident shock polar to the left of the zero-deflection line. The shock structure at the von Neumann condition is shown in Figure 2.15.

A representative shock polar at the von Neumann condition is shown in Figure 2.16. The Mach number, behind the leading oblique shock, at this condition is

$$(M_1)_{vN} = M(M_\infty, \gamma, \alpha_{vN}). \quad (2.22)$$

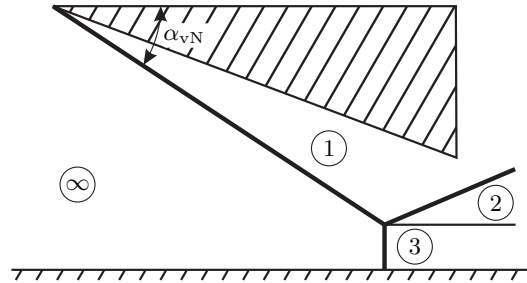


Figure 2.15: Flow over a wedge producing a triple point. At the von Neumann condition the Mach stem is normal to the free-stream flow and therefore the flow behind it is parallel to the bottom surface. In addition, both the pressure and flow angle behind that reflected shock match that of the normal Mach stem.

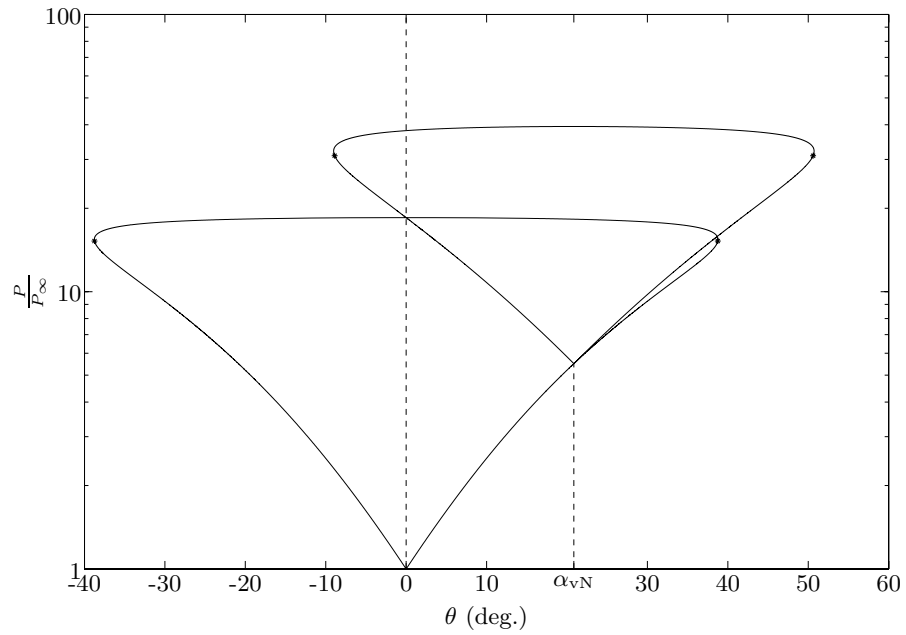


Figure 2.16: Example of the von Neumann condition for $M = 4$ and $\gamma = 1.4$. Note that the intersection of the incident and reflected shock polars corresponds to a normal incident shock. The * denotes the sonic point of the shock loci.

For the von Neumann condition to be satisfied, the following two equations must be true:

$$\xi \left(M_{\infty}, \gamma, \frac{\pi}{2} \right) = \xi \left(M_{\infty}, \gamma, \alpha_{vN} \right) \xi \left((M_1)_{vN}, \gamma, (\alpha_1)_{vN} \right), \quad (2.23)$$

$$\theta \left(M_{\infty}, \gamma, \alpha_{vN} \right) = \theta \left((M_1)_{vN}, \gamma, (\alpha_1)_{vN} \right), \quad (2.24)$$

where $(\alpha_1)_{vN}$ is the angle of the reflected shock with respect to the flow in region 1. The first of these two equations can easily be solved by inverting Equation 2.1,

$$\frac{2\gamma (M_1)_{vN}^2 \sin^2 (\alpha_1)_{vN} - (\gamma - 1)}{\gamma + 1} = \frac{\xi \left(M_{\infty}, \gamma, \frac{\pi}{2} \right)}{\xi \left(M_{\infty}, \gamma, \alpha_{vN} \right)}. \quad (2.25)$$

Therefore,

$$(\alpha_1)_{vN} = \sin^{-1} \sqrt{\frac{(\gamma - 1) + (\gamma + 1) \frac{\xi \left(M_{\infty}, \gamma, \frac{\pi}{2} \right)}{\xi \left(M_{\infty}, \gamma, \alpha_{vN} \right)}}{2\gamma (M_1)_{vN}^2}}. \quad (2.26)$$

The final solution for α_{vN} is found numerically using the following equation:

$$\theta \left(M_{\infty}, \gamma, \alpha_{vN} \right) = \theta \left((M_1)_{vN}, \gamma, \sin^{-1} \sqrt{\frac{(\gamma - 1) + (\gamma + 1) \frac{\xi \left(M_{\infty}, \gamma, \frac{\pi}{2} \right)}{\xi \left(M_{\infty}, \gamma, \alpha_{vN} \right)}}{2\gamma (M_1)_{vN}^2}} \right). \quad (2.27)$$

Note that this equation does not have a solution for all Mach numbers. Specifically, the free-stream Mach number, M_{∞} , must be above a certain value, $(M_{\infty})_{vN}^s$. To calculate this value, let $\alpha_{vN} = \sin^{-1} \frac{1}{(M_{\infty})_{vN}^s} + \epsilon$, where ϵ is a small positive value. From equation 2.2 we see that

$$\theta \left((M_{\infty})_{vN}^s, \gamma, \sin^{-1} \frac{1}{(M_{\infty})_{vN}^s} + \epsilon \right) = \frac{4 [(M_{\infty})_{vN}^s]^2 - 4}{[(M_{\infty})_{vN}^s]^2 (\gamma + 1)} \epsilon + \mathcal{O}(\epsilon^2). \quad (2.28)$$

Similarly, from Equation 2.1,

$$\xi \left((M_{\infty})_{vN}^s, \gamma, \sin^{-1} \frac{1}{(M_{\infty})_{vN}^s} + \epsilon \right) = 1 + \frac{4\sqrt{[(M_{\infty})_{vN}^s]^2 - 1}\gamma}{\gamma + 1} \epsilon + \mathcal{O}(\epsilon^2), \quad (2.29)$$

$$\xi \left((M_{\infty})_{vN}^s, \gamma, \frac{\pi}{2} \right) = \frac{2\gamma [(M_{\infty})_{vN}^s]^2 - (\gamma - 1)}{\gamma + 1}, \quad (2.30)$$

and, from Equation 2.3, we can find the Mach number behind the incident shock in this

special case, $(M_1)_{\text{vN}}^s$, to be

$$(M_1)_{\text{vN}}^s = (M_\infty)_{\text{vN}}^s \frac{2 \left[\sqrt{1 - \frac{1}{[(M_\infty)_{\text{vN}}^s]^2}} \left(2 + [(M_\infty)_{\text{vN}}^s]^2 (\gamma - 1) \right) \right]}{\gamma + 1} \epsilon + \mathcal{O}(\epsilon^2). \quad (2.31)$$

Substituting Equations 2.28 through 2.31 into Equation 2.27, produces

$$-\frac{2 \left([(M_\infty)_{\text{vN}}^s]^2 - 1 \right)^{\frac{5}{4}} \sqrt{-2 + \frac{4[(M_\infty)_{\text{vN}}^s]^2 - 4}{\gamma + 1}}}{(M_\infty)_{\text{vN}}^s \left(2 + [(M_\infty)_{\text{vN}}^s]^2 (\gamma - 1) \right)} \sqrt{\epsilon} + \mathcal{O}(\epsilon) = 0. \quad (2.32)$$

To lowest order this is satisfied when

$$-2 + \frac{4[(M_\infty)_{\text{vN}}^s]^2 - 4}{\gamma + 1} = 0. \quad (2.33)$$

This equation has two solutions, one positive and one negative, we will take the positive solution,

$$(M_\infty)_{\text{vN}}^s = \sqrt{\frac{\gamma + 3}{2}}. \quad (2.34)$$

Again, in order for the von Neumann condition to exist, the free-stream Mach number must be greater than $(M_\infty)_{\text{vN}}^s$. At this Mach number, von Neumann reflection occurs when the incident shock is a Mach wave; therefore, the shock angle at this limiting condition, α_{vN}^s , is

$$\alpha_{\text{vN}}^s = \sin^{-1} \sqrt{\frac{2}{\gamma + 3}}. \quad (2.35)$$

It is also interesting to look at the limiting value of α_{vN} as M_∞ goes to ∞ . Taking the limit of the left-hand side of Equation 2.27 as M_∞ goes to ∞ gives

$$\lim_{M_\infty \rightarrow \infty} \theta(M_\infty, \gamma, \alpha_{\text{vN}}) = \cot^{-1} \left[\tan \alpha_{\text{vN}} \left(\frac{\gamma + 1}{2 \sin^2 \alpha_{\text{vN}}} - 1 \right) \right]. \quad (2.36)$$

Also, as M_∞ goes to infinity, the pressure ratios become

$$\lim_{M_\infty \rightarrow \infty} \xi(M_\infty, \gamma, \frac{\pi}{2}) = \frac{2\gamma M_\infty^2}{\gamma + 1}, \quad (2.37)$$

$$\lim_{M_\infty \rightarrow \infty} \xi(M_\infty, \gamma, \alpha_{\text{vN}}) = \frac{2\gamma M_\infty^2 \sin^2 \alpha_{\text{vN}}}{\gamma + 1}, \quad (2.38)$$

and the Mach number behind the leading oblique shock becomes

$$\begin{aligned}\lim_{M_\infty \rightarrow \infty} (M_1)_{vN} &= \lim_{M_\infty \rightarrow \infty} M(M_\infty, \gamma, \alpha_{vN}) \\ &= \frac{(\gamma + 1)^2 - 4\gamma \sin^2 \alpha_{vN}}{2\gamma (\gamma - 1) \sin^2 \alpha_{vN}}.\end{aligned}\quad (2.39)$$

Substituting Equations 2.36 through 2.39 into 2.27, taking the cotangent of both sides and squaring both sides produces

$$\lim_{M_\infty \rightarrow \infty} \frac{L_1 \sin^6 \alpha_{vN} - L_2 \sin^4 \alpha_{vN} + L_3 \sin^2 \alpha_{vN} - L_4}{2(\gamma^2 - 1) \sin^2 \alpha_{vN} (\sin^2 \alpha_{vN} - 1)^2 [\sin^2 \alpha_{vN} (\gamma + 1) - 2]} = 0 \quad (2.40)$$

where

$$L_1 = 8\gamma^2 (\gamma + 1), \quad (2.41)$$

$$L_2 = 2\gamma (3\gamma^3 + 5\gamma^2 + 9\gamma - 1), \quad (2.42)$$

$$L_3 = (\gamma^5 + 3\gamma^4 + 10\gamma^3 + 6\gamma^2 - 3\gamma - 1), \quad (2.43)$$

$$L_4 = (\gamma - 1)(\gamma + 1)^3. \quad (2.44)$$

The numerator of this equation has three solutions; the only physical solution is

$$\lim_{M_\infty \rightarrow \infty} \alpha_{vN} = \sin^{-1} \left(\sqrt{\frac{\gamma^3 + \gamma^2 + 3\gamma - 1 - \sqrt{\gamma^6 + 2\gamma^5 - \gamma^4 - 4\gamma^3 + 15\gamma^2 + 2\gamma + 1}}{4\gamma(\gamma + 1)}} \right). \quad (2.45)$$

An example of the reflection domain, considering only the von Neumann condition, is shown in Figure 2.17.

2.3.5 Sonic Reflected Shock Condition

An important condition is that for which the flow behind the reflected shock in the Mach reflection configuration is sonic. This is important because if the flow is supersonic behind the reflected shock, the reflected shock can not be forward-facing.

In addition, if the flow behind the reflected shock is supersonic, then inverted Mach reflection is not a physical solution. This is because, as was discussed earlier, whenever inverted Mach reflection is possible regular reflection is also possible, as is seen in Fig-

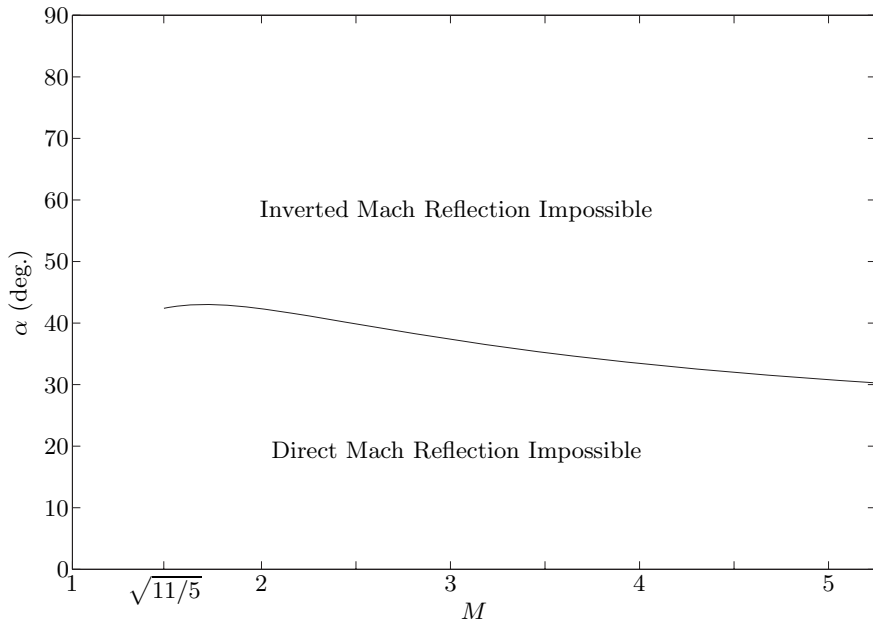


Figure 2.17: Shock reflection domain, for $\gamma = 1.4$ considering only the von Neumann condition.

ure 2.7(b). Therefore, in order for the inverted Mach reflection to be chosen over regular reflection the back pressure must be raised and this increase in back pressure must be communicated to the reflected shock. Figure 2.18 shows an example of the flow at the sonic reflected shock condition. An example of this condition is shown in Figure 2.19. The sonic reflected shock condition can be written as

$$\xi(M_\infty, \gamma, (\alpha_s)_{SRS}) = \xi(M_\infty, \gamma, \alpha_{SRS}) \xi((M_1)_{SRS}, \gamma, (\alpha_1)_{SRS}), \quad (2.46)$$

$$\theta(M_\infty, \gamma, (\alpha_s)_{SRS}) = |\theta(M_\infty, \gamma, \alpha_{SRS}) - \theta((M_1)_{SRS}, \gamma, (\alpha_1)_{SRS})|, \quad (2.47)$$

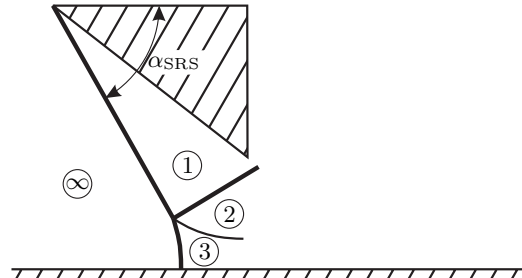


Figure 2.18: Flow over a wedge producing sonic flow behind the reflected shock. That is to say, $M_2 = 1$.

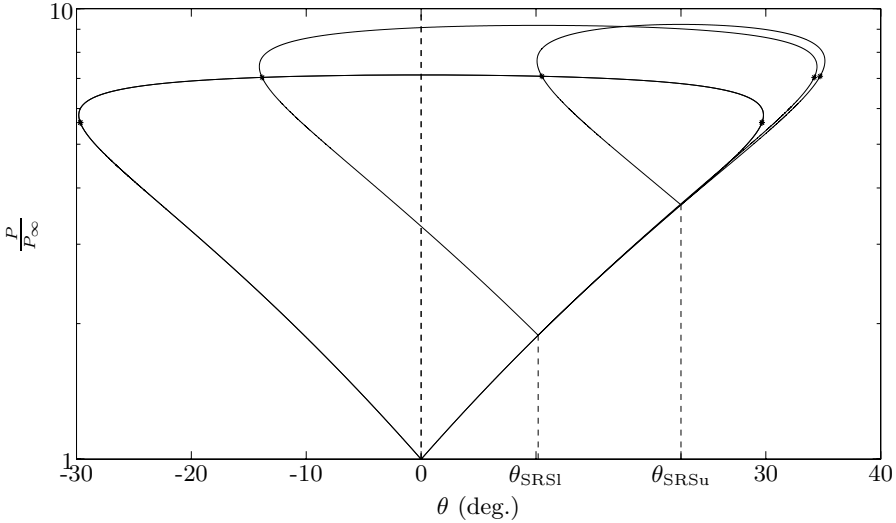


Figure 2.19: Example of the sonic reflected shock condition for $M = 2.5$ and $\gamma = 1.4$. Note that there are two reflected shock loci that intersect the incident shock locus at their sonic point. The * denotes the sonic point of the shock loci.

where $(\alpha_s)_{SRS}$ is the angle of the Mach stem with respect to the incoming flow, and since the flow behind the reflected shock is sonic,

$$(\alpha_1)_{SRS} = \alpha^*((M_1)_{SRS}, \gamma), \quad (2.48)$$

$$(M_1)_{SRS} = M(M_\infty, \gamma, \alpha_{SRS}). \quad (2.49)$$

Equation 2.46 can, after much algebra, be solved for $(\alpha_s)_{SRS}$. The solution is

$$(\alpha_s)_{SRS} = \sin^{-1} \sqrt{\frac{\gamma - 1 - \frac{1+\gamma(2M_\infty^2 \sin^2 \alpha_{SRS} - 1)}{2} \left(\zeta_{SRS} - 1 + \sqrt{\frac{(\zeta_{SRS}-3)^2 + \gamma(\zeta_{SRS}+1)^2}{\gamma+1}} \right)}{2M_\infty^2 \gamma}}, \quad (2.50)$$

where

$$\zeta_{SRS} = \frac{4 + 4M_\infty^2 \sin^2 \alpha_{SRS} (\gamma - 1) + M_\infty^4 \sin^2 \alpha_{SRS} [\gamma^2 + \gamma (2 - 4 \sin^2 \alpha_{SRS}) + 1]}{[2 + M_\infty^2 \sin^2 \alpha_{SRS} (\gamma - 1)] [1 + \gamma (2M_\infty^2 \sin^2 \alpha_{SRS} - 1)]}. \quad (2.51)$$

The sonic reflection condition can then be found by numerically solving

$$\theta(M_\infty, \gamma, (\alpha_s)_{SRS}) = |\theta(M_\infty, \gamma, \alpha_{SRS}) - \theta((M_1)_{SRS}, \gamma, (\alpha_1)_{SRS})|, \quad (2.52)$$

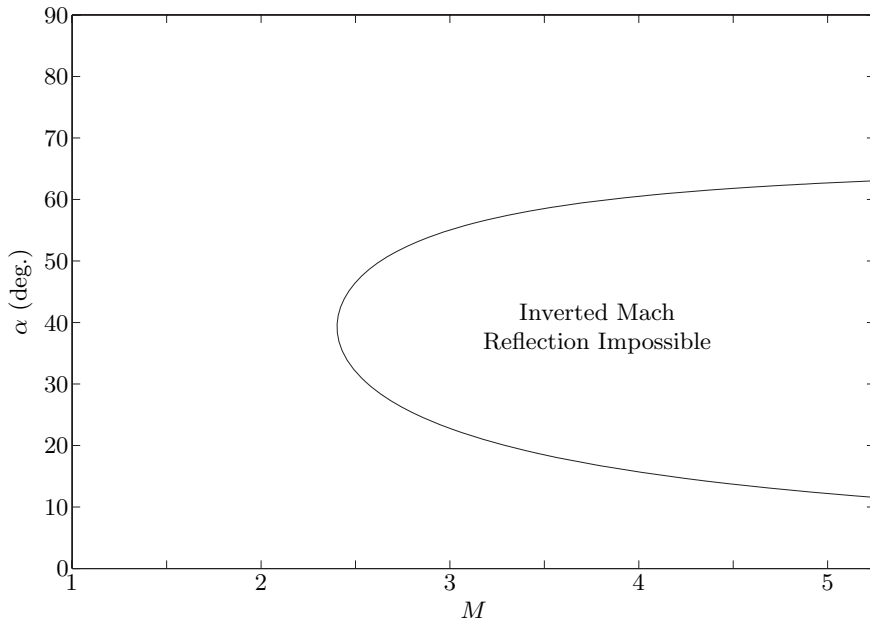


Figure 2.20: Shock reflection domain, for $\gamma = 1.4$ considering only the sonic reflected shock condition.

for α_{SRS} . Note that for Mach numbers below a certain value, no physical solution for α_{SRS} exists.

An example of the reflection domain, considering only the sonic reflected shock condition, is shown in Figure 2.20.

2.3.6 Normal Reflected Shock Condition

The normal reflected shock condition occurs when the reflected shock is perpendicular to the flow behind the incident shock. This condition separates regions where the reflected shock is inclined forward from where the reflected shock is declined, with respect to the incoming flow. A sample shock structure for the normal reflected shock condition is shown in Figure 2.21. An example of a shock polar at this condition is shown in Figure 2.22. The normal reflected shock condition can be expressed as

$$\xi(M_\infty, \gamma, (\alpha_s)_{\text{NRS}}) = \xi(M_\infty, \gamma, \alpha_{\text{NRS}}) \xi\left((M_1)_{\text{NRS}}, \gamma, \frac{\pi}{2}\right), \quad (2.53)$$

$$\theta(M_\infty, \gamma, (\alpha_s)_{\text{NRS}}) = \theta(M_\infty, \gamma, \alpha_{\text{NRS}}) - \theta\left((M_1)_{\text{NRS}}, \gamma, \frac{\pi}{2}\right), \quad (2.54)$$

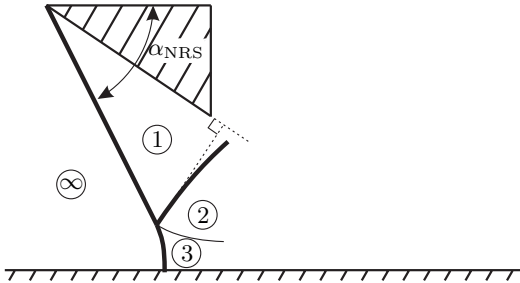


Figure 2.21: Flow over a wedge producing a reflected shock that is perpendicular to the flow behind the incident shock.

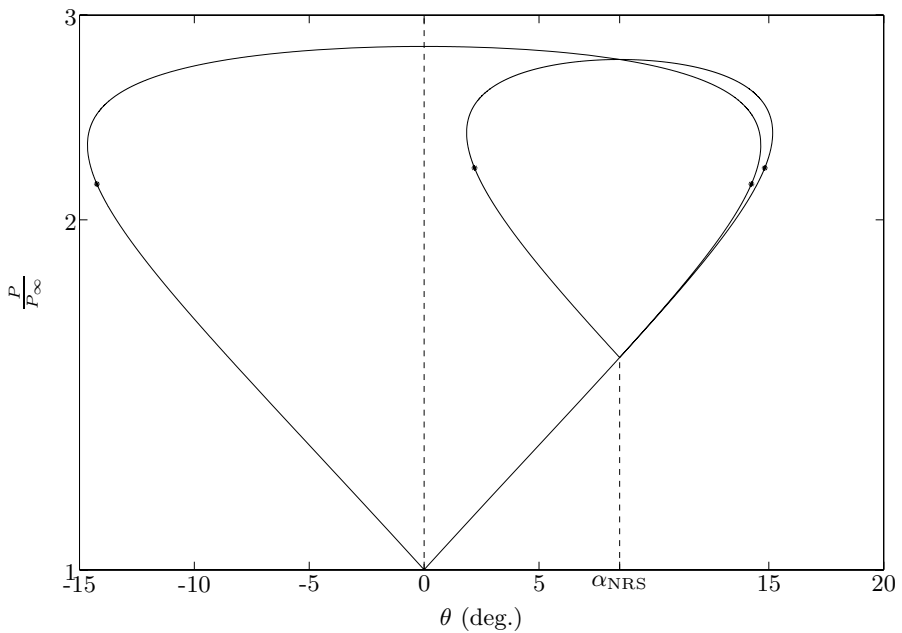


Figure 2.22: Example of the normal reflected shock condition for $M = 1.6$ and $\gamma = 1.4$. Note that the intersection of the reflected and incident shock polars occurs when the reflected shock is normal. The * denotes the sonic point of the shock loci.

where $(M_1)_{\text{NRS}}$ is the Mach number behind the incident shock, and $(\alpha_s)_{\text{NRS}}$ is the angle of the Mach stem. Since,

$$\theta \left((M_1)_{\text{NRS}}, \gamma, \frac{\pi}{2} \right) = 0, \quad (2.55)$$

Equation 2.54 can easily be solved for $(\alpha_s)_{\text{NRS}}$ in terms of α_{NRS} . Finally, the incident shock angle at the normal reflected shock condition, α_{NRS} , can be found numerically by solving

$$\xi(M_\infty, \gamma, (\alpha_s)_{\text{NRS}}) = \xi(M_\infty, \gamma, \alpha_{\text{NRS}}) \xi \left((M_1)_{\text{NRS}}, \gamma, \frac{\pi}{2} \right). \quad (2.56)$$

For incident shock angles greater than α_{NRS} Mach reflection with a backward-facing reflected shock is impossible, whereas for shock angles less than α_{NRS} Mach reflection with a forward-facing reflected shock is impossible. Note that a solution to this equation only exists for Mach numbers above a critical value, $(M_\infty)_{\text{NRS}}^s$. This critical value will correspond to $(M_\infty)_{\text{vN}}^s$, since for a Mach wave, a normal reflected shock will intersect the incident shock polar along the zero deflection axis; therefore,

$$(M_\infty)_{\text{NRS}}^s = (M_\infty)_{\text{vN}}^s = \sqrt{\frac{\gamma + 3}{2}}. \quad (2.57)$$

As before, the shock angle at this limiting condition, α_{vN}^s , is

$$\alpha_{\text{NRS}}^s = \alpha_{\text{vN}}^s = \sin^{-1} \sqrt{\frac{2}{\gamma + 3}}. \quad (2.58)$$

An example of the reflection domain, considering only the normal reflected shock condition, is shown in Figure 2.23.

2.3.7 Sonic Forward-Facing Reflected Shock Condition

Another important condition is when the sonic point of a forward-facing reflected shock polar intersects the incident shock polar. For incident shock angles above this value, α_{SFRS} , no forward-facing Mach reflection is possible. Figure 2.24 shows an example of the shock structure when the reflected shock is forward facing, and the flow behind the reflected shock is sonic. An example of this condition is shown in Figure 2.25. The sonic forward-facing

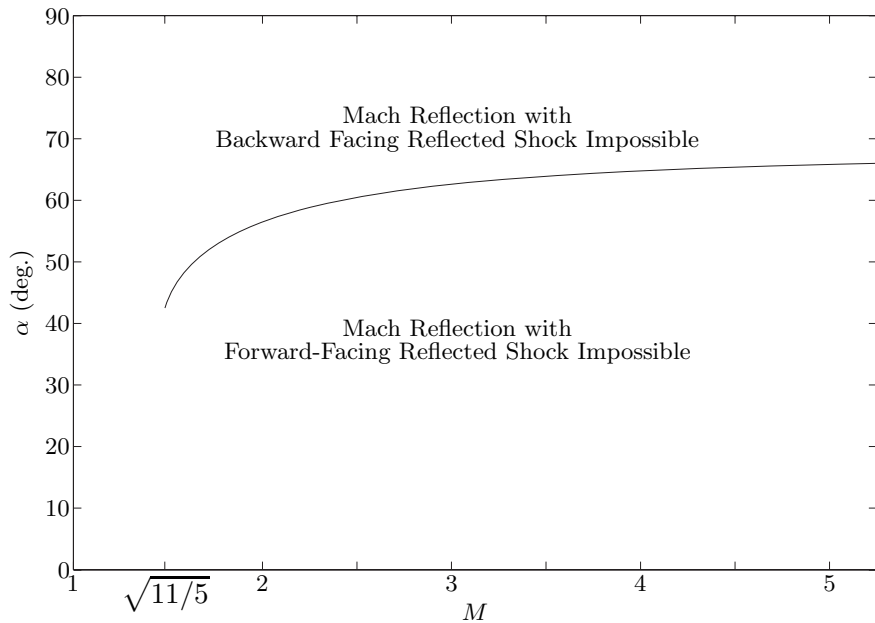


Figure 2.23: Shock reflection domain, for $\gamma = 1.4$ considering only the normal reflected shock condition.

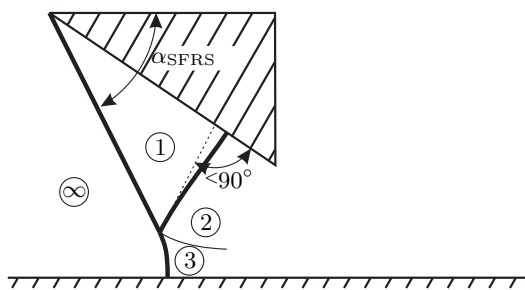


Figure 2.24: Flow over a wedge producing sonic flow behind the forward-facing reflected shock.

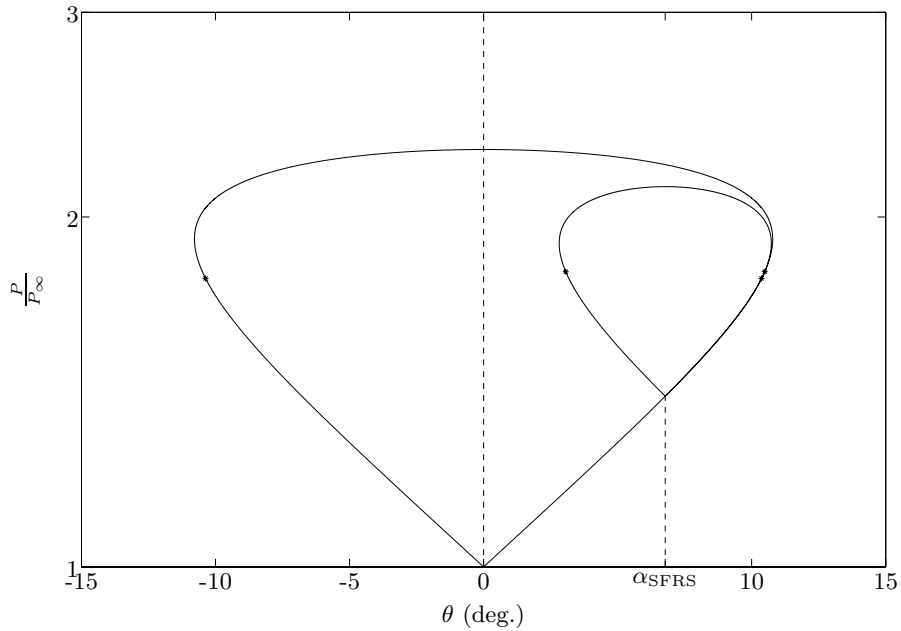


Figure 2.25: Example of the sonic forward-facing reflected shock condition for $M = 1.45$ and $\gamma = 1.4$. Note that the intersection of the reflected and incident shock polars occurs when the reflected shock is forward facing and at its sonic point. The * denotes the sonic point of the shock loci.

reflected shock condition can be written as

$$\xi(M_\infty, \gamma, (\alpha_s)_{\text{SFRS}}) = \xi(M_\infty, \gamma, \alpha_{\text{SFRS}}) \xi((M_1)_{\text{SFRS}}, \gamma, (\alpha_1)_{\text{SFRS}}), \quad (2.59)$$

$$\theta(M_\infty, \gamma, (\alpha_s)_{\text{SFRS}}) = \theta(M_\infty, \gamma, \alpha_{\text{SFRS}}) + \theta((M_1)_{\text{SFRS}}, \gamma, (\alpha_1)_{\text{SFRS}}), \quad (2.60)$$

where $(\alpha_s)_{\text{SFRS}}$ is the angle of the Mach stem with respect to the incoming flow, and

$$(\alpha_1)_{\text{SFRS}} = \alpha^*((M_1)_{\text{SFRS}}, \gamma), \quad (2.61)$$

$$(M_1)_{\text{SFRS}} = M(M_\infty, \gamma, \alpha_{\text{SFRS}}). \quad (2.62)$$

Note that Equations 2.59 through 2.62 are identical to Equations 2.46 through 2.49 except for a sign difference between Equations 2.60 and 2.47. As was done for the sonic reflected

shock condition, Equation 2.59 can be solved for $(\alpha_s)_{\text{SFRS}}$. The solution is

$$(\alpha_s)_{\text{SFRS}} = \sin^{-1} \sqrt{\frac{\gamma - 1 - \frac{1+\gamma(2M_\infty^2 \sin^2 \alpha_{\text{SFRS}} - 1)}{2} \left(\zeta_{\text{SFRS}} - 1 + \sqrt{\frac{(\zeta_{\text{SFRS}} - 3)^2 + \gamma(\zeta_{\text{SFRS}} + 1)^2}{\gamma + 1}} \right)}{2M_\infty^2 \gamma}}, \quad (2.63)$$

where

$$\zeta_{\text{SFRS}} = \frac{4 + 4M_\infty^2 \sin^2 \alpha_{\text{SFRS}} (\gamma - 1) + M_\infty^4 \sin^2 \alpha_{\text{SFRS}} [\gamma^2 + \gamma (2 - 4 \sin^2 \alpha_{\text{SFRS}}) + 1]}{[2 + M_\infty^2 \sin^2 \alpha_{\text{SFRS}} (\gamma - 1)] [1 + \gamma (2M_\infty^2 \sin^2 \alpha_{\text{SFRS}} - 1)]}. \quad (2.64)$$

The sonic forward-facing reflected shock condition can then be found by numerically solving

$$\theta(M_\infty, \gamma, (\alpha_s)_{\text{SFRS}}) = \theta(M_\infty, \gamma, \alpha_{\text{SFRS}}) + \theta((M_1)_{\text{SFRS}}, \gamma, (\alpha_1)_{\text{SFRS}}), \quad (2.65)$$

for α_{SFRS} .

Note that for Mach numbers below a certain value, $(M_\infty)_{\text{SFRS}}^s$, no physical solution for α_{SFRS} exists. At this limiting Mach number, the shock angle corresponds to a Mach wave. We can therefore set $\alpha_{\text{SFRS}} = \sin^{-1} \frac{1}{(M_\infty)_{\text{SFRS}}^s} + \epsilon$, where ϵ is a small positive value, and performing much algebra, yields

$$(M_\infty)_{\text{SFRS}}^s = \sqrt{\frac{\gamma^2 - 6\gamma + 2 + 2\sqrt{4\gamma^4 + 18\gamma^3 - 8\gamma^2 - 54\gamma + 49} \cos \sigma_{\text{SFRS}}}{3(\gamma^2 - 1)}}, \quad (2.66)$$

where,

$$\sigma_{\text{SFRS}} = \frac{1}{3} \tan^{-1} \frac{3\sqrt{3(\gamma + 1)^3 (\gamma^3 - 5\gamma + 4)^2 (5\gamma^3 + 113\gamma^2 + 220\gamma - 104)}}{11\gamma^6 - 6\gamma^4 + 378\gamma^3 - 21\gamma^2 - 1134\gamma + 718}. \quad (2.67)$$

At this limiting value of Mach number and at the sonic forward-facing reflected shock condition the shock angle, α_{SFRS}^s , is

$$\alpha_{\text{SFRS}}^s = \sin^{-1} \frac{1}{(M_\infty)_{\text{SFRS}}^s}. \quad (2.68)$$

An example of the reflection domain, considering only the sonic forward-facing reflected shock condition, is shown in Figure 2.26.

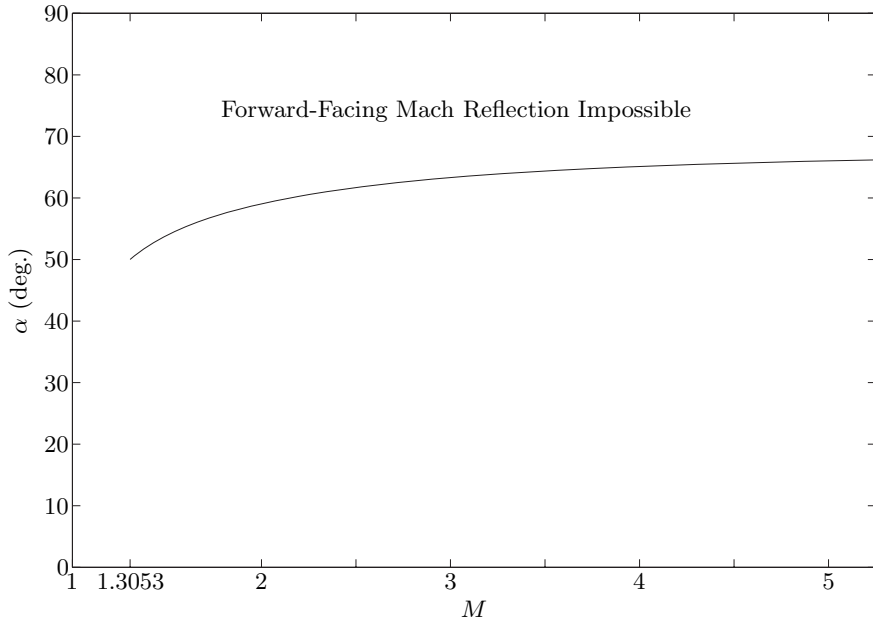


Figure 2.26: Shock reflection domain, for $\gamma = 1.4$ considering only the sonic forward-facing reflected shock condition.

2.3.8 Sonic Condition

A final condition is when the flow behind the reflected shock of a regular reflection is sonic. This corresponds very nearly to the detachment criterion, since the sonic shock angle is very nearly the maximum deflection shock angle. The sonic condition can be written as

$$\theta(M_\infty, \gamma, \alpha_S) = \theta((M_1)_S, \gamma, (\alpha_1)_S), \quad (2.69)$$

where

$$(\alpha_1)_S = \alpha^*((M_1)_S, \gamma). \quad (2.70)$$

Through an identical process as was used for the detachment condition, we can write a sixth-order polynomial in $\sin^2 \alpha_S$,

$$S_0 + S_1 \sin^2 \alpha_S + S_2 \sin^4 \alpha_S + S_3 \sin^6 \alpha_S + S_4 \sin^8 \alpha_S + S_5 \sin^{10} \alpha_S + S_6 \sin^{12} \alpha_S = 0, \quad (2.71)$$

where

$$S_0 = -8(\gamma + 1) + 20M_\infty^2 - 4\gamma^2 M_\infty^2, \quad (2.72)$$

$$\begin{aligned} S_1 &= 8M_\infty^2 - 44M_\infty^4 + 4M_\infty^6 + 16\gamma M_\infty^2 + 52\gamma M_\infty^4 + 16\gamma M_\infty^6 - 24\gamma^2 M_\infty^2 \\ &\quad + 12\gamma^2 M_\infty^4 + 16\gamma^2 M_\infty^6 - 20\gamma^3 M_\infty^4 - 4\gamma^4 M_\infty^6, \end{aligned} \quad (2.73)$$

$$\begin{aligned} S_2 &= 6M_\infty^4 + 25M_\infty^6 - 4M_\infty^8 + M_\infty^{10} - 54\gamma M_\infty^4 - 130\gamma M_\infty^6 - 16\gamma M_\infty^8 + 4\gamma M_\infty^{10} \\ &\quad + 16\gamma^2 M_\infty^2 + 82\gamma^2 M_\infty^4 + 4\gamma^2 M_\infty^6 - 8\gamma^2 M_\infty^8 + 6\gamma^2 M_\infty^{10} + 14\gamma^3 M_\infty^4 \\ &\quad + 66\gamma^3 M_\infty^6 + 16\gamma^3 M_\infty^8 + 4\gamma^3 M_\infty^{10} + 3\gamma^4 M_\infty^6 + 12\gamma^4 M_\infty^8 + \gamma^4 M_\infty^{10}, \end{aligned} \quad (2.74)$$

$$\begin{aligned} S_3 &= -4M_\infty^6 - 2M_\infty^8 - 2M_\infty^{10} + 100\gamma M_\infty^6 + 88\gamma M_\infty^8 - 8\gamma M_\infty^{10} - 64\gamma^2 M_\infty^4 \\ &\quad - 140\gamma^2 M_\infty^6 - 52\gamma^2 M_\infty^8 - 20\gamma^2 M_\infty^{10} - 52\gamma^3 M_\infty^6 - 88\gamma^3 M_\infty^8 - 24\gamma^3 M_\infty^{10} \\ &\quad - 10\gamma^4 M_\infty^8 - 10\gamma^4 M_\infty^{10}, \end{aligned} \quad (2.75)$$

$$\begin{aligned} S_4 &= -2M_\infty^8 + 2M_\infty^{10} - 62\gamma M_\infty^8 - 6\gamma M_\infty^{10} + 96\gamma^2 M_\infty^6 + 130\gamma^2 M_\infty^8 + 46\gamma^2 M_\infty^{10} \\ &\quad + 62\gamma^3 M_\infty^8 + 46\gamma^3 M_\infty^{10} + 8\gamma^4 M_\infty^{10}, \end{aligned} \quad (2.76)$$

$$S_5 = 8\gamma M_\infty^{10} - 64\gamma^2 M_\infty^8 - 48\gamma^2 M_\infty^{10} - 24\gamma^3 M_\infty^{10}, \quad (2.77)$$

$$S_6 = 16\gamma^2 M_\infty^{10}. \quad (2.78)$$

In the limit of M_∞ going to ∞ , the polynomial from Equation 2.71 becomes

$$\begin{aligned} &(\gamma^4 + 4\gamma^3 + 6\gamma^2 + 4\gamma + 1) \sin^4 \alpha_S - (10\gamma^4 + 24\gamma^3 + 20\gamma^2 + 8\gamma + 2) \sin^6 \alpha_S \\ &\quad + (8\gamma^4 + 46\gamma^3 + 46\gamma^2 - 6\gamma + 2) \sin^8 \alpha_S - (24\gamma^3 + 48\gamma^2 - 8\gamma) \sin^{10} \alpha_S \\ &\quad + 16\gamma^2 \sin^{12} \alpha_S = 0. \end{aligned} \quad (2.79)$$

Excluding the case where $\sin^2 \alpha_S = 0$, there are four solutions for $\sin^2 \alpha_S$. The only physical solution is

$$\lim_{M_\infty \rightarrow \infty} \alpha_S = \sin^{-1} \sqrt{\frac{3\gamma(2 + \gamma - \zeta_S) - 1 - \zeta_S - \sqrt{2(\gamma - 1)(\gamma[9 - 6\zeta_S + \gamma(6 + \gamma - \zeta_S)] - \zeta_S)}}{8\gamma}}, \quad (2.80)$$

where

$$\zeta_S = \sqrt{\gamma^2 - 1}. \quad (2.81)$$

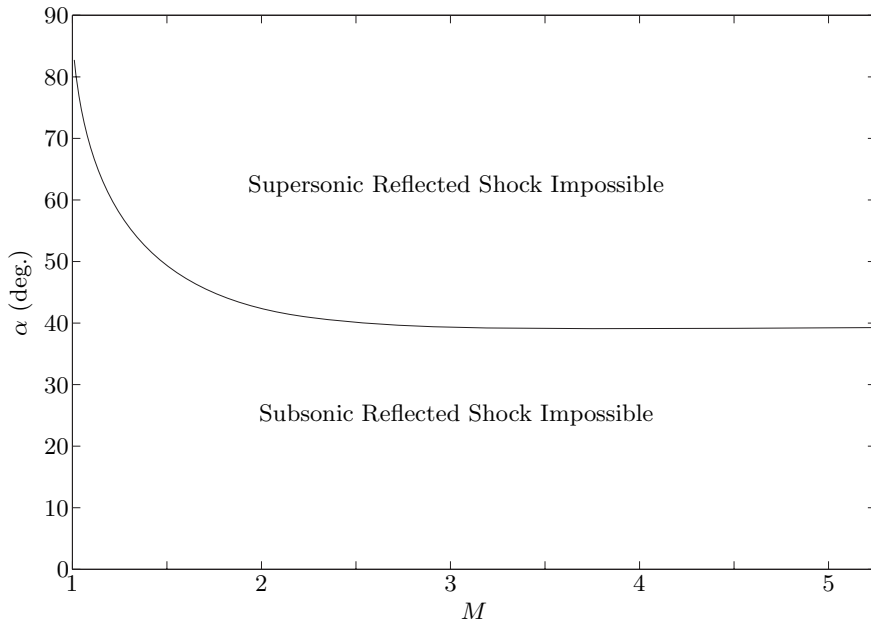


Figure 2.27: The shock reflection domain, for $\gamma = 1.4$ considering only the sonic condition.

An example of the reflection domain, considering only the sonic condition, is shown in Figure 2.27.

2.3.9 Complete Reflection Domain

There are seven possible types of reflection: supersonic regular reflection (RR), subsonic regular reflection (RRs), Mach reflection with a supersonic backward-facing reflected shock (MR), Mach reflection with a subsonic backward-facing reflected shock (MRS), Mach reflection with a forward-facing reflected shock (MRf), inverted Mach reflection (IMR), and von Neumann reflection (vNR). Combining all of the conditions mentioned earlier, and systematically removing impossible shock configurations from each region produces the final result shown in Figure 2.29 for a ratio of specific heats of 1.4. Appendix A shows the Mach reflection domain for other values of the ratio of specific heats. The general curves separating the various regions are in good agreement with those of Chapman [17].

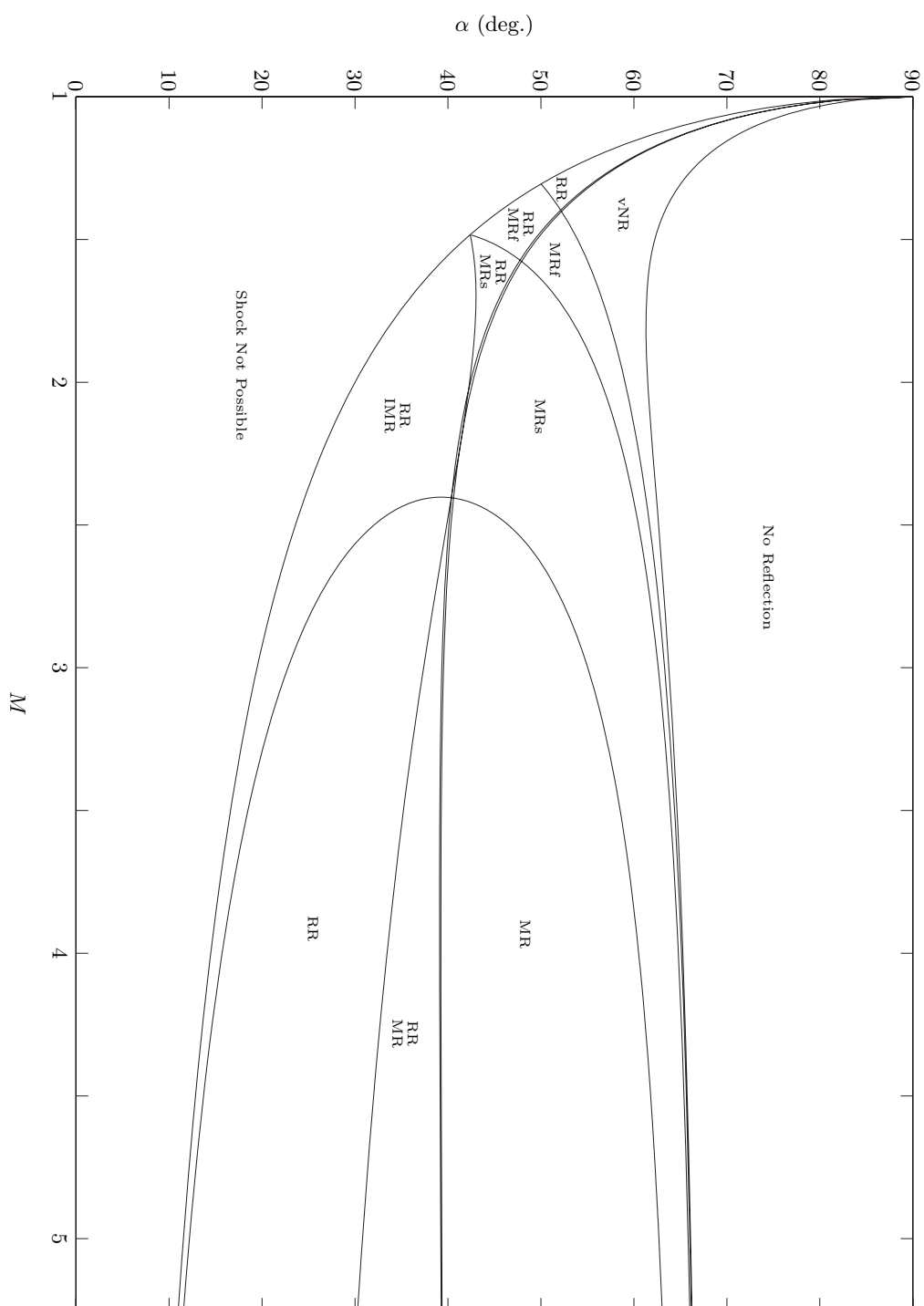


Figure 2.28: Complete shock reflection domain for $\gamma = 1.4$, note that in the small region between the sonic and detachment condition RR is replaced by RRs.

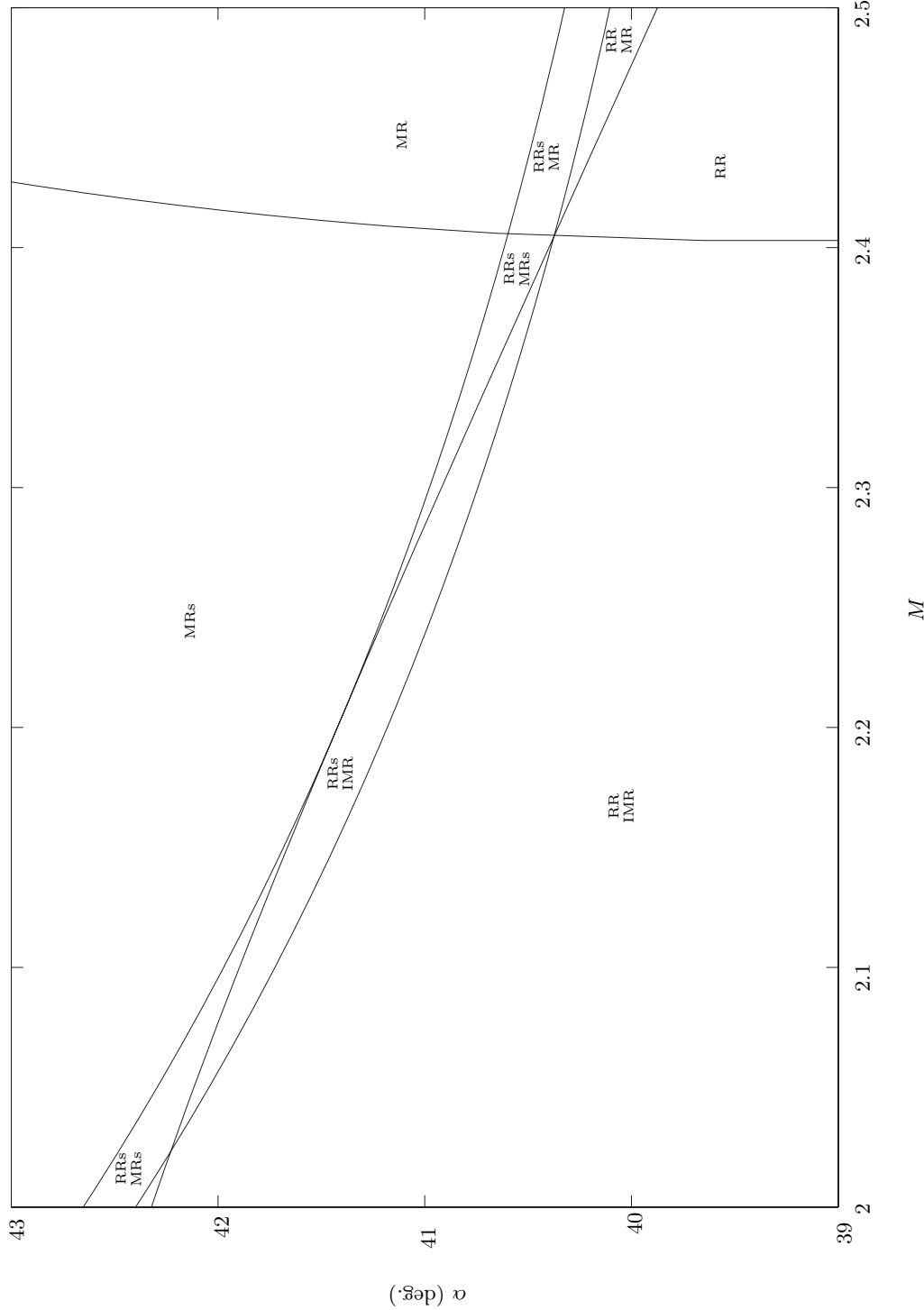


Figure 2.29: Detailed shock reflection domain for $\gamma = 1.4$, showing the region between Mach 2 and Mach 2.5.

Chapter 3

Mach Stem Height Prediction

Consider the reflection of a shock, generated by a wedge in steady supersonic flow, from a wall (single wedge configuration) or from a plane of symmetry (double wedge configuration). For a sufficiently high free-stream Mach number, there exists a range of wedge angles (the dual-solution domain) in which both regular and Mach reflection are possible. To date there is no accurate method of predicting the height of a Mach stem in steady flow. Predictions of Mach stem height can be important in the design of supersonic inlets if the inlet is expected to experience Mach reflection. An accurate prediction of the Mach stem height may also be useful in understanding the behavior of the shock reflection in the dual-solution domain.

Azevedo [7, 18] (see also Ben-Dor [19]) developed a theory based on the location of the sonic throat formed by the initially converging flow behind the Mach stem. However, his prediction consistently underestimated the actual Mach stem height. The aims of the present work are to relax some of the assumptions made by Azevedo in order to obtain more accurate predictions of Mach stem height, and to analyze the rate of growth of a Mach stem starting from a regular reflection in the dual solution domain. Work by Li and Ben-Dor [20] corrects some of the flaws in the theory of Azevedo, but gives very similar approximations of Mach stem height, which differ significantly from the experimental work of Hornung and Robinson [6]. The works by Li et al [21] and Schotz et al. [22] consider downstream influences on Mach stem height; however, the experimental work of Chpoun and Leclerc [23] shows that the Mach stem height does not vary with downstream conditions. This is as expected, since the flow in the expansion region and downstream of the sonic throat is supersonic and therefore these influences cannot affect Mach stem height. There is therefore no need in the current work to consider the flow downstream of the expansion wave corresponding to the sonic throat.

3.1 Problem Setup

The problem setup is shown graphically in Figure 3.1. We can either consider two opposing wedges, or for inviscid flow, a wedge above a flat plate. The wedge, with a length w , is declined at an angle θ_1 with respect to the free-stream flow and produces a shock at an angle α . The height of the triple point above the surface is the Mach stem height, denoted s . In the case of two symmetric wedges, s is half the total Mach stem height. At the triple point a slipline is created, which is initially declined at an angle δ with respect to the surface or plane of symmetry. The reflected shock from the triple point is inclined at an angle ϕ with respect to the surface.

In general the Mach stem height, s , is a function of the Mach number, M , the ratio of specific heats, γ , the spacing between the wedge and the flat surface, g , the angle of the wedge, θ_1 , and the wedge length, w . That is to say

$$s = f(M, \gamma, g, \theta_1, w), \quad (3.1)$$

where f is an unknown function. Nondimensionalizing this relationship we find that

$$s^+ = f^+(M, \gamma, g^+, \theta_1), \quad (3.2)$$

where f^+ is the nondimensional version of f , $s^+ = \frac{s}{w}$, and $g^+ = \frac{g}{w}$. Normalizing lengths by w is a good choice, since, in experiments, w will almost always be a fixed length and not a function of the wedge angle θ_1 .

3.2 Mass and Momentum Balance

Azevedo [7] considers a problem setup as shown in Figure 3.1 subject to several assumptions. First, he assumes that the sonic throat occurs where the leading characteristic of the expansion fan intersects the slipline. Second, he assumes that the region between the slipline and the symmetry plane, and between the Mach stem and the sonic throat is an isentropically converging ideal gas flow with a straight streamline \overline{TH} . To analyze the flow Azevedo applies conservation of mass and momentum.

Azevedo first considers the conservation of mass. Specifically, he considers the mass

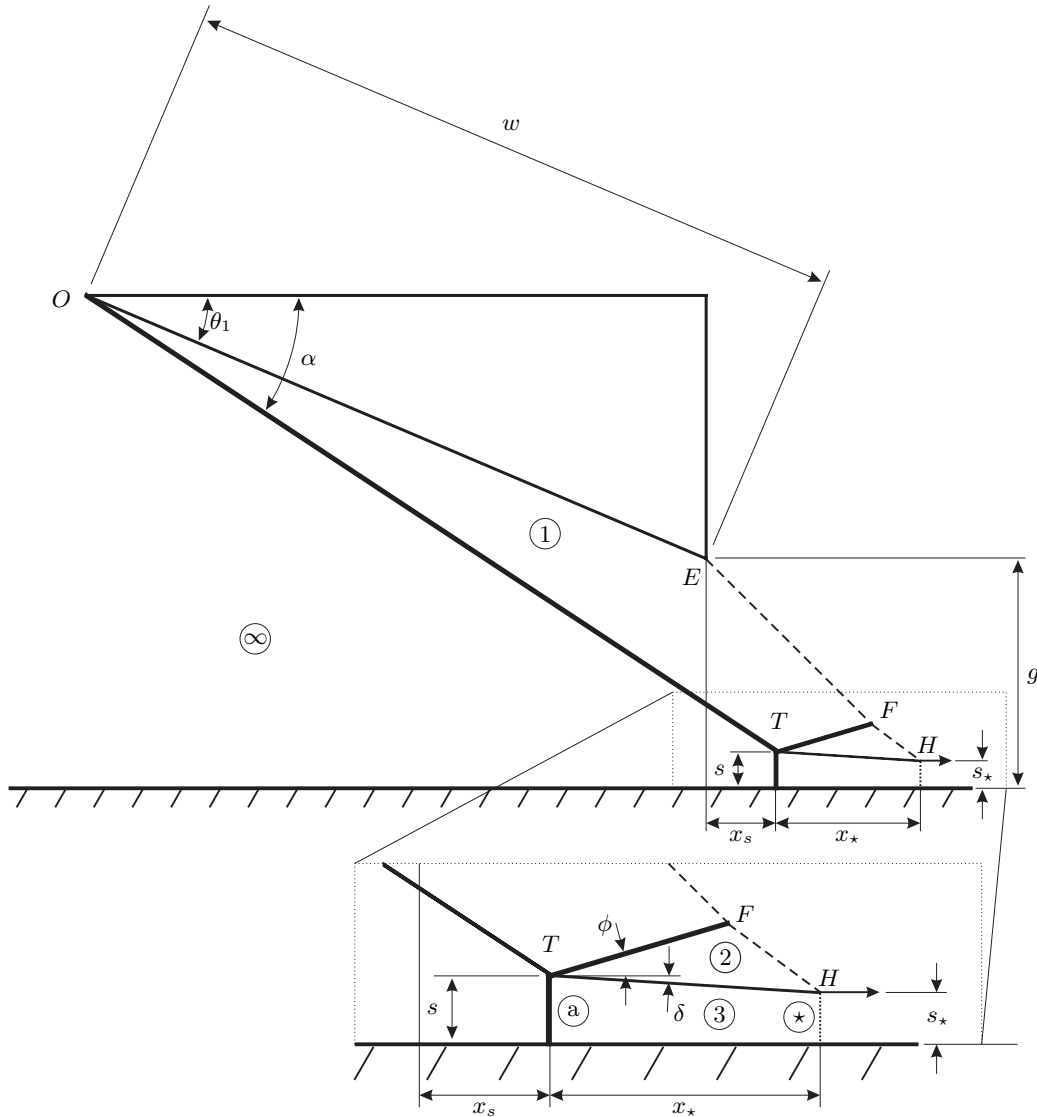


Figure 3.1: Flow setup used by Azevedo [7] to predict Mach stem height.

flow entering between the wedge tip, O , and the symmetry plane. This mass flow can then be equated to the mass flow through \overline{EF} , \overline{FH} , and s_* . Equating these two mass fluxes produces the following equation:

$$\rho_\infty u_\infty (g + w \sin \theta_1) = \rho_1 u_1 \sin \mu_1 \overline{EF} + \rho_2 u_2 \sin \mu_2 \overline{FH} + \rho_* u_* s_*, \quad (3.3)$$

where μ_1 and μ_2 are the Mach angles and are given by

$$\mu_1 = \sin^{-1} \frac{1}{M_1}, \quad (3.4)$$

$$\mu_2 = \sin^{-1} \frac{1}{M_2}. \quad (3.5)$$

Next, he considers the conservation of momentum in the free-stream flow direction. Equating the pressure and momentum flux between the wedge tip and the solid surface with the pressure and the momentum flux through \overline{EF} , \overline{FH} , and s_* produces

$$\begin{aligned} P_\infty (g + w \sin \theta_1) - P_1 (w \sin \theta_1 + \sin(\mu_1 + \theta_1) \overline{EF}) - P_2 \sin(\mu_2 + \delta) \overline{FH} - P_* s_* \\ = \rho_1 u_1^2 \sin \mu_1 \cos \theta_1 \overline{EF} + \rho_2 u_2^2 \sin \mu_2 \cos \delta \overline{FH} + \rho_* u_*^2 s_* - \rho_\infty u_\infty^2 (g + w \sin \theta_1). \end{aligned} \quad (3.6)$$

Similarly, for conservation of momentum perpendicular to the free-stream flow direction, he finds that

$$\begin{aligned} P_\infty (x_s + w \cos \theta_1) + P_3 x_* - P_1 (w \cos \theta_1 + \cos(\mu_1 + \theta_1) \overline{EF}) - P_2 \cos(\mu_2 + \delta) \overline{FH} \\ = -\rho_1 u_1^2 \sin \mu_1 \sin \theta_1 \overline{EF} - \rho_2 u_2^2 \sin \mu_2 \sin \delta \overline{FH}. \end{aligned} \quad (3.7)$$

Azevedo takes P_3 to be the average pressure in Region 3, which is the average of the pressure at the sonic throat and the pressure right behind the Mach stem. The numerical result is almost identical if we take P_3 to be the integrated pressure using the area ratio relationship.

Equations 3.3, 3.6 and 3.7 can be written in nondimensional form with the superscript $+$ referring to nondimensional quantities. Specifically, density is normalized by the free-stream density, ρ_∞ , velocities are normalized by the free-stream velocity, u_∞ , pressures are normalized by twice the free-stream dynamic pressure, $\rho_\infty u_\infty^2$, and distances are normalized

by the wedge length, w . With these normalizations, equations 3.3 through 3.7 become

$$g^+ + \sin \theta_1 = \rho_1^+ u_1^+ \sin \mu_1 \overline{EF}^+ + \rho_2^+ u_2^+ \sin \mu_2 \overline{FH}^+ + \rho_\star^+ u_\star^+ s_\star^+, \quad (3.8)$$

$$\begin{aligned} P_\infty^+ (g^+ + \sin \theta_1) - P_1^+ (\sin \theta_1 + \sin (\mu_1 + \theta_1) \overline{EF}^+) - P_2^+ \sin (\mu_2 + \delta) \overline{FH}^+ - P_\star^+ s_\star^+ \\ = \rho_1^+ (u_1^+)^2 \sin \mu_1 \cos \theta_1 \overline{EF}^+ + \rho_2^+ (u_2^+)^2 \sin \mu_2 \cos \delta \overline{FH}^+ + \rho_\star^+ (u_\star^+)^2 s_\star^+ - g^+ - \sin \theta_1, \end{aligned} \quad (3.9)$$

$$\begin{aligned} P_\infty^+ (x_s^+ + \cos \theta_1) + P_3^+ x_\star^+ - P_1^+ (\cos \theta_1 + \cos (\mu_1 + \theta_1) \overline{EF}^+) - P_2^+ \cos (\mu_2 + \delta) \overline{FH}^+ \\ = -\rho_1^+ (u_1^+)^2 \sin \mu_1 \sin \theta_1 \overline{EF}^+ - \rho_2^+ (u_2^+)^2 \sin \mu_2 \sin \delta \overline{FH}^+. \end{aligned} \quad (3.10)$$

Note that

$$P_\infty^+ = \frac{P_\infty}{\rho_\infty u_\infty^2} = \frac{1}{\gamma M_\infty^2}. \quad (3.11)$$

We can now apply the shock jump conditions and the equation of state for a perfect gas. Specifically, we will use the following relations:

$$\frac{\rho_1 u_1}{\rho_\infty u_\infty} = \frac{\sin \alpha}{\sin (\alpha - \theta_1)}, \quad (3.12)$$

$$\frac{\rho_2 u_2}{\rho_1 u_1} = \frac{\sin (\theta_1 + \phi)}{\sin (\phi + \delta)}, \quad (3.13)$$

$$\frac{\rho_\star u_\star}{\rho_\infty u_\infty} = \frac{s}{s_\star}, \quad (3.14)$$

$$\rho_1 u_1^2 = \gamma P_1 M_1^2, \quad (3.15)$$

$$\rho_2 u_2^2 = \gamma P_2 M_2^2, \quad (3.16)$$

$$\rho_\star u_\star^2 = \gamma P_\star, \quad (3.17)$$

which in nondimensional form can be written as

$$\rho_1^+ u_1^+ = \frac{\sin \alpha}{\sin(\alpha - \theta_1)}, \quad (3.18)$$

$$\rho_2^+ u_2^+ = \frac{\sin \alpha \sin(\theta_1 + \phi)}{\sin(\alpha - \theta_1) \sin(\phi + \delta)}, \quad (3.19)$$

$$\rho_\star^+ u_\star^+ = \frac{s_\star^+}{s_\star^+}, \quad (3.20)$$

$$\rho_1^+ (u_1^+)^2 = \gamma P_1^+ M_1^2, \quad (3.21)$$

$$\rho_2^+ (u_2^+)^2 = \gamma P_2^+ M_2^2, \quad (3.22)$$

$$\rho_\star^+ (u_\star^+)^2 = \gamma P_\star^+. \quad (3.23)$$

With these relations we can rewrite Equations 3.8 through 3.10 as

$$g^+ + \sin \theta_1 = \frac{\sin \alpha}{\sin(\alpha - \theta_1)} \sin \mu_1 \overline{EF}^+ + \frac{\sin \alpha \sin(\theta_1 + \phi)}{\sin(\alpha - \theta_1) \sin(\phi + \delta)} \sin \mu_2 \overline{FH}^+ + s^+, \quad (3.24)$$

$$\begin{aligned} & \frac{1}{\gamma M_\infty^2} (g^+ + \sin \theta_1) - P_1^+ (\sin \theta_1 + \sin(\mu_1 + \theta_1) \overline{EF}^+) - P_2^+ \sin(\mu_2 + \delta) \overline{FH}^+ - P_\star^+ s_\star^+ \\ &= \gamma P_1^+ M_1^2 \sin \mu_1 \cos \theta_1 \overline{EF}^+ + \gamma P_2^+ M_2^2 \sin \mu_2 \cos \delta \overline{FH}^+ + \gamma P_\star^+ s_\star^+ - g^+ - \sin \theta_1, \end{aligned} \quad (3.25)$$

$$\begin{aligned} & \frac{1}{\gamma M_\infty^2} (x_s^+ + \cos \theta_1) + P_3^+ x_\star^+ - P_1^+ (\cos \theta_1 + \cos(\mu_1 + \theta_1) \overline{EF}^+) - P_2^+ \cos(\mu_2 + \delta) \overline{FH}^+ \\ &= -\gamma P_1^+ M_1^2 \sin \mu_1 \sin \theta_1 \overline{EF}^+ - \gamma P_2^+ M_2^2 \sin \mu_2 \sin \delta \overline{FH}^+. \end{aligned} \quad (3.26)$$

At this point there are five unknowns, x_s^+ , x_\star^+ , s_\star^+ , \overline{EF}^+ , and \overline{FH}^+ , but only three equations. Therefore, to close the system, Azevedo uses two geometric relationships, which state that the expansion fans must connect the sonic throat with the aft wedge corner:

$$x_\star = \cos(\mu_1 + \theta_1) \overline{EF} + \cos(\mu_2 + \delta) \overline{FH} - x_s, \quad (3.27)$$

$$s_\star = g - \sin(\mu_1 + \theta_1) \overline{EF} - \sin(\mu_2 + \delta) \overline{FH}. \quad (3.28)$$

These equations can be written in nondimensional form as

$$x_{\star}^+ = \cos(\mu_1 + \theta_1) \overline{EF}^+ + \cos(\mu_2 + \delta) \overline{FH}^+ - x_s^+, \quad (3.29)$$

$$s_{\star}^+ = g^+ - \sin(\mu_1 + \theta_1) \overline{EF}^+ - \sin(\mu_2 + \delta) \overline{FH}^+. \quad (3.30)$$

There are now five equations for five unknowns. They can now be written in matrix form and solved. We will use the fact that

$$M_1^2 \sin \mu_1 = M_1 \quad (3.31)$$

$$M_2^2 \sin \mu_2 = M_2 \quad (3.32)$$

The matrix equation is

$$\begin{pmatrix} 0 & 0 & A_r & a_{14} & a_{15} \\ 0 & 0 & a_{23} & a_{24} & a_{25} \\ \frac{1}{\gamma M_{\infty}^2} & P_3^+ & 0 & a_{34} & a_{35} \\ 1 & 1 & 0 & a_{44} & a_{45} \\ 0 & 0 & 1 & a_{54} & a_{55} \end{pmatrix} \begin{pmatrix} x_s^+ \\ x_{\star}^+ \\ s_{\star}^+ \\ \overline{EF}^+ \\ \overline{FH}^+ \end{pmatrix} = \begin{pmatrix} g^+ + \sin \theta_1 \\ \frac{g^+ + \sin \theta_1}{\gamma M_{\infty}^2} + g^+ + \sin \theta_1 - P_1^+ \sin \theta_1 \\ -\frac{1}{\gamma M_{\infty}^2} \cos \theta_1 + P_1^+ \cos \theta_1 \\ 0 \\ g^+ \end{pmatrix}, \quad (3.33)$$

where

$$a_{14} = \frac{\sin \alpha}{\sin(\alpha - \theta_1)} \sin \mu_1, \quad (3.34)$$

$$a_{15} = \frac{\sin \alpha \sin(\theta_1 + \phi)}{\sin(\alpha - \theta_1) \sin(\phi + \delta)} \sin \mu_2, \quad (3.35)$$

$$a_{23} = \gamma P_\star^+ + P_\star^+, \quad (3.36)$$

$$a_{24} = \gamma P_1^+ M_1 \cos \theta_1 + P_1^+ \sin(\mu_1 + \theta_1), \quad (3.37)$$

$$a_{25} = \gamma P_2^+ M_2 \cos \delta + P_2^+ \sin(\mu_2 + \delta), \quad (3.38)$$

$$a_{34} = \gamma P_1^+ M_1 \sin \theta_1 - P_1^+ \cos(\mu_1 + \theta_1), \quad (3.39)$$

$$a_{35} = \gamma P_2^+ M_2 \sin \delta - P_2^+ \cos(\mu_2 + \delta), \quad (3.40)$$

$$a_{44} = -\cos(\mu_1 + \theta_1), \quad (3.41)$$

$$a_{45} = -\cos(\mu_2 + \delta), \quad (3.42)$$

$$a_{54} = \sin(\mu_1 + \theta_1), \quad (3.43)$$

$$a_{55} = \sin(\mu_2 + \delta), \quad (3.44)$$

and A_r is the area ratio between s^+ and s_\star^+ . This matrix equation agrees with the results of Azevedo.

Given the geometry, the Mach number, and the ratio of specific heats, all the parameters of the matrix equation can be calculated. The shock angle, α , the Mach number and the pressure behind the leading oblique shock, M_1 and P_1 , can be calculated using the oblique shock relations:

$$\cot \theta_1 = \tan \alpha \left(\frac{(\gamma + 1) M_\infty^2}{2(M_\infty^2 \sin^2 \alpha - 1)} - 1 \right), \quad (3.45)$$

$$P_1 = P_\infty \frac{2\gamma M_\infty^2 \sin^2 \alpha - (\gamma - 1)}{\gamma + 1}, \quad (3.46)$$

$$M_1^2 = \frac{(\gamma - 1) M_\infty^2 \sin^2 \alpha + 2}{\sin^2(\alpha - \theta_1) (2\gamma M_\infty^2 \sin^2 \alpha - (\gamma - 1))}. \quad (3.47)$$

Equation 3.46 can be expressed in nondimensional form as

$$P_1^+ = \frac{1}{\gamma M_\infty^2} \frac{2\gamma M_\infty^2 \sin^2 \alpha - (\gamma - 1)}{\gamma + 1}. \quad (3.48)$$

Since Azevedo assumes that the Mach stem is a normal shock, the Mach number and

pressure just behind the Mach stem, M_a , and P_a can be found using the normal shock relations,

$$P_a = P_\infty \frac{2\gamma M_\infty^2 - (\gamma - 1)}{\gamma + 1}, \quad (3.49)$$

$$M_a^2 = \frac{(\gamma - 1) M_\infty^2 + 2}{2\gamma M_\infty^2 - (\gamma - 1)}. \quad (3.50)$$

Nondimensionalizing Equation 3.49 gives

$$P_a^+ = \frac{1}{\gamma M_\infty^2} \frac{2\gamma M_\infty^2 - (\gamma - 1)}{\gamma + 1}. \quad (3.51)$$

Again using the oblique shock relations we find the flow angle, the pressure, and the Mach number in Region 2 to be

$$\cot(\theta_1 - \delta) = \tan(\phi + \theta_1) \left(\frac{(\gamma + 1) M_1^2}{2(M_1^2 \sin^2(\phi + \theta_1) - 1)} - 1 \right), \quad (3.52)$$

$$P_2 = P_1 \frac{2\gamma M_1^2 \sin^2(\phi + \theta_1) - (\gamma - 1)}{\gamma + 1}, \quad (3.53)$$

$$M_2^2 = \frac{(\gamma - 1) M_1^2 \sin^2(\phi + \theta_1) + 2}{\sin^2(\phi + \delta) (2\gamma M_\infty^2 \sin^2 \alpha - (\gamma - 1))}. \quad (3.54)$$

As before, P_2 can be written in nondimensional form as

$$P_2^+ = P_1^+ \frac{2\gamma M_1^2 \sin^2(\phi + \theta_1) - (\gamma - 1)}{\gamma + 1}. \quad (3.55)$$

The angle of the slipline, δ , can be calculated using triplepoint theory. This theory states that the pressure and flow angle must be continuous across the slipline. Up to this point, we have been assuming that the Mach stem is a normal shock; however, to accurately analyze the local flow around the triple point, the angle of the Mach stem must be considered. A close-up of the triple point is shown in Figure 3.2. Note that the region behind the Mach stem is referred to as a' rather than a , for the purposes of calculating the triple point deflection angle when an oblique Mach stem is used; whereas, for calculating the flow in the converging flow behind the Mach stem a normal Mach stem is considered. There is no closed-form solution to this problem, so an iterative scheme must be used. The two

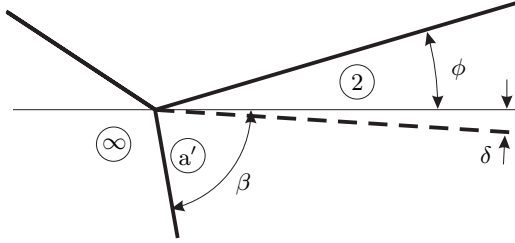


Figure 3.2: Triple point with a Mach stem that is not perpendicular to the flow.

following equations are solved for ϕ and β :

$$P_2^+ = P_{a'}^+, \quad (3.56)$$

$$\delta_2 = \delta_{a'}. \quad (3.57)$$

These equations are

$$P_1^+ \frac{2\gamma M_1^2 \sin^2(\phi + \theta_1) - (\gamma - 1)}{\gamma + 1} = \frac{1}{\gamma M_\infty^2} \frac{2\gamma M_\infty^2 \sin^2 \beta - (\gamma - 1)}{\gamma + 1}, \quad (3.58)$$

$$\tan(\phi + \theta_1) \left(\frac{(\gamma + 1) M_1^2}{M_1^2 \sin^2(\phi + \theta_1) - 1} - 2 \right) = \tan \beta \left(\frac{(\gamma + 1) M_\infty^2}{M_\infty^2 \sin^2 \beta - 1} - 2 \right). \quad (3.59)$$

With ϕ known, Equation 3.52 can be used to solve for δ . Finally, in order to solve Equation 3.33, the area ratio, A_r , and pressure ratio, $\frac{P_\star}{P_a}$, of the converging flow behind the Mach stem must be calculated. These are

$$A_r = \frac{1}{M_a} \left(\frac{2}{\gamma + 1} \left(1 + \frac{\gamma - 1}{2} M_a^2 \right) \right)^{\frac{\gamma + 1}{2(\gamma - 1)}}, \quad (3.60)$$

$$\frac{P_\star}{P_a} = \left(\frac{2}{\gamma + 1} \left(1 + \frac{\gamma - 1}{2} M_a^2 \right) \right)^{\frac{\gamma}{\gamma - 1}}, \quad (3.61)$$

since the point \star corresponds to the sonic throat. At this point, all the terms in the matrix in Equation 3.33 are known and the linear system can be solved. Finally, Azevedo solves for the Mach stem height by using the geometric relationship

$$s = g + w \sin \theta_1 - (w \cos \theta_1 + x_s) \tan \alpha. \quad (3.62)$$

In nondimensional form this is

$$s^+ = g^+ + \sin \theta_1 - (x_s^+ + \cos \theta_1) \tan \alpha. \quad (3.63)$$

This last equation is not needed since we see that in Equation 3.33 there is a subsystem of equations for s_\star^+ , \overline{EF}^+ , and \overline{FH}^+ , which is sufficient to solve for the Mach stem height given that $s^+ = A_r s_\star^+$. We can write this system simply as

$$\begin{pmatrix} A_r & a_{14} & a_{15} \\ a_{23} & a_{24} & a_{25} \\ 1 & a_{54} & a_{55} \end{pmatrix} \begin{pmatrix} s_\star^+ \\ \overline{EF}^+ \\ \overline{FH}^+ \end{pmatrix} = \begin{pmatrix} -\frac{1}{\gamma M_\infty^2} \cos \theta_1 + P_1^+ \cos \theta_1 \\ 0 \\ g^+ \end{pmatrix}. \quad (3.64)$$

In this case the Mach stem height would be calculated using the area relationship of the sonic throat behind the Mach stem,

$$s = A_r s_\star, \quad (3.65)$$

or

$$s^+ = A_r s_\star^+. \quad (3.66)$$

The analysis so far produces a geometry which is not self-consistent. Specifically, the pressure in Region 2 is taken to be constant, which is not consistent with the fact that the flow in Region 3 is of varying pressure. Furthermore, there are two other equally valid solutions for s^+ , besides that given in Equation 3.66.

Specifically, as Azevedo writes,

$$s^+ = g^+ + \sin \theta_1 - (x_s^+ + \cos \theta_1) \tan \alpha, \quad (3.67)$$

which states that the height of the Mach stem must be equal to g plus the height of the wedge minus the height of the incident shock. Another equally valid way of writing the Mach stem height is

$$s^+ = s_\star^+ + x_\star^+ \tan \delta. \quad (3.68)$$

All three of these calculations, Equations 3.66, 3.67 and 3.68, for the Mach stem height produce slightly different answers. Again, this is due to the fact that the pressure in Region 3 varies and is not consistent with the assumption of constant pressure in Region 2. It is

important to note that there is no simple way of matching the pressure across the slipline. Since the pressure is not correct a solution that tries to conserve momentum is also incorrect and produces an inconsistent geometry. Therefore, it may be useful to fix the geometry and continue to allow the pressure across the slipline to be mismatched.

3.3 Geometric Solution

In Azevedo's solution the most restrictive assumption is that the sonic throat occurs at the leading characteristic of the expansion fan. Also, Azevedo does not force the geometry to be self-consistent, specifically, the condition that the slipline, \overline{TH} intersects the expansion wave, \overline{FH} , and the sonic throat at a point is not imposed. To solve the latter problem we can write five equations that fix the geometry, assuming that all shocks and sliplines are straight. It is important to note that these equations implicitly satisfy the mass and momentum equations because the shock-jump conditions, which are used to generate the geometry, satisfy the mass and momentum equations. These equations are

$$\sin \alpha \overline{OT} + s = g + w \sin \theta_1, \quad (3.69)$$

$$s_* + \sin(\delta + \mu_2) \overline{FH} + \sin(\mu_1 + \theta_1) \overline{EF} = g, \quad (3.70)$$

$$\cos \alpha \overline{OT} + \cos \delta \overline{TH} - \cos(\delta + \mu_2) \overline{FH} - \cos(\mu_1 + \theta_1) \overline{EF} = w \cos \theta_1, \quad (3.71)$$

$$\cos \alpha \overline{OT} + \cos \phi \overline{TF} - \cos(\mu_1 + \theta_1) \overline{EF} = w \cos \theta_1, \quad (3.72)$$

$$\sin \alpha \overline{OT} - \sin \phi \overline{TF} - \sin(\mu_1 + \theta_1) \overline{EF} = w \sin \theta_1. \quad (3.73)$$

Given the area ratio between s and s_* , we can write $\cos \delta \overline{TH}$ as

$$\cos \delta \overline{TH} = \cot \delta (A_r - 1) s_*. \quad (3.74)$$

Making the substitution for \overline{TH} , and nondimensionalizing the equations, produces

$$\sin \alpha \overline{OT}^+ + A_r s_*^+ - \sin \theta_1 = g^+, \quad (3.75)$$

$$s_*^+ + \sin(\delta + \mu_2) \overline{FH}^+ + \sin(\mu_1 + \theta_1) \overline{EF}^+ = g^+, \quad (3.76)$$

$$\cos \alpha \overline{OT}^+ + \cot \delta (A_r - 1) s_*^+ - \cos(\delta + \mu_2) \overline{FH}^+ - \cos(\mu_1 + \theta_1) \overline{EF}^+ = \cos \theta_1, \quad (3.77)$$

$$\cos \alpha \overline{OT}^+ + \cos \phi \overline{TF}^+ - \cos(\mu_1 + \theta_1) \overline{EF}^+ = \cos \theta_1, \quad (3.78)$$

$$\sin \alpha \overline{OT}^+ - \sin \phi \overline{TF}^+ - \sin(\mu_1 + \theta_1) \overline{EF}^+ = \sin \theta_1. \quad (3.79)$$

This can then be written in matrix form as

$$\begin{pmatrix} \sin \alpha & A_r & 0 & 0 & 0 \\ 0 & 1 & \sin(\delta + \mu_2) & \sin(\mu_1 + \theta_1) & 0 \\ -\cos \alpha & -\cot \delta (A_r - 1) & \cos(\delta + \mu_2) & \cos(\mu_1 + \theta_1) & 0 \\ -\cos \alpha & 0 & 0 & \cos(\mu_1 + \theta_1) & -\cos \phi \\ -\sin \alpha & 0 & 0 & \sin(\mu_1 + \theta_1) & \sin \phi \end{pmatrix} \begin{pmatrix} \overline{OT}^+ \\ s_*^+ \\ \overline{FH}^+ \\ \overline{EF}^+ \\ \overline{TF}^+ \end{pmatrix} = \begin{pmatrix} g^+ + \sin \theta_1 \\ g^+ \\ -\cos \theta_1 \\ -\cos \theta_1 \\ -\sin \theta_1 \end{pmatrix}. \quad (3.80)$$

Finally, the Mach stem height, s , can be calculated using Equation 3.66. These equations, unlike those used by Azevedo, do not explicitly include the conservation of mass and momentum. However, if we consider the slipline to be a solid wall, we see that mass and momentum are conserved. This is because if the slipline were a solid wall the assumptions made in this analysis are exact, since the entire geometry is self-consistent, and all of the shock jump conditions used conserve mass and momentum. Unfortunately, like Azevedo's solution, the pressure across the slipline is not continuous.

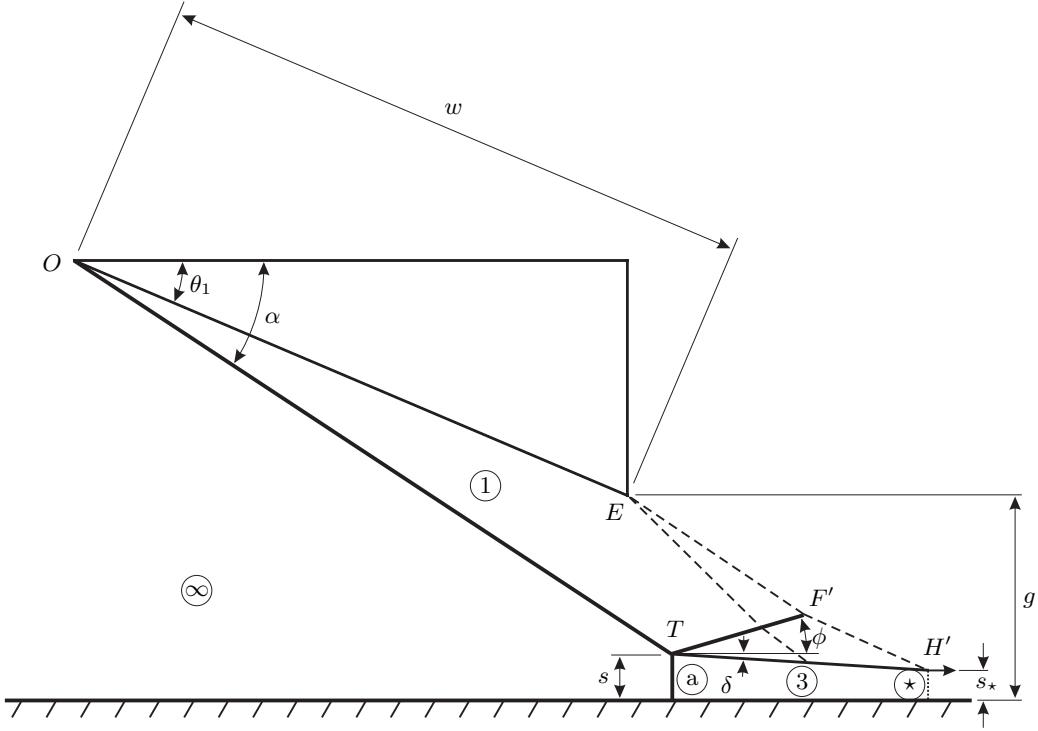


Figure 3.3: Flow setup, allowing for a sonic throat downstream of the leading characteristic, used to predict the Mach stem height.

3.4 Generalized Geometric Solution

The problem still remains that all of these solutions assume that the sonic throat of the flow behind the Mach stem occurs at the leading characteristic of the expansion fan. To eliminate this problem, we will allow the sonic throat to occur further downstream. This generalized setup is shown in Figure 3.3. The geometrical considerations are the same as those leading to Equation 3.80, with F and H replaced by F' and H' , respectively. Also, $\mu_{1'}$ and $\mu_{2'}$ refer to the Mach angle along the characteristic corresponding to the sonic throat, rather than along the leading characteristic. A key point of this theory is that the flow right

above the sonic throat is parallel to the free-stream flow.

$$\begin{pmatrix}
 \sin \alpha & A_r & 0 & 0 & 0 \\
 0 & 1 & \sin(\delta + \mu_{2'}) & \sin(\mu_{1'} + \theta_1) & 0 \\
 -\cos \alpha & \cot \delta (1 - A_r) & \cos(\delta + \mu_{2'}) & \cos(\mu_{1'} + \theta_1) & 0 \\
 -\cos \alpha & 0 & 0 & \cos(\mu_{1'} + \theta_1) & -\cos \phi \\
 -\sin \alpha & 0 & 0 & \sin(\mu_{1'} + \theta_1) & \sin \phi
 \end{pmatrix}
 \begin{pmatrix}
 \overline{OT}^+ \\
 s_*^+ \\
 \overline{F'H'}^+ \\
 \overline{EF'}^+ \\
 \overline{TF'}^+
 \end{pmatrix}
 = \begin{pmatrix}
 g^+ + \sin \theta_1 \\
 g^+ \\
 -\cos \theta_1 \\
 -\cos \theta_1 \\
 -\sin \theta_1
 \end{pmatrix}. \quad (3.81)$$

The slipline angle, δ , and the reflected shock angle, ϕ , are calculated as before using triple point theory. The Mach angle along the characteristic, $\mu_{2'}$, is calculated knowing that the flow just above the slipline must turn through an angle of δ in order to be parallel to the free-stream just above the sonic throat,

$$\delta = \nu(M_{2'}) - \nu(M_2), \quad (3.82)$$

where the Prandtl-Meyer function, ν , is defined as

$$\nu(M) = \sqrt{\frac{\gamma+1}{\gamma-1}} \tan^{-1} \sqrt{\frac{\gamma-1}{\gamma+1} (M^2 - 1)} - \tan^{-1} \sqrt{M^2 - 1}. \quad (3.83)$$

Since M_2 is known from Equation 3.54, solutions for $M_{2'}$ and $\mu_{2'}$ may be obtained. $\mu_{1'}$ is more difficult to determine since the flow deflection angle is not simply δ , because the flow has passed through part of the expansion before it reaches the shock, as opposed to the flow in Region 2, which first goes through the reflected shock. This means that the flow in Region 1 must turn through an angle of $\delta + \delta_e$, where δ_e is the extra turning required to compensate for the fact that the reflected shock is weaker at F' than at T . Specifically, the reflected shock at the point F' must turn the flow through $\theta_1 - \delta - \delta_e$. Using oblique shock

relations produces

$$\cot(\theta_1 - \delta - \delta_e) = \tan(\theta_1 - \delta - \delta_e + \phi) \left(\frac{(\gamma + 1) M_{1'}^2}{2(M_{1'}^2 \sin^2(\theta_1 - \delta - \delta_e + \phi) - 1)} - 1 \right), \quad (3.84)$$

where $M_{1'}$ is given by the Prandtl-Meyer function,

$$\delta + \delta_e = \nu(M_{1'}) - \nu(M_1). \quad (3.85)$$

Equations 3.84 and 3.85 can then be solved simultaneously for δ_e and $M_{1'}$. At this point, $\mu_{1'}$ is known and Equation 3.81 can be solved. Once the matrix equation has been solved, the Mach stem height, s , can be calculated using Equation 3.66.

3.5 Numerical Calculations

Numerical simulations of the flow were performed for various conditions using the Amrita software system. This software system has been constructed by James Quirk [24] and has been extensively tested by the current author [25]. It is a system that automates and packages computational tasks in such a way that the packages can be combined (dynamically linked) according to instructions written in a high-level scripting language. The present application uses features of Amrita that include the automatic construction of an Euler solver, automatic adaptive mesh refinement according to simply chosen criteria, and scripting-language-driven computation and postprocessing of the results. The Euler solver generated for the present computation was an operator-split scheme with HLLE flux and kappa-MUSCL reconstruction.

The coarse grid for the Mach stem height calculations was 330×140 , to which two levels of adaptive mesh refinement by a factor of 2 were applied. This results in an effective grid of 1320×560 . The mesh was refined based on a density gradient criterion as well as along the surface of the wedge. An example of the grid is shown in Figure 3.4, with an enlarged section shown in Figure 3.5.

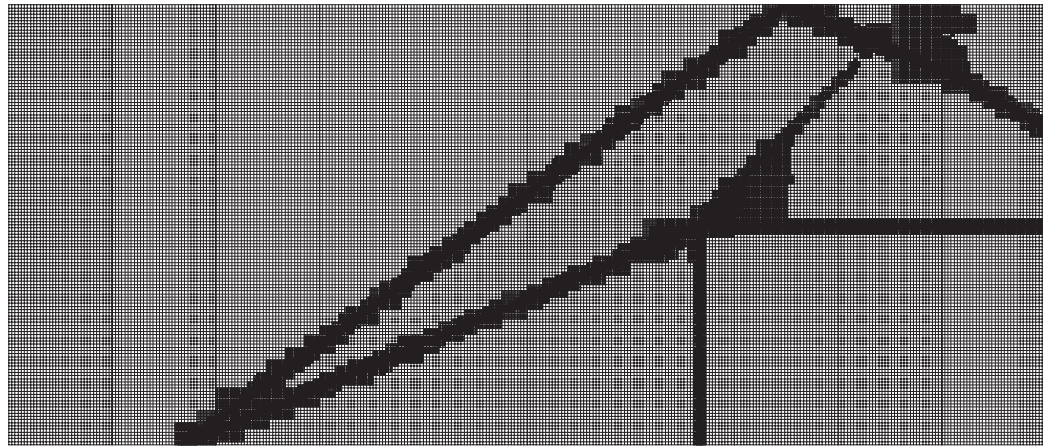


Figure 3.4: Representative mesh refinement for the calculation of the Mach stem height using Amrita.

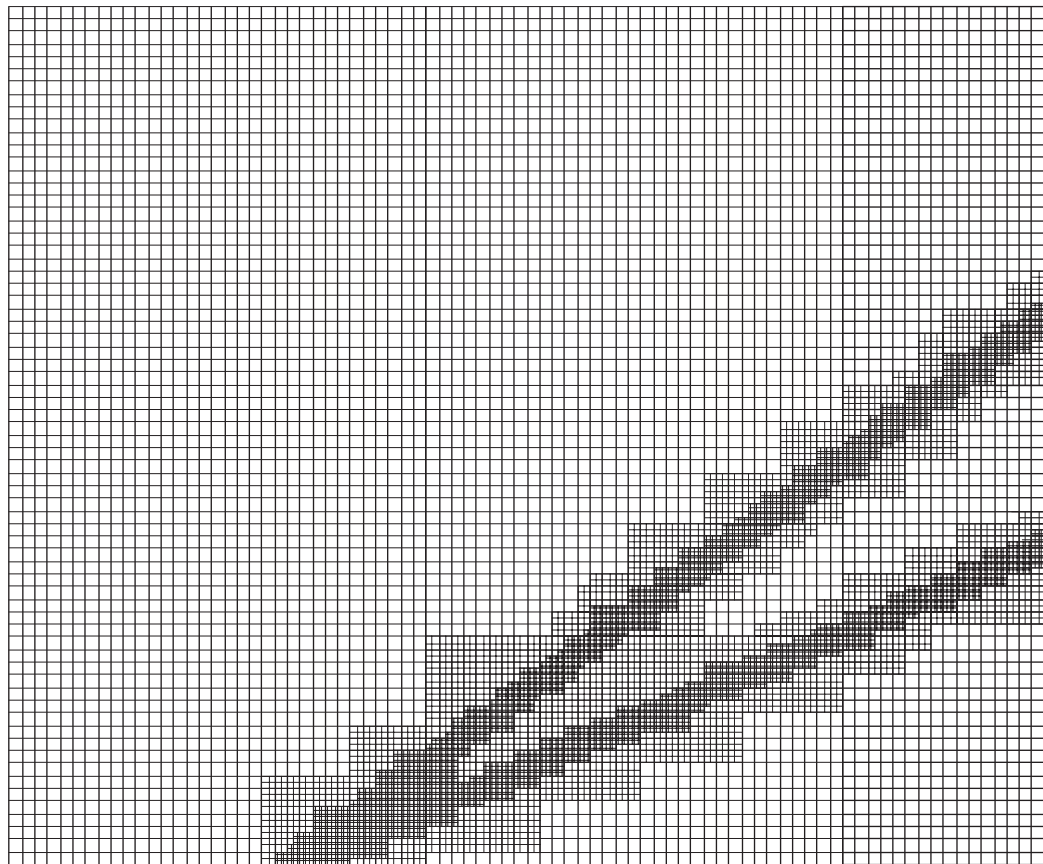


Figure 3.5: Enlarged region of a representative mesh refinement for the calculation of the Mach stem height using Amrita.

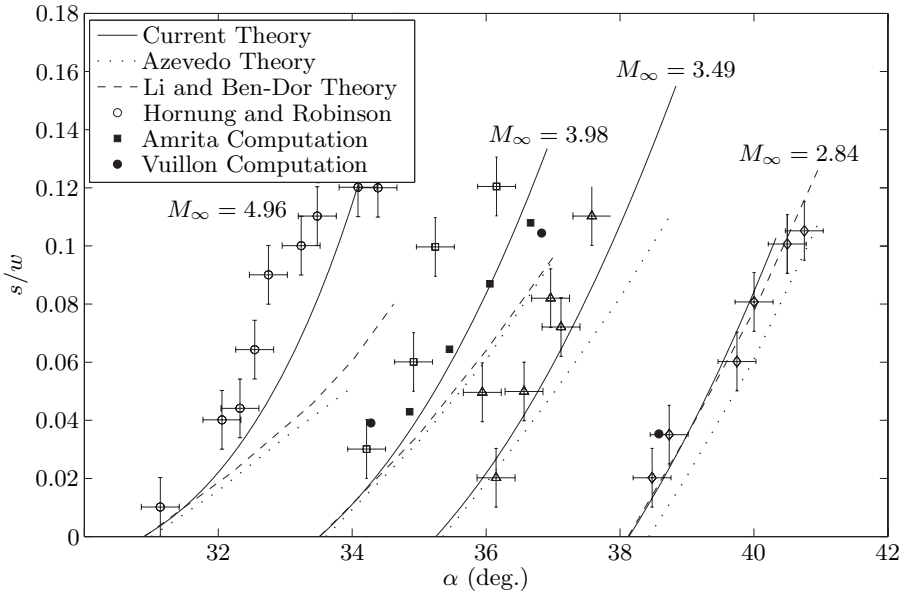


Figure 3.6: Comparison of current Mach stem height calculations against those of Azevedo [7, 18] and of Li [20], measurements by Hornung and Robinson [6], computations by Vuillon et al. [26], and current computations done using Amrita. $\gamma = 1.4$ and $g/w \approx 0.4$.

3.6 Mach Stem Height Results

A comparison of the current theory with that of Azevedo [7, 18] as well as the theory of Li and Ben-Dor [20], the numerical results of Amrita, and the experimental results of Hornung and Robinson [6] is shown in Figure 3.6. This figure shows the significant improvement made using the generalized geometric solution. Overall agreement with the experimental data of Hornung and Robinson and with computational results is good. Of course differences between theory, computations and experiments remain. There are several reasons for these discrepancies. First, the slipline originating from the triple point is not in fact straight. Second, the reflected shock will curve through the expansion fan. Third, viscous effects will cause a shear layer with negative displacement effect to develop along the slipline.

It is important to note that the data which both Azevedo [7, 18] and Li and Ben-Dor [20] attribute to Hornung and Robinson [6] are in fact not the data presented in that paper. The actual data of Hornung and Robinson are significantly different and show higher Mach stem heights than what is presented by Azevedo and by Li and Ben-Dor. Figure 3.6 shows the actual results presented by Hornung and Robinson.

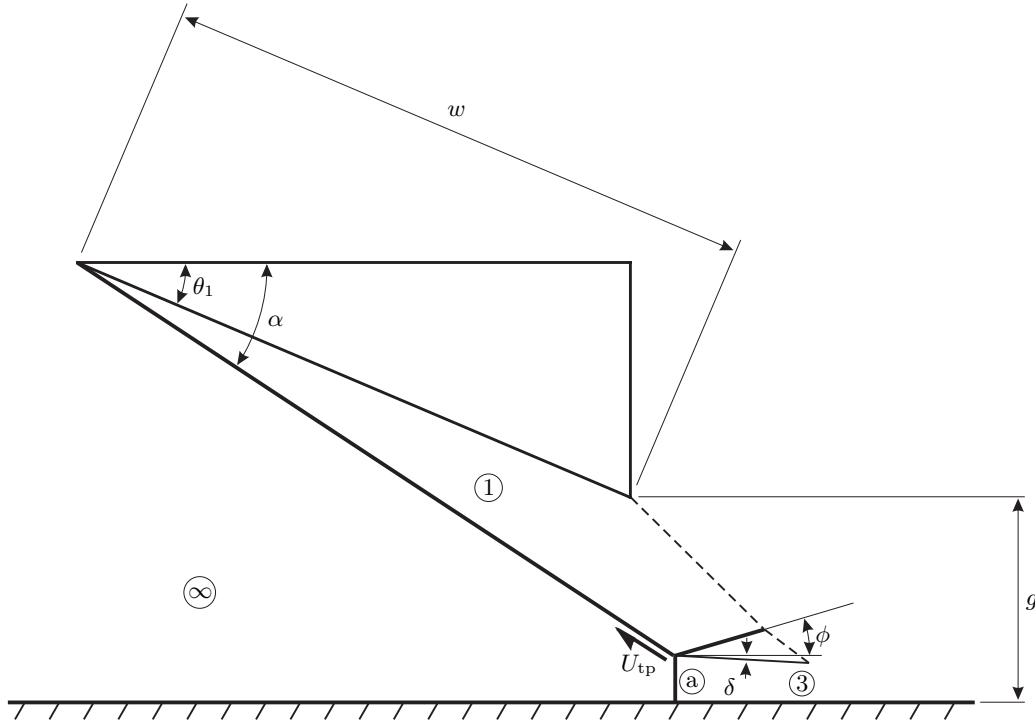


Figure 3.7: Flow setup, allowing for a moving triple point, used to calculate the Mach stem height growth.

3.7 Moving Triple Point Analysis

The triple point analysis presented earlier assumed a stationary Mach stem. We will now consider the case where the Mach stem moves with an upstream velocity, U_{Ms} , subject to a quasi-steady flow assumption. This may occur in a steady free stream, e.g., if transition to Mach reflection is initiated by some disturbance when the flow is initially in the dual-solution region. The rate at which the Mach stem moves upstream, U_{Ms} , is related to the speed at which the triple point travels up along the lead shock, U_{tp} , by

$$U_{tp} = \frac{U_{Ms}}{\cos \alpha}. \quad (3.86)$$

Figure 3.7 shows the flow setup when the triple point is moving.

To perform the triple-point analysis we must examine the flow both in the lab-fixed reference frame and in the frame of the triple point. Quantities calculated in the reference frame of the triple point are denoted with a superscript ^{tp}. The flow Mach number coming

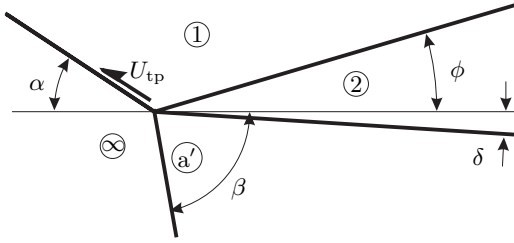


Figure 3.8: Moving triple point with a Mach stem that is not perpendicular to the flow.

into the Mach stem, M_∞^{tp} , is

$$M_\infty^{\text{tp}} = \sqrt{(M_\infty + M_{\text{tp}} \cos \alpha)^2 + (M_{\text{tp}} \sin \alpha)^2}, \quad (3.87)$$

where

$$M_{\text{tp}} = \frac{U_{\text{tp}}}{a_\infty}. \quad (3.88)$$

Since the leading oblique shock is stationary in the lab frame we can write the Mach number in region 1, M_1 , and the normalized pressure in region 1, P_1^+ , as

$$P_1^+ = \xi(M_\infty, \gamma, \alpha), \quad (3.89)$$

$$M_1 = M(M_\infty, \gamma, \alpha). \quad (3.90)$$

To calculate the flow in region 2, we must consider the flow first in the reference frame of the triple point. The normalized pressure, Mach number and flow angle in region 2 can be written as

$$P_2^+ = P_1^+ \xi(M_1^{\text{tp}}, \gamma, \phi^{\text{tp}}), \quad (3.91)$$

$$M_2^{\text{tp}} = M(M_1^{\text{tp}}, \gamma, \phi^{\text{tp}}), \quad (3.92)$$

$$\theta_2^{\text{tp}} = \theta_1^{\text{tp}} - \theta(M_1^{\text{tp}}, \gamma, \phi^{\text{tp}}), \quad (3.93)$$

where

$$M_1^{\text{tp}} = \left(\frac{(M_1 a_1 \cos \theta_1 + U_{\text{tp}} \cos \alpha)^2 + (M_1 a_1 \sin \theta_1 + U_{\text{tp}} \sin \alpha)^2}{a_1^2} \right)^{1/2}, \quad (3.94)$$

$$\theta_1^{\text{tp}} = \tan^{-1} \frac{M_1 a_1 \sin \theta_1 + U_{\text{tp}} \sin \alpha}{M_1 a_1 \cos \theta_1 + U_{\text{tp}} \cos \alpha}. \quad (3.95)$$

Converting back into lab-fixed coordinates, we see that

$$\phi = \phi^{\text{tp}} - \theta_1^{\text{tp}}. \quad (3.96)$$

Similarly, the normalized pressure, Mach number, and flow angle in region a' can be written as

$$P_{a'}^+ = \xi(M_\infty^{\text{tp}}, \gamma, \beta^{\text{tp}}), \quad (3.97)$$

$$M_{a'}^{\text{tp}} = M(M_\infty^{\text{tp}}, \gamma, \beta^{\text{tp}}), \quad (3.98)$$

$$\theta_{a'}^{\text{tp}} = \theta_\infty^{\text{tp}} - \theta(M_\infty^{\text{tp}}, \gamma, \beta^{\text{tp}}), \quad (3.99)$$

where

$$M_\infty^{\text{tp}} = \sqrt{(M_\infty + M_{\text{tp}} \cos \alpha)^2 + (M_{\text{tp}} \sin \alpha)^2}, \quad (3.100)$$

$$\theta_\infty^{\text{tp}} = \tan^{-1} \frac{M_{\text{tp}} \sin \alpha}{M_\infty + M_{\text{tp}} \cos \alpha}. \quad (3.101)$$

Converting these values back into lab-fixed coordinates, produces

$$\beta = \beta^{\text{tp}} - \theta_\infty^{\text{tp}}, \quad (3.102)$$

$$\delta_{a'} = \tan^{-1} \frac{M_{a'}^{\text{tp}} a_{a'} \cos \theta_{a'}^{\text{tp}} - U_{\text{tp}} \cos \alpha}{M_{a'}^{\text{tp}} a_{a'} \sin \theta_{a'}^{\text{tp}} - U_{\text{tp}} \sin \alpha}, \quad (3.103)$$

where $a_{a'}$ is the speed of sound in region a' .

As we did earlier in Equations 3.56 and 3.57, we impose

$$P_2^+ = P_{a'}^+, \quad (3.104)$$

$$\delta_2 = \delta_{a'}. \quad (3.105)$$

The effect of a moving Mach stem is shown in Figure 3.9. As one would expect, if the Mach stem is moving upstream, the pressure behind the Mach stem is higher, and if the Mach stem moves downstream, the pressure is lower than in the stationary case. The speed at which the Mach stem can move downstream is limited by the fact that a reflected shock must be able to exist. Specifically, it is not possible for the triple point to

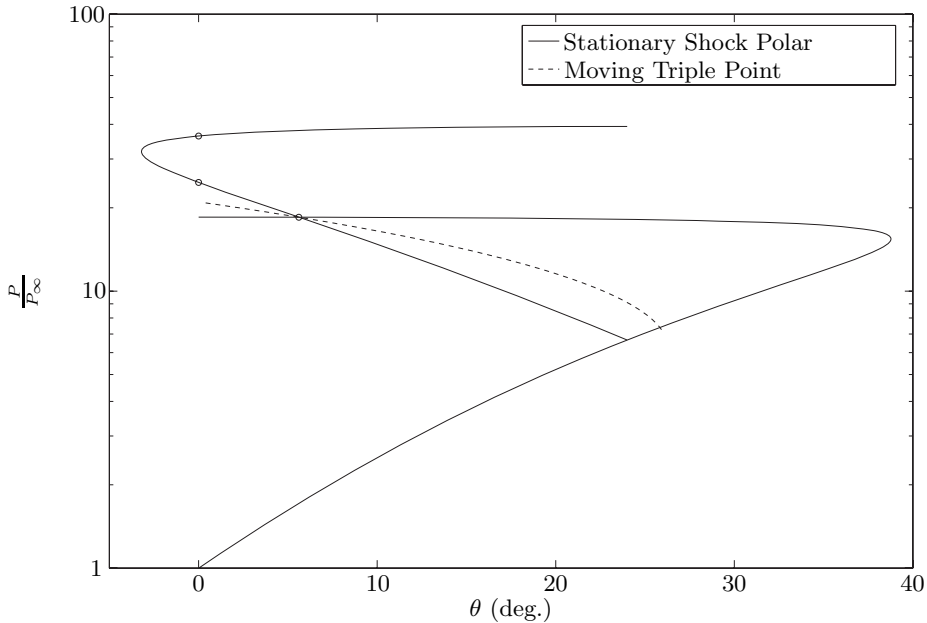


Figure 3.9: Shock polar illustrating the effects of a moving Mach stem. In the case where the Mach stem is moving upstream the pressure ratio is higher than the stationary-case value, and vice-versa. Each point on the moving triple point curve represents the pressure and deflection angle for a given M_{tp} . $M_\infty=4$, $\gamma=1.4$, $\theta_w=24^\circ$.

be moving downstream so fast that the relative flow into the reflected shock is subsonic. This means that the perpendicular component of the flow into the reflected shock must be supersonic. As the flow speed into the reflected shock decreases, the pressure rise across the reflected shock also decreases, and we would expect the pressure and the flow deflection to be similar to that of the leading shock alone. In other words, as the triple point moves downstream, the jump across the reflected shock becomes weaker and the flow deflection across the reflected shock decreases. This is indeed seen in Figure 3.9, where the moving triple-point line terminates near the incident shock point.

3.8 Mach Stem Height Variation

As the Mach stem grows, it also slows down. Thus, for a given Mach stem speed a corresponding Mach stem height exists. Using Equation 3.81 and substituting the modified flow parameters, as found in Section 3.7, it is possible to calculate the Mach stem height at a given Mach stem speed. Conversely, given a Mach stem height, the Mach stem speed can

be calculated. At the steady-state Mach stem height, the Mach stem velocity will of course be zero. Of special interest is the speed of the Mach stem when the height is different than the steady-state height, in particular, the speed of the Mach stem during the Mach stem growth phase.

To understand the growth phase of the Mach stem, let us consider a very small Mach stem, as is shown in Figure 3.10. If the Mach stem were stationary, the slipline originating from the triple point would have a finite angle and therefore reach the wall before the leading characteristic. Since it is not physically possible for the slipline to intersect the wall we know that this solution can not be correct, and therefore the Mach stem must move in order to produce a different slipline angle. Specifically, we need the slipline angle to be at a small enough angle such that it reaches the first characteristic. We therefore now know that the triple point must move in a way as to decrease the slipline angle. Let us now consider a slipline angle sufficiently small that it intersects the first characteristic just above the wall. In this case, the area ratio between the Mach stem and the intersection of the slipline with the first characteristic would be very large.

From Figure 3.9, we see that the deflection angle is decreased if the shock is moving upstream. Additionally, the flow Mach number behind the Mach stem will decrease if the Mach stem moves upstream, which produces a large area ratio. Based on this we can hypothesize that for small Mach stems, the Mach stem must travel upstream. Based simply on geometry, a Mach stem traveling upstream also increases in height.

The moving Mach stem changes the slipline angle, δ , the reflected shock angle, ϕ , the Mach angle in region 2', and the area ratio between the Mach stem and the sonic throat, A_r . Assuming quasi-steady flow, that is to say, the speed at which the triple point grows is slow compared to the flow speed, Equation 3.80, with modifications taking into account

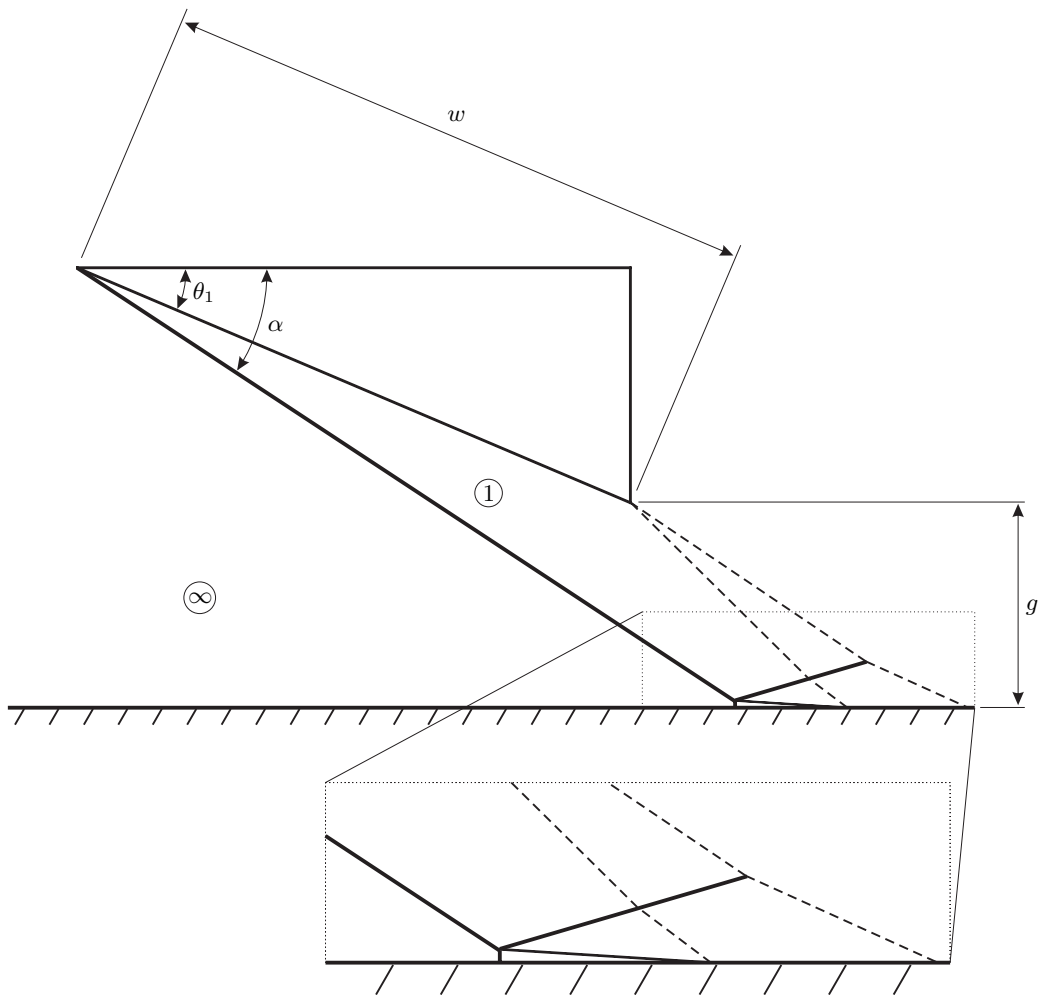


Figure 3.10: A very small Mach stem with a finite angle slipline. If the Mach stem is small enough, the slipline will intersect the axis of symmetry before it reaches the first expansion wave.

the moving Mach stem, becomes

$$\begin{pmatrix} \sin \alpha & \tilde{A}_r & 0 & 0 & 0 \\ 0 & 1 & \sin(\delta + \tilde{\mu}_2) & \sin(\mu_1 + \theta_1) & 0 \\ -\cos \alpha & -\cot \tilde{\delta} (\tilde{A}_r - 1) & \cos(\delta + \tilde{\mu}_2) & \cos(\mu_1 + \theta_1) & 0 \\ -\cos \alpha & 0 & 0 & \cos(\mu_1 + \theta_1) & -\cos \tilde{\phi} \\ -\sin \alpha & 0 & 0 & \sin(\mu_1 + \theta_1) & \sin \tilde{\phi} \end{pmatrix} \begin{pmatrix} \overline{OT}^+ \\ s_*^+ \\ \overline{FH}^+ \\ \overline{EF}^+ \\ \overline{TF}^+ \end{pmatrix} = \begin{pmatrix} g^+ + \sin \theta_1 \\ g^+ \\ -\cos \theta_1 \\ -\cos \theta_1 \\ -\sin \theta_1 \end{pmatrix}, \quad (3.106)$$

where \sim denotes the value depending on the speed of the Mach stem. These modified values are derived from Equations 3.96, 3.103, 3.92 and 3.100.

Figure 3.11 illustrates the solution to the relationship between Mach stem velocity and Mach stem height as given by Equation 3.106.

Given the numerical relationship between M_{tp} and s/w it is possible to calculate the evolution of the Mach stem. Specifically,

$$\frac{ds}{dt} = U_{tp} \sin \alpha. \quad (3.107)$$

In non-dimensional form, this becomes,

$$\frac{d(s/w)}{d(a_\infty t/w)} = M_{tp} \sin \alpha, \quad (3.108)$$

where M_{tp} is dependent on s/w , M_∞ , g/w , γ , and θ_1 . The calculation is quite straightforward and a comparison between the expected Mach stem growth and a numerical calculation done using Amrita is shown in Figure 3.13. Figure 3.6 shows that the steady-state Mach stem height grows rapidly with wedge angle. This means that even small errors can result in a large height difference. It is therefore reasonable to expect better agreement at lower steady-state Mach stem heights. Figure 3.12 shows the comparison of the Mach stem

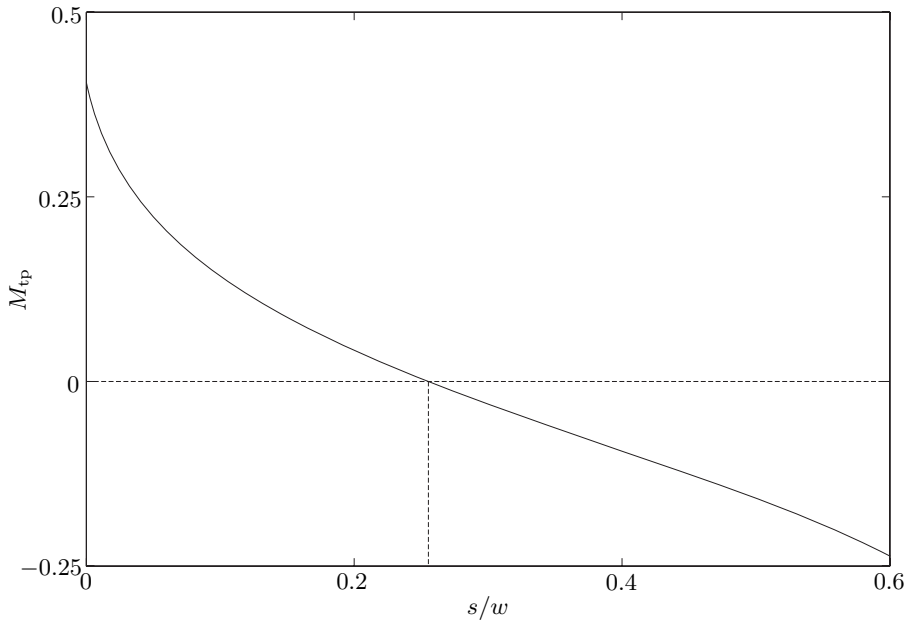


Figure 3.11: Mach stem velocity as a function of Mach stem height based on Equation 3.80. Positive M_{tp} indicates upstream speed. Calculated for $M_\infty=4$, $g/w=0.4$, $\gamma=1.4$, and $\theta_1=25^\circ$.

height growth for a wedge angle of $\theta_1=23^\circ$.

In Figure 3.13 we see that the predicted Mach stem height is about 60% greater than in the numerical computation. This figure represents what is a relatively extreme case. Specifically, the numerically calculated Mach stem height, s/w , is slightly under 0.2, whereas most theoretical predictions of Mach stem height, including those presented in this thesis, only appear to be valid for Mach stem heights below about 0.1. Experimental results presented later in this thesis show that for large Mach stems, the theory developed in this thesis significantly over predicts the Mach stem height. We see in Figure 3.14, that there is a significant difference between the shape of the slipline originating from the triple point and the slipline used in the theoretical estimate. Specifically, the computed slipline gradually approaches 0° thereby giving it a lower average angle. This lower average angle causes a decrease in the Mach stem height. For the cases considered, the theory appears to locate the throat formed by the flow downstream of the Mach stem quite accurately.

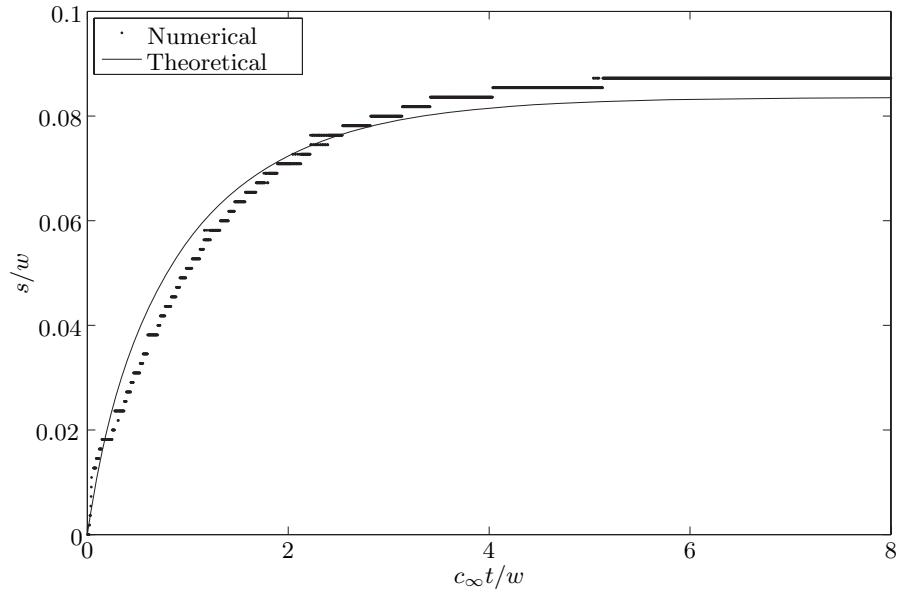


Figure 3.12: Theoretical and numerical results for the height of the Mach stem as a function of time as it grows from an initial regular reflection condition. Calculated for $M_\infty = 4$, $g/w = 0.3907$, $\gamma = 1.4$, and $\theta_1 = 23^\circ$.

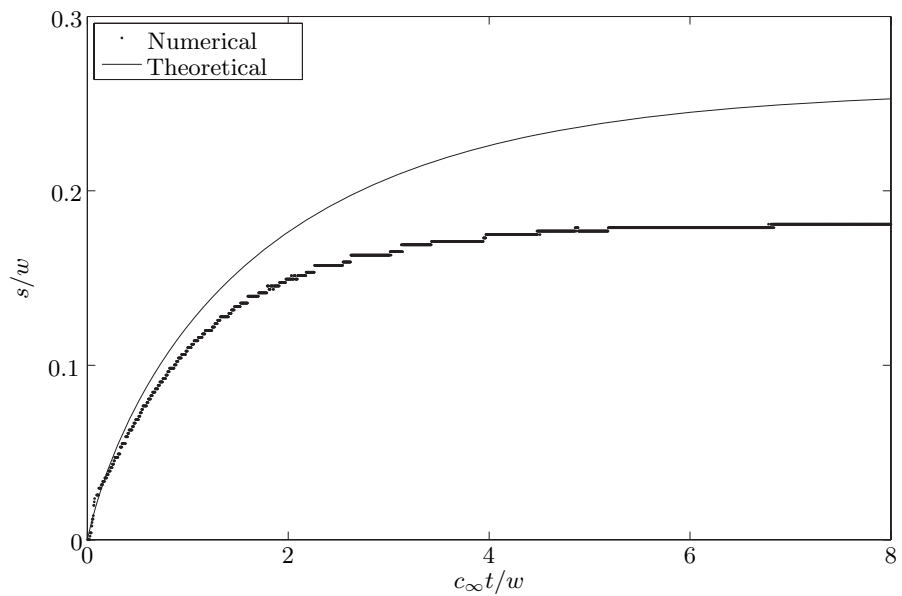


Figure 3.13: Theoretical and numerical results for the height of the Mach stem as a function of time as it grows from an initial regular reflection condition. Calculated for $M_\infty = 4$, $g/w = 0.42$, $\gamma = 1.4$, and $\theta_1 = 25^\circ$.

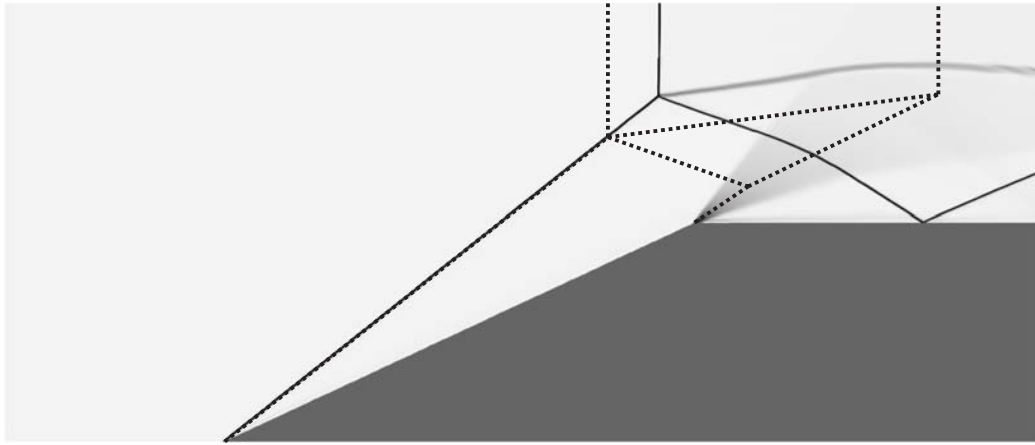


Figure 3.14: A quasi-schlieren image showing a comparison between the theoretical shock structure and an Euler computation. The image shows that the shape of the slipline in the computation is significantly different from what is assumed in the theory. This difference between computation and theory most likely accounts for most of the error between the two. The theoretical lines are shown as dotted lines. Calculated for $M_\infty = 4$, $g/w = 0.42$, $\gamma = 1.4$, and $\theta_1 = 25^\circ$.

3.9 Three-Dimensional Mach Stem Growth

Consider a three-dimensional flow with a regular reflection in the dual-solution domain. When a Mach stem is first formed, it is both small in height and in width in the spanwise direction. As it grows it both increases in height and expands outward in the spanwise direction. This opening is referred to as a mouth because of its shape [11]. The spanwise region where the transition from a Mach stem to a regular reflection occurs is characterized by a 5-point theory. This point exists at the intersection of five shocks, those being the incoming shock, the regularly reflected shock, the Mach stem, the Mach stem reflected shock, and a fifth shock dividing the downstream flow region between the regular reflection and the Mach reflection. Farther away from this point, we can expect the behavior of the Mach stem to follow that of the two-dimensional theory in the appropriate frame of reference. We can therefore conclude that the expansion rate of the Mach stem in the spanwise direction is determined by a complex system of five shocks; whereas, the overall change in height of the Mach stem is governed by the two-dimensional theory presented in Section 3.8. Using the two-dimensional theory for the height and setting the spanwise expansion of the Mach stem to a constant, produces the evolution of a Mach stem that is seen in Figure 3.15. This figure shows the Mach stem as it would be seen by an observer looking downstream.

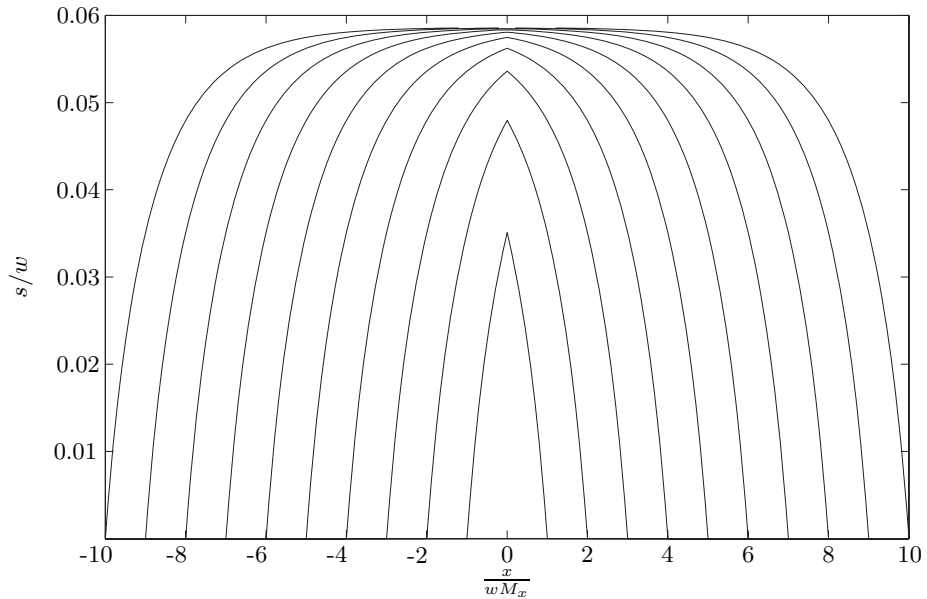


Figure 3.15: Three-dimensional growth of Mach stem with height s , and spanwise width x , which is propagating outward at a Mach number M_x . Curves for flow times, $(a_\infty t / w)$, between 1 and 10, in increments of 1, with the lower curves corresponding to lower times. Calculated for $M_\infty = 3$, $g/w = 0.4516$, $w = 150$, $\gamma = 1.4$, and $\theta_1 = 21^\circ$.

This theory assumes that the Mach stem starts at a point and therefore predicts a cusp at the center of the Mach stem corresponding to the point where the Mach stem started. This, however, is not seen in computations and is believed to be because, in the computations, the tripping from regular reflection to Mach reflection occurs over a finite span portion of the regular reflection. This initial finite span is most likely due to the fact that the disturbance given is more than what is required to trip from regular reflection to Mach reflection. Essentially, in the computations, the Mach stem starts with a finite width. For accurate comparisons with computations, an additional parameter, the initial width of the Mach stem, must be included. This initial width essentially separates the two halves of Figure 3.15 and produces curves similar to Figure 3.16.

For comparison with three-dimensional calculations done using AMROC [27], the two-dimensional theory was used to calculate the change in height as a function of time at each spanwise point along the Mach stem. The expansion rate in the spanwise direction was taken to be a constant and was set to the best-fit value as was the initial Mach stem width. From dimensional analysis we can see that indeed the spanwise growth should be constant, since

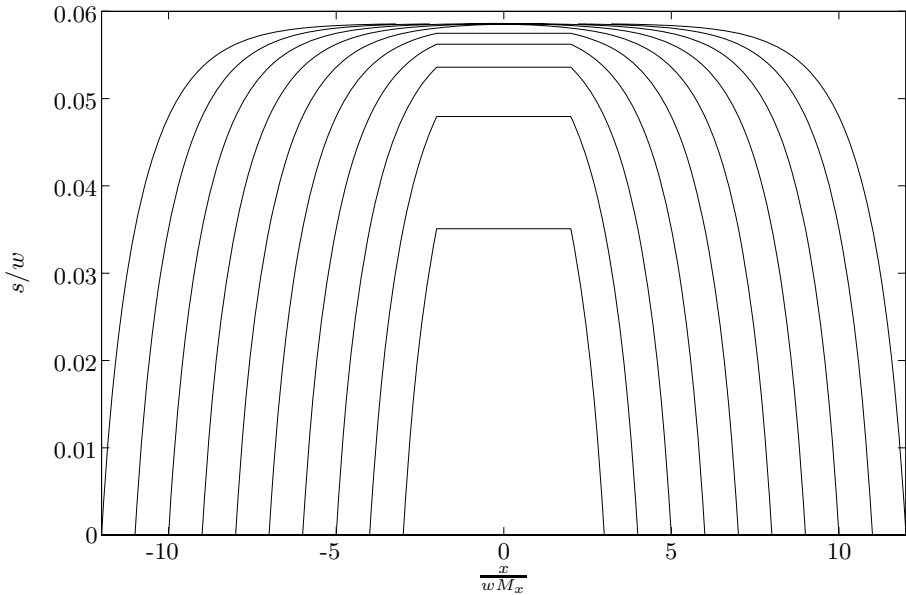


Figure 3.16: Growth of a Mach stem considering a Mach stem with an initial finite width, s , and spanwise width of Mach stem, x , which is propagating outward at a Mach number, M_x . Curves for flow times ($a_\infty t / w$) between 1 and 10, in increments of 1, with the lower curves corresponding to lower times. Calculated for $M_\infty = 3$, $g/w = 0.4516$, $w = 150$, $\gamma = 1.4$, and $\theta_1 = 21^\circ$.

it will depend only on the local flow conditions around the five shock solutions; therefore,

$$\frac{x}{c_\infty t} = h(M_\infty, \gamma, \theta_w), \quad (3.109)$$

which gives a constant spanwise expansion speed for any given flow parameters. The use of the two-dimensional theory from Section 3.7 and the best-fit spanwise growth rate yields very good agreement to computations. Figures 3.17 through 3.19 show the progression of the three-dimensional Mach stem with time, both computationally and theoretically.

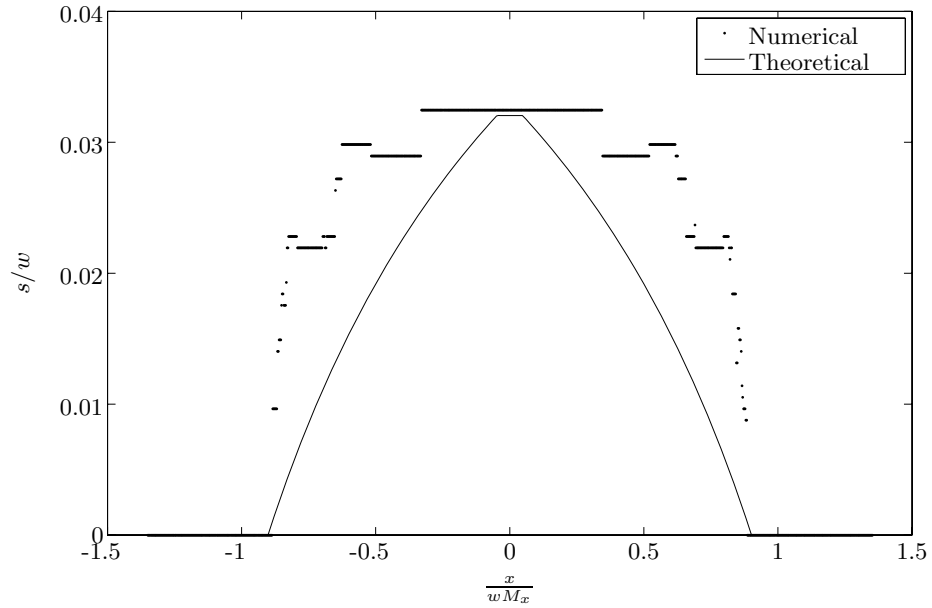


Figure 3.17: Numerical and theoretical growth of Mach stem height, s , and growth in the spanwise direction, x , at $a_\infty t/w=0.11$. The Mach stem is propagating outward at a Mach number, $M_x = 0.5916$. Calculated for $M_\infty = 3$, $g/w = 0.4516$, $w = 150$, $\gamma = 1.4$, and $\theta_1 = 21^\circ$.

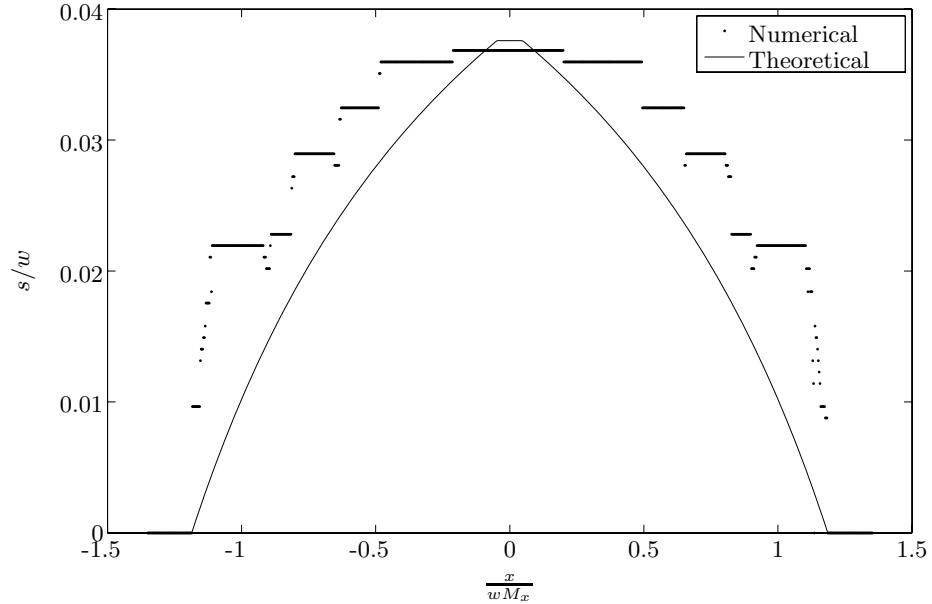


Figure 3.18: Numerical and theoretical growth of Mach stem height, s , and growth in the spanwise direction, x at $c_\infty t/w=0.39$. The Mach stem is propagating outward at a Mach number, $M_x = 0.5916$. Calculated for $M_\infty = 3$, $g/w = 0.4516$, $w = 150$, $\gamma = 1.4$, and $\theta_1 = 21^\circ$.

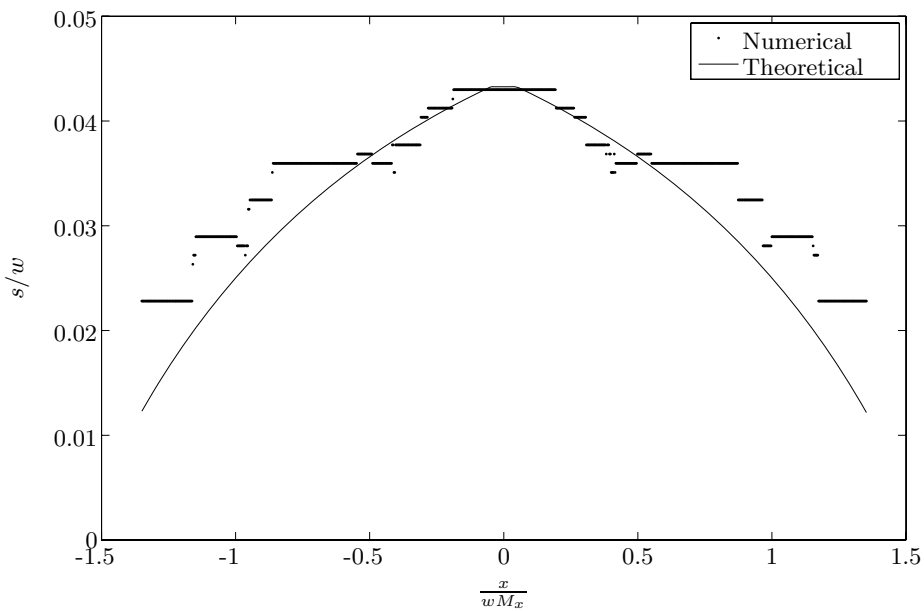


Figure 3.19: Numerical and theoretical growth of Mach stem height, s , and growth in the spanwise direction, x , at $c_\infty t/w=0.79$. The Mach stem is propagating outward at a Mach number, $M_x = 0.5916$. Calculated for $M_\infty = 3$, $g/w = 0.4516$, $w = 150$, $\gamma = 1.4$, and $\theta_1 = 21^\circ$.

Chapter 4

Dense Gas Disturbances

It has been observed by Sudani et al. [11] that water vapor can cause transition to occur closer to the von Neumann condition than it does otherwise. The studies by Sudani et al. did not fully account for the mechanism by which water vapor causes transition from regular reflection to Mach reflection. This section will present two-dimensional computations where water vapor is modeled as a dense and cold region of gas. Calculations where the impact of the dense gas on the wedge is modeled as an energy deposition are also presented. In the case of energy being deposited on the surface of the wedge, a minimum required energy for transition is given. In addition, several three-dimensional calculations were performed. In all computations presented here, the free-stream pressure and density are set to unity.

4.1 High Density Gas Region

Numerical studies using high-density gas regions were conducted in both two dimensions and three dimensions. The results of these studies are presented in this section.

The first set of numerical studies model the disturbance as a small, cold, and dense region of gas. Initially, the gas has the same pressure and velocity as the free stream. All two-dimensional computations were performed using Amrita [24] with the assistance of James Quirk. The details of the Amrita system are discussed in Section 3.5. In all the cases, the free-stream Mach number was set to 4, and the ratio of specific heats was set to 1.4. The computational domain was 300 cells wide and 240 cells high. Each cell could be refined to either 9 cells or 81 cells depending on the local density gradient. The geometry in all calculations is two symmetric wedges with a wedge spacing, g , of 50 cells. The wedge

length, w , depends on the wedge angle, θ_1 , and is given by

$$w = 70 / \sin(\theta_1). \quad (4.1)$$

A schematic of the important parameters of the computational setup is shown in Figure 4.1.

4.1.1 Evolution of High Density Gas Region

In the computations, the dense gas is inserted upstream of the leading oblique shock and has an initial radius of 1 cell. An example quasi-schlieren image shows the dense gas just after it is inserted is shown in Figure 4.2.

As the region of gas travels downstream, it will pass through the leading shock and into the slower region behind the leading shock. Once the particle is in Region 1, a bow shock will form in front of it. An example of the bow shock in front of the lump of gas is shown in Figure 4.3. With respect to the lump of gas the flow is from upper right to lower left, and we should therefore expect an oblique shock to the upper right of the lump of gas. In addition to the bow shock, there is also a small disturbance on the leading oblique shock where the particle crossed it.

At a later time, the bow shock of the dense gas will impact the wedge and reflect. This is seen in Figure 4.4. The recompression shocks behind the dense gas are also seen, and the disturbance on the leading oblique shock has smoothed out. Since the dense gas is not solid, it is stretching and does not remain circular.

After the bow shock first impacts the wedge the dense gas will travel through the reflected bow shock and impact the wedge. The passing of the dense gas through the reflected bow shock will cause a disturbance on that shock. These shocks are seen and labeled in Figure 4.5

The reflected bow shock and shock due to the impacting of the dense gas on the wedge propagate outwards from the impact point and convect downstream with the flow; this is seen in Figure 4.6.

If the reflected bow shock and impact shock are sufficiently strong they will both impact the leading oblique shock. Depending on the strength of the two shocks, it is possible for both to reach the leading oblique shock, neither to reach the leading oblique shock, or only the reflected bow shock reaches the leading shock. In this particular case, as is shown in

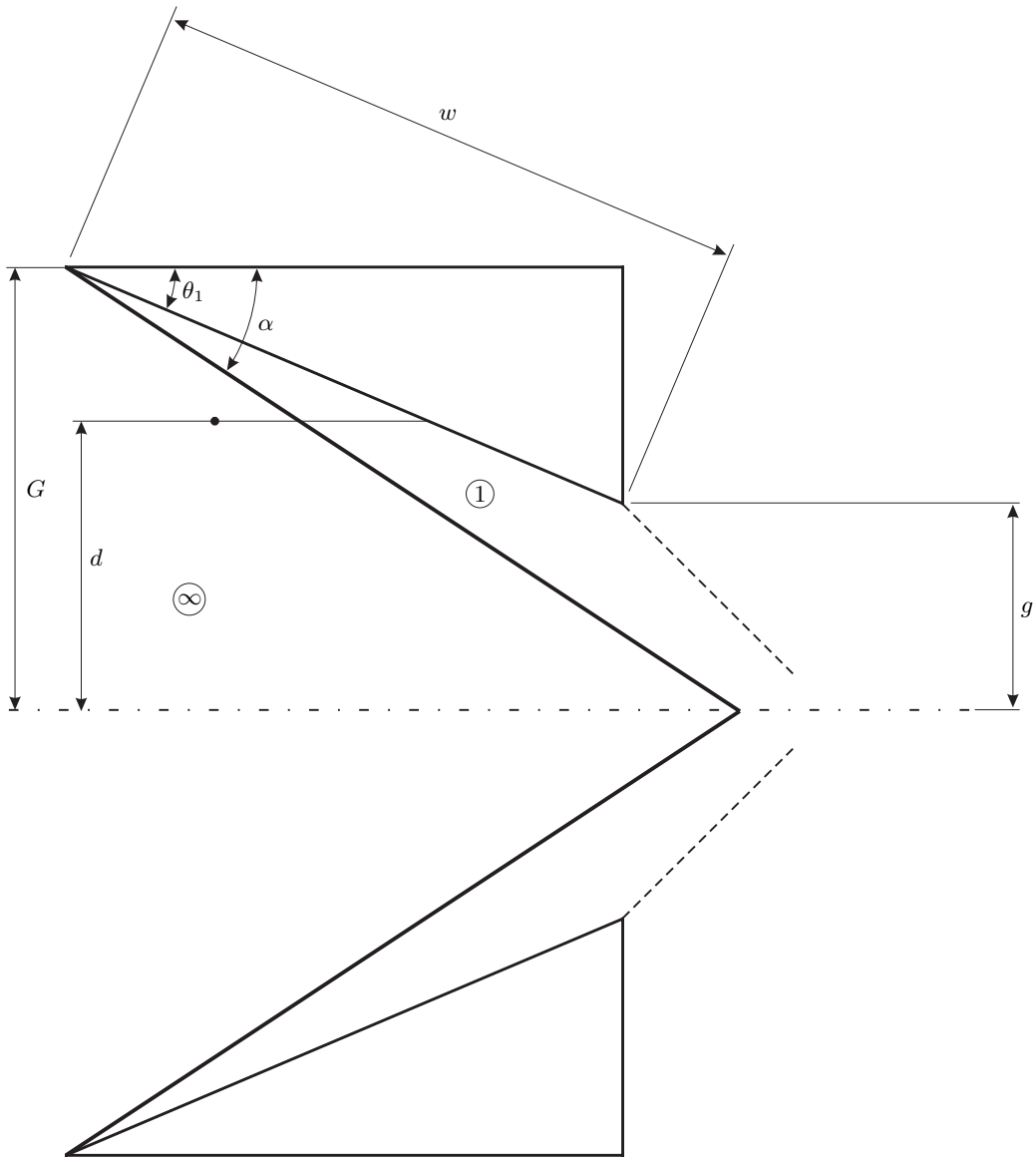


Figure 4.1: Flow setup used for the Amrita simulations of dense gas disturbances.

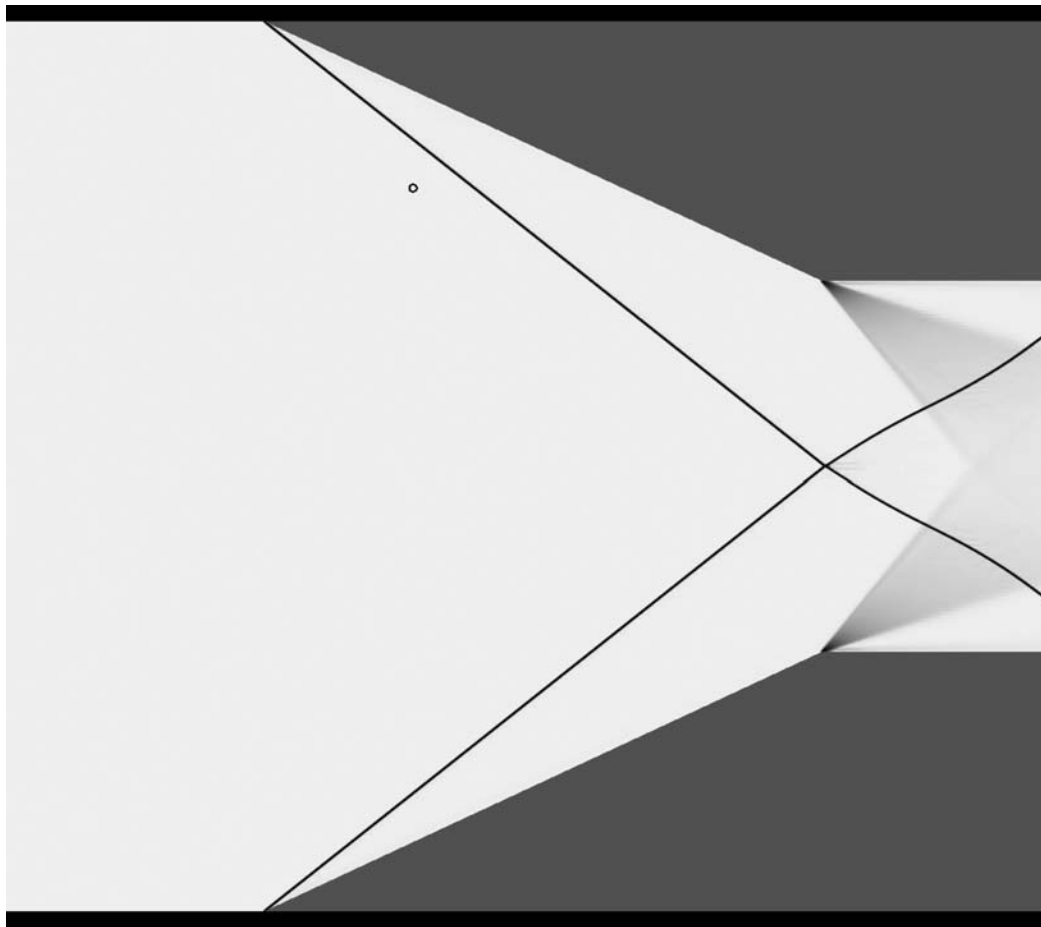


Figure 4.2: Quasi-schlieren image showing a circular area of gas with a radius of 1 cell and a density of 1500 times the free-stream density. The particle is 75 cells above the centerline, and the wedge angle is 25° .

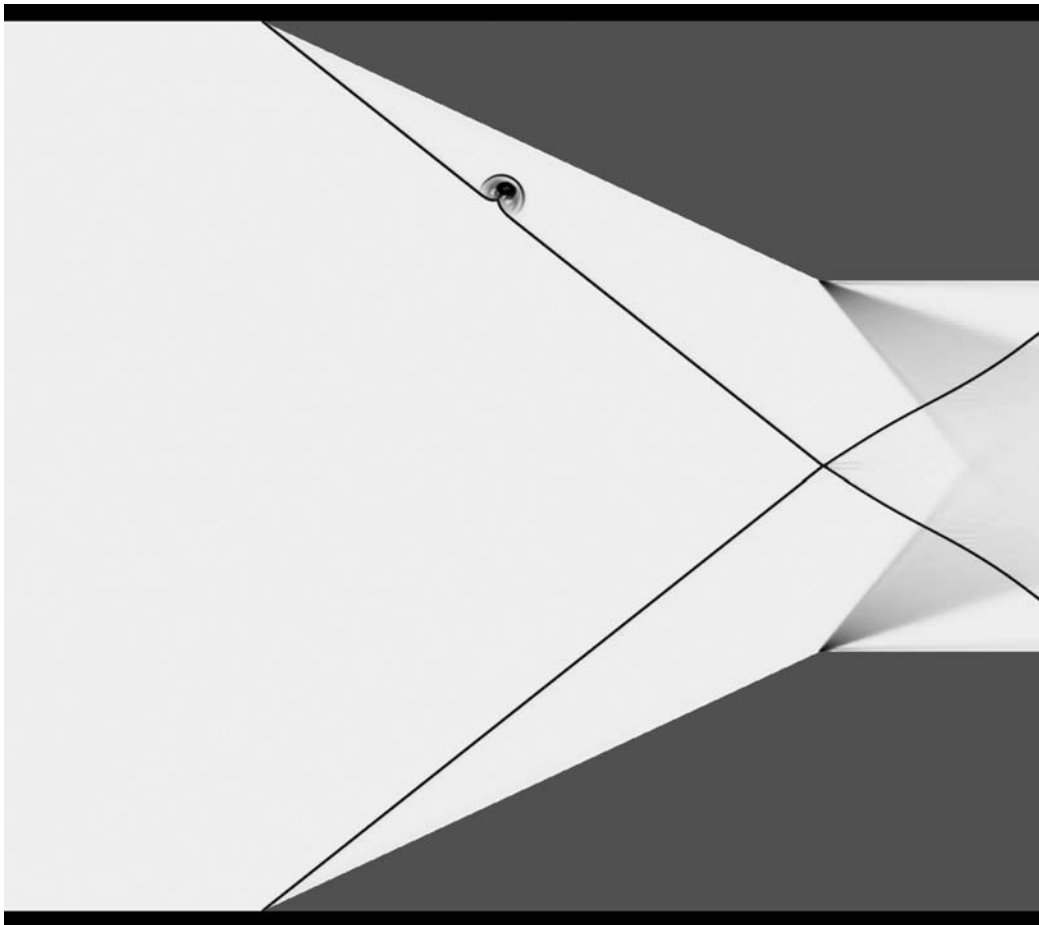


Figure 4.3: Quasi-schlieren image showing an area of gas with an initial radius of 1 cell and an initial density of 1500 times the free-stream density, after it has propagated downstream through the leading oblique shock. The dense gas originated 75 cells above the centerline, and the wedge angle is 25° .

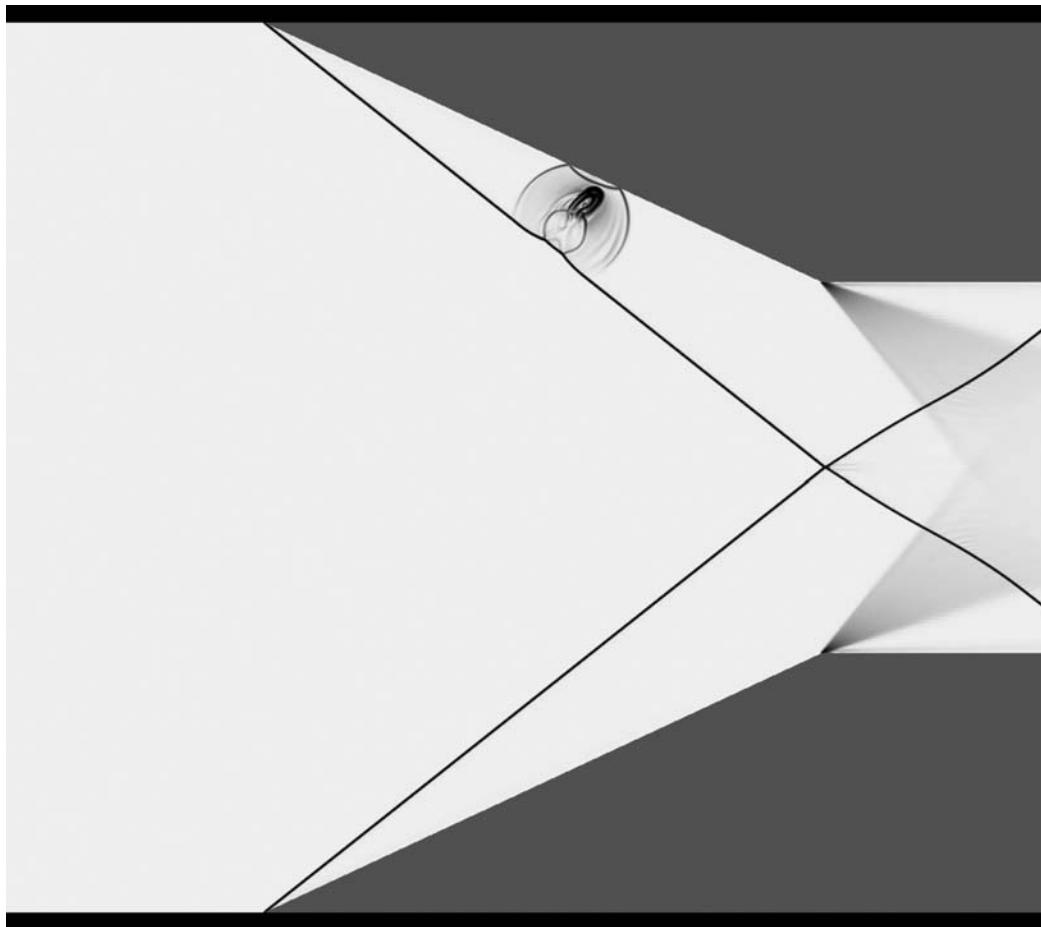


Figure 4.4: Quasi-schlieren image showing an area of gas with an initial radius of 1 cell and an initial density of 1500 times the free-stream density, after its bow shock has impacted the wedge. The lump of gas originated 75 cells above the centerline, and the wedge angle is 25° .

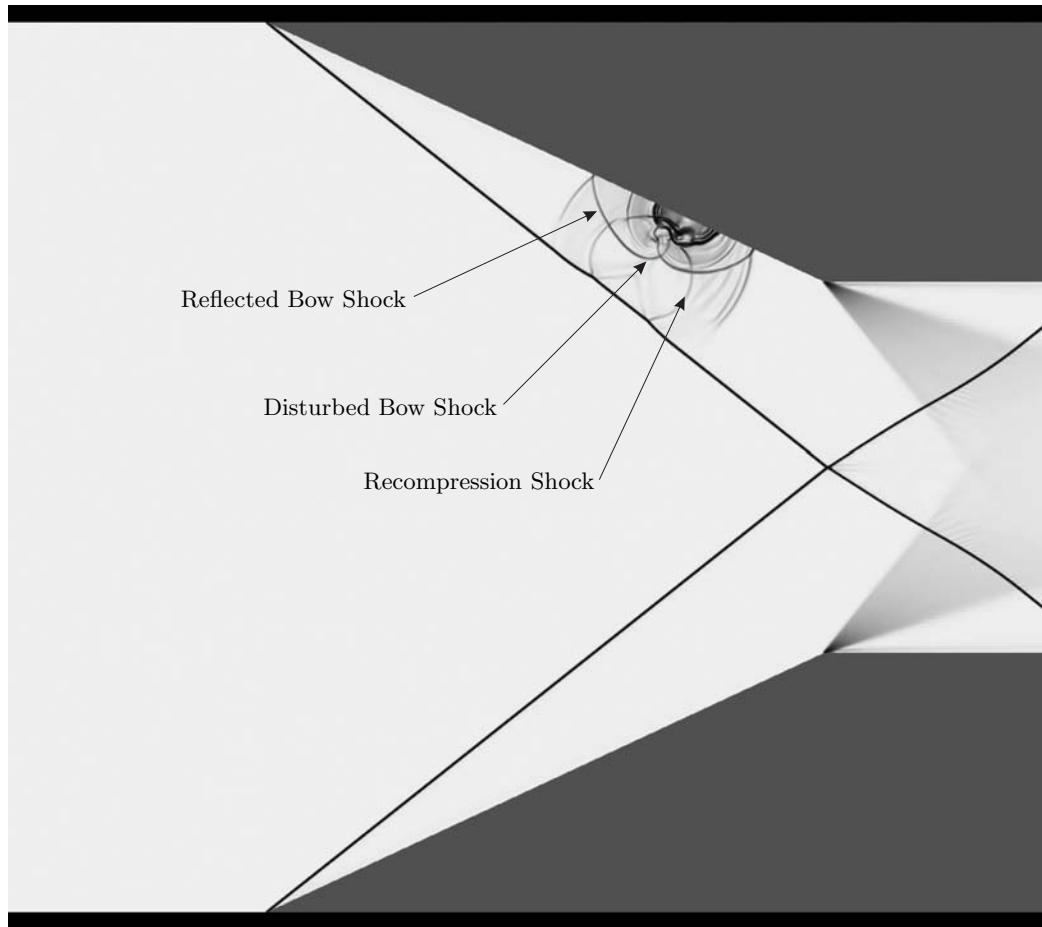


Figure 4.5: Quasi-schlieren image showing an area of gas with an initial radius of 1 cell and an initial density of 1500 times the free-stream density, after it has impacted the wedge. The dense gas originated 75 cells above the centerline, and the wedge angle is 25° .

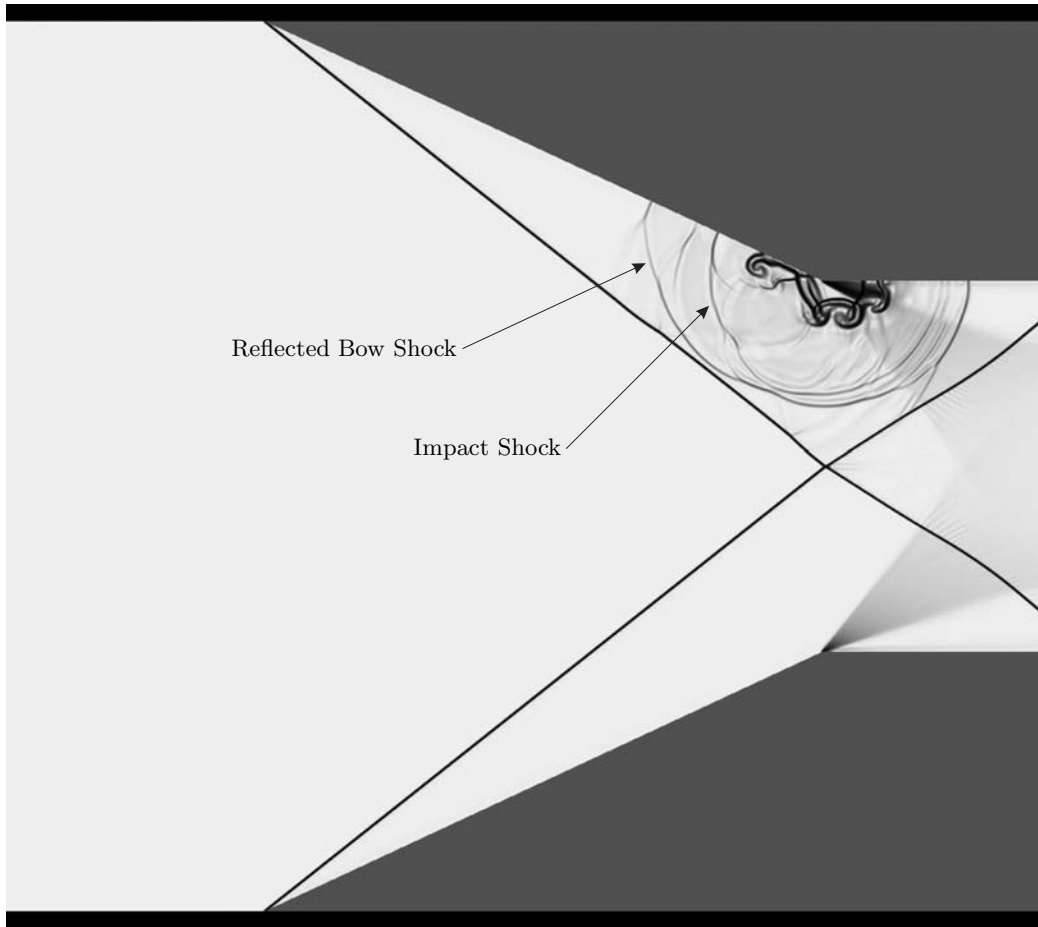


Figure 4.6: Quasi-schlieren image showing the reflected bow shock and impact shock from an area of gas with an initial radius of 1 cell and an initial density of 1500 times the free-stream density as the reflected bow shock and the impact shock reach the incident shock. The dense gas originated 75 cells above the centerline, and the wedge angle is 25° .

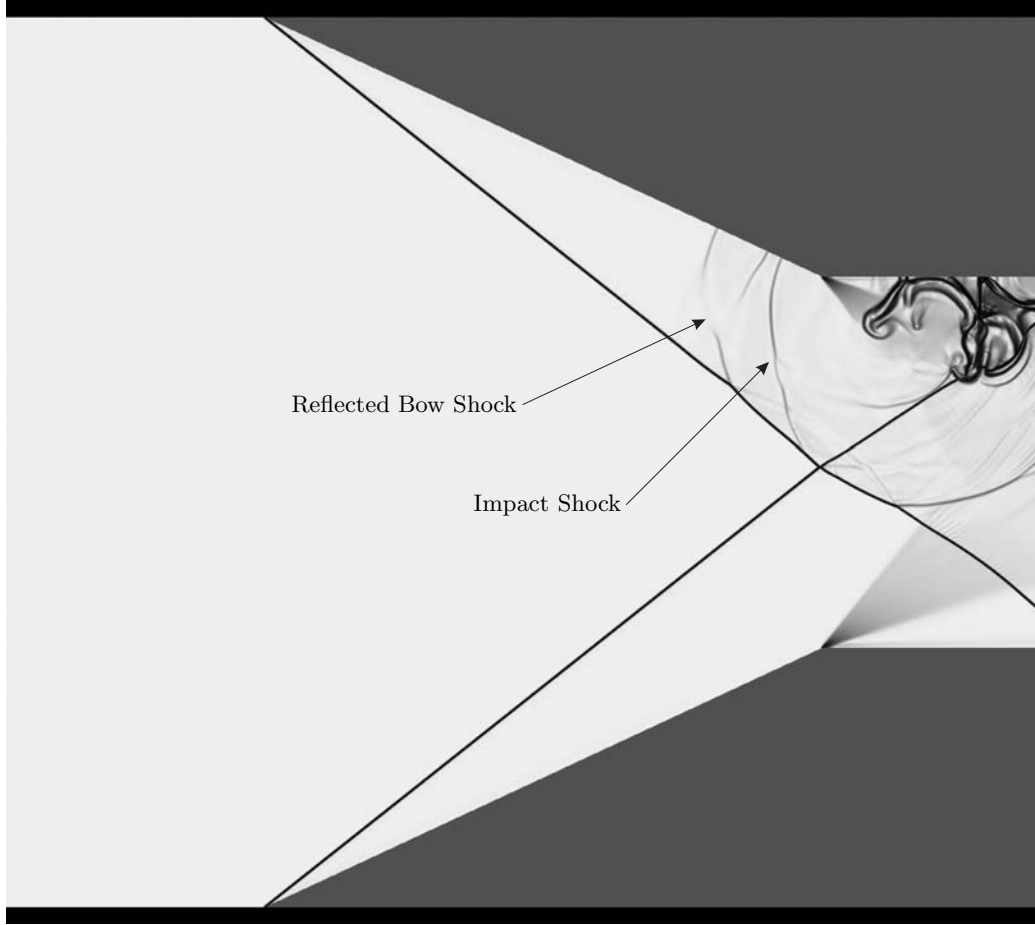


Figure 4.7: Quasi-schlieren image showing the reflected bow shock and impact shock from an area of gas with an initial radius of 1 cell and an initial density of 1500 times the free-stream density after they have reached the leading oblique shock. The dense gas originated 75 cells above the centerline, and the wedge angle is 25° .

Figure 4.7, both the reflected bow shock and the impact shock reach the leading shock.

As the impact shock travels downstream it will pass over the reflection point, and locally increase the shock angle. This is seen in Figure 4.8.

If the disturbance is strong enough, a Mach stem will form. The first sign of a Mach stem is shown in Figure 4.9.

Once the Mach stem is formed a communication link between the expansion wave and the Mach stem is created. This communication tells the Mach stem how large it should be, and it will continue to grow until it reaches its steady state height. An example of this growth is shown in Figure 4.10.

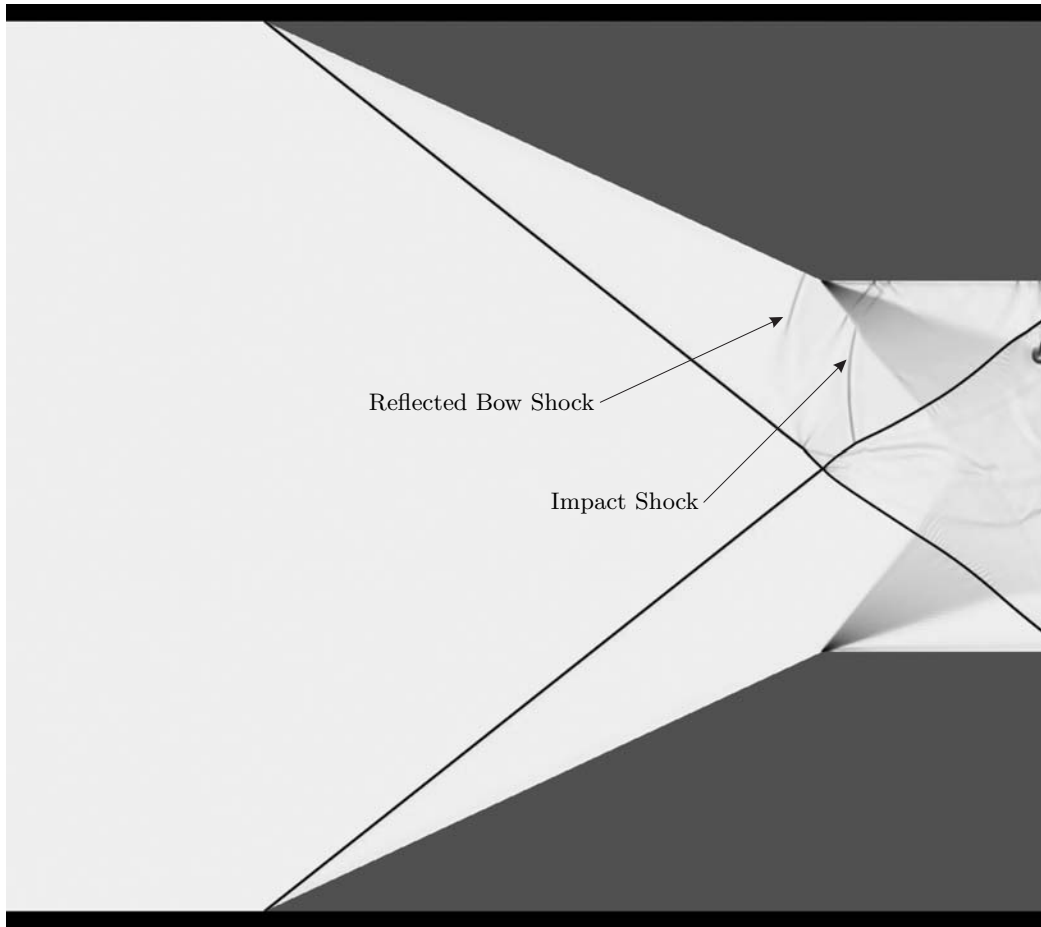


Figure 4.8: Quasi-schlieren image showing the reflected bow shock and impact shock from an area of gas with an initial radius of 1 cell and an initial density of 1500 times the free-stream density after the impact shock has passed over the reflection point. The dense gas originated 75 cells above the centerline, and the wedge angle is 25° .

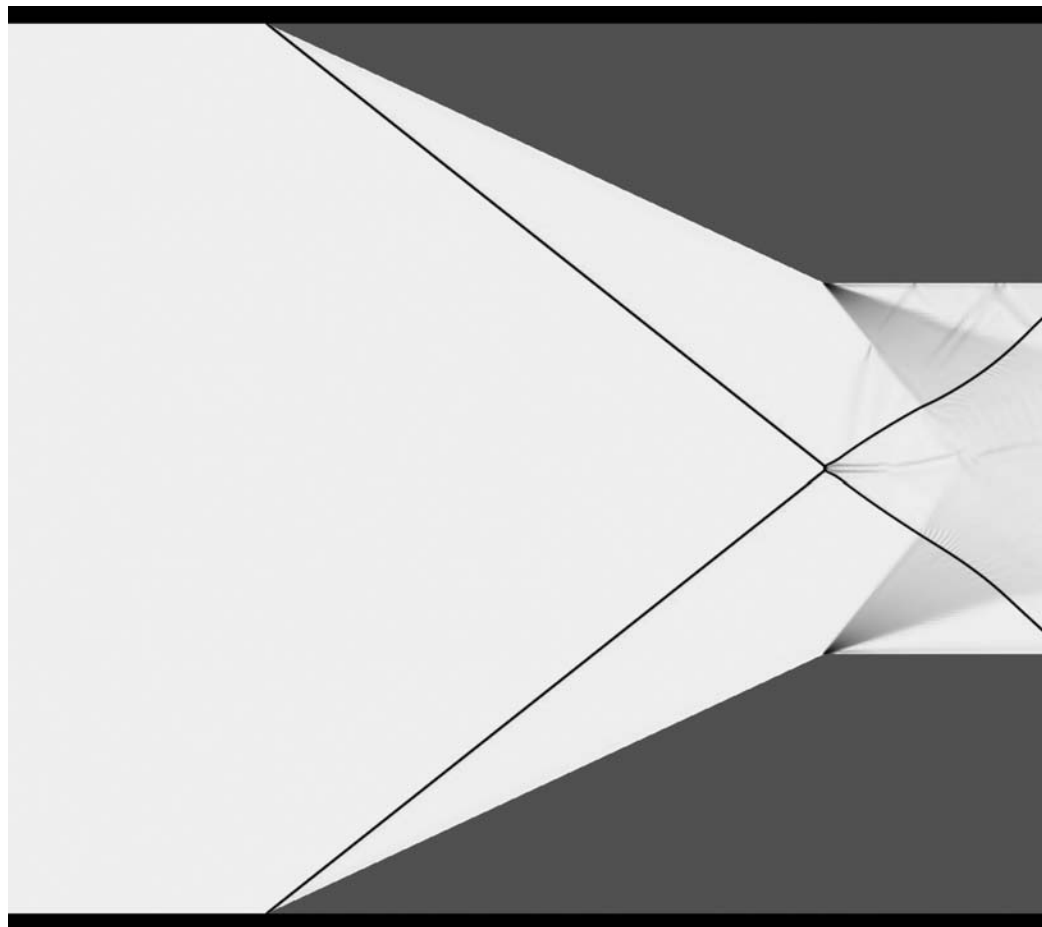


Figure 4.9: Quasi-schlieren image showing the creation of a Mach stem due to an area of gas with an initial radius of 1 cell and an initial density of 1500 times the free-stream density impacting the wedge. The dense gas originated 75 cells above the centerline, and the wedge angle is 25° .

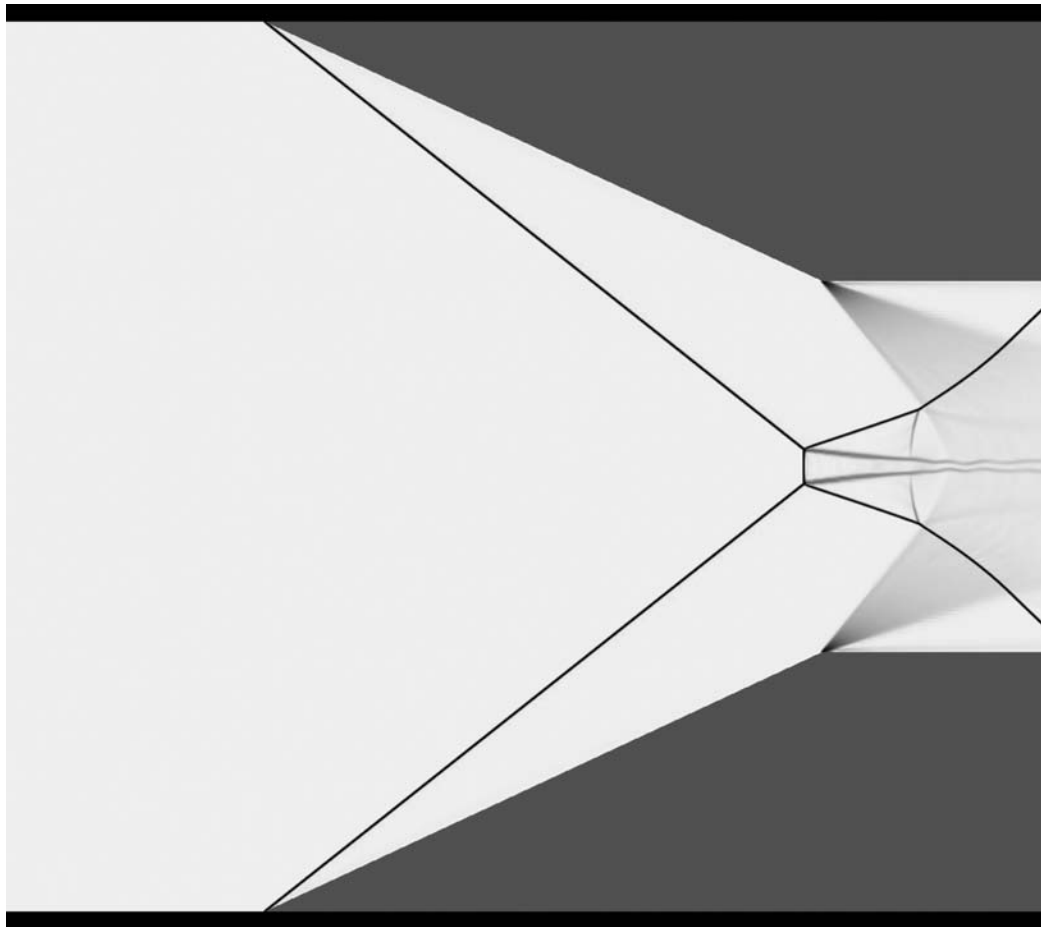


Figure 4.10: Quasi-schlieren image showing the growth of the Mach stem created by an area of gas with an initial radius of 1 cell and an initial density of 1500 times the free-stream density impacting the wedge. The dense gas originated 75 cells above the centerline, and the wedge angle is 25° .

4.1.2 Mechanism of Transition

There are two significant shocks produced by the dense gas impacting the wedge. The first is the bow shock and the second is the impact shock. Assuming that a gas region of a given size is sufficiently dense that the speed of the gas region does not change significantly, the bow shock will be independent of the gas density. However, the impact shock will depend heavily on the total mass, or more specifically, the kinetic energy of the dense gas. Because of this difference between the bow shock and impact shock it is useful to study whether or not transition happens as a function of the mass of the dense gas region.

We will examine two cases; one where transition does occur, and one where it does not. Specifically, we will consider a wedge angle of 25° , a dense gas with an initial radius of 1 cell located 75 cells above the centerline, a free-stream Mach number of 4, and a ratio of specific heats of 1.4.

The first case we will consider is a density ratio between the gas region and the free stream of 1300. Figure 4.11 shows a quasi-schlieren image taken at the time when the impact shock is closest to the leading shock. In the figure, the impact shock almost reaches the reflection point. In this case, transition from regular reflection to Mach reflection will not occur.

If we increase the density by less than 8%, to 1400 times the free-stream density, transition will occur. Figure 4.12 shows a quasi-schlieren image taken at the time when the impact shock is closest to the leading shock. In the figure, the impact shock reaches the leading shock just upstream of the reflection point.

Since, in both cases, the bow shock is virtually identical, we see that the determining factor in whether or not transition from regular reflection to Mach reflection occurs is the strength of the impact shock. This suggests that to understand the mechanism by which a dense gas region can cause transition we should study the impact shock.

4.1.3 Three-Dimensional Results

While the two-dimensional computations provide great computational efficiency, three-dimensional computations were also performed to confirm that the general phenomena observed in the two-dimensional calculations are indeed accurate.

All three-dimensional computations were done using AMROC [27] and performed in

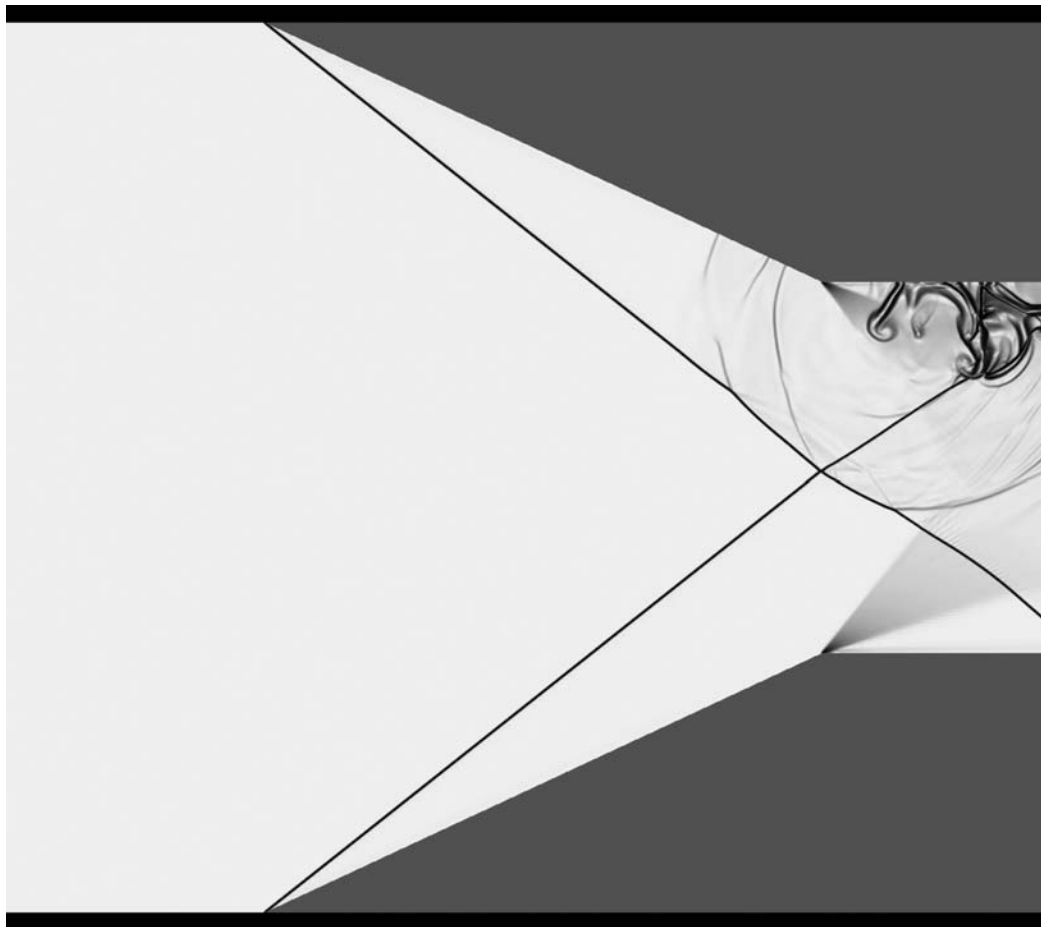


Figure 4.11: Quasi-schlieren image at the time when the impact shock is closest to the leading shock. In this case transition to Mach reflection will not occur. The initial density ratio between the gas region and the free stream is 1300.

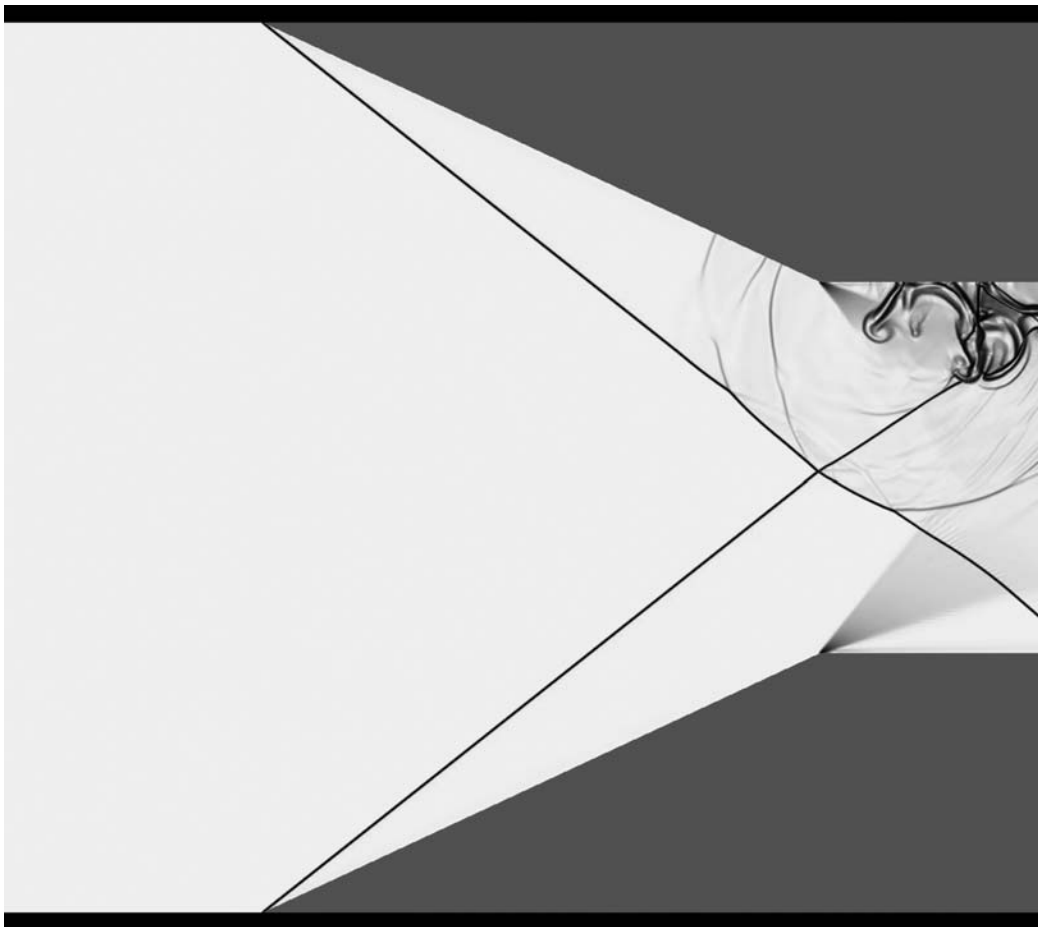


Figure 4.12: Quasi-schlieren image at the time when the impact shock is closest to the leading shock. In this case transition to Mach reflection will occur. The initial density ratio between the lump of gas and the free-stream density is 1400.

collaboration with Ralf Deiterding. The domain consisted of $90 \times 90 \times 90$ cells, with each cell being able to be refined up to $4 \times 4 \times 4$. The front and back of the domain were set to extrapolate, thereby producing infinite span wedges. By doing this the three-dimensional effects of the flow at the ends of the wedges were neglected. The computations were performed on DataStar at the San Diego Supercomputer Center at University of California, San Diego.

The domain size was set to $240 \times 240 \times 240$ (i.e., each unrefined cell had a side length of $8/3$). The wedge length, w , was set to 150, and the wedge spacing, g , was set to 50. The free-stream Mach number, M_∞ , was 4 in all cases and the ratio of specific heats, γ , was 1.4.

In the three-dimensional calculations a single reasonably sized region of dense gas was not sufficient to cause transition from regular reflection to Mach reflection. Only if the single region of gas were about 10,000 times denser than the free stream and a few percent of the wedge length would transition occur. In order to be a reasonable representation of experimental observations, which show that many very small particles can cause transition, it was necessary to model a series of dense regions of gas instead of just one; this is seen in Figure 4.13. Using a series of dense regions of gas, it is possible for the individual regions of gas to be 1,500 times denser than the free stream and only a few cells wide. An example of 55 individual regions of gas, each with a density 1,500 times the free-stream density and with a particle radius divided by the wedge length that is 0.0133, is seen in Figure 4.13.

After the 55 particles pass through the leading shocks some of them impact the wedge and produce impact shocks like those seen in the two-dimensional calculations. These disturbances then effects the leading shock waves and produce a bulge in them that looks like a pair of lips. This is seen in Figure 4.14.

Figure 4.15 shows the beginning of the Mach stem growth. The center region of the figure shows a small Mach stem. The three-dimensional growth of the Mach stem is sometimes compared to the opening of a mouth, because of the way the Mach stem gains in height while simultaneously spreading outwards.

After the Mach stem has had sufficient time, it reaches the steady-state size at the center, while the outer parts continue to grow. This is seen in Figure 4.16.

Finally, the entire Mach stem will reach its steady-state height, this is seen in Figure 4.17.

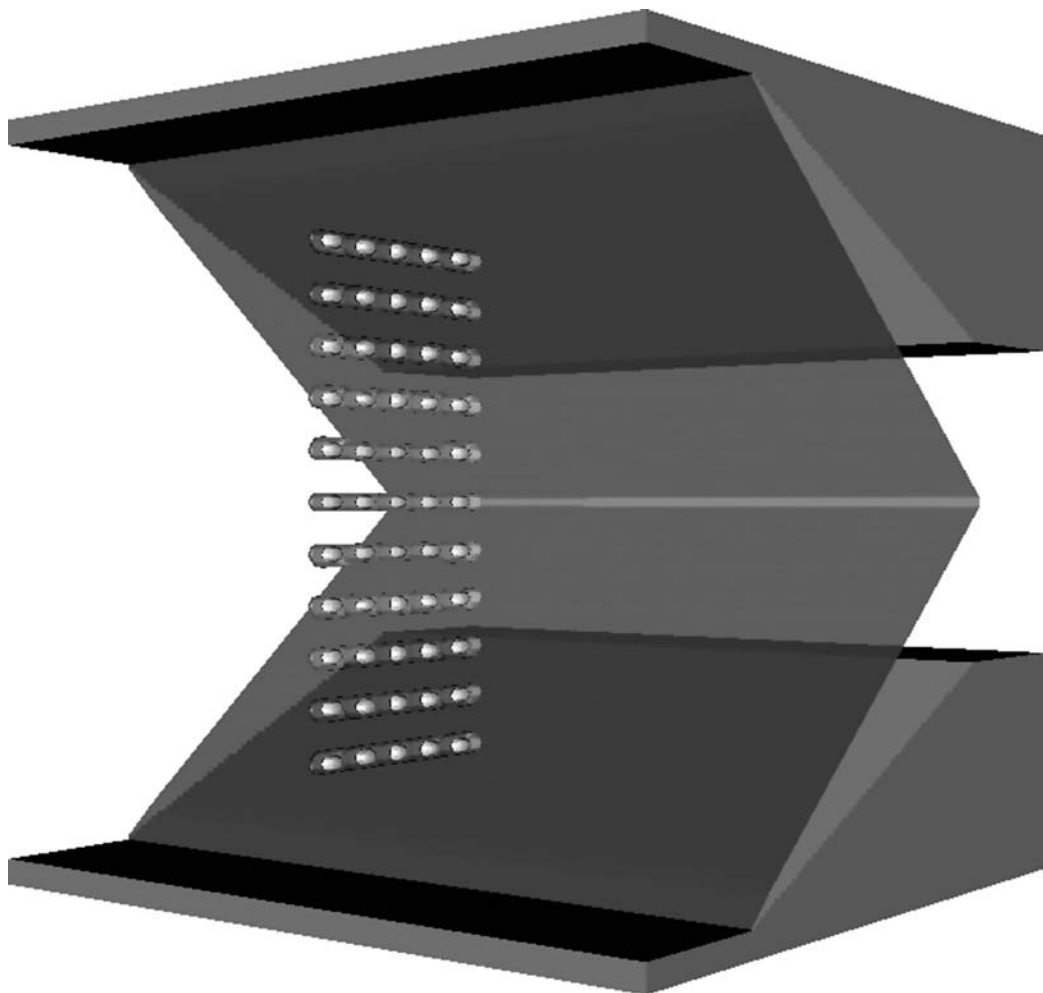


Figure 4.13: 55 lumps of dense gas inserted upstream of the leading shock waves. Unlike the two-dimensional computations, many individual lumps of gas are required to cause tripping.

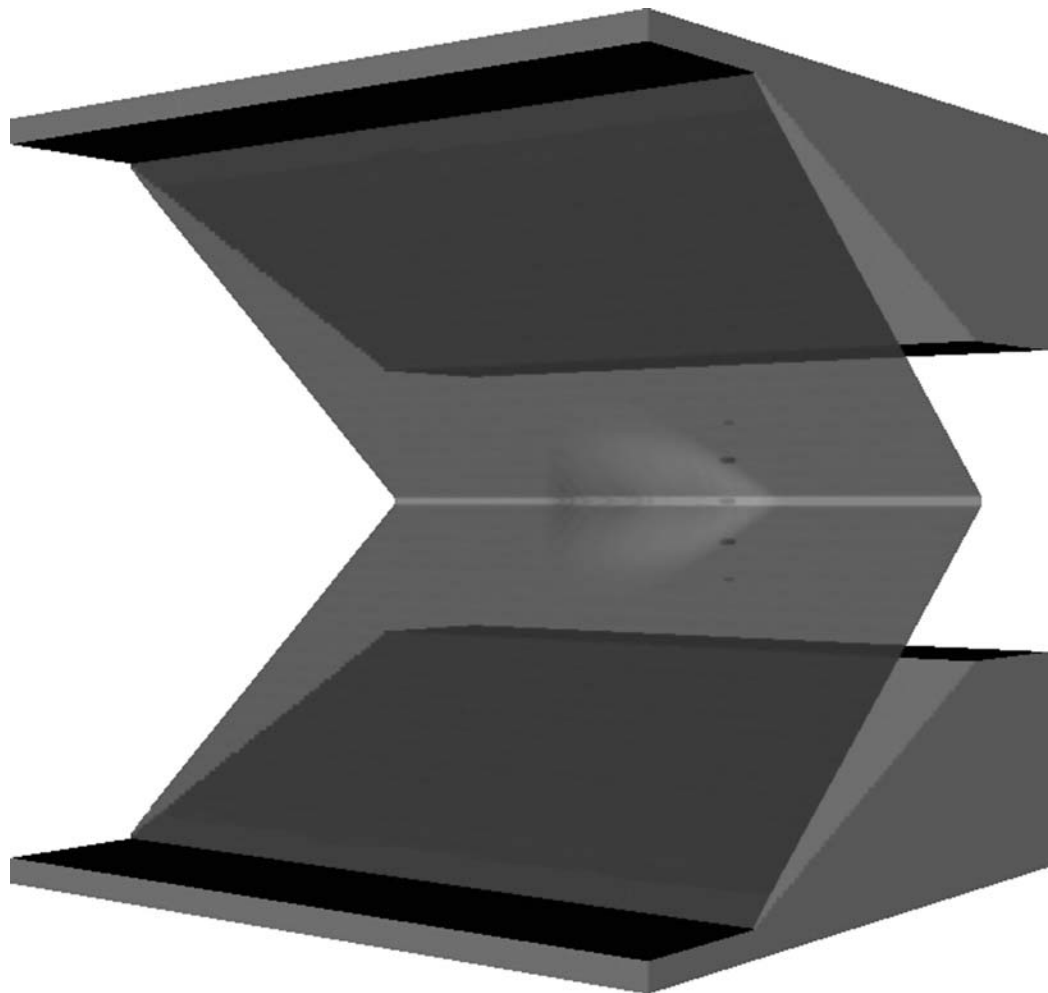


Figure 4.14: The 55 lumps of dense gas inserted upstream of the leading shock waves have passed through them and left a small disturbance on the leading shocks. This disturbance looks like a pair of lips.

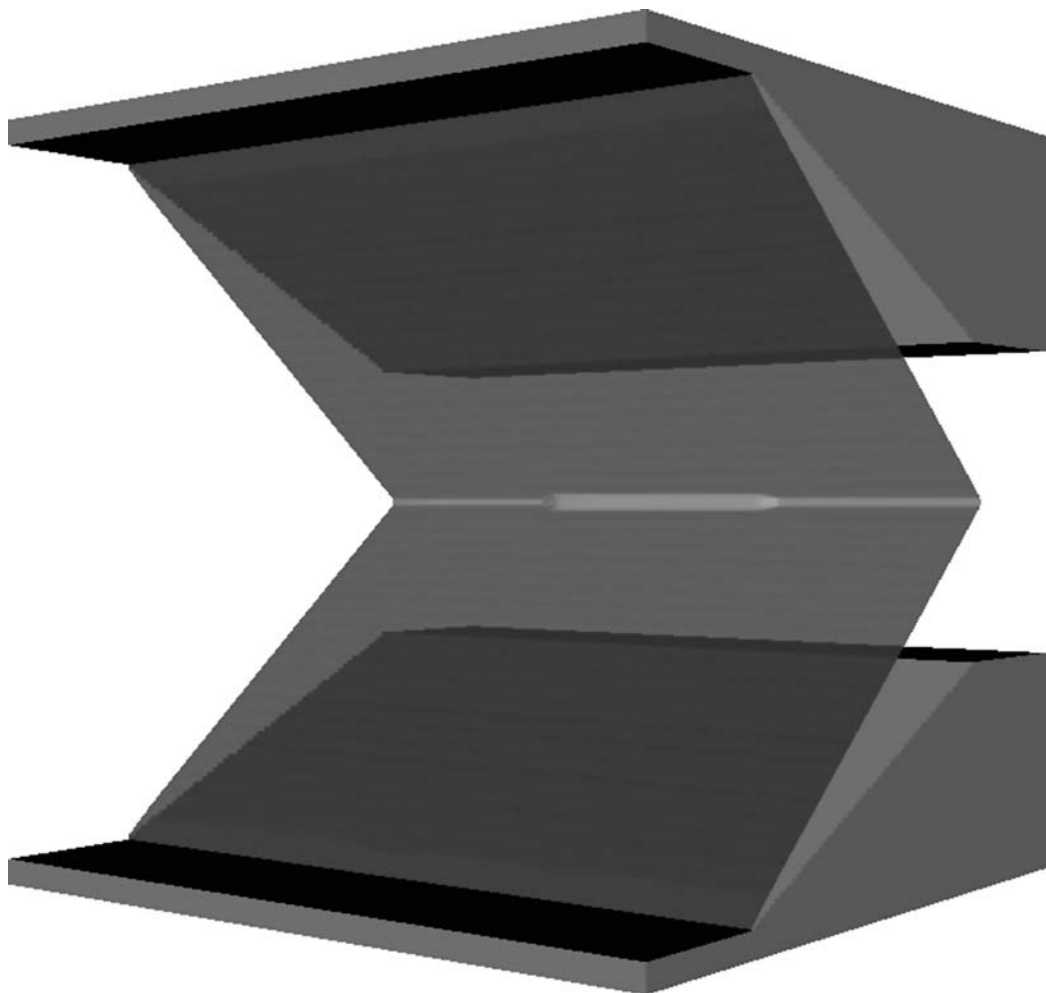


Figure 4.15: The disturbance of the 55 lumps of dense gas has caused the regular reflection to begin to transition to Mach reflection.

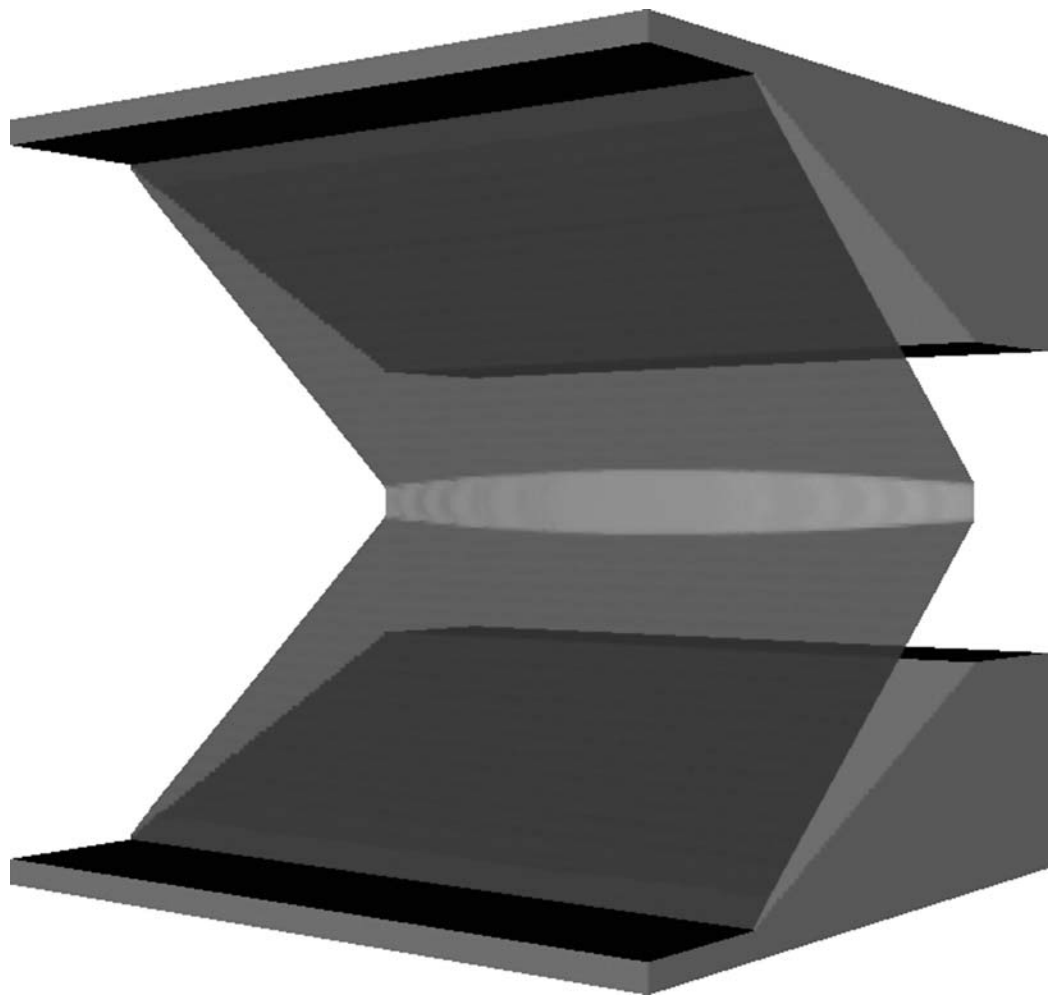


Figure 4.16: Portions of the Mach stem have reached their steady-state height, while in the outer regions the Mach stem continues to grow.

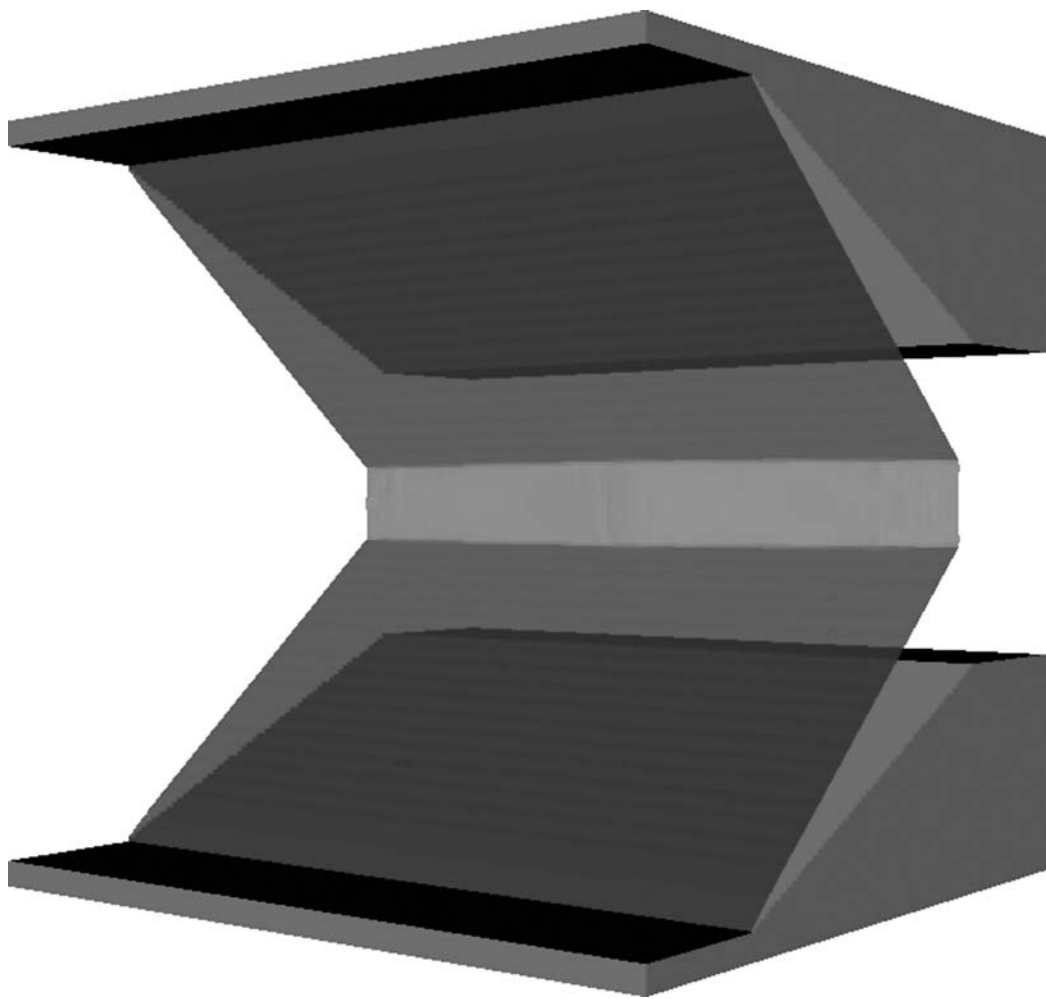


Figure 4.17: The entire Mach stem has reached its steady-state height.

4.2 Energy Deposition

The study of a dense lump of gas impacting the wedge suggested that it is the shock formed by the impact itself that is key in determining whether transition from regular reflection to Mach reflection occurs. Because of this, it is useful to study the simplified case of energy deposition directly on the wedge surface. In the two-dimensional case, the shock formed by this energy deposition will be cylindrical, and while it is strong will behave according to blast-wave equation for strong shocks, as obtained by Sedov [28].

4.2.1 Minimum Energy Requirement

A minimum required energy can be constructed by the fact that the blast wave must reach the leading shock in order to have an influence on whether or not transition from regular reflection to Mach reflection occurs. In order to determine if the blast wave will reach the leading shock, we must know the trajectory of the shock as a function of time and of the amount of energy deposited. This analysis neglects the effects of the leading oblique shock on the blast wave and of the expansion wave off the aft wedge corner. Summarizing the work of Sedov [28], we can write the radius of the blast wave, R_s , as a function of the time, t , the energy deposited, E_0 , and the density and pressure into which the blast wave is propagating, ρ_1 and P_1 , respectively. R_s can then be written as

$$R_s = f(t, E_0, \rho_1, P_1), \quad (4.2)$$

where f is a function yet to be determined.

The rank of the dimensional matrix consisting of R_s , t , E_0 , ρ_1 , and P_0 is three; therefore, we can form two non-dimensional groups. The non-dimensional form of Equation 4.2 is

$$R_s \left(\frac{P_1}{E_0} \right)^{1/\nu} = f \left(\sqrt{\frac{\gamma P_1}{\rho_1}} \left(\frac{P_1}{E_0} \right)^{1/\nu} t \right), \quad (4.3)$$

where ν equals 1, 2, 3 for planar, cylindrical, and spherical shock waves, respectively. The two-dimensional computations presented in this thesis correspond to $\nu = 2$, whereas the experimental results using energy deposition and the three-dimensional computations correspond to $\nu = 3$.

If the shock is strong, the shock jump conditions become

$$v'_2 = \frac{2}{\gamma + 1} v_s, \quad (4.4)$$

$$\rho'_2 = \frac{\gamma + 1}{\gamma - 1} \rho_1, \quad (4.5)$$

$$P'_2 = \frac{2}{\gamma + 1} \rho_1 v_s^2, \quad (4.6)$$

$$(4.7)$$

where v_s is the speed of the shock, v'_2 , ρ'_2 , P'_2 , are the velocity, density, and pressure, respectively, immediately behind the shock. We see that for a strong shock, the shock jump conditions do not involve P_1 . When the shock is strong we will denote $f(x)$ as $f^{\text{strong}}(x)$, which is given by

$$f^{\text{strong}}(x) = K_1 x^{\frac{2}{\nu+2}}, \quad (4.8)$$

where K_1 is a constant, for a given γ and a given symmetry. We can then solve for the radius of a strong blast shock, R_s^{strong} , which gives

$$R_s^{\text{strong}} = K_2 E_0^{\left(\frac{1}{\nu} - \frac{2}{\nu(\nu+2)}\right)} \rho_1^{-\frac{1}{\nu+2}} t^{\frac{2}{\nu+2}}, \quad (4.9)$$

where K_2 is another constant and is related to K_1 by

$$K_2 = K_1 \gamma^{\frac{1}{\nu+2}}. \quad (4.10)$$

Equation 4.9 simplifies to

$$R_s^{\text{strong}} = K_2 \left(\frac{E_0}{\rho_1} \right)^{\frac{1}{\nu+2}} t^{\frac{2}{\nu+2}}. \quad (4.11)$$

This equation is known as Sedov's Equation, and applies only for strong shocks. By defining a scaled energy, E , where $E = \alpha(\gamma, \nu) E_0$, Equation 4.11 can be written as

$$R_s^{\text{strong}} = \left(\frac{E}{\rho_1} \right)^{\frac{1}{\nu+2}} t^{\frac{2}{\nu+2}}. \quad (4.12)$$

The flow in the entire region behind the shock, assuming a strong shock, is given by

Sedov [28]. The flow equations are

$$\frac{v_2^{\text{strong}}}{v'_2} = \frac{(\nu + 2)(\gamma + 1)}{4} V \frac{r}{R_s^{\text{strong}}}, \quad (4.13)$$

$$\begin{aligned} \frac{\rho_2^{\text{strong}}}{\rho'_2} &= \left[\frac{\gamma + 1}{\gamma - 1} \left(\frac{(\nu + 2)\gamma}{2} V - 1 \right) \right]^{\alpha_3} \left[\frac{\gamma + 1}{\gamma - 1} \left(1 - \frac{\nu + 2}{2} V \right) \right]^{\alpha_5} \\ &\times \left[\frac{(\nu + 2)(\gamma + 1)}{(\nu + 2)(\gamma + 1) - 2[2 + \nu(\gamma + 1)]} \left(1 - \frac{2 + \nu(\gamma - 1)}{2} V \right) \right]^{\alpha_4}, \end{aligned} \quad (4.14)$$

$$\begin{aligned} \frac{P_2^{\text{strong}}}{P'_2} &= \left[\frac{(\nu + 2)(\gamma + 1)}{2} V \right]^{2\nu/(\nu+2)} \left[\frac{\gamma + 1}{\gamma - 1} \left(1 - \frac{\nu + 2}{2} V \right) \right]^{\alpha_5+1} \\ &\times \left[\frac{(\nu + 2)(\gamma + 1)}{(\nu + 2)(\gamma + 1) - 2[2 + \nu(\gamma + 1)]} \left(1 - \frac{2 + \nu(\gamma - 1)}{2} V \right) \right]^{\alpha_4-2\alpha_1}. \end{aligned} \quad (4.15)$$

V is given by the following relationship:

$$\begin{aligned} \frac{r}{R_s} &= \left[\frac{(\nu + 2)(\gamma + 1)}{2} V \right]^{-2/(\nu+2)} \left[\frac{\gamma + 1}{\gamma - 1} \left(\frac{(\nu + 2)\gamma}{2} V - 1 \right) \right]^{\alpha_2} \\ &\times \left[\frac{(\nu + 2)(\gamma + 1)}{(\nu + 2)(\gamma + 1) - 2[2 + \nu(\gamma + 1)]} \left(1 - \frac{2 + \nu(\gamma - 1)}{2} V \right) \right]^{-\alpha_1}. \end{aligned} \quad (4.16)$$

The exponents α_1 , α_2 , α_3 , α_4 , and α_5 are given by

$$\alpha_1 = \frac{(\nu + 2)\gamma}{2 + \nu(\gamma - 1)} \left[\frac{2\nu(2 - \gamma)}{\gamma(\nu + 2)^2} - \alpha_2 \right], \quad (4.17)$$

$$\alpha_2 = \frac{1 - \gamma}{2(\gamma - 1) + \nu}, \quad (4.18)$$

$$\alpha_3 = \frac{\nu}{2(\gamma - 1) + \nu}, \quad (4.19)$$

$$\alpha_4 = \frac{\alpha_1(\nu + 2)}{2 - \gamma}, \quad (4.20)$$

$$\alpha_5 = \frac{2}{\gamma - 2}. \quad (4.21)$$

The total energy added to the flow, E_0 , is given by

$$E_0 = k_\nu \int_0^{R_s^{\text{strong}}} \left(\frac{P_2^{\text{strong}}}{\gamma - 1} + \frac{\rho_2^{\text{strong}} (v_2^{\text{strong}})^2}{2} \right) r^{\nu-1} dr, \quad (4.22)$$

where $k_\nu = 1, 2\pi, 4\pi$, for $\nu = 1, 2, 3$, respectively. This can be rewritten as

$$E_0 = k_\nu \int_0^{R_s^{\text{strong}}} \left(\frac{\frac{P_2^{\text{strong}}}{P'_2} P'_2}{\gamma - 1} + \frac{\frac{\rho_2^{\text{strong}}}{\rho'_2} \rho'_2 \left(\frac{v_2^{\text{strong}}}{v'_2} v'_2 \right)^2}{2} \right) r^{\nu-1} dr, \quad (4.23)$$

Substituting in the values for strong shocks from Equations 4.4 through 4.7 produces

$$E_0 = k_\nu \int_0^{R_s^{\text{strong}}} \left(\frac{\frac{P_2^{\text{strong}}}{P'_2} \frac{2}{\gamma+1} \rho_1 v_s^2}{\gamma - 1} + \frac{\frac{\rho_2^{\text{strong}}}{\rho'_2} \rho_1 \frac{\gamma+1}{\gamma-1} \left(\frac{v_2^{\text{strong}}}{v'_2} \frac{2}{\gamma+1} v_s \right)^2}{2} \right) r^{\nu-1} dr. \quad (4.24)$$

The speed at which the shock travels, v_s^{strong} , can be found by differentiating the radius of the shock, R_s^{strong} , as given in Equation 4.12 with respect to time. This produces

$$v_s^{\text{strong}} = \frac{dR_s^{\text{strong}}}{dt} = \frac{2}{\nu + 2} \left(\frac{E}{\rho_1} \right)^{\frac{1}{\nu+2}} t^{-\frac{\nu}{\nu+2}}. \quad (4.25)$$

Substituting Equation 4.25 into Equation 4.24 gives

$$E_0 = k_\nu \frac{8\rho_1}{(\nu + 2)^2} \left(\frac{E}{\rho_1} \right)^{\frac{2}{\nu+2}} t^{-\frac{2\nu}{\nu+2}} \int_0^{R_s^{\text{strong}}} \left(\frac{\frac{P_2^{\text{strong}}}{P'_2} + \frac{\rho_2^{\text{strong}}}{\rho'_2} \left(\frac{v_2^{\text{strong}}}{v'_2} \right)^2}{(\gamma - 1)(\gamma + 1)} \right) r^{\nu-1} dr. \quad (4.26)$$

Letting $\lambda = \frac{r}{R_s^{\text{strong}}}$ and changing the limits of integration produces

$$E_0 = k_\nu \frac{8\rho_1}{(\nu + 2)^2} \left(\frac{E}{\rho_1} \right)^{\frac{2}{\nu+2}} t^{-\frac{2\nu}{\nu+2}} (R_s^{\text{strong}})^\nu \int_0^1 \left(\frac{\frac{P_2^{\text{strong}}}{P'_2} + \frac{\rho_2^{\text{strong}}}{\rho'_2} \left(\frac{v_2^{\text{strong}}}{v'_2} \right)^2}{(\gamma - 1)(\gamma + 1)} \right) \lambda^{\nu-1} d\lambda. \quad (4.27)$$

Substituting into Equation 4.12 gives

$$\frac{E_0}{E} = k_\nu \frac{8}{(\nu + 2)^2} \int_0^1 \left(\frac{\frac{P_2^{\text{strong}}}{P'_2} + \frac{\rho_2^{\text{strong}}}{\rho'_2} \left(\frac{v_2^{\text{strong}}}{v'_2} \right)^2}{(\gamma - 1)(\gamma + 1)} \right) \lambda^{\nu-1} d\lambda. \quad (4.28)$$

The function $f(x)$, defined in Equation 4.3, must be determined computationally for non-strong shocks. In order to compute $f(x)$ an Euler solver developed by Nicolas Ponchaut was used [29]. The solver uses a domain between the origin and the shock. Because the domain is bounded by the shock, shock refinement is not needed, since there are no discontinuities

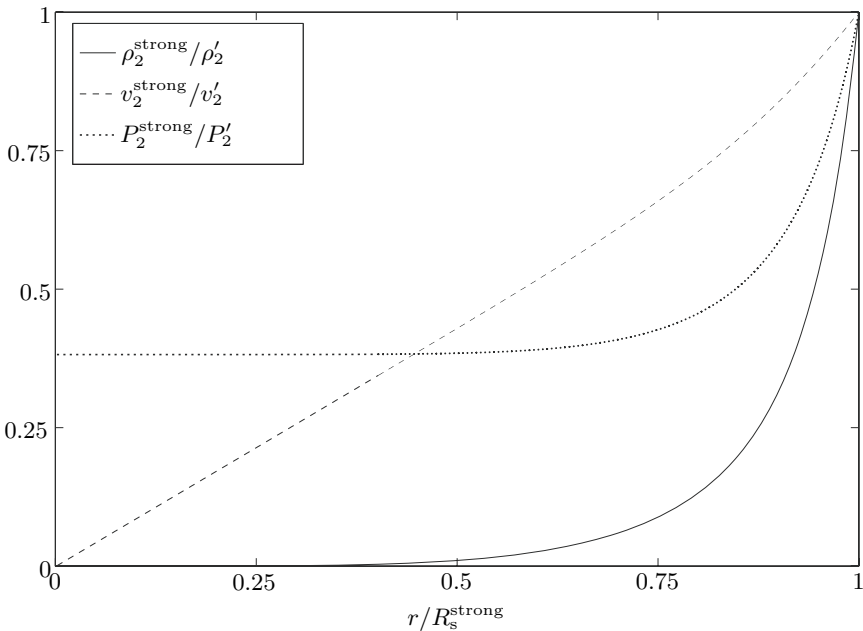


Figure 4.18: Initial density, pressure, and velocity profiles for the Euler solver based on Sedov's equations with $\nu = 2$ and $\gamma = 1.4$

in the flow. For the computation, 500 cells were used, and the cells expanded as the domain grew. The code ran with a CFL of 0.5 for 691,320 time steps. The code was run with cylindrical symmetry and a ratio of specific heats of 1.4. The pressure and density in front of the shock were both set to unity, and the energy added was 1000. The initial condition was set to be Sedov's strong shock flow solution. This initial condition is shown in Figure 4.18.

The numerical solution for $f(x)$ was then matched with $f^{\text{strong}}(x)$ at early times. This matching is shown in Figure 4.19

Knowing the complete solution for $f(x)$ it is possible to find the energy, E_0 , required for the blast wave to reach the leading oblique shock. The blast wave will convect downstream with the mean flow in Region 1 as is shown in Figure 4.20. The limiting case of the blast wave reaching the leading shock, is when it reaches the reflection point. Therefore, the limiting case is defined as the energy required for the blast wave to just reach the reflection point. Based on Figure 4.20, we can write the minimum distance, l_{\min} between the blast wave and the reflection point as

$$l_{\min} = \sqrt{(l_1 - u_1 t)^2 + l_2^2} - R_s, \quad (4.29)$$

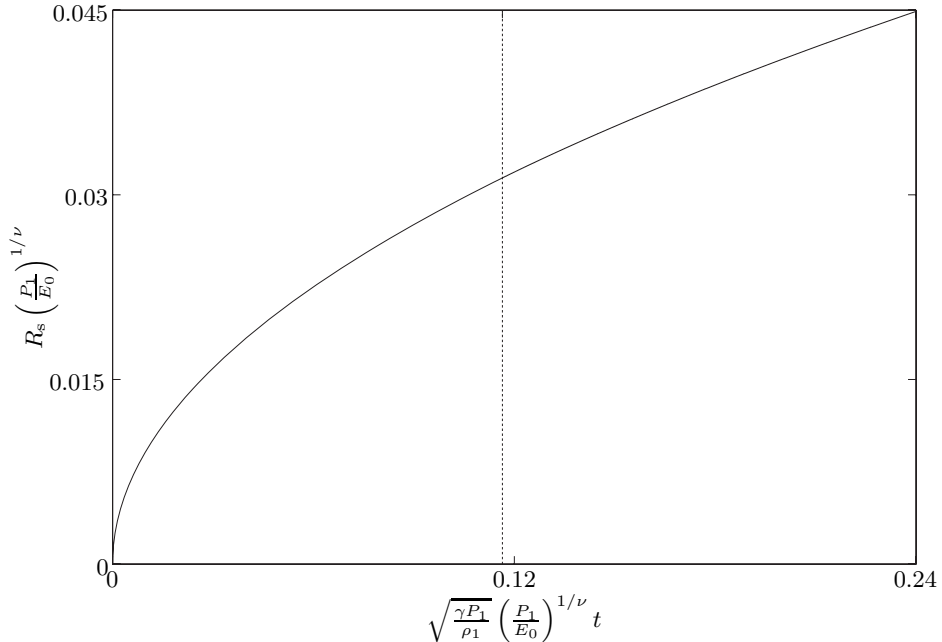


Figure 4.19: The graph to the left of 0.1164 is from Sedov's exact solution for strong shocks, and the graph to the right of 0.1164 is the Euler solution. Very good continuation of Sedov's solution is seen. $\nu = 2$ and $\gamma = 1.4$.

where u_1 is the flow speed in Region 1, and

$$l_1 = d \cos \left(\tan^{-1} \left(\frac{d}{x_2 - x_1} \right) - \theta_1 \right), \quad (4.30)$$

$$l_2 = d \sin \left(\tan^{-1} \left(\frac{d}{x_2 - x_1} \right) - \theta_1 \right). \quad (4.31)$$

x_1 and x_2 are given by

$$x_1 = -d \cot \theta_1, \quad (4.32)$$

$$x_2 = G \cot \alpha - G \cot \theta_1, \quad (4.33)$$

The conditions for the minimum energy required for the blast wave to reach the reflection

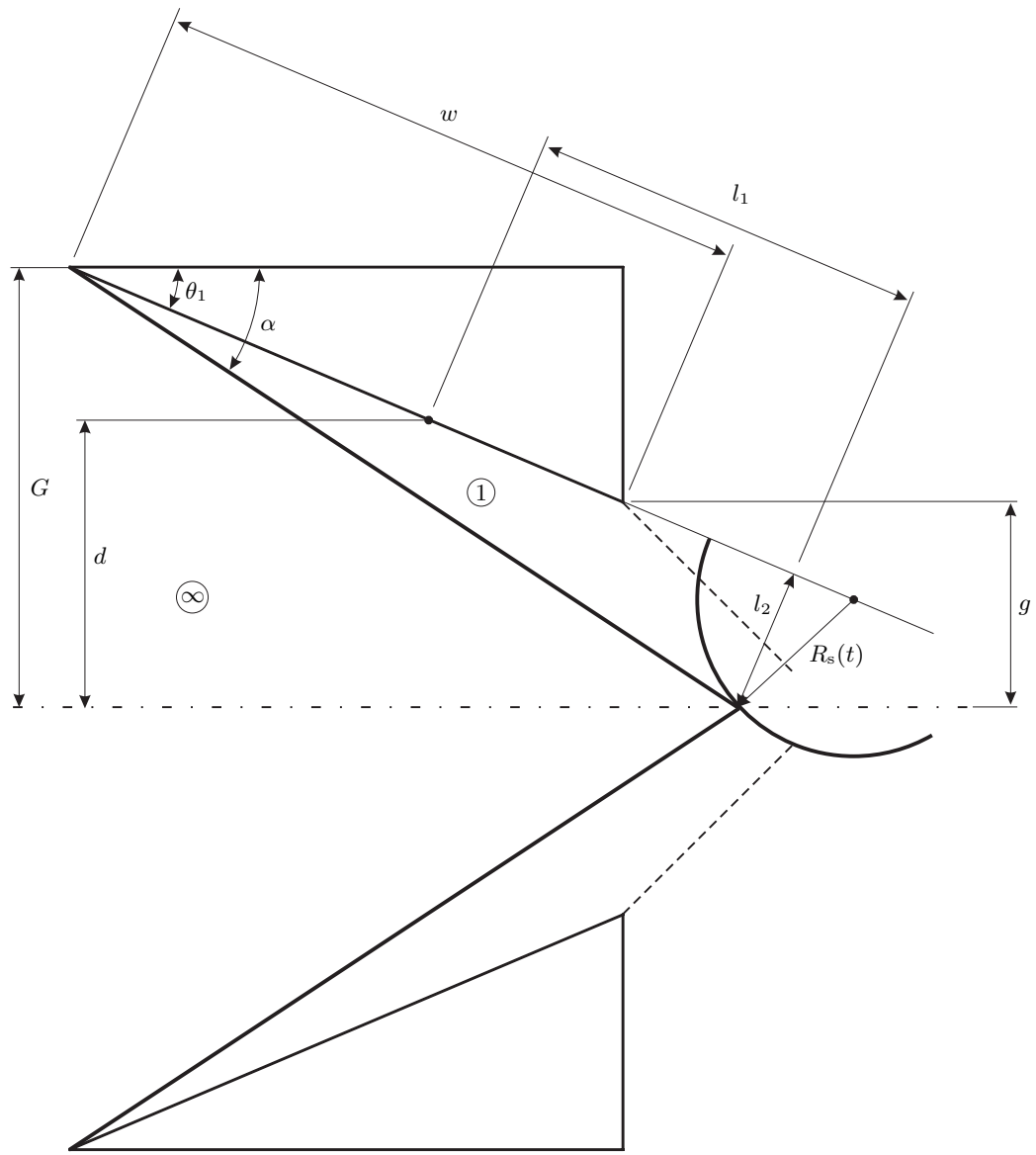


Figure 4.20: Flow setup considering energy deposition along the wedge surface showing the blast wave just reaching the point of reflection.

point is

$$R_s = \sqrt{(l_1 - u_1 t)^2 + l_2^2}, \quad (4.34)$$

$$U_s = \frac{dR_s}{dt} = \frac{u_1 (u_1 t - l_1)}{\sqrt{(l_1 - u_1 t)^2 + l_2^2}}. \quad (4.35)$$

This condition states that in the minimum energy case, the blast wave will reach the reflection point and then retreat from the reflection point. When the blast wave originates sufficiently far from the reflection point even a Mach wave can reach the reflection point, in this case the minimum energy required is zero. This occurs when

$$\frac{l_1}{l_2} \geq M_1. \quad (4.36)$$

Substituting in the values of l_1 and l_2 , gives a limiting value of d ,

$$\cot \left(\tan^{-1} \left(\frac{d}{x_2 - x_1} \right) - \theta_1 \right) \geq M_1. \quad (4.37)$$

Figure 4.21 shows a lower bound on the energy required when the free-stream Mach number is 4, the ratio of specific heats is 1.4, wedge angles are between 22° and 25.5° in increments of 0.5° and the wedge opening, G , is 120.

For a spherical, rather than a cylindrical, blast wave, the energy required dramatically increases, as is seen in Figure 4.22.

Using Amrita [24] and an iterative technique, the energy required to cause transition can be calculated. The Euler solver was set to run a case and then output whether or not transition to Mach reflection occurred. A standard bisection method was then employed using this information. To increase the speed of the routine, previous results were used to calculate a first guess when a different wedge angle was used. The results of 47 separate cases are plotted in Figure 4.23.

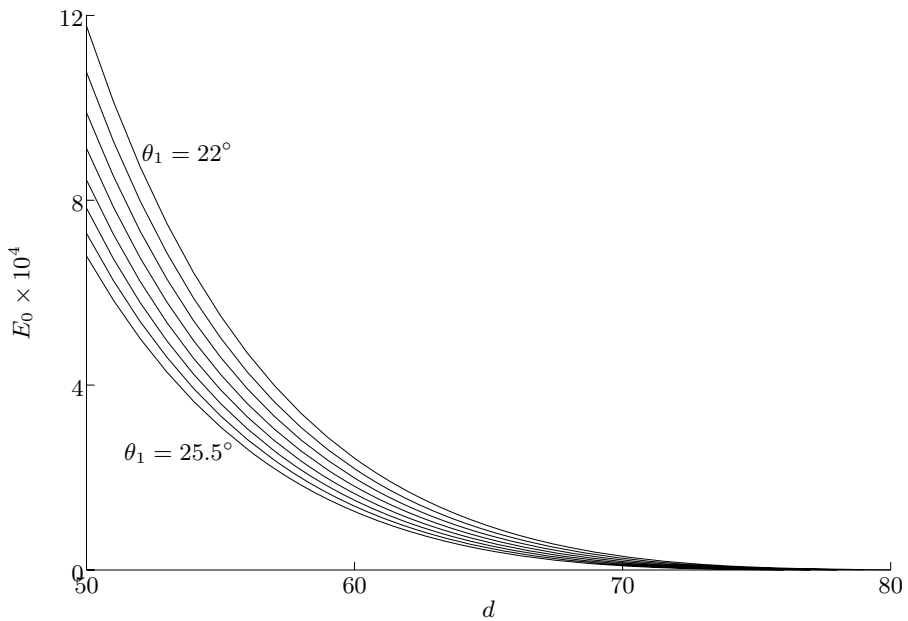


Figure 4.21: A lower bound on the energy, E_0 , required for the blast wave to reach the point of reflection. If the energy added is less than this minimum energy, transition from regular to Mach reflection is impossible. Computations done for $M = 4$, $\rho_\infty = 1$, $\nu = 2$, $\gamma = 1.4$, and $G = 120$. The wedge angle, θ_1 , varies between 22° and 25.5° in increments of 0.5° .

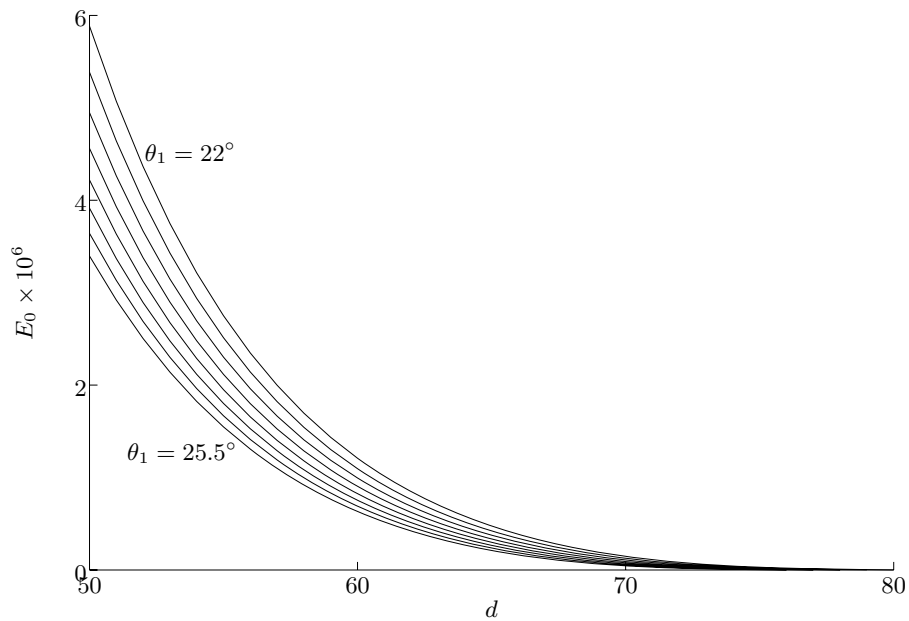


Figure 4.22: A lower bound on the energy, E_0 , required for the blast wave to reach the point of reflection. If the energy added is less than this minimum energy, transition from regular to Mach reflection is impossible. Computations done for $M = 4$, $\rho_\infty = 1$, $\nu = 3$, $\gamma = 1.4$, and $G = 120$. The wedge angle, θ_1 , varies between 22° and 25.5° in increments of 0.5° .

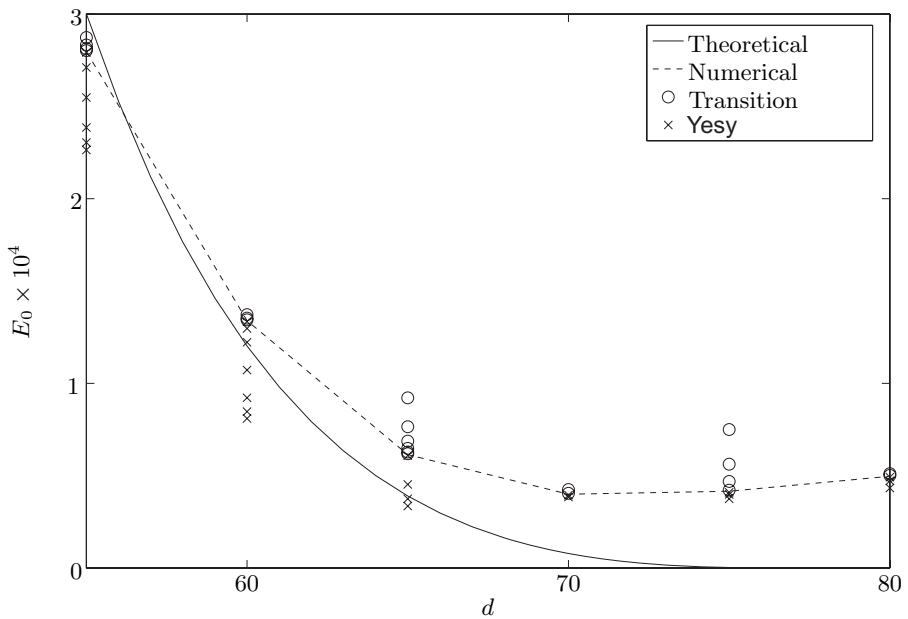


Figure 4.23: Energy, E_0 , required for transition from regular to Mach reflection to occur. The solid line represents the theoretical minimum energy curve as discussed earlier in this section, the dashed line represents the curve fit to the computational results. The \times indicates that transition did not occur at the given condition; whereas, the \circ indicates that transition did occur. Computations done for $M = 4$, $\rho_\infty = 1$, $\nu = 2$, $\gamma = 1.4$, $G = 120$, and wedge angle, $\theta_1 = 25^\circ$.

Chapter 5

Asymmetric Oblique Shocks

The theory for the reflection of two shocks at different angles with respect to the flow can be developed in much the same way as was done in Chapter 2. A generalized setup allowing for different oblique shock angles is presented in Figure 5.1.

For the purposes of this section, we will limit ourselves to higher Mach numbers, and consider only Mach reflection and regular reflection, allowing for subsonic flow downstream of the reflected shock. First we will consider the detachment condition. For shock angles greater than this condition, regular reflection can not exist. In Section 2.3.3, we said the flow angle behind the reflected shock must be equal to that of the incoming flow; however, when there are two incident shocks of different angles this is no longer true. The flow directions after the reflected shocks must be the same; however, they do not need to be parallel to the free-stream flow. An example shock polar at the detachment condition is shown in Figure 5.2. The detachment condition for asymmetric wedges is defined simply as the point at which the two reflected shock polars intersect once and are tangent at the intersection. This condition can also be thought of as the point where any further separation of the reflected shock polars would result in no intersection of the two polars. A plot of the detachment condition for various Mach number is shown in Figure 5.3. Figure B.1 is the detachment condition plotted with shock angles rather than deflection angles.

Similarly, an example shock polar at the von Neumann condition is shown in Figure 5.4. This condition occurs when both reflected shock polars and the incident shock polar intersect one another at a single point. A plot of this condition for various Mach numbers is shown in Figure 5.5. Figure B.2 is a similar plot of the von Neumann condition, but plots the shock angles instead of the deflection angles.

The von Neumann and detachment conditions at Mach 4, are shown together in Fig-

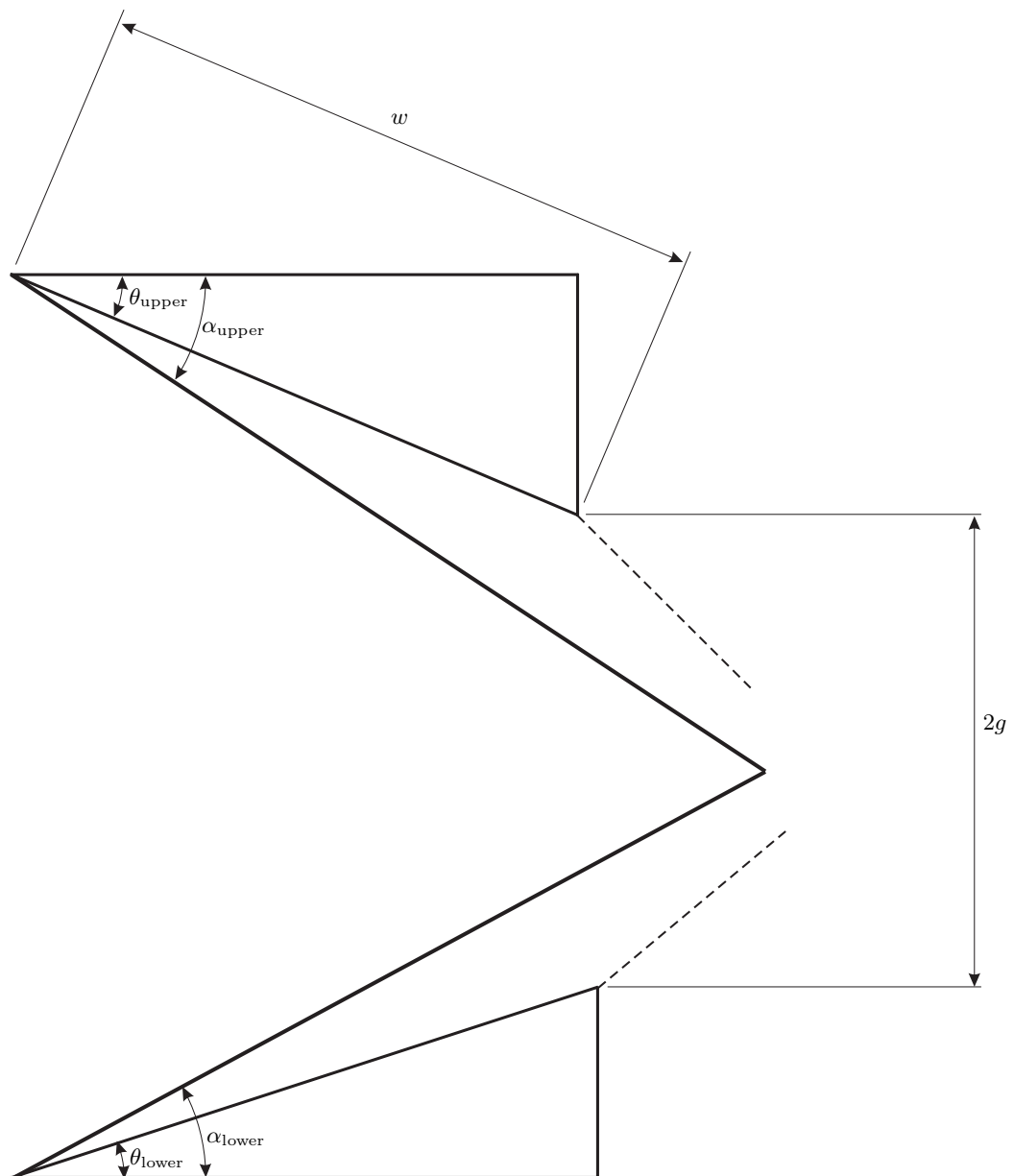


Figure 5.1: Flow setup with asymmetric wedges.

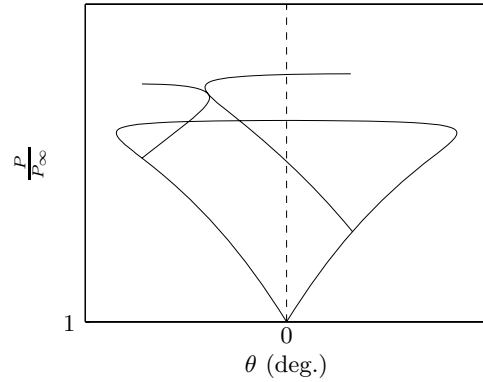


Figure 5.2: Example shock polar at the detachment condition with asymmetric wedges.

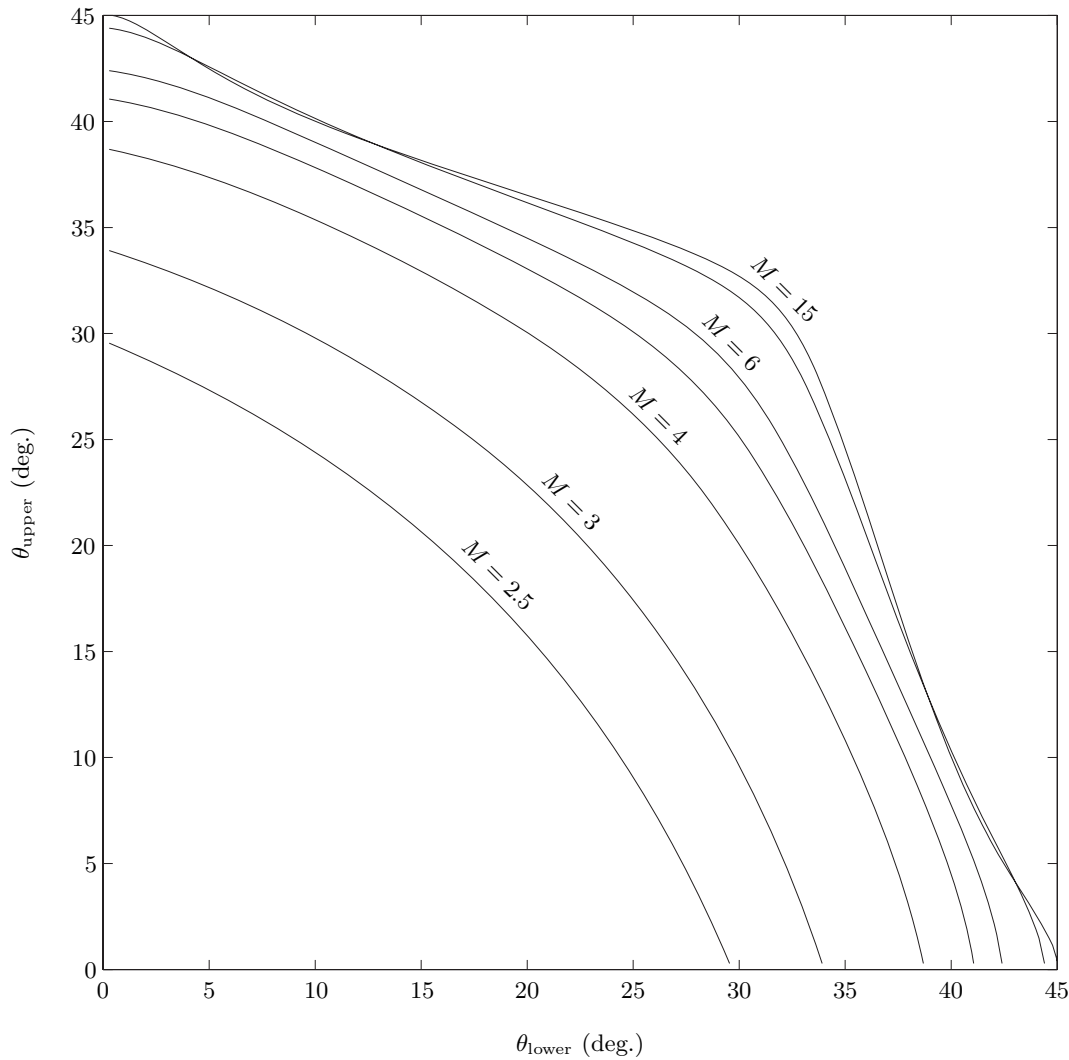


Figure 5.3: Detachment condition for asymmetric wedges. Curves are for Mach number 2.5, 3, 4, 5, 6, 10, and 15.

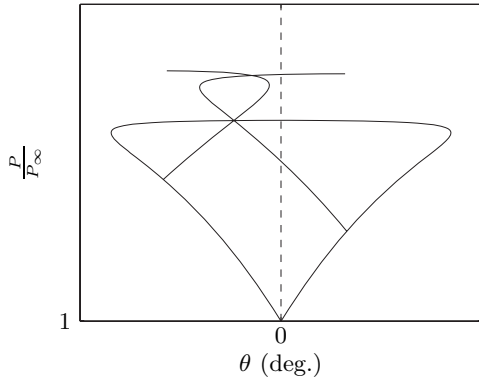


Figure 5.4: Example shock polar at the von Neumann condition with asymmetric wedges.

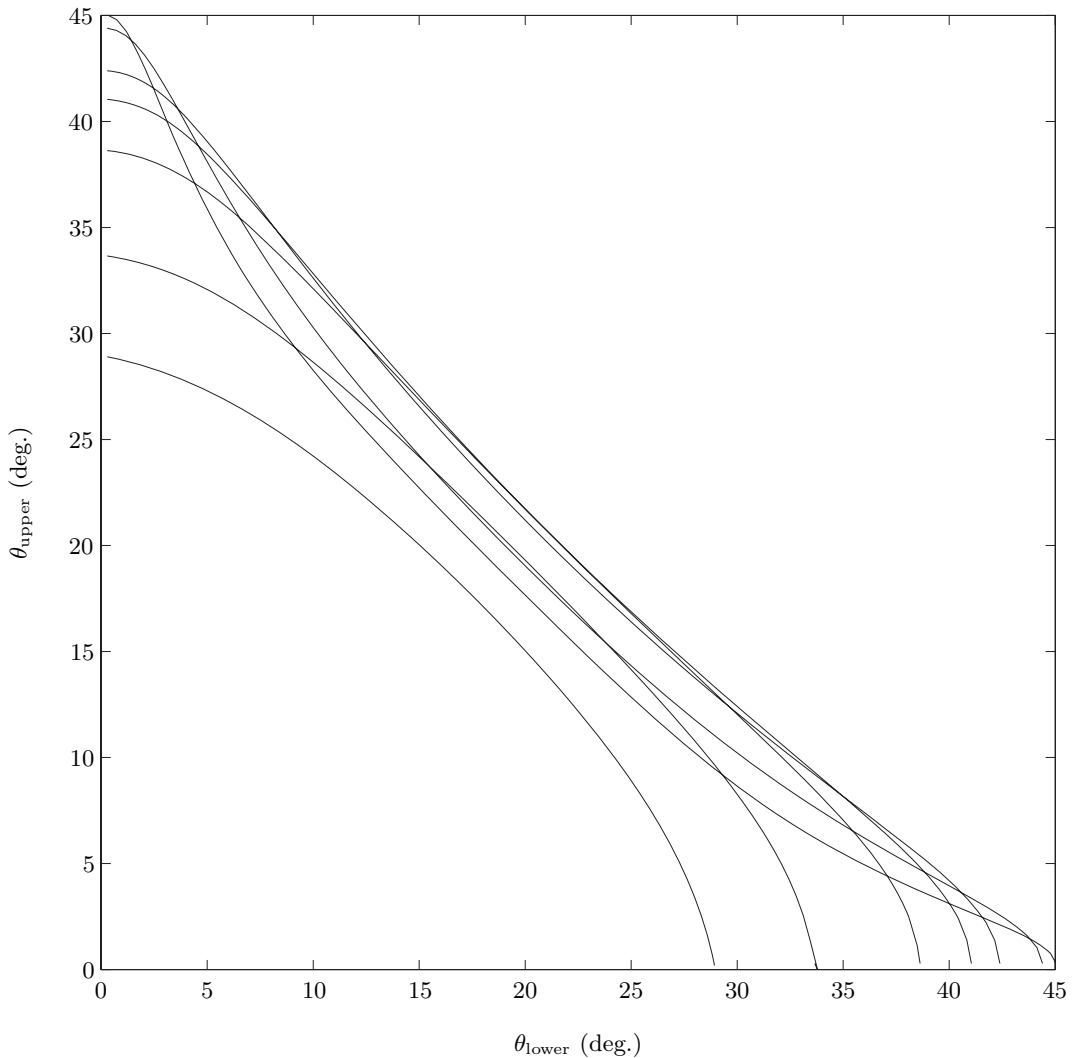


Figure 5.5: Von Neumann condition for asymmetric wedges. Curves are for Mach number 2.5, 3, 4, 5, 6, 10, and 15. Increasing Mach number is found by increasing along the y-axis.

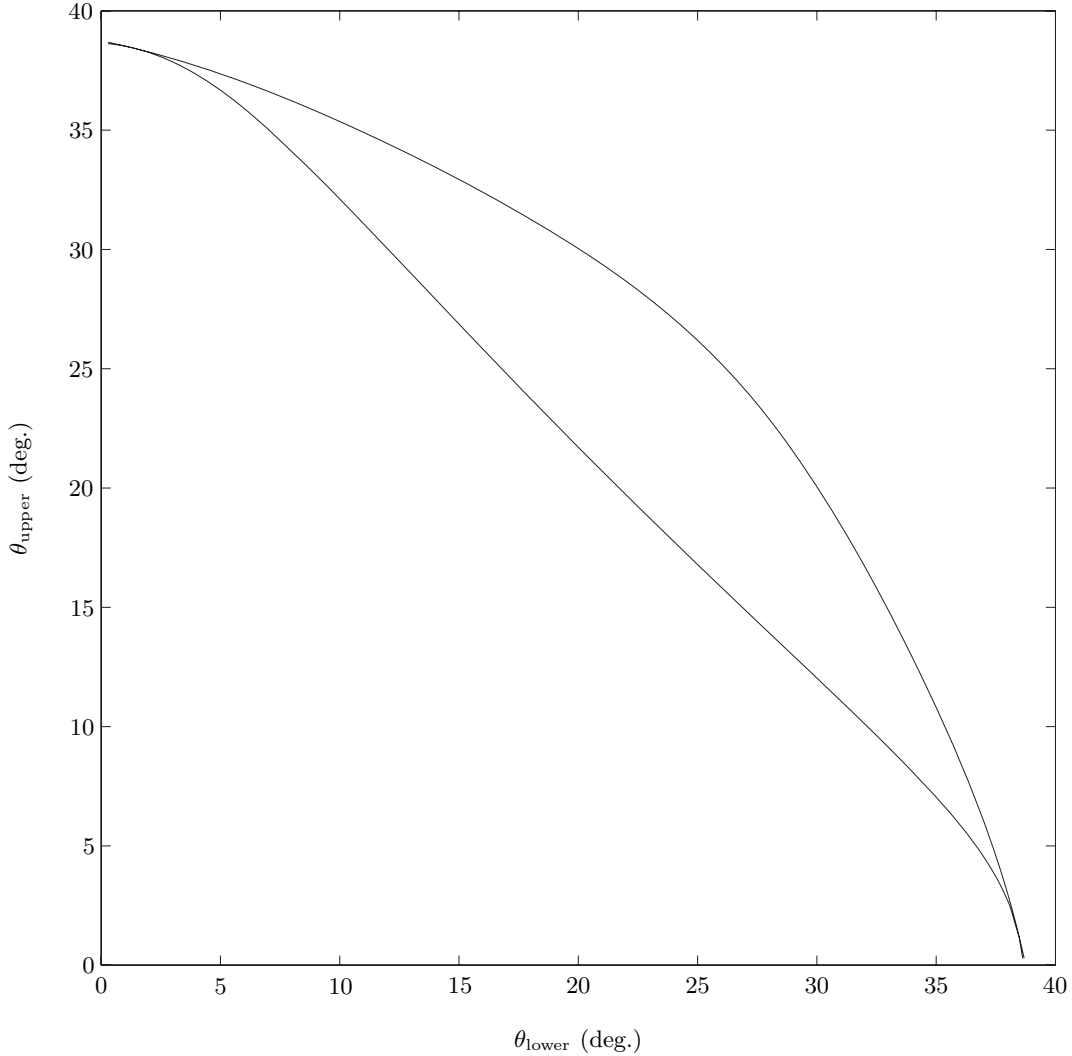


Figure 5.6: Dual solution domain for $M=4$ for asymmetric wedges. The lower curve is the von Neumann condition, the upper curve is the detachment condition.

ure 5.6 and Figure B.3. The region between the two curves represents the dual-solution domain for asymmetric wedges. A line of slope 1 through these curves would produce the dual-solution domain for symmetric wedges.

5.1 Symmetric Analogy

The steady-state Mach stem height and growth rate were examined experimentally. The theory developed in Chapter 3 was based on a symmetric wedge configuration, whereas the current experimental work uses asymmetric wedges for experimental simplicity. For configurations that are near symmetric, a conversion based on the distance, in the shock

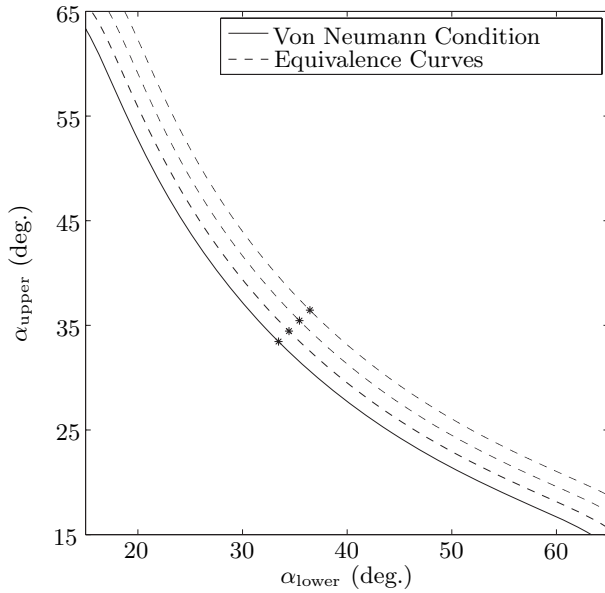


Figure 5.7: Dashed lines represent equivalence curves, with the * representing the symmetric case. Cases that are only slightly different than the symmetric case can be related to the symmetric case that lies on their equivalence curves.

angle space, from the von Neumann condition can be used. These equivalence curves, i.e., curves equidistant from the von Neumann condition, are shown in Figure 5.7.

Chapter 6

Experimental Setup

Several experiments were conducted using the Ludwieg Tube at the Graduate Aeronautical Laboratories of the California Institute of Technology (GALCIT). The details of the facility and the specific test setup will be discussed in this chapter.

6.1 Ludwieg Tube

A Mach 4 nozzle was designed, constructed and taken into operation for the existing Ludwieg tube at GALCIT. The Ludwieg tube consists of a 17 m long 300 mm inner diameter tube, a transition piece to allow for the upstream insertion of particles, an axisymmetric nozzle, a diaphragm station (located either just upstream of the throat or downstream of the test section) and a dump tank; see Figure 6.1.

Before a run, the tube is filled with the test gas at a pressure of up to 700 kPa and the dump tank is evacuated. To start the run, the diaphragm is ruptured, thus causing an expansion wave to propagate through the nozzle and into the tube. When the diaphragm is in the downstream position, the diaphragm is ruptured in a controlled way using a cutting device. In the future upstream position, the diaphragm is ruptured by creating a sufficient pressure difference across the diaphragm, since any cutting device upstream of the nozzle would disrupt the flow. During the time it takes for the expansion wave to travel to the end of the tube and for the reflected wave to return to the nozzle, the reservoir conditions for the nozzle flow are almost perfectly uniform, thus giving a constant condition test time of 80 to 100 ms.

A Mach number of 4 was chosen because it is necessary to operate at a Mach number for which the dual-solution domain has a shock angle range that is not too small. Also, to

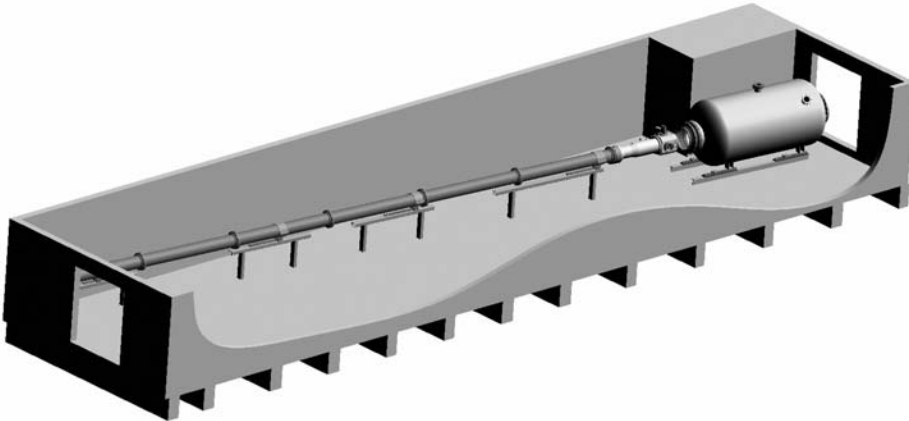


Figure 6.1: Overview drawing of the Ludwieg tube laboratory. The dump tank is shown on the right, the expansion tube on the left, and the test section in between.

avoid having to heat the gas in the tube, it is necessary to operate at a Mach number no higher than 4, to avoid condensation of the test gas in the nozzle expansion.

At this Mach number it was better to make the nozzle axisymmetric rather than rectangular. In part, this is to eliminate the unavoidable secondary flow in the corners, and the complications of a circular to rectangular transition piece. Since the test rhombus is very slender at Mach 4, a considerable portion of the test rhombus lies downstream of the nozzle exit, so that a useful portion of the test section can be fitted with flat windows set back from the nozzle edge, so that no reentrant corner is visible to the flow.

The contours for the Mach 4.0 nozzle, shown in Figure 6.4 and listed in Table C.1, and the original Mach 2.3 nozzle were designed by J. J. Korte of NASA Langley Research Center. Korte [30, 31, 32] uses an efficient code to solve the parabolized Navier-Stokes equations and couples this with a least-squares optimization procedure. The objective function of the least-squares routine consists of the Mach number distribution along the centerline and the exit profile of both the Mach number and flow angle. By doing this, the nozzle contour is designed to compensate for viscous effects. Detailed drawings of the Mach 4.0 nozzle are shown in Appendix C. The Mach 2.3 nozzle has been calibrated by using the weak Mach wave technique. Weak waves are generated by thin adhesive strips taped to the walls. These are visualized using the schlieren technique, thus giving a pattern of lines that correspond very closely to the characteristics in the flow, see Figure 6.2. Measurement of the angles at the intersection of these lines gives the Mach number and flow angle distribution in the entire nozzle flow. The resulting distribution of Mach number along the centerline of the

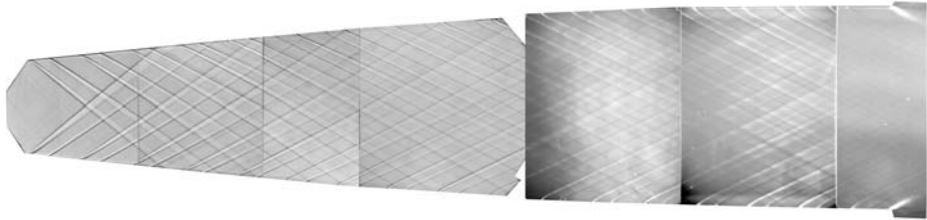


Figure 6.2: Composite schlieren image of the Mach waves generated in the Ludwieg tube nozzle by thin transverse strips of adhesive tape attached to the top and bottom walls [33].

nozzle is compared with the design curve in Figure 6.3. The results established that the Mach number is constant in the test rhombus at 2.30 ± 0.05 and the flow angle is constant across the test rhombus at $0 \pm 1^\circ$, i.e., to within the measurement error of the method. [33]

6.1.1 Governing Equations

The flow properties in the test section can be determined based the geometry of the Ludwieg tube and the initial conditions. Specifically, the stagnation pressure, P_0 in the test section will depend on the initial pressure, P_i , and the area ratio between the throat and the expansion tube, $\frac{A_t}{A_i}$. The flow Mach number in the expansion tube is given by,

$$\frac{A_t}{A_i} = \left(\frac{\gamma + 1}{2} \right)^{\frac{\gamma+1}{2(\gamma-1)}} M_i \left(1 + \frac{\gamma - 1}{2} M_i^2 \right)^{-\frac{\gamma+1}{2(\gamma-1)}}. \quad (6.1)$$

The stagnation pressure, P_0 , can then be calculated by considering the characteristic through the expansion wave, in particular,

$$\frac{P_0}{P_i} = \left(\frac{1 + \frac{\gamma-1}{2} M_i^2}{\left(1 + \frac{\gamma-1}{2} M_i \right)^2} \right)^{\frac{\gamma}{\gamma-1}}. \quad (6.2)$$

6.2 Mach 4 Nozzle

Since the expansion takes only about 100 ms to travel from the nozzle to the end of the tube and back, any time that the flow needs to establish itself in the nozzle reduces the test time. It is therefore important that the nozzle design allows for a relatively fast start-up process. Computations done assuming an infinite dump tank and a diaphragm downstream of the nozzle are shown in Figure 6.5. The image shows the initial condition at $t = 0$ ms,

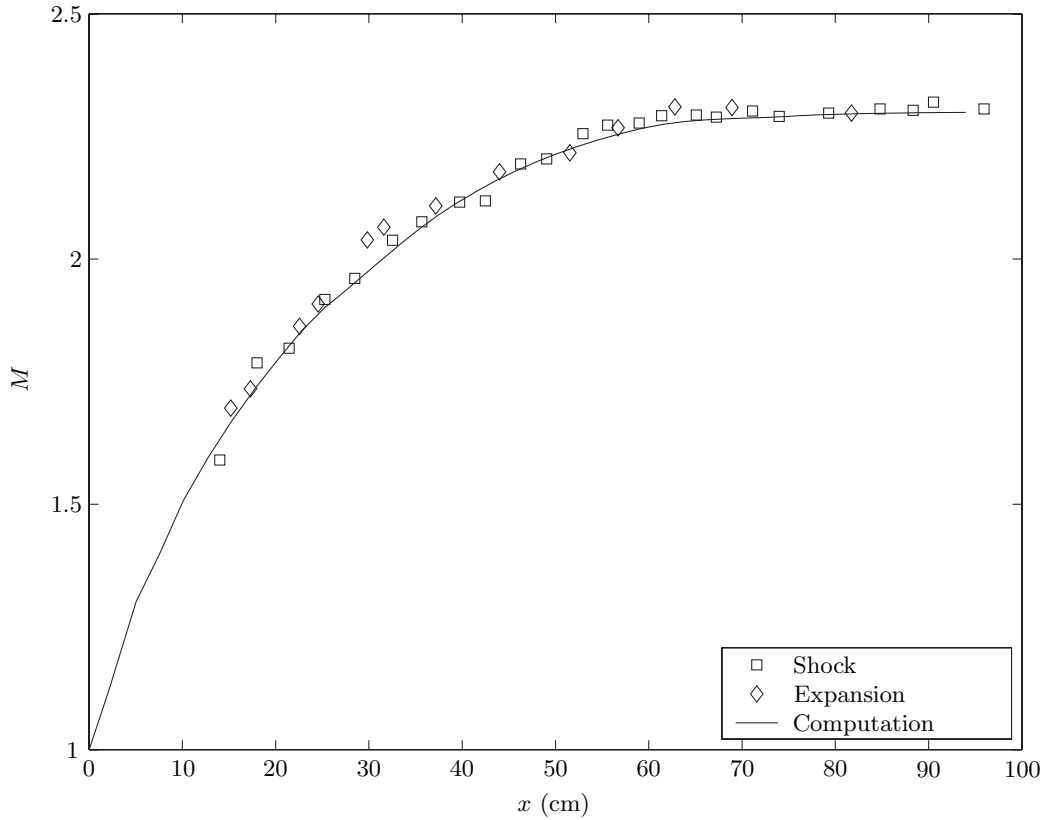


Figure 6.3: Distribution of Mach number along the centerline of the Ludwieg tube nozzle from measurements of the Mach wave angles in Figure 6.2. Here, the notation “shock” indicates the waves from the front of adhesive tape, “expansion” those from the back. The solid line represents Korte’s design computation [33].

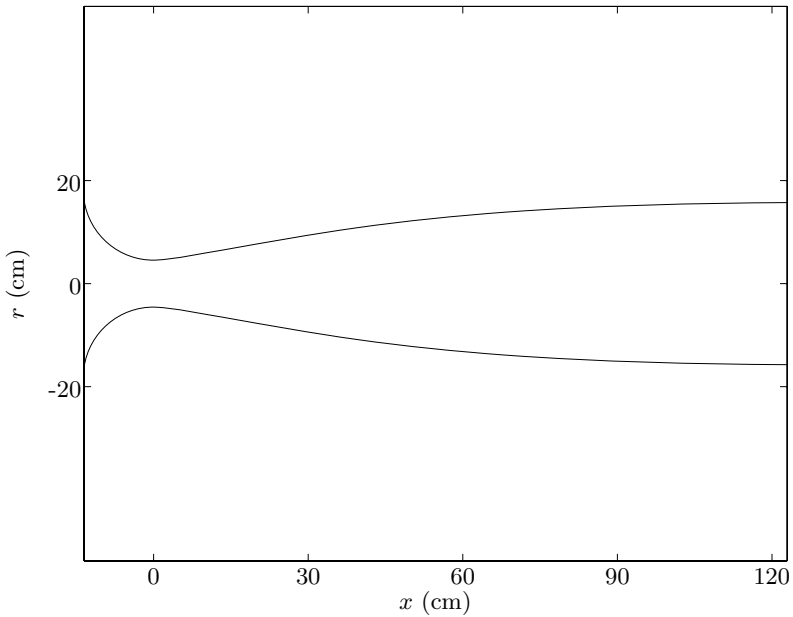


Figure 6.4: Mach 4.0 nozzle contour designed by J. J. Korte of NASA Langley Research Center.

when the diaphragm separates the high pressure gas in the tube and nozzle from the low pressure region in the dump tank. At $t = 4$ ms the shock generated by the diaphragm rupture has traveled downstream into the dump tank and an expansion wave propagates upstream through the nozzle. At $t = 8$ ms the expansion wave has partially reflected from the nozzle and formed a reflected shock, this shock is seen just downstream of the throat. At $t = 12$ ms and $t = 16$ ms the reflected shock continues to travel downstream through the nozzle. It is important to note that the reflected shock is moving against the nozzle flow and therefore travels slowly in the lab-fixed frame. At $t = 20$ ms the reflected shock has traveled downstream past the first expansion characteristic from the end of the nozzle, and steady flow in the test section is established. A 20 ms startup time is quite acceptable and is almost identical to the startup time with the previous Mach 2.3 nozzle.

Early experiments showed that the flow, using the downstream diaphragm, did not properly start. An image taken halfway through the test time is shown in Figure 6.6. The maximum steady flow time achieved with this configuration was no more than 20 ms.

Amrita simulations were conducted to understand the problem, in particular, the problem was modeled with a finite dump tank to understand the importance of the back pressure

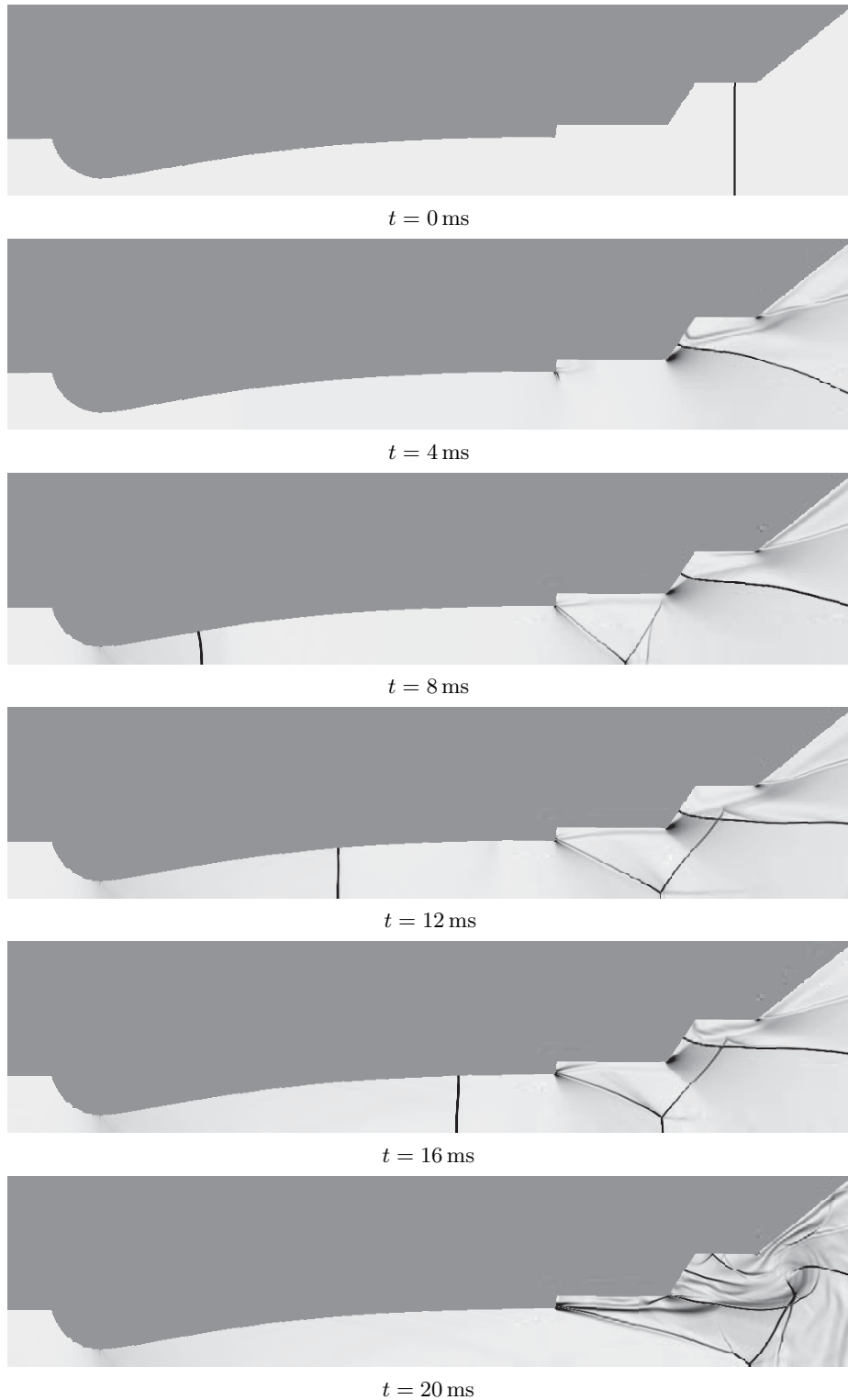


Figure 6.5: Start-up process of the Mach 4 nozzle computed using Amrita. Each image represents that value at a different time in the start-up process assuming an infinite dump tank.

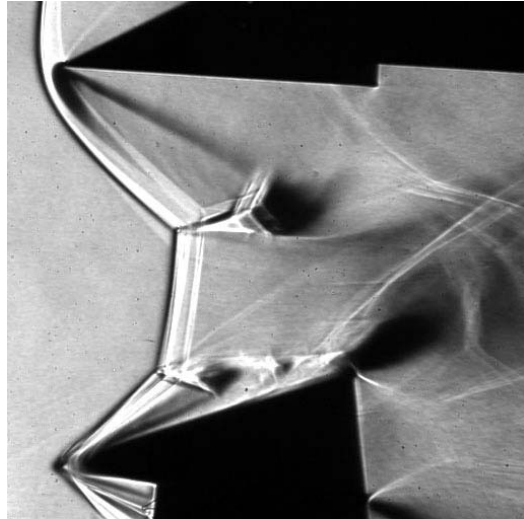


Figure 6.6: Experimental flow at approximately 50 ms into the test time showing unstart.

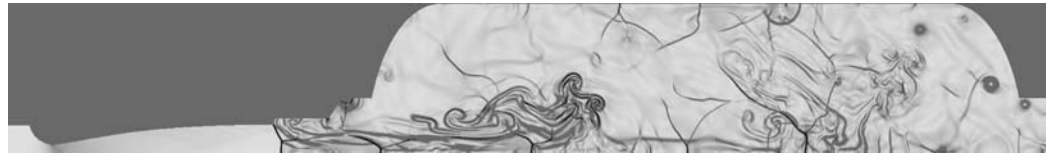


Figure 6.7: Simulation showing the unstart of the nozzle, 51.8 ms after the rupturing of the diaphragm, as a result of the reflected shock from the end of the dump tank. The left boundary condition, just upstream of the throat, is extrapolated, while the right boundary condition, at the end of the dump tank, and the outer wall of the dump tank are reflective.

and the shock generated when the diaphragm is ruptured.

6.3 Dump Tank

In previous experiments using the Ludwieg tube with a Mach 2.3 nozzle the shock that propagated into the dump tank and reflected back posed no problems. However, with the Mach 4.0 nozzle this reflected shock returned to the section and disrupted the flow. Computations using Amrita with the dump tank fully modeled confirmed this problem. An extensive study of possible solutions was made to find a way both to reduce the strength of this reflected shock and to prevent it from reentering the test section. Figure 6.7 is a simulation done using Amrita and shows the reflected shock from the dump tank inside the test section and Figure 6.8 shows an x - t diagram of this computation.

In the simulations, the addition of a baffle and a tube extension inside the dump tank, at least computationally, solved the problems associated with the reflected startup shock.

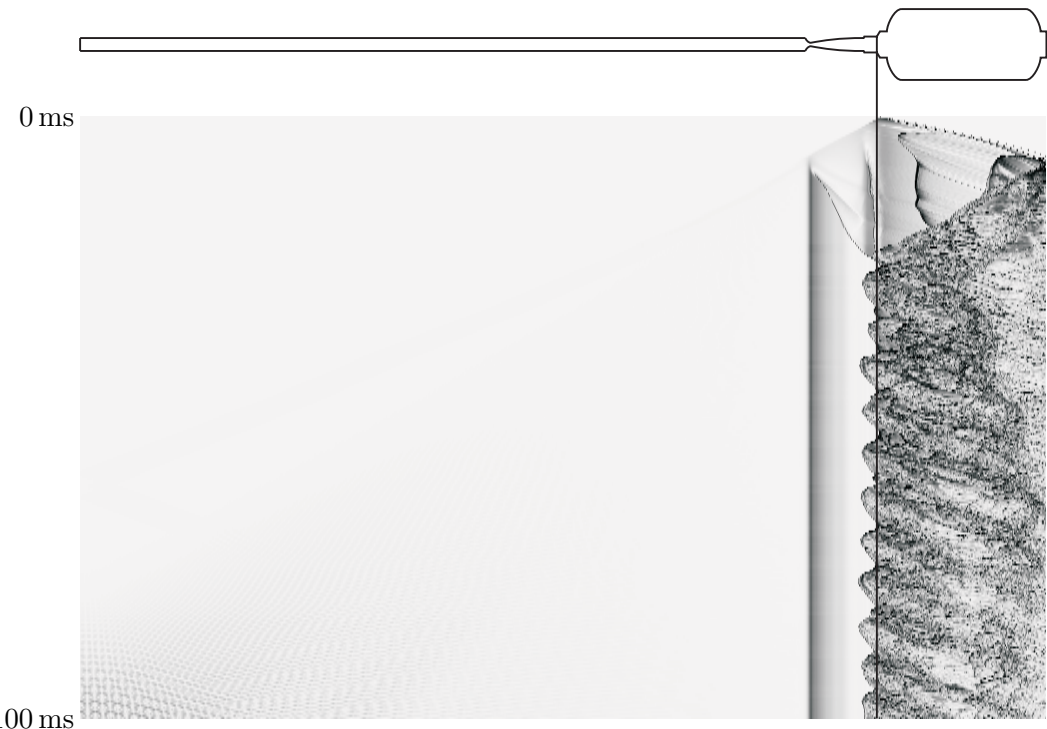


Figure 6.8: Quasi-schlieren $x-t$ diagram of the nozzle unstart with the downstream diaphragm. The quasi-schlieren image is taken at progressive times along the centerline of the Ludwieg tube. The solid vertical line represents the downstream end of the test section; clean flow is obtained if the reflected shock in the dump tank should not cross this line.

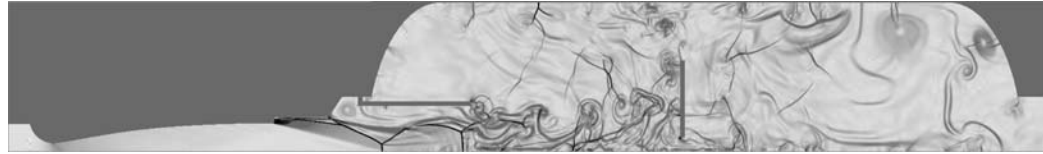


Figure 6.9: Simulation showing undisturbed flow in the test section, 51.7 ms after diaphragm rupture. The influence of the reflected shock has been kept away from the test section as the result of the addition of the baffle and tube extension. The left boundary condition, just upstream of the throat, is extrapolated, while the right boundary condition, at the end of the dump tank, and the outer wall of the dump tank are reflective.

Figure 6.9 shows an Amrita computation with the addition of the baffle and the tube extension. The flow inside the test section remains steady throughout the 100 ms of test time. The design and placement of the baffle and extension tube are shown in Figure 6.10. The baffle is supported by three Unistruts attached to the dump tank flange. There is also a 505 mm outer diameter tube placed between the three Unistruts and attached to the dump tank flange.

A sensitivity study in Amrita with respect to the location of the baffle showed that the baffle had to be placed within about one foot of the design location, which, given the limits to fully model the physics of the problem, was cause for concern. Experiments with these modifications to the dump tank again resulted in flow unstart, very similar to what is seen in Figure 6.6. The more drastic modification of moving the diaphragm upstream of the throat was then considered.

6.4 Upstream Diaphragm Station

Further computations done using Amrita, with the diaphragm moved just upstream of the converging nozzle section, showed no problems with flow unstart and also produced a flow start time of only 3 ms, as opposed to the 20 ms required with the downstream diaphragm. Two quasi-schlieren images of the flow after the rupturing of the upstream diaphragm are seen in Figures 6.11 and 6.12. Figure 6.13 shows an x - t diagram of this computation.

Unfortunately, there are significant drawbacks to having the diaphragm upstream of the test section. Specifically, the ruptured diaphragm will cause disturbances due to its presence and due to the production of small pieces of debris. Experiments conducted using an upstream mylar diaphragm of 5 mils had a first startup process, and unstart of the flow

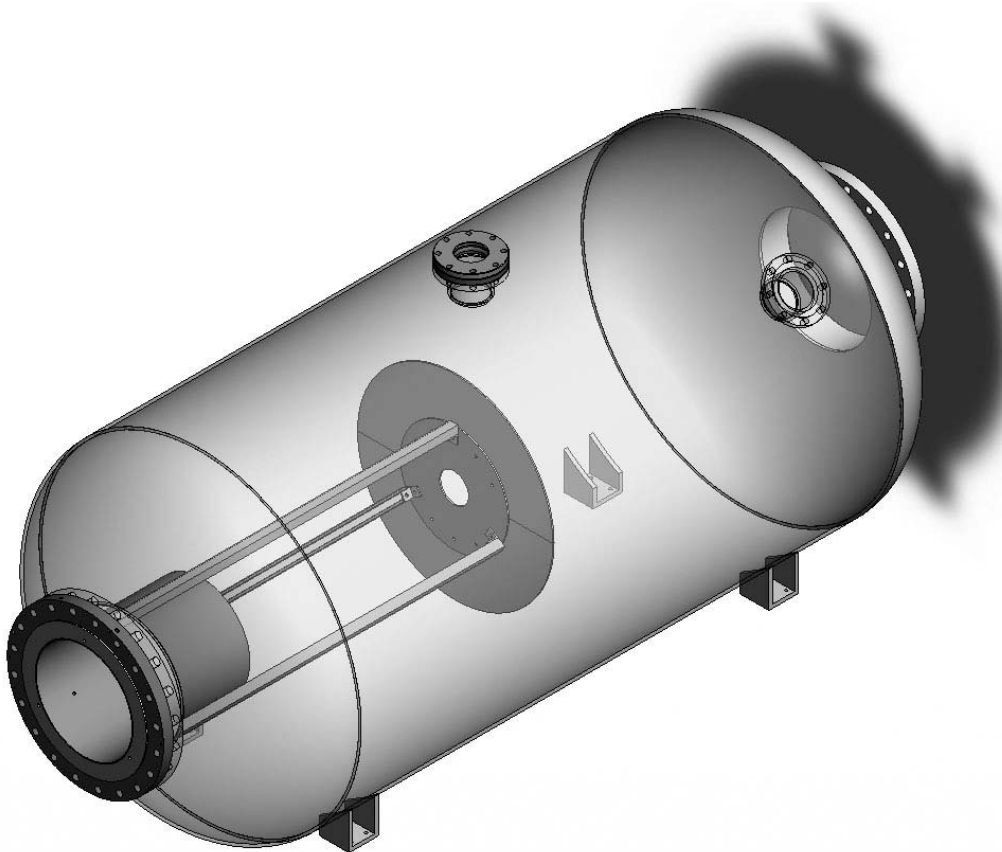


Figure 6.10: Dump tank with modifications including the addition of a baffle and a tube extension. The baffle is connected to the dump tank with a series of unistruts.



Figure 6.11: Simulation showing the starting of the nozzle, 2.7 ms after the rupturing of the diaphragm located just upstream of the converging section of the nozzle. The left boundary condition, just upstream of the throat, is extrapolated, while the right boundary condition, at the end of the dump tank, and the outer wall of the dump tank are reflective.

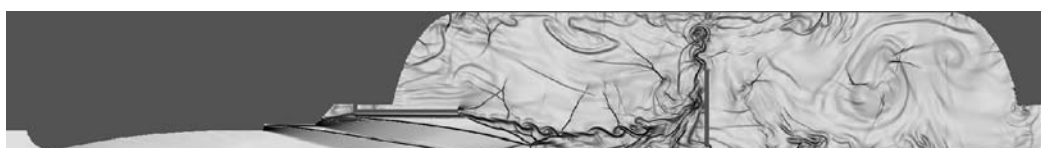


Figure 6.12: Simulation showing the correctly started flow 50.1 ms after the rupturing of the diaphragm located just upstream of the converging section of the nozzle. The left boundary condition, just upstream of the throat, is extrapolated, while the right boundary condition, at the end of the dump tank, and the outer wall of the dump tank are reflective.

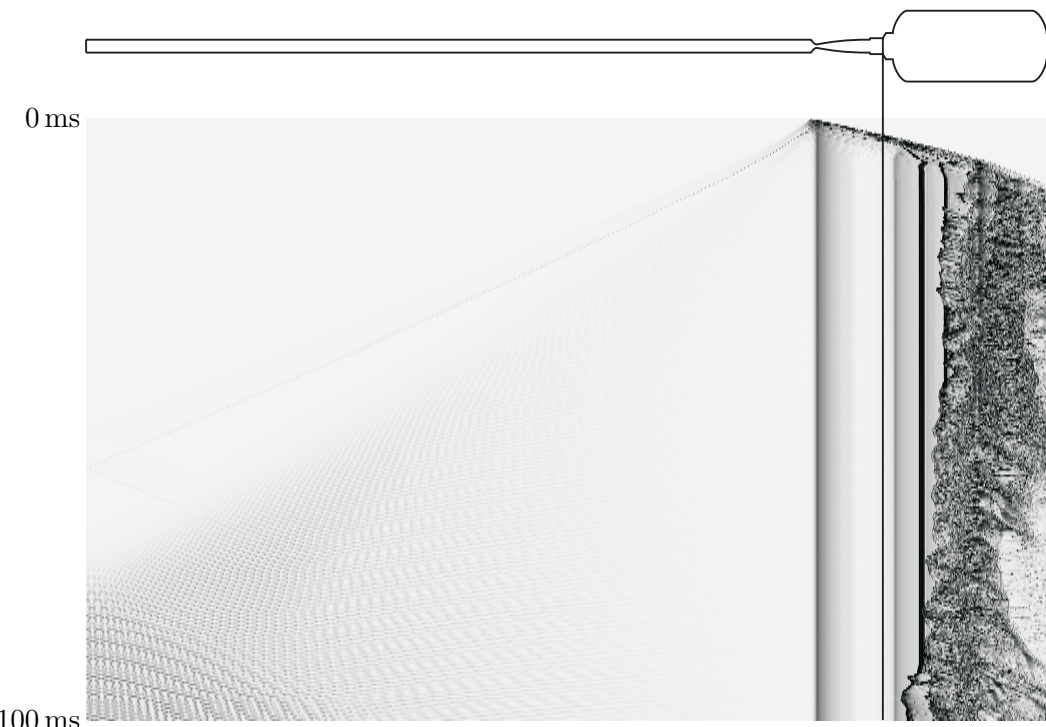


Figure 6.13: Quasi-schlieren x - t diagram of the nozzle successfully starting with the upstream diaphragm. The quasi-schlieren image is taken at progressive times along the centerline of the Ludwieg tube. The solid vertical line represents the downstream end of the test section; clean flow is obtained if the reflected shock in the dump tank should not cross this line.

was not experienced until after the reflected expansion wave from the tube returned to the test section.

6.5 Adjustable Wedge Model

A double wedge model was constructed with the lower wedge being fixed at an angle of 23.6° and the upper wedge being adjustable. The upper wedge angle is controlled using a rotary servo motor with a 5:1 gear ratio. The assembly of the adjustable wedge is shown in Figure 6.14. The wedge is supported by two vertical posts, and its motion is controlled by a connecting rod, which is connected to the motor.

6.5.1 Motor and Gear Box

A Parker Electromechanical BE342KR brushless servo motor with a Bayside PX34-005 inline planetary gearhead with a 5:1 gear ratio is used. The motor itself provides a maximum speed of 5000 rpm and maximum torque $3.12 \text{ N}\cdot\text{m}$. This provides a maximum speed of 1000 rpm and a maximum torque of $15.6 \text{ N}\cdot\text{m}$ after the gearhead. It is estimated that aerodynamic forces on the wedge generate a torque on the wedge not exceeding $7 \text{ N}\cdot\text{m}$. In most cases, since the initial tube pressure in the present experiments is less than the maximum tube pressure, the actual torque on the wedge will be significantly smaller.

The motor is controlled by a Parker Compax3 programmable servo positioner. The position of the motor as a function of time is specified by 4 parameters, those being the change in angle, $\Delta\theta_1$, the maximum angular speed, $\dot{\theta}_1^*$, the maximum angular acceleration, $\ddot{\theta}_1^*$, and the maximum angular jerk, $\dddot{\theta}_1^*$. These 4 parameters then specify the time the move will take. For experimental purposes, we would prefer to specify the angle change, $\Delta\theta_1$, the time in which this should occur, T , and the fact that we would like to follow a smooth “S-curve”. Given these requirements, we can relate the various move parameters,

$$\dot{\theta}_1^* = 2 \frac{\Delta\theta_1}{T}, \quad (6.3)$$

$$\ddot{\theta}_1^* = 8 \frac{\Delta\theta_1}{T^2}, \quad (6.4)$$

$$\dddot{\theta}_1^* = 32 \frac{\Delta\theta_1}{T^3}. \quad (6.5)$$

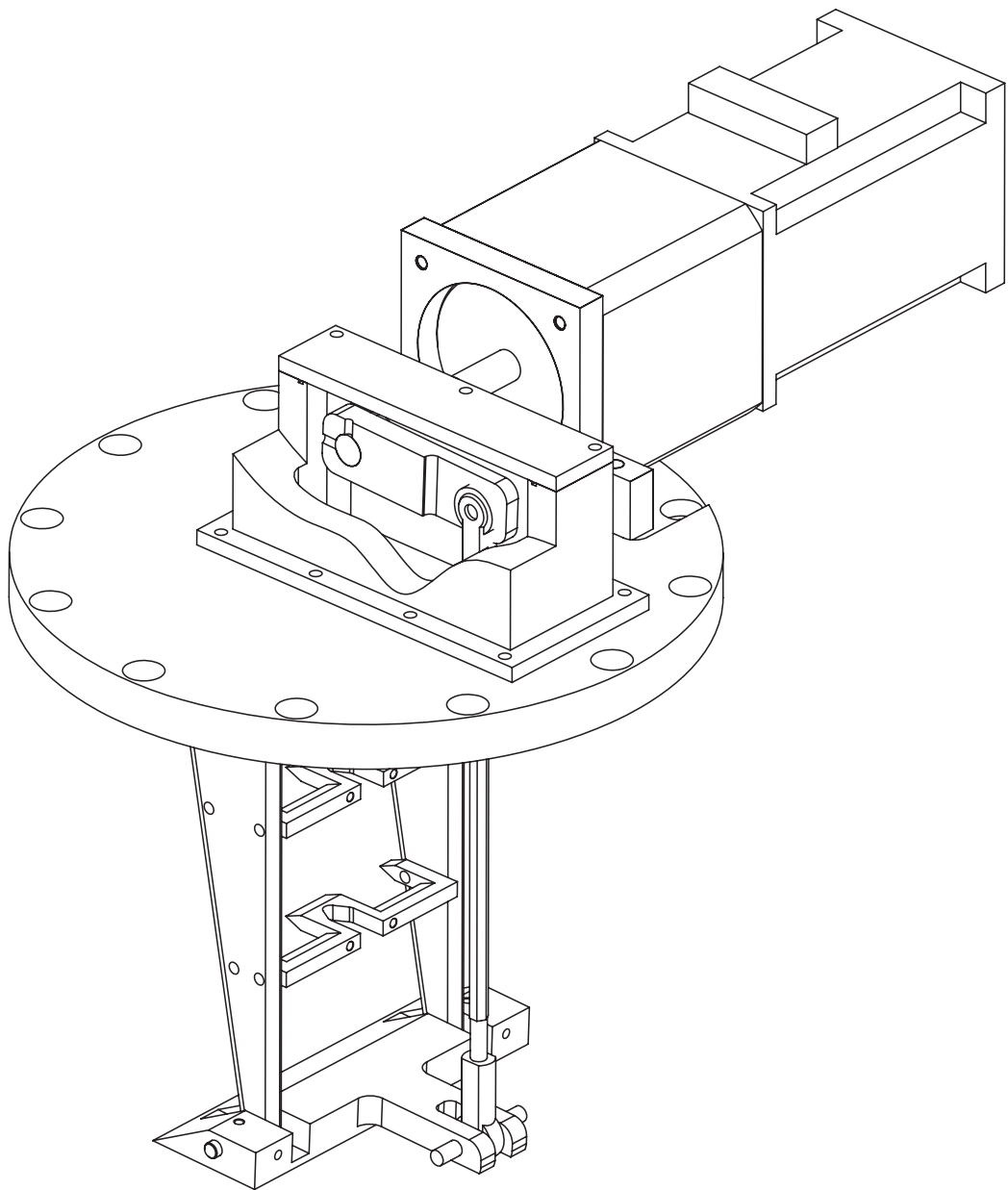


Figure 6.14: Wedge assembly consisting of a wedge, a connecting rod, a support structure, a motor, and a gearhead. The wedge rotates about the rod that runs through the wedge and the two vertical supports.

6.6 High Speed Schlieren Photography

The Ludwieg tube was equipped with a high speed schlieren system. The primary component of the system is a Visible Solutions Phantom v7.1 camera. At the full resolution of 800×600 px the camera has a frame rate of 4,800 fps. The frame rate increases to 8,300 fps at 512×512 px and to 27,000 fps at 256×256 px. A key feature of the camera is the ability for the user to specify the exact aspect ratio and resolution. By doing this, no pixels are wasted on uninteresting parts of the flow, this results in the effective resolution and the speed being higher compared to that of a fixed-aspect-ratio camera.

The light source for the system is an Oriel 66181 and a corresponding power supply. The unit has a 1000 W Quartz Tungsten Halogen lamp. The remainder of the schlieren setup is a standard Z-fold configuration.

Chapter 7

Experimental Hysteresis

Computationally, the hysteresis phenomenon is easily demonstrated. However, experimentally, due to tunnel noise, the hysteresis phenomenon is more difficult to show and the range of angles over which the hysteresis occurs is reduced. Examining the hysteresis in the Ludwieg tube provides a metric of the quietness of the tunnel. That is to say, the further one can go into the dual-solution domain while maintaining regular reflection, the quieter and cleaner the tunnel. This can be measured as a percentage between the von Neumann condition and the detachment condition.

In order to demonstrate the hysteresis phenomenon, the upper adjustable wedge was set so that the shocks are below the von Neumann condition, and therefore only regular reflection is possible. This initial configuration is shown in Figure 7.1.

The angle of the upper wedge was then slowly increased, over 40 ms, to bring the shocks into the dual-solution domain, while maintaining regular reflection. Figure 7.2 shows regular reflection inside the dual-solution domain, and illustrates the highest angles obtainable in the Ludwieg tube, without transitioning to Mach reflection.

A slight increase in the upper wedge angle will cause a transition to Mach reflection inside the dual-solution domain. Figure 7.3 shows a schlieren image just after transition to Mach reflection has begun. The image shows the three-dimensionality of the Mach stem, with both regular reflection and Mach reflection being visible in the image.

As the upper wedge angle continues to increase, the Mach stem grows in size. This larger Mach stem, corresponding to the high incident shock angle from the upper adjustable wedge, is shown in Figure 7.4.

With Mach reflection established, the wedge angle can be decreased. Figure 7.5 shows Mach reflection inside the dual solution domain, where previously between Figures 7.1 and

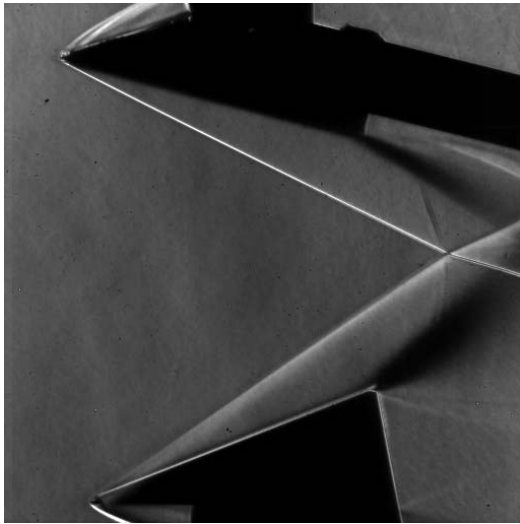


Figure 7.1: Demonstration of the hysteresis phenomenon in the Ludwieg Tube. The initial wedge angles were set so that only regular reflection was possible. $M = 4.0$, $\alpha_{\text{lower}} = 33.9^\circ$, $\alpha_{\text{upper}} = 25.9^\circ$, $t = 13.4$ ms.

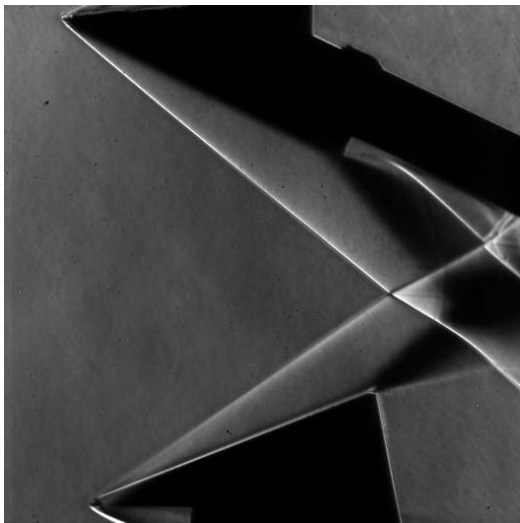


Figure 7.2: Demonstration of the hysteresis phenomenon in the Ludwieg Tube. The conditions are within the dual solution domain, just below the point where transition to Mach reflection will occur due to tunnel disturbances. $M = 4.0$, $\alpha_{\text{lower}} = 33.9^\circ$, $\alpha_{\text{upper}} = 39.8^\circ$, $t = 49.0$ ms.

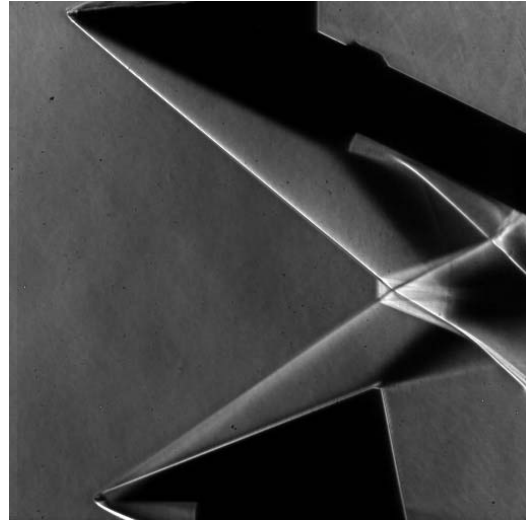


Figure 7.3: Demonstration of the hysteresis phenomenon in the Ludwieg Tube. Transition to Mach reflection is just beginning to occur due to tunnel disturbances. $M = 4.0$, $\alpha_{\text{lower}} = 33.9^\circ$, $\alpha_{\text{upper}} = 39.9^\circ$, $t = 49.3$ ms.

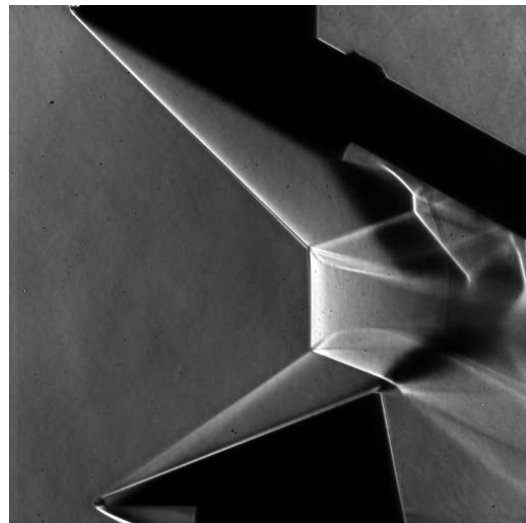


Figure 7.4: Demonstration of the hysteresis phenomenon in the Ludwieg Tube. The upper wedge angle is relatively large, and a large Mach stem exists. $M = 4.0$, $\alpha_{\text{lower}} = 33.9^\circ$, $\alpha_{\text{upper}} = 45.0^\circ$, $t = 64.6$ ms.

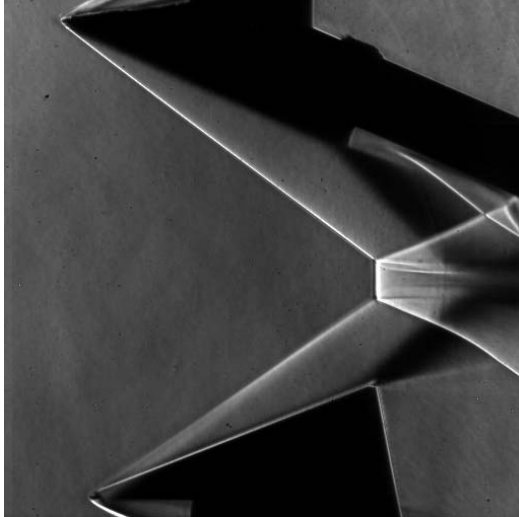


Figure 7.5: Demonstration of the hysteresis phenomenon in the Ludwieg Tube. The upper wedge angle is relatively large, and a large Mach stem exists. $M = 4.0$, $\alpha_{\text{lower}} = 33.9^\circ$, $\alpha_{\text{upper}} = 37.9^\circ$, $t = 81.7 \text{ ms}$.

7.2 there was regular reflection.

As the upper wedge angle is decreased further, the von Neumann condition is approached. Once this condition is reached, the Mach reflection must cease and the reflection will return to regular reflection. The angles at which the transition back to regular reflection occurs agree very well with the theoretical von Neumann condition of $\alpha_{\text{upper}} = 33.9^\circ$ and $\alpha_{\text{lower}} = 33.0^\circ$.

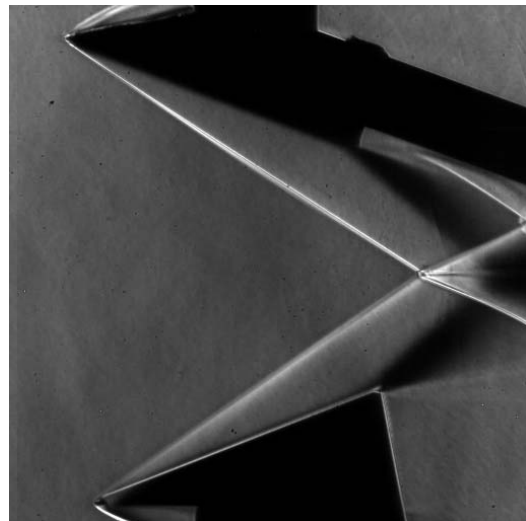


Figure 7.6: Demonstration of the hysteresis phenomenon in the Ludwieg Tube. Return to regular reflection as the von Neumann condition is approached. $M = 4.0$, $\alpha_{\text{lower}} = 33.9^\circ$, $\alpha_{\text{upper}} = 33^\circ$, $t = 85.7 \text{ ms}$.

Chapter 8

Experimental Transition

Besides transitioning from regular reflection to Mach reflection by increasing the wedge angle to a sufficient extent that the tunnel disturbances cause transition, it is also possible to introduce a disturbance to induce this transition.

In the current experiments, a laser is focused on the fixed wedge and energy is deposited on it. The effects of energy deposition are explored computationally and analytically in Section 4.2. This deposition of energy can cause transition from regular reflection to Mach reflection.

In order to enter into the dual-solution domain with regular reflection, the hysteresis phenomenon explored in Chapter 7 is utilized. In particular, the upper adjustable wedge is first set to an angle such that only regular reflection is possible (as seen in Figure 8.1), and is then slowly rotated into the dual solution domain (as seen in Figure 8.2), while remaining below the point where tunnel disturbances would cause transition. The vertical black line seen in the images is used to properly compensate the images for any rotation, so that shock angles can be accurately measured.

Visualization of the blast wave created by the energy deposition, as discussed in Section 4.2, was done by examining the deposition of energy without flow. Figure 8.3 shows the deposition of energy on the lower wedge and the resulting single blast wave. Unfortunately, in order to detect the blast wave a high pressure and density were required, both of which were much higher than what is experienced during the actual flow experiment. As a result, the blast wave is weak, since the energy is normalized by the pressure, as is seen in Equation 4.3.

The disturbance on the leading shock, due to the blast wave from the energy deposition, results in an outward bulging of the leading shock. This is seen in Figure 8.4.

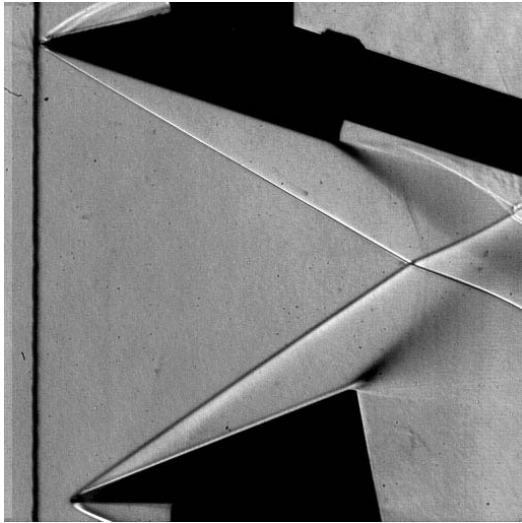


Figure 8.1: Initial shock configuration below the von Neumann condition. Only regular reflection is possible. $M = 4$, $\alpha_{\text{lower}} = 33.8^\circ$, $\alpha_{\text{upper}} = 29.9^\circ$.

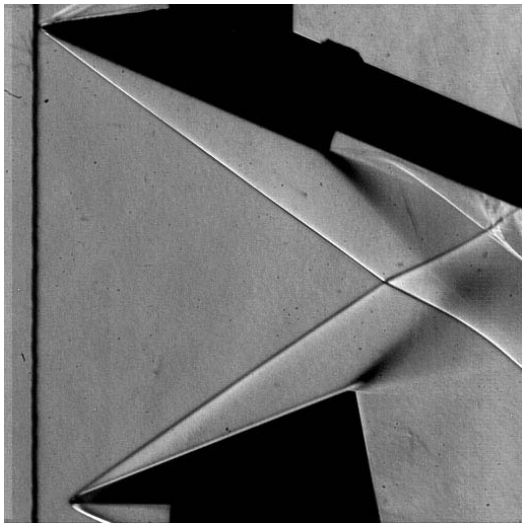


Figure 8.2: Shock configuration before laser energy is deposited onto the lower wedge. Both regular reflection and Mach reflection are possible. $M = 4$, $\alpha_{\text{lower}} = 33.8^\circ$, $\alpha_{\text{upper}} = 36.0^\circ$.

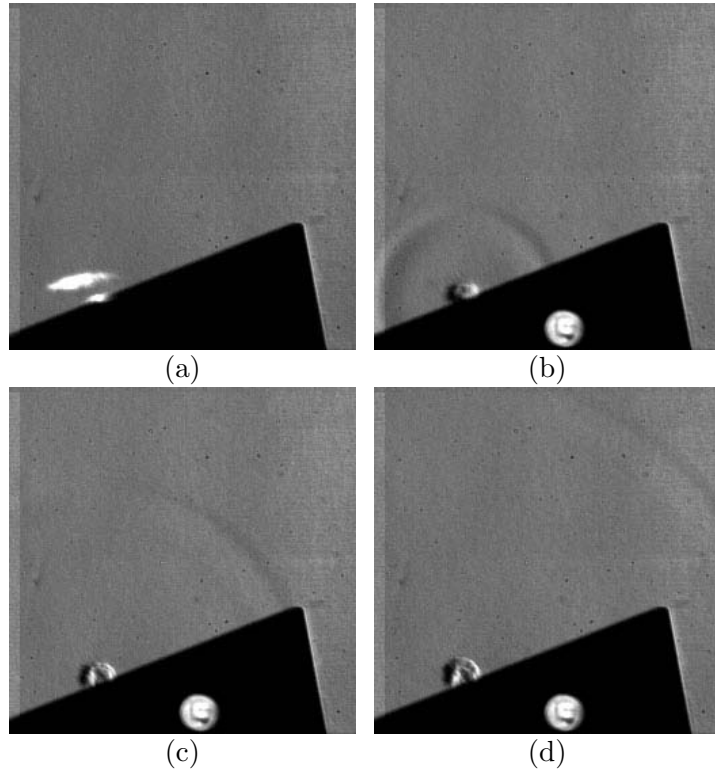


Figure 8.3: Blast wave resulting from the deposition of energy on the lower wedge using a laser. The exposure of each image was $3\mu\text{s}$, with $38\mu\text{s}$ between exposures. The circular light seen inside the lower wedge in images (b), (c), and (d) is used to indicate that the laser has fired.

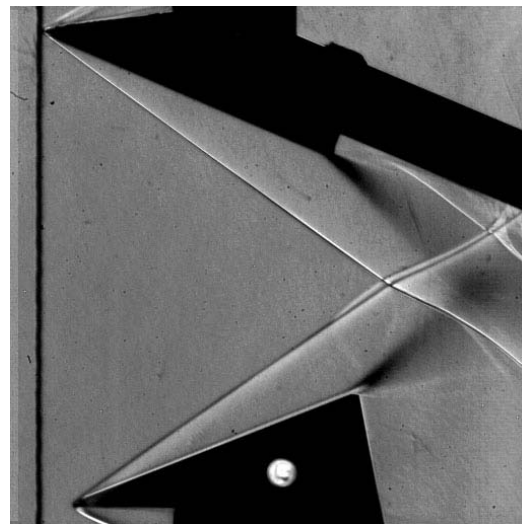


Figure 8.4: The leading shock is disturbed in the region of the reflection due to the laser energy, which was previously deposited. Transition to Mach reflection will immediately follow. $M = 4$, $\alpha_{\text{lower}} = 34.5^\circ$, $\alpha_{\text{upper}} = 35.8^\circ$.

Table 8.1: Summary of transition for various energy deposition locations.

<i>Location (d/G)</i>	<i>Transition from RR → MR</i>
0.553	Yes
0.594	Yes
0.645	Yes
0.689	Yes
0.752	Yes
0.811	No
0.867	No

8.1 Energy Deposition Location

Figure 4.23 shows the importance of energy deposition location on the possibility for transition to occur from regular reflection to Mach reflection. This was studied experimentally by focusing the laser at various positions along the wedge. For positions on the wedge close to the centerline, i.e., small d , transition from regular reflection to Mach reflection always occurred. However, it was found that there was a maximum distance from the centerline beyond which transition would not occur. This is because, for large d , the blast wave has a large distance to travel before reaching the reflection point, and hence becomes too weak to cause transition once it does reach the reflection point. The fact that transition occurs for small d means that the energy is sufficient for the blast wave to reach the reflection point in all cases. A summary of the six energy location experiments is given in Table 8.1. For the asymmetric case, G is taken to be half the distance between the leading edges of the two wedges, and d is measured from this dividing line.

These results are shown graphically in Figure 8.5, where the energy deposition points that caused transition are marked with a \circ , and deposition points that did not lead to transition are denoted with a \times .

8.2 Tunnel Disturbances

Disturbances inherent to the test facility can also cause the flow to trip from regular reflection to Mach reflection. To explore this, the wedge was moved at different speeds into the dual-solution domain without any artificially added disturbances. The angle at which transition occurred was then measured, which provides a qualitative measure of the flow quality. Since the test time of the GALCIT Ludwieg tube is limited to about 100 ms of

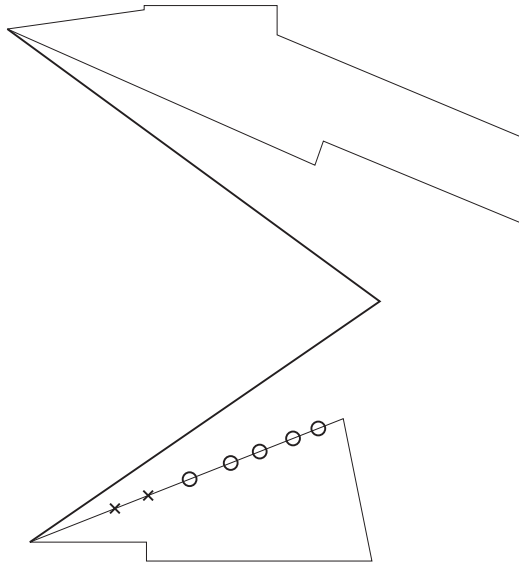


Figure 8.5: Energy deposition points on the lower wedge. Deposition points which lead to transition are denoted with a \circ ; whereas, deposition points that did not lead to transition are denoted with a \times .

flow time, the wedge must be moved relatively quickly. Although the move occurs over many flow times, the effect of the wedge rotation speed on tripping from regular to Mach reflection was explored. One might expect that as the wedge is moved faster, transition would occur earlier; however, it was found that at higher speeds it was possible to obtain higher shock angles while maintaining regular reflection.

The characteristic flow time for the lower wedge is

$$\tau = \frac{w}{U_1}, \quad (8.1)$$

where U_1 is the speed behind the incident shock of the lower wedge. For the current experiments, $w=50.8$ mm, and $U_1=983$ m/s, which gives a characteristic flow time, τ , of $59\ \mu\text{s}$. Figure 8.6 shows the effect of wedge rotation speed on the transition point. Transition from regular reflection to Mach reflection occurs approximately halfway into the dual-solution domain.

Most often when transition from regular reflection to Mach reflection occurs due to tunnel disturbances, no visible disturbance is noticed. However, in a few cases, a significant disturbance just before tripping from regular reflection to Mach reflection is observed. Figure 8.7 shows a small piece of dust, possibly a piece of the diaphragm, traveling down-

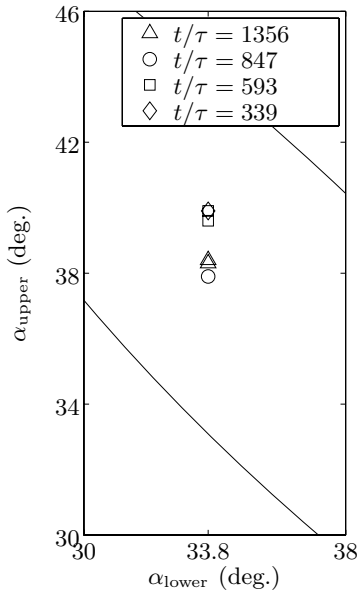


Figure 8.6: Effect of wedge rotation speed on tripping due to tunnel disturbances. As the wedge is rotated faster, higher shock angles are obtained while maintaining regular reflection. The lower curve is the von Neumann condition and the upper curve is the detachment condition. Transition occurs approximately halfway into the dual-solution domain.

stream near the centerline. Because of the speed of the object, it is only seen in one frame. Immediately after this object leaves the field of view, transition to Mach reflection begins.

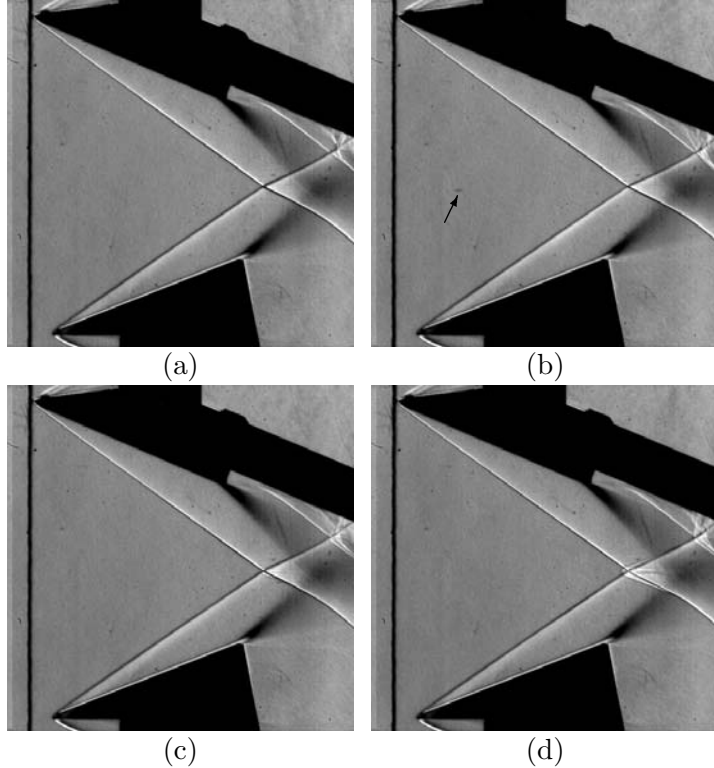


Figure 8.7: Tunnel disturbances, such as dust, are capable of tripping the flow from regular reflection to Mach reflection. Frame (b) shows a small piece of dust near the centerline. After the piece of dust crosses the incident shocks transition to Mach reflection begins. Images taken with a $3\ \mu\text{s}$ exposure and $121\ \mu\text{s}$ between frames. $M = 4$, $\alpha_{\text{lower}} = 33.9^\circ$, $\alpha_{\text{upper}} = 36.4^\circ$

Chapter 9

Experimental Mach Stem Heights

Table 9 gives Mach stem height results for various upper wedge angles from the current experiments.

The results shown in Table 9 are plotted, along with the theoretical calculations of Chapter 3, the previous experimental results of Hornung and Robinson [6], and the current computations discussed in Section 3.5, in Figure 9.1. Very good agreement between the theoretical, computational, and current experimental work is seen. The experimental work of Hornung and Robinson consistently show higher Mach stem heights than the current experiments. The current experimental results show smaller than predicted Mach stem heights at high incident shock angles. The behavior of the Mach stem at high incident shock angles is consistent with the numerical results shown in Figure 3.13. The reason for this is believed to be due to the curvature of the slipline.

Table 9.1: Mach stem heights measured at various upper wedge angles.

α_{upper}	α_{lower}	$\alpha_{\text{equiv.}}$	g/w	s/w
34.7	33.6	34.1	0.395	0.027
35.8	34.4	35.1	0.394	0.047
36.8	33.5	35.1	0.391	0.055
39.6	33.3	36.2	0.383	0.099
39.9	33.7	36.5	0.384	0.106
43.0	33.5	37.6	0.380	0.146
42.8	34.2	37.9	0.381	0.147

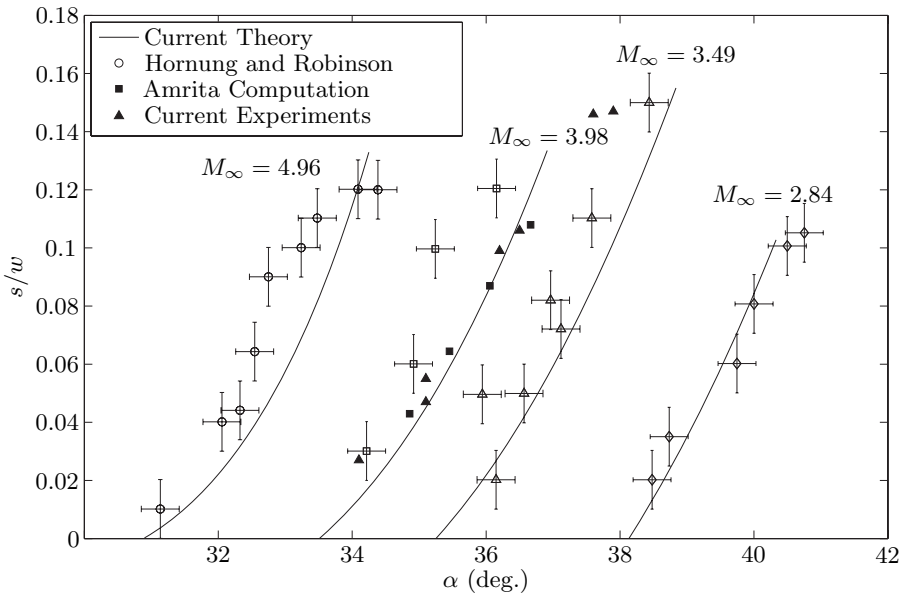


Figure 9.1: Comparison of current experimental Mach stem height results against the theoretical estimates of Chapter 3, measurements by Hornung and Robinson [6], and current computational work done using Amrita. $\gamma = 1.4$ and $g/w \approx 0.4$.

9.1 Experimental Mach Stem Growth

A theoretical growth rate for a Mach stem starting at regular reflection is presented in Sections 3.8 and 3.9. The growth rate can be measured from the new experimental data. With the wedges in the dual-solution domain with regular reflection, energy was deposited on the lower wedge, as discussed in Chapter 8. The deposition of energy causes the flow to trip from regular reflection to Mach reflection. Since the initial flow is inside the dual-solution domain, where the steady-state Mach stem height is finite, the Mach stem quickly grows to this steady-state height.

Figure 9.2 shows the measured Mach stem heights at various times together with the theoretical estimate of Section 3.8. The experiments show a near linear growth rate, until the steady-state height is reached. The initial rapid growth of and subsequent asymptotic approach to the steady state predicated by the theory is not observed. Very good agreement is seen between the steady-state height, as well as with the time required to reach the steady-state height. The video from which the growth rate was measured was recorded with $38\ \mu\text{s}$ between frames.

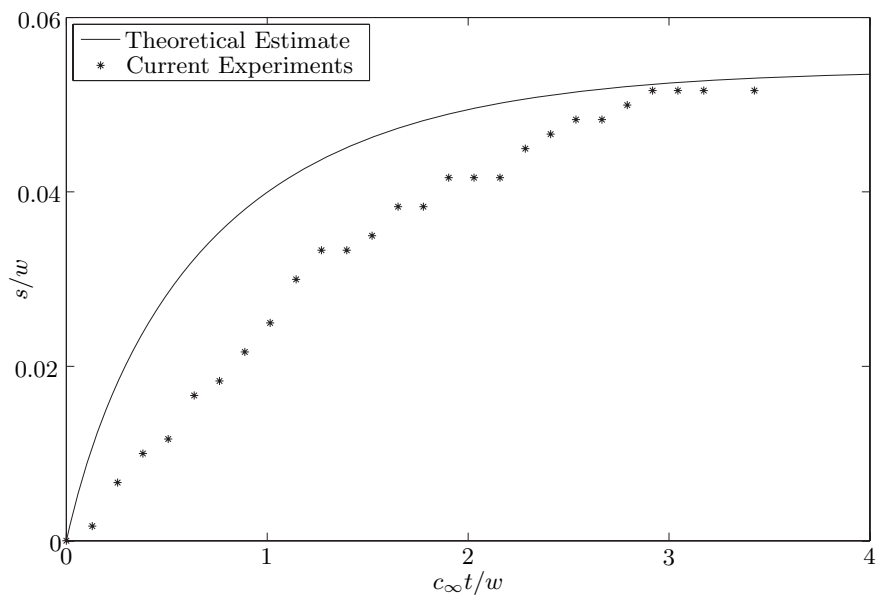


Figure 9.2: Comparison of current experimental Mach stem growth rates with the theoretical estimate of Sections 3.8. $\gamma = 1.4$ and $g/w \approx 0.4$.

Chapter 10

Conclusions and Future Work

The entire shock-reflection domain for steady flow is examined. Conditions defining boundaries between different possible shock reflection solutions are given. Where possible, analytic expressions for these conditions are presented. The detachment condition and the sonic condition are found to be solutions to a fifth-order polynomial and a sixth-order polynomial, respectively. Simple, previously known solutions for the sonic incident shock condition and the Mach wave condition are also given. Nonlinear equations for the von Neumann condition, for the normal reflected shock condition, for the sonic forward-facing reflected shock condition, and for the sonic reflected shock condition are given, all of which can be solved numerically. Many limiting cases, specifically, solutions for high Mach number or for minimum required Mach number, are found. In the case of the sonic incident shock condition, the detachment condition, the von Neumann condition, and the sonic condition, analytic solutions for the infinite Mach number limit are given. Minimum Mach numbers for the von Neumann condition, for the normal reflected shock condition, and for the sonic forward-facing reflected-shock condition are found to have simple analytic solutions.

A new, more accurate, estimate of the steady-state Mach stem height is presented. The theoretical estimate is based on geometric considerations of the flow. In particular, there exists a sonic throat behind the Mach stem as a result of the converging nozzle formed by the slipline generated behind the triple point. The placement of this sonic throat may occur anywhere behind the first characteristic of the expansion fan generated by the aft corner of the wedge. This theoretical estimate is compared with previous theoretical, computational, and experimental work. In addition, new computations of the steady-state Mach stem height are presented. Very good agreement between the current computations and current theoretical estimate is observed. Comparisons with previous computational and

experimental work show that the theory presented here more accurately predicts the Mach stem height than previous models. A limiting assumption of the current theory is that the slipline generated by the triple point is straight until it reaches the sonic throat. Future efforts should allow for a curved slipline, which should produce a more accurate estimate of Mach stem height.

The Mach stem height theory developed here is also generalized by allowing for a moving triple point. Considering the relationship between the speed of the triple point and the quasi-steady Mach stem height, a Mach stem growth rate theory is developed. This theory agrees well with the computational study of Mach stem growth rates presented. The Mach stem growth rate theory is then compared to three-dimensional numerical results. There currently exists no estimate for the spanwise growth rate of the Mach stem. Therefore, the spanwise growth rate is fitted to the numerical data and the Mach stem height, at any given location, is based on a time-shifted value of the two-dimensional Mach stem height. Relatively good agreement between the numerical and the theoretical calculations of the three-dimensional Mach stem heights is observed. Because of the need for a finite disturbance to cause the transition to Mach reflection, the initial Mach stem shape is not consistent with the theoretical estimates, but this difference diminishes with time.

Numerical computations of the effects of water vapor disturbances are presented. These disturbances are modeled as high-density regions of gas. These dense regions of gas are placed upstream of the incident shock and allowed to convect downstream. Because of the additional momentum associated with it, this region of gas will, if properly placed, impact the wedge. There will be both a reflection of the bow shock of the dense region and an impact shock. The numerical investigation shows that it is the impact shock that is pivotal in determining whether or not transition from regular reflection to Mach reflection will occur. In the two-dimensional calculations, where the dense region of gas is essentially an infinitely long cylinder, only one small region of dense gas is required to cause transition. In three-dimensional studies, where these dense regions are spherical, it is shown that a large number of these dense regions are required to cause transition.

Because of the complexities associated with particles impacting the wedge, and for experimental simplicity, it is possible to consider the impact of the dense gas on the wedge as a form of energy deposition. A theoretical estimate of the minimum energy required to cause transition from regular reflection to Mach reflection is presented. This limit is

calculated based on the condition that the blast wave from energy deposition must be sufficiently strong to reach, and therefore influence, the transition point. An exact solution for strong shocks and an Euler computation for weak shocks are combined to calculate the minimum energy required for the energy deposition to influence the reflection point. This estimate of minimum required energy is compared with numerical results and very good agreement is seen when the energy is deposited close to the reflection point.

Experimental results using an asymmetric wedge configuration, for experimental simplicity, are presented. However, the theory developed in this thesis is based on symmetric wedges. Therefore, calculations of the dual-solution domain for asymmetric wedges is presented. In addition, an approximate method to compare asymmetric results with symmetric results is given.

The Ludwieg tube facility at the California Institute of Technology was retrofitted with a Mach 4.0 nozzle. This Mach number is large enough to provide a sufficiently large dual-solution domain, while being small enough not to require preheating of the gas. The test time of the facility is 100 ms, which requires high-speed cinematography and a fast motor to rotate the wedge.

The first experiments conducted on shock reflection in the Ludwieg tube verified the hysteresis phenomenon. The ability to enter the dual-solution domain with regular reflection is a qualitative measure of the quietness of the facility. Hysteresis was successfully demonstrated in the Ludwieg tube facility. The experiments show that in the Ludwieg tube facility, regular reflection could be maintained until approximately halfway between the von Neumann condition and the detachment condition.

Energy deposition studies were performed using a 200 mJ Nd:YAG laser. The disturbance caused by the blast wave from the laser is seen to affect the incident shock, and in some cases, causes transition from regular reflection to Mach reflection. The location on the wedge where the energy is deposited is important in determining whether or not transition occurs. This finding is consistent with the numerical work presented in this thesis, which shows that the energy required to cause transition depends on the location where the energy is deposited. Future studies should measure the amount of energy deposited on the wedge, so that an accurate minimum energy for transition can be calculated as a function of deposition location. The best way to measure the energy deposited is to visualize the blast wave caused by the energy deposition. Attempts to do this in the current experiments were

unsuccessful, because the densities required to visualize the blast wave were so high that the blast wave was effectively a Mach wave, and therefore an energy could not be estimated.

Experiments were also performed to measure Mach stem height and its growth rate. These results are compared with the theoretical estimates presented in this thesis. Excellent agreement between the steady-state Mach stem height and the theoretical estimate is seen. Comparisons of Mach stem growth rate with theoretical estimates show significant differences, but do show good agreement in the time required to reach the steady-state height. The reasons for these differences are unknown, and may be attributable to three-dimensional effects.

Appendix A

Mach Reflection Domain

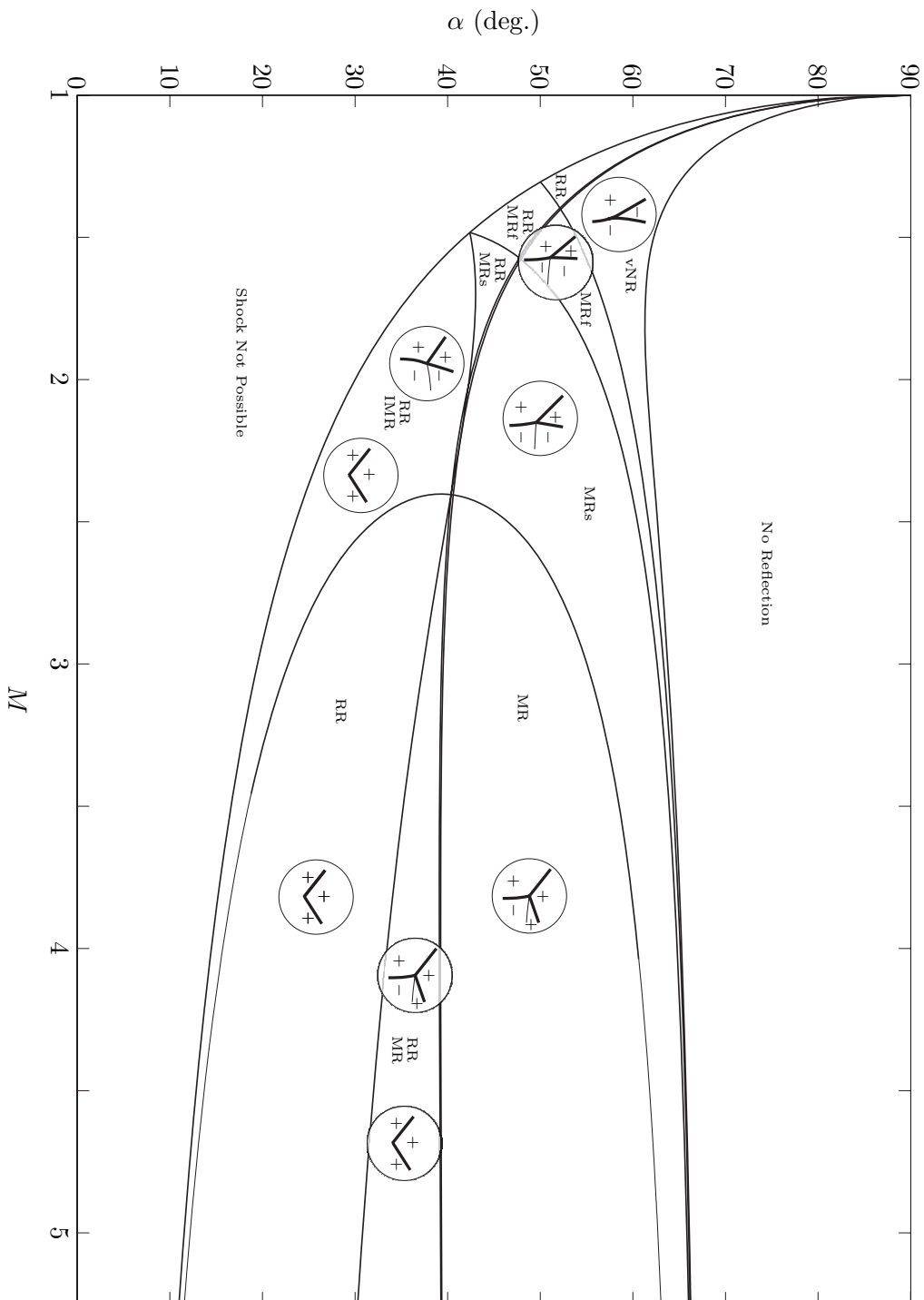


Figure A.1: Complete shock reflection domain, for $\gamma = 1.4$, note that in the small region between the sonic and detachment condition RR is replaced by RRs. The symbol + refers to supersonic conditions and the symbol – refers to subsonic conditions.

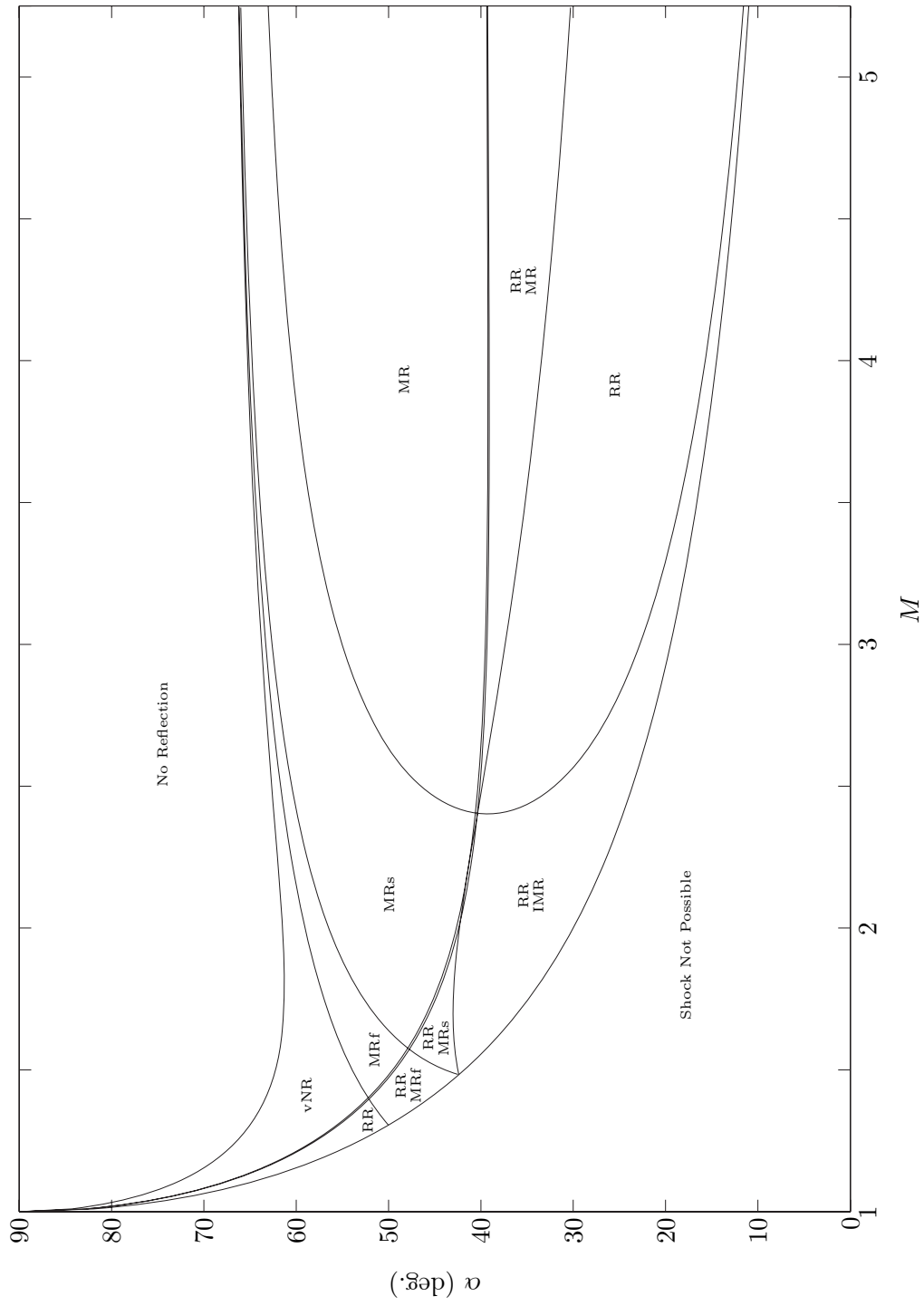


Figure A.2: Complete shock reflection domain, for $\gamma = 1.4$, note that in the small region between the sonic and detachment condition RR is replaced by RRs.

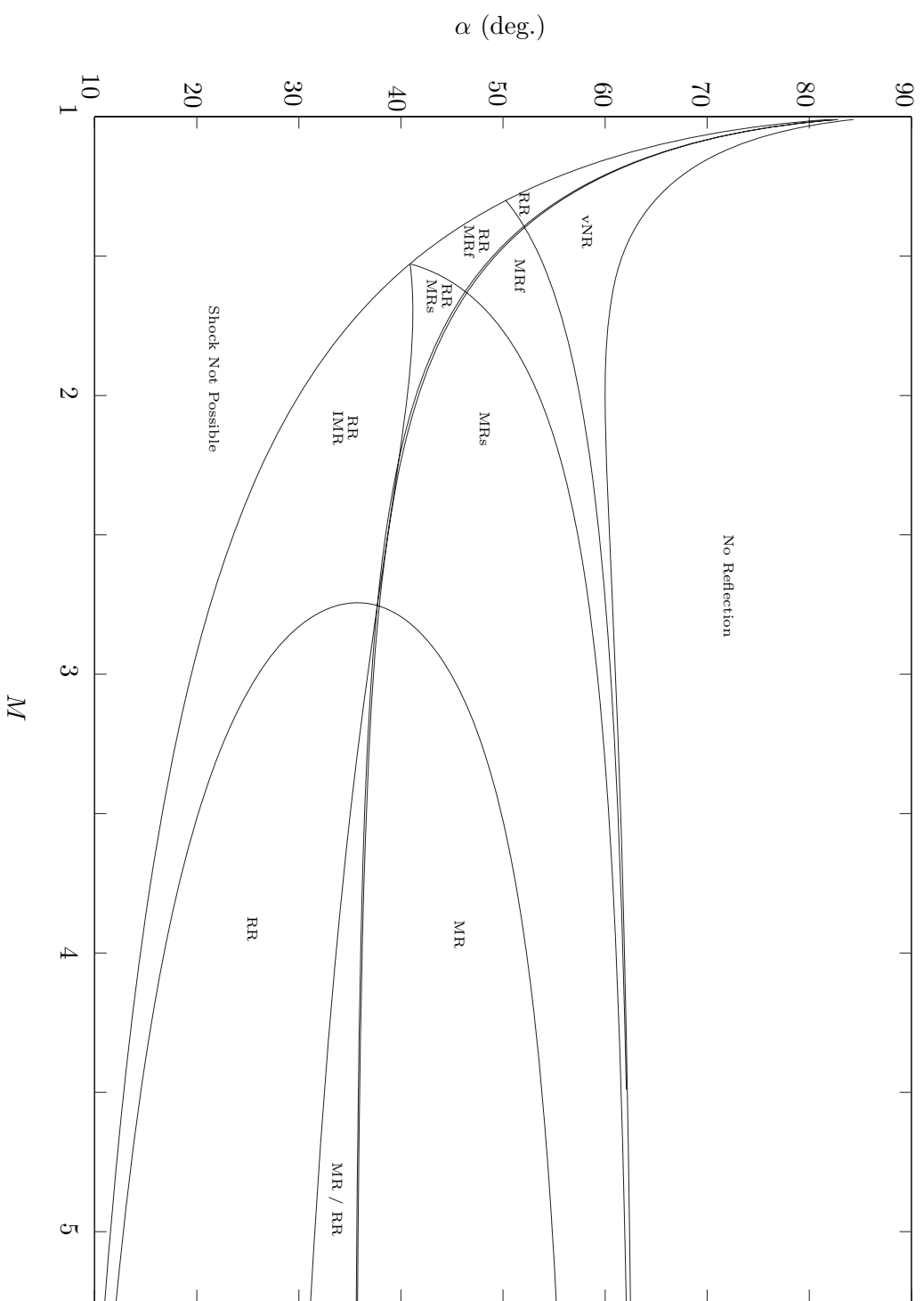


Figure A.3: Complete shock reflection domain, for $\gamma = 5/3$, note that in the small region between the sonic and detachment condition RR is replaced by RRs.

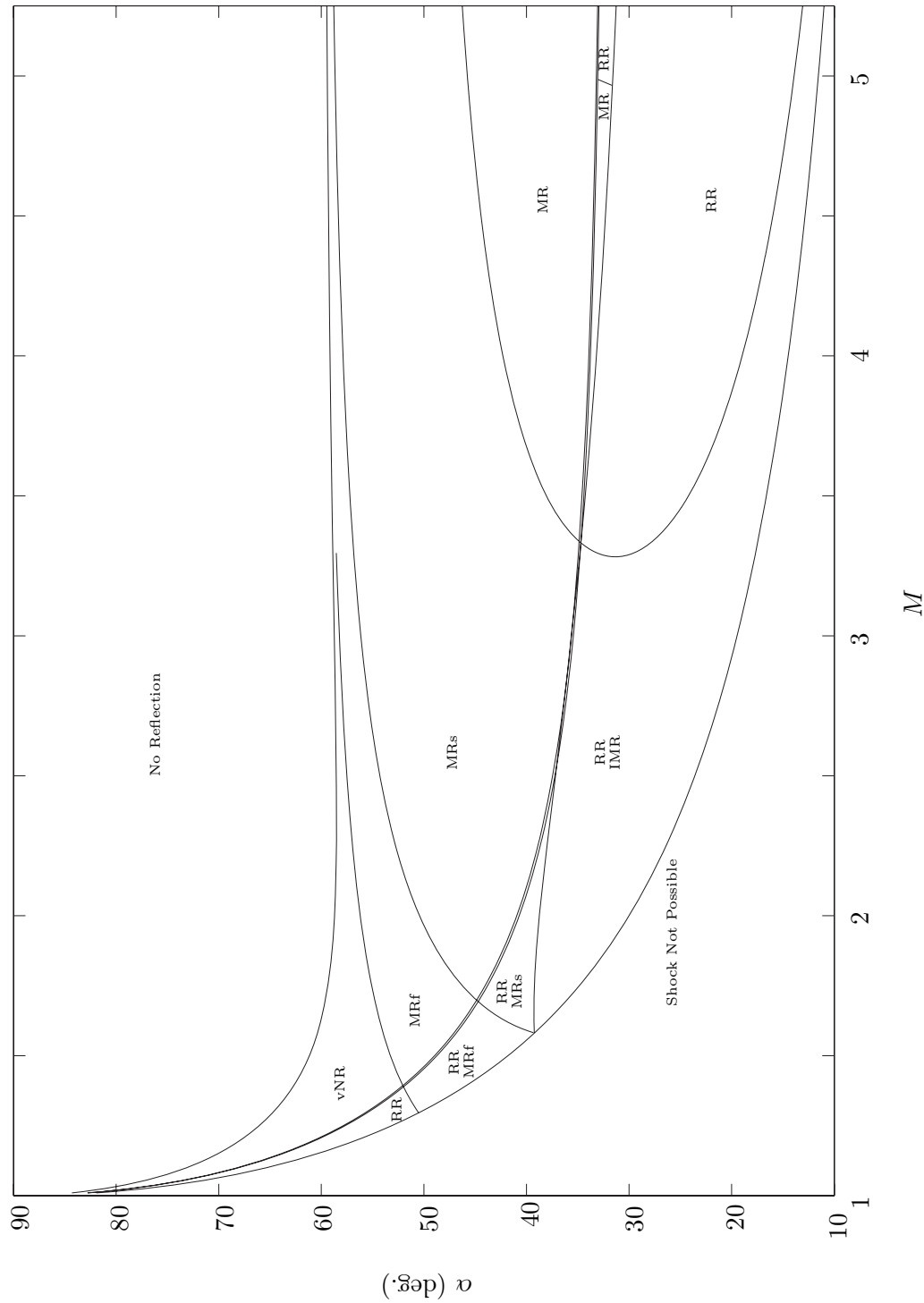


Figure A.4: Complete shock reflection domain, for $\gamma = 2$, note that in the small region between the sonic and detachment condition RR is replaced by RR_s.

Appendix B

Alternative Plots

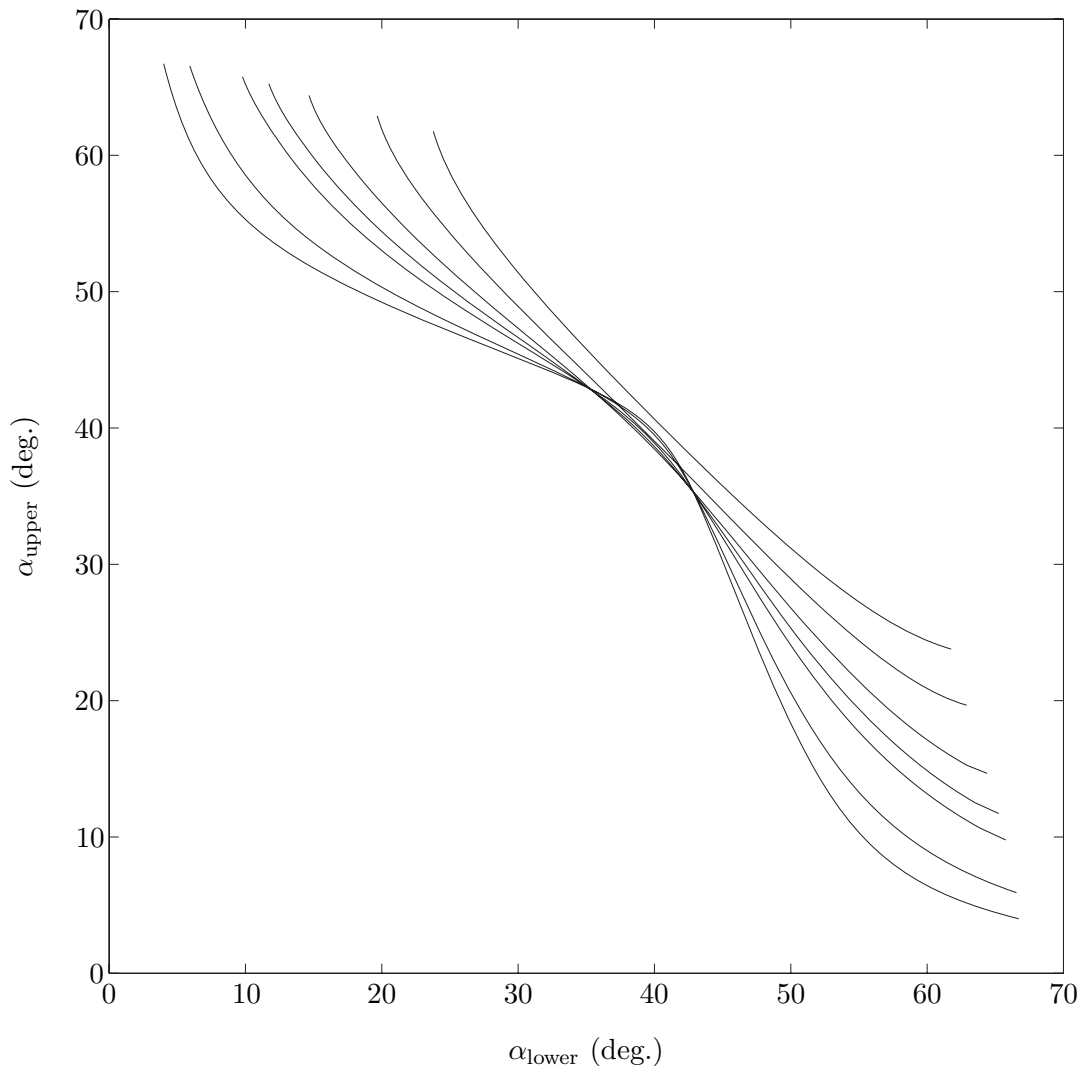


Figure B.1: Detachment condition for asymmetric wedges. Curves are for Mach number 2.5, 3, 4, 5, 6, 10, and 15. The lower curves correspond to higher Mach number.

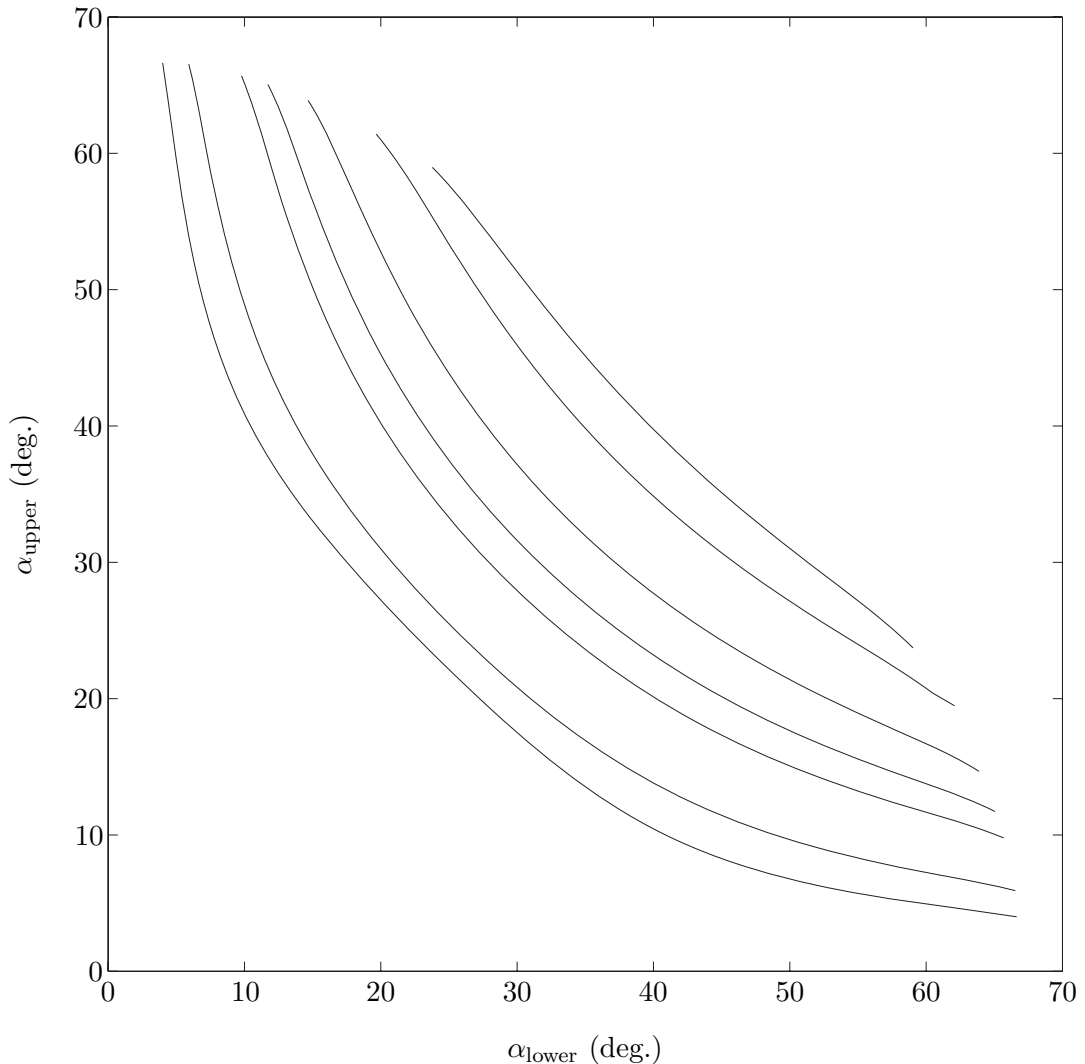


Figure B.2: Von Neumann condition for asymmetric wedges. Curves are for Mach number 2.5, 3, 4, 5, 6, 10, and 15. The lower curves correspond to higher Mach number.

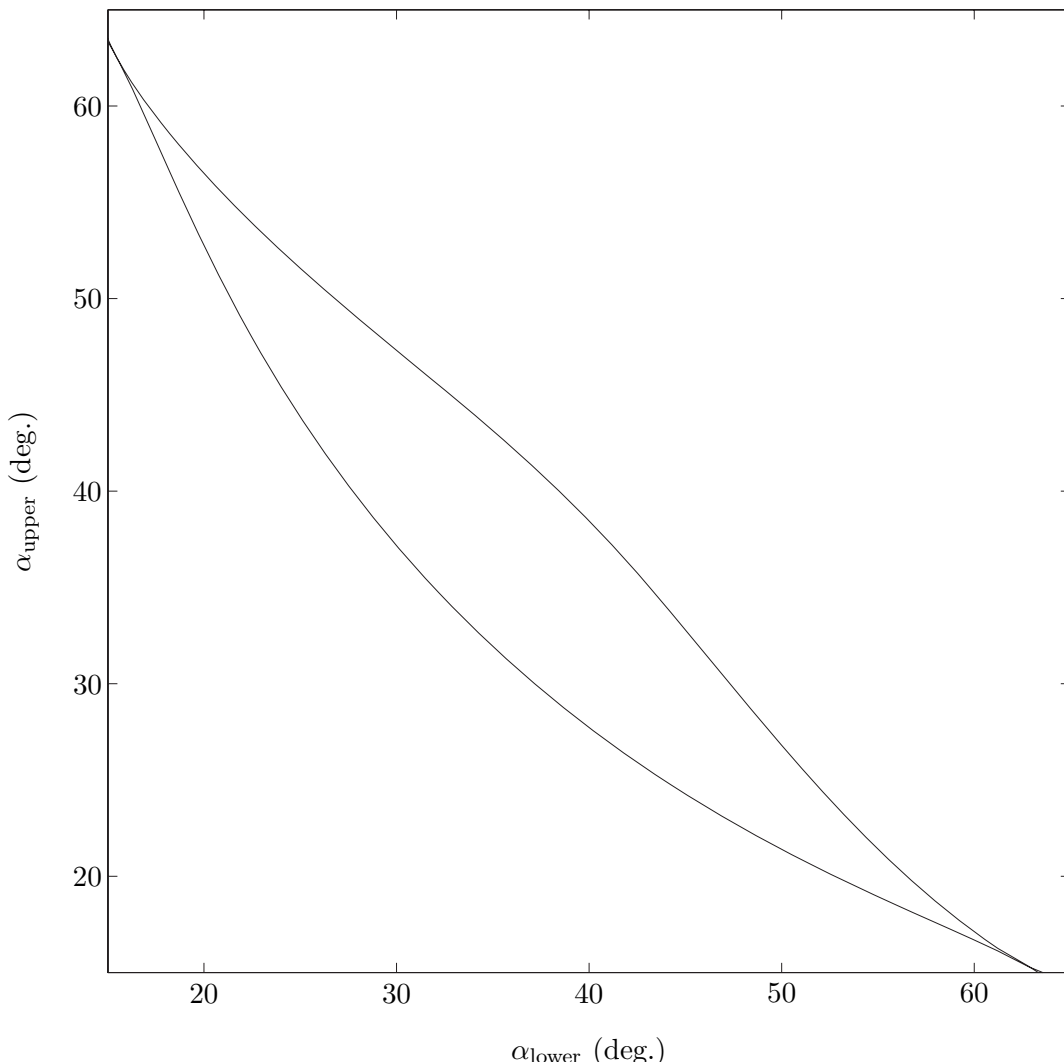


Figure B.3: Dual solution domain for $M=4$ for asymmetric wedges. The lower curve is the von Neumann condition, the upper curve is the detachment condition.

Appendix C

Mach 4 Nozzle Design

Table C.1: Mach 4 nozzle contour (in inches) by J. J. Korte.

Distance	Radius	Distance	Radius	Distance	Radius
-5.2395	6.0000	-3.2977	2.9220	-1.2765	1.9447
-5.2125	5.8616	-3.1913	2.8414	-1.1701	1.9198
-5.1061	5.4924	-3.0849	2.7648	-1.0638	1.8972
-4.9997	5.1968	-2.9785	2.6921	-0.9574	1.8768
-4.8933	4.9454	-2.8722	2.6230	-0.8510	1.8587
-4.7869	4.7242	-2.7658	2.5575	-0.7446	1.8427
-4.6806	4.5259	-2.6594	2.4952	-0.6383	1.8289
-4.5742	4.3454	-2.5530	2.4362	-0.5319	1.8172
-4.4678	4.1796	-2.4467	2.3803	-0.4255	1.8077
-4.3614	4.0262	-2.3403	2.3274	-0.3191	1.8003
-4.2551	3.8833	-2.2339	2.2773	-0.2128	1.7951
-4.1487	3.7498	-2.1275	2.2301	-0.1064	1.7919
-4.0423	3.6245	-2.0212	2.1855	0.0000	1.7909
-3.9359	3.5065	-1.9148	2.1436	0.0392	1.7910
-3.8296	3.3953	-1.8084	2.1044	0.0791	1.7914
-3.7232	3.2901	-1.7020	2.0676	0.1196	1.7922
-3.6168	3.1906	-1.5956	2.0333	0.1608	1.7932
-3.5104	3.0963	-1.4893	2.0014	0.2027	1.7946
-3.4041	3.0069	-1.3829	1.9719	0.2451	1.7963

Continued on Next Page...

Table C.1 – Continued from Previous Page

Distance	Radius	Distance	Radius	Distance	Radius
0.2882	1.7983	2.1594	2.0292	4.2953	2.3951
0.3319	1.8006	2.2672	2.0466	4.3816	2.4103
0.3764	1.8033	2.3799	2.0651	4.4688	2.4257
0.4215	1.8062	2.4979	2.0846	4.5569	2.4412
0.4673	1.8095	2.6215	2.1052	4.6458	2.4569
0.5139	1.8131	2.6477	2.1096	4.7356	2.4727
0.5614	1.8170	2.6859	2.1160	4.8260	2.4886
0.6099	1.8212	2.7305	2.1236	4.9173	2.5047
0.6593	1.8257	2.7797	2.1319	5.0092	2.5209
0.7099	1.8306	2.8326	2.1409	5.1018	2.5372
0.7617	1.8358	2.8886	2.1504	5.1950	2.5537
0.8148	1.8413	2.9474	2.1604	5.2888	2.5702
0.8694	1.8472	3.0086	2.1709	5.3832	2.5868
0.9255	1.8535	3.0720	2.1818	5.4781	2.6036
0.9833	1.8603	3.1374	2.1930	5.5735	2.6204
1.0429	1.8674	3.2047	2.2046	5.6694	2.6373
1.1044	1.8750	3.2738	2.2166	6.4149	2.7688
1.1681	1.8831	3.3444	2.2288	6.5255	2.7883
1.2341	1.8917	3.4166	2.2413	6.6358	2.8077
1.3024	1.9008	3.4903	2.2541	6.7459	2.8271
1.3734	1.9105	3.5654	2.2672	6.8557	2.8465
1.4471	1.9208	3.6418	2.2805	6.9654	2.8658
1.5237	1.9317	3.7195	2.2941	7.0749	2.8851
1.6035	1.9433	3.7984	2.3079	7.1842	2.9044
1.6866	1.9556	3.8785	2.3220	7.2935	2.9237
1.7732	1.9687	3.9598	2.3362	7.4027	2.9429
1.8636	1.9825	4.0421	2.3506	7.5120	2.9622
1.9579	1.9972	4.1255	2.3653	7.6213	2.9814
2.0564	2.0127	4.2099	2.3801	7.7306	3.0007

Continued on Next Page...

Table C.1 – Continued from Previous Page

Distance	Radius	Distance	Radius	Distance	Radius
7.8401	3.0200	11.2621	3.6102	15.6508	4.2852
7.9498	3.0393	11.3943	3.6321	15.8229	4.3092
8.0597	3.0586	11.5278	3.6542	15.9964	4.3332
8.1699	3.0780	11.6626	3.6764	16.1711	4.3571
8.2804	3.0974	11.7986	3.6988	16.3471	4.3810
8.3912	3.1168	11.9360	3.7212	16.5243	4.4048
8.5024	3.1363	12.0747	3.7438	16.7028	4.4286
8.6141	3.1559	12.2148	3.7664	16.8825	4.4524
8.7262	3.1755	12.3562	3.7892	17.0634	4.4761
8.8389	3.1952	12.4990	3.8121	17.2454	4.4997
8.9521	3.2150	12.6431	3.8351	17.4286	4.5232
9.0660	3.2349	12.7887	3.8582	17.6130	4.5467
9.1805	3.2548	12.9357	3.8814	17.7984	4.5700
9.2957	3.2749	13.0841	3.9047	17.9849	4.5933
9.4116	3.2950	13.2339	3.9280	18.1724	4.6165
9.5283	3.3152	13.3851	3.9515	18.3610	4.6396
9.6458	3.3356	13.5378	3.9750	18.5506	4.6625
9.7641	3.3560	13.6919	3.9986	18.7411	4.6853
9.8833	3.3765	13.8474	4.0223	18.9327	4.7080
10.0035	3.3972	14.0043	4.0460	19.1252	4.7306
10.1246	3.4179	14.1627	4.0698	19.3186	4.7531
10.2466	3.4388	14.3224	4.0936	19.5129	4.7754
10.3697	3.4598	14.4836	4.1175	19.7081	4.7975
10.4938	3.4809	14.6462	4.1414	19.9097	4.8202
10.6190	3.5022	14.8102	4.1653	19.9609	4.8259
10.7453	3.5235	14.9756	4.1893	20.0120	4.8315
10.8728	3.5450	15.1424	4.2133	20.0632	4.8372
11.0013	3.5666	15.3105	4.2373	20.1143	4.8428
11.1311	3.5883	15.4800	4.2612	20.1655	4.8485

Continued on Next Page...

Table C.1 – Continued from Previous Page

Distance	Radius	Distance	Radius	Distance	Radius
20.2166	4.8541	21.7001	5.0097	23.1835	5.1534
20.2678	4.8597	21.7512	5.0149	23.2346	5.1581
20.3189	4.8652	21.8024	5.0200	23.2858	5.1628
20.3701	4.8708	21.8535	5.0251	23.3370	5.1675
20.4212	4.8763	21.9047	5.0303	23.3881	5.1722
20.4724	4.8819	21.9558	5.0354	23.4393	5.1769
20.5235	4.8874	22.0070	5.0404	23.4904	5.1816
20.5747	4.8928	22.0581	5.0455	23.5416	5.1863
20.6258	4.8983	22.1093	5.0505	23.5927	5.1909
20.6770	4.9038	22.1604	5.0556	23.6439	5.1955
20.7282	4.9092	22.2116	5.0606	23.6950	5.2001
20.7793	4.9146	22.2627	5.0656	23.7462	5.2047
20.8305	4.9200	22.3139	5.0706	23.7973	5.2093
20.8816	4.9254	22.3650	5.0756	23.8485	5.2139
20.9328	4.9308	22.4162	5.0806	23.8996	5.2184
20.9839	4.9362	22.4674	5.0855	23.9508	5.2230
21.0351	4.9415	22.5185	5.0904	24.0019	5.2275
21.0862	4.9469	22.5697	5.0954	24.0531	5.2320
21.1374	4.9522	22.6208	5.1003	24.1042	5.2365
21.1885	4.9575	22.6720	5.1052	24.1554	5.2410
21.2397	4.9628	22.7231	5.1101	24.2066	5.2455
21.2908	4.9680	22.7743	5.1149	24.2577	5.2499
21.3420	4.9733	22.8254	5.1198	24.3089	5.2544
21.3931	4.9786	22.8766	5.1246	24.3600	5.2588
21.4443	4.9838	22.9277	5.1295	24.4112	5.2632
21.4954	4.9890	22.9789	5.1343	24.4623	5.2676
21.5466	4.9942	23.0300	5.1391	24.5135	5.2720
21.5978	4.9994	23.0812	5.1438	24.5646	5.2764
21.6489	5.0046	23.1323	5.1486	24.6158	5.2807

Continued on Next Page...

Table C.1 – Continued from Previous Page

Distance	Radius	Distance	Radius	Distance	Radius
24.6669	5.2851	26.6107	5.4396	28.7009	5.5845
24.7181	5.2894	26.6828	5.4450	28.7730	5.5892
24.7692	5.2937	26.7549	5.4503	28.8451	5.5938
24.8204	5.2980	26.8269	5.4556	28.9172	5.5984
24.8715	5.3023	26.8990	5.4609	28.9892	5.6029
24.9227	5.3066	26.9711	5.4661	29.0613	5.6075
24.9738	5.3108	27.0432	5.4713	29.1334	5.6120
25.0250	5.3151	27.1152	5.4765	29.2055	5.6165
25.0971	5.3210	27.1873	5.4817	29.2775	5.6210
25.1692	5.3270	27.2594	5.4869	29.3496	5.6254
25.2412	5.3328	27.3315	5.4920	29.4217	5.6298
25.3133	5.3387	27.4035	5.4971	29.4938	5.6342
25.3854	5.3446	27.4756	5.5021	29.5659	5.6386
25.4575	5.3504	27.5477	5.5072	29.6379	5.6430
25.5295	5.3562	27.6198	5.5122	29.7100	5.6473
25.6016	5.3619	27.6919	5.5172	29.7821	5.6516
25.6737	5.3676	27.7639	5.5222	29.8542	5.6559
25.7458	5.3733	27.8360	5.5271	29.9262	5.6602
25.8178	5.3790	27.9081	5.5320	29.9983	5.6644
25.8899	5.3847	27.9802	5.5369	30.0704	5.6687
25.9620	5.3903	28.0522	5.5418	30.1425	5.6729
26.0341	5.3959	28.1243	5.5466	30.2145	5.6771
26.1062	5.4014	28.1964	5.5515	30.2866	5.6812
26.1782	5.4070	28.2685	5.5563	30.3587	5.6854
26.2503	5.4125	28.3405	5.5610	30.4308	5.6895
26.3224	5.4180	28.4126	5.5658	30.5029	5.6936
26.3945	5.4234	28.4847	5.5705	30.5749	5.6977
26.4665	5.4289	28.5568	5.5752	30.6470	5.7017
26.5386	5.4343	28.6289	5.5799	30.7191	5.7058

Continued on Next Page...

Table C.1 – Continued from Previous Page

Distance	Radius	Distance	Radius	Distance	Radius
30.7912	5.7098	32.8814	5.8173	34.9716	5.9085
30.8632	5.7138	32.9535	5.8207	35.0437	5.9113
30.9353	5.7177	33.0256	5.8241	35.1158	5.9142
31.0074	5.7217	33.0976	5.8274	35.1879	5.9170
31.0795	5.7256	33.1697	5.8308	35.2599	5.9198
31.1516	5.7295	33.2418	5.8341	35.3320	5.9226
31.2236	5.7334	33.3139	5.8374	35.4041	5.9254
31.2957	5.7373	33.3859	5.8407	35.4762	5.9282
31.3678	5.7411	33.4580	5.8440	35.5483	5.9309
31.4399	5.7450	33.5301	5.8473	35.6203	5.9336
31.5119	5.7488	33.6022	5.8505	35.6924	5.9364
31.5840	5.7526	33.6742	5.8537	35.7645	5.9391
31.6561	5.7563	33.7463	5.8569	35.8366	5.9417
31.7282	5.7601	33.8184	5.8601	35.9086	5.9444
31.8002	5.7638	33.8905	5.8633	35.9807	5.9470
31.8723	5.7675	33.9626	5.8664	36.0528	5.9497
31.9444	5.7712	34.0346	5.8695	36.1249	5.9523
32.0165	5.7748	34.1067	5.8726	36.1969	5.9549
32.0886	5.7785	34.1788	5.8757	36.2690	5.9574
32.1606	5.7821	34.2509	5.8788	36.3411	5.9600
32.2327	5.7857	34.3229	5.8818	36.4132	5.9625
32.3048	5.7893	34.3950	5.8849	36.4853	5.9650
32.3769	5.7929	34.4671	5.8879	36.5573	5.9676
32.4489	5.7964	34.5392	5.8909	36.6294	5.9700
32.5210	5.7999	34.6112	5.8938	36.7015	5.9725
32.5931	5.8034	34.6833	5.8968	36.7736	5.9750
32.6652	5.8069	34.7554	5.8997	36.8456	5.9774
32.7372	5.8104	34.8275	5.9027	36.9177	5.9798
32.8093	5.8138	34.8996	5.9056	36.9898	5.9823

Continued on Next Page...

Table C.1 – Continued from Previous Page

Distance	Radius	Distance	Radius	Distance	Radius
37.0619	5.9846	39.1521	6.0472	41.2423	6.0973
37.1339	5.9870	39.2242	6.0491	41.3144	6.0989
37.2060	5.9894	39.2963	6.0510	41.3865	6.1004
37.2781	5.9917	39.3683	6.0529	41.4586	6.1019
37.3502	5.9940	39.4404	6.0548	41.5306	6.1034
37.4223	5.9964	39.5125	6.0567	41.6027	6.1048
37.4943	5.9987	39.5846	6.0585	41.6748	6.1063
37.5664	6.0009	39.6566	6.0603	41.7469	6.1077
37.6385	6.0032	39.7287	6.0622	41.8190	6.1092
37.7106	6.0054	39.8008	6.0640	41.8910	6.1106
37.7826	6.0077	39.8729	6.0658	41.9631	6.1120
37.8547	6.0099	39.9450	6.0676	42.0352	6.1134
37.9268	6.0121	40.0170	6.0693	42.1073	6.1148
37.9989	6.0143	40.0891	6.0711	42.1793	6.1162
38.0709	6.0164	40.1612	6.0728	42.2514	6.1175
38.1430	6.0186	40.2333	6.0746	42.3235	6.1189
38.2151	6.0207	40.3053	6.0763	42.3956	6.1202
38.2872	6.0229	40.3774	6.0780	42.4676	6.1215
38.3593	6.0250	40.4495	6.0797	42.5397	6.1229
38.4313	6.0271	40.5216	6.0813	42.6118	6.1242
38.5034	6.0291	40.5936	6.0830	42.6839	6.1254
38.5755	6.0312	40.6657	6.0846	42.7560	6.1267
38.6476	6.0332	40.7378	6.0863	42.8280	6.1280
38.7196	6.0353	40.8099	6.0879	42.9001	6.1292
38.7917	6.0373	40.8820	6.0895	42.9722	6.1305
38.8638	6.0393	40.9540	6.0911	43.0443	6.1317
38.9359	6.0413	41.0261	6.0927	43.1163	6.1329
39.0080	6.0433	41.0982	6.0942	43.1884	6.1341
39.0800	6.0452	41.1703	6.0958	43.2605	6.1353

Continued on Next Page...

Table C.1 – Continued from Previous Page

Distance	Radius	Distance	Radius	Distance	Radius
43.3326	6.1365	45.4228	6.1660	47.5130	6.1871
43.4047	6.1377	45.4949	6.1668	47.5851	6.1877
43.4767	6.1388	45.5670	6.1677	47.6572	6.1883
43.5488	6.1400	45.6390	6.1685	47.7293	6.1889
43.6209	6.1411	45.7111	6.1694	47.8013	6.1894
43.6930	6.1422	45.7832	6.1702	47.8734	6.1900
43.7650	6.1433	45.8553	6.1710	47.9455	6.1906
43.8371	6.1444	45.9273	6.1718	48.0176	6.1911
43.9092	6.1455	45.9994	6.1726	48.0897	6.1916
43.9813	6.1466	46.0715	6.1734	48.1617	6.1922
44.0533	6.1477	46.1436	6.1741	48.2338	6.1927
44.1254	6.1487	46.2157	6.1749	48.3059	6.1932
44.1975	6.1498	46.2877	6.1757	48.3780	6.1937
44.2696	6.1508	46.3598	6.1764	48.4500	6.1942
44.3417	6.1519	46.4319	6.1771	48.4811	6.1945
44.4137	6.1529	46.5040	6.1779		
44.4858	6.1539	46.5760	6.1786		
44.5579	6.1549	46.6481	6.1793		
44.6300	6.1558	46.7202	6.1800		
44.7020	6.1568	46.7923	6.1807		
44.7741	6.1578	46.8644	6.1814		
44.8462	6.1587	46.9364	6.1820		
44.9183	6.1597	47.0085	6.1827		
44.9903	6.1606	47.0806	6.1834		
45.0624	6.1615	47.1527	6.1840		
45.1345	6.1624	47.2247	6.1846		
45.2066	6.1633	47.2968	6.1853		
45.2787	6.1642	47.3689	6.1859		

Table C.2: Primary components of the Mach 4 nozzle.

Part Number	Part Name	Quantity
1	Mach 4 Nozzle	1
2	Expansion Tube	1
4	Expansion Tube Female Flange	1
5	Upstream Diaphragm Housing	1
6	Test Section	1
9	Window Housing	2
10	Window Clamp	2
11	Test Section Flange	1
12	Window Blank	2
13	Feedthrough Plug	8
14	Injector Flange	1
15	Injector Block	1

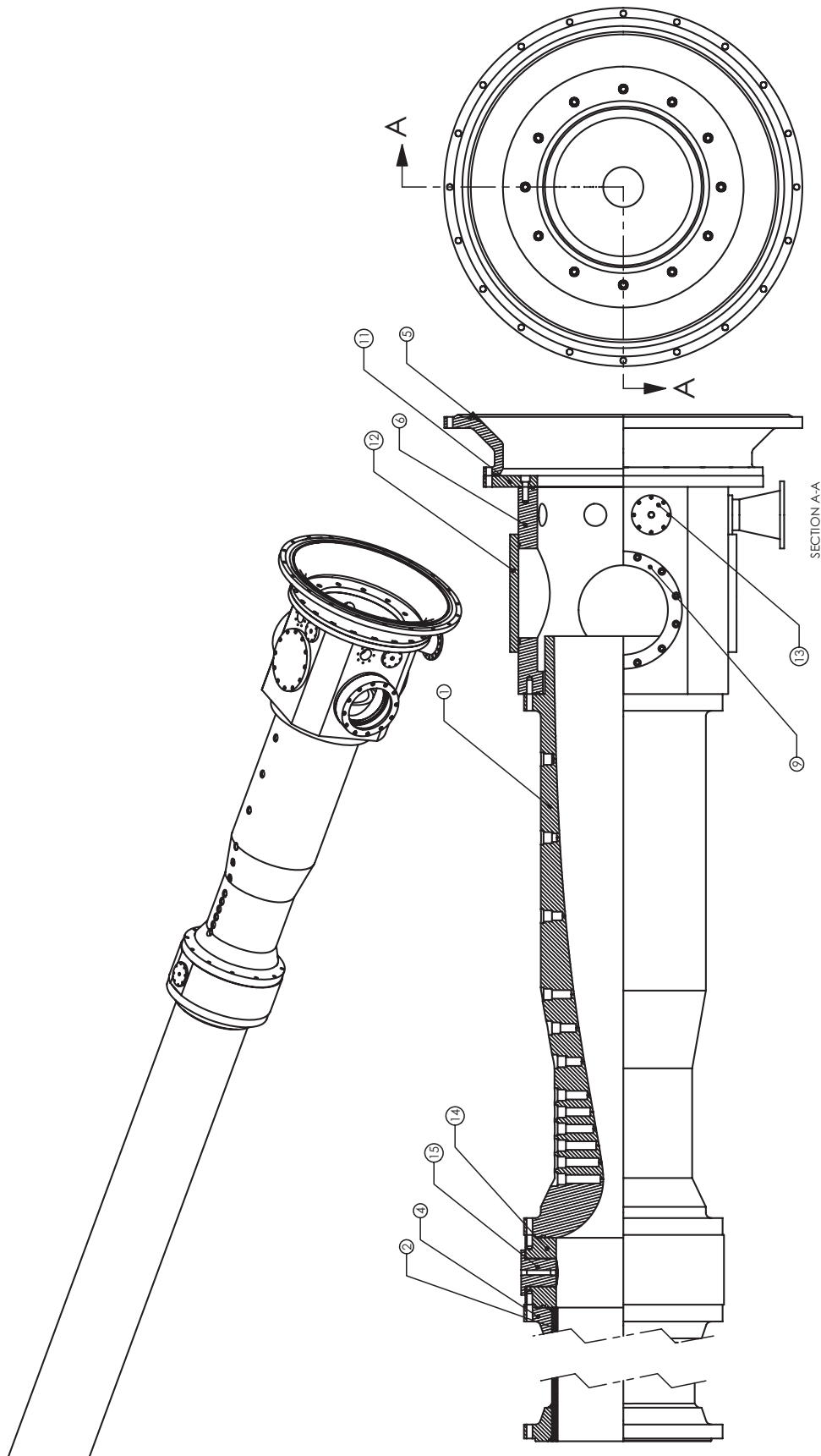


Figure C.1: Mach 4.0 nozzle assembly drawing of the various primary components and their relationships to each other.

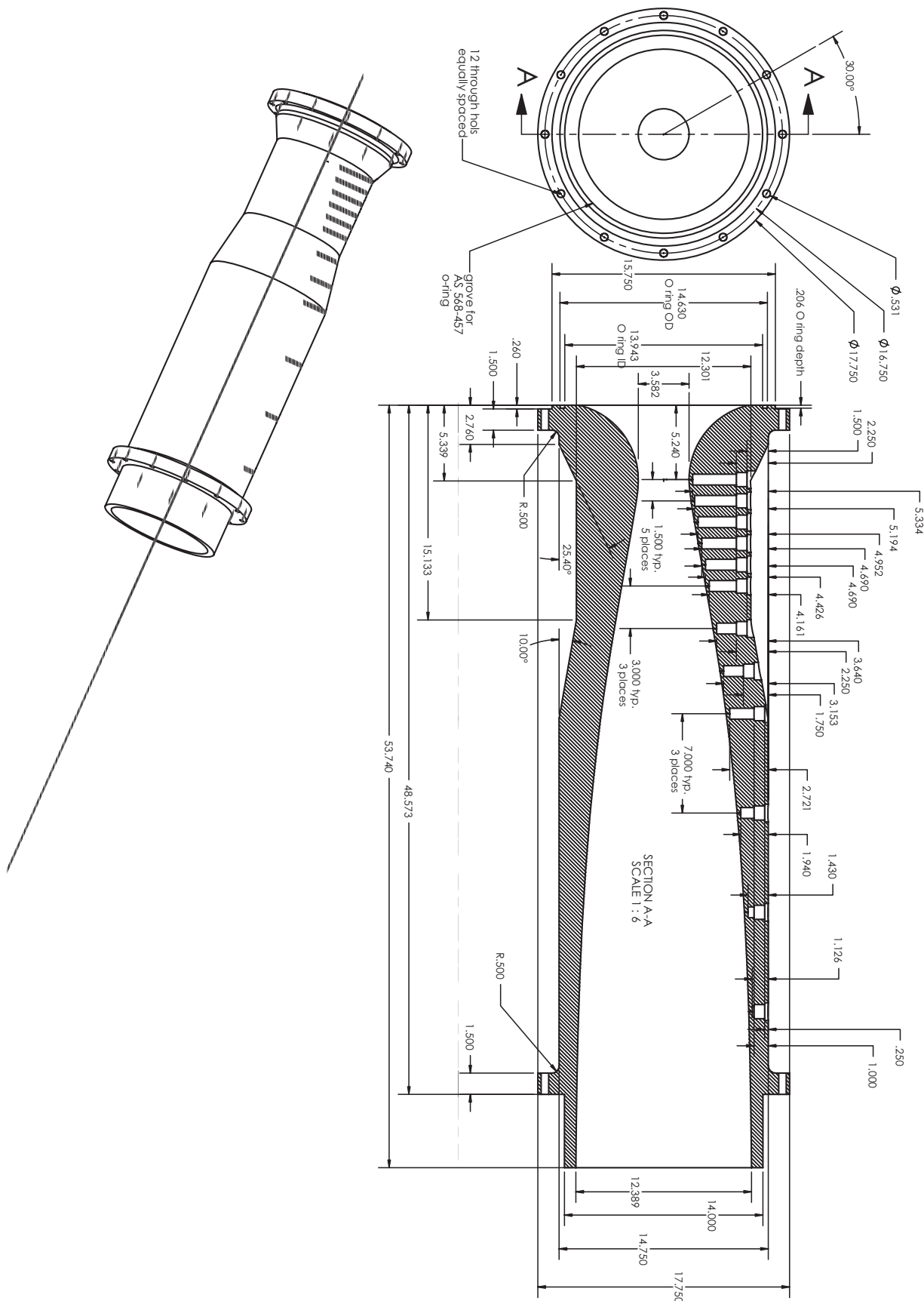


Figure C.2: Mach 4 nozzle (part 1) drawing.

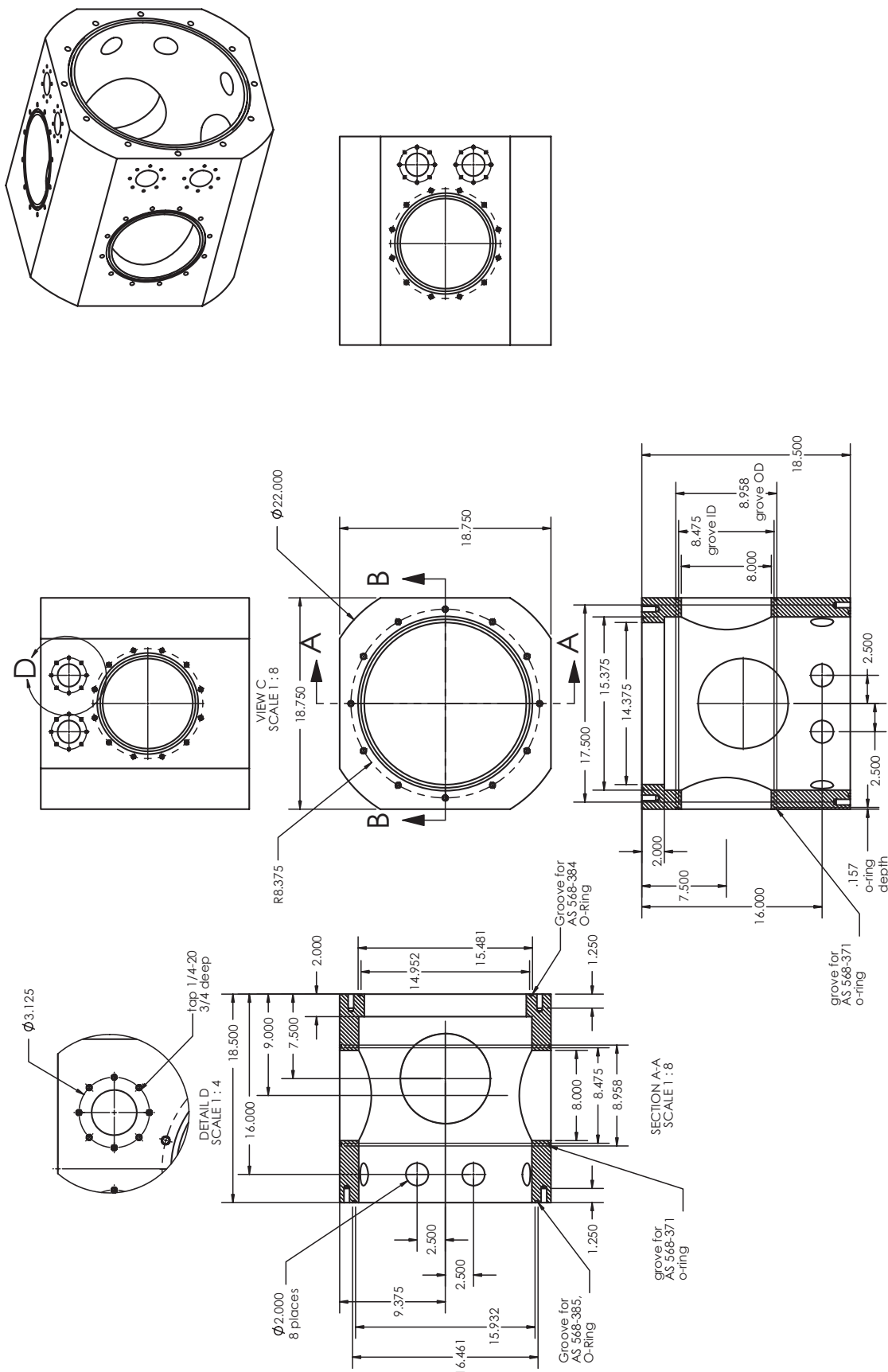


Figure C.3: Test section (part 6) drawing.

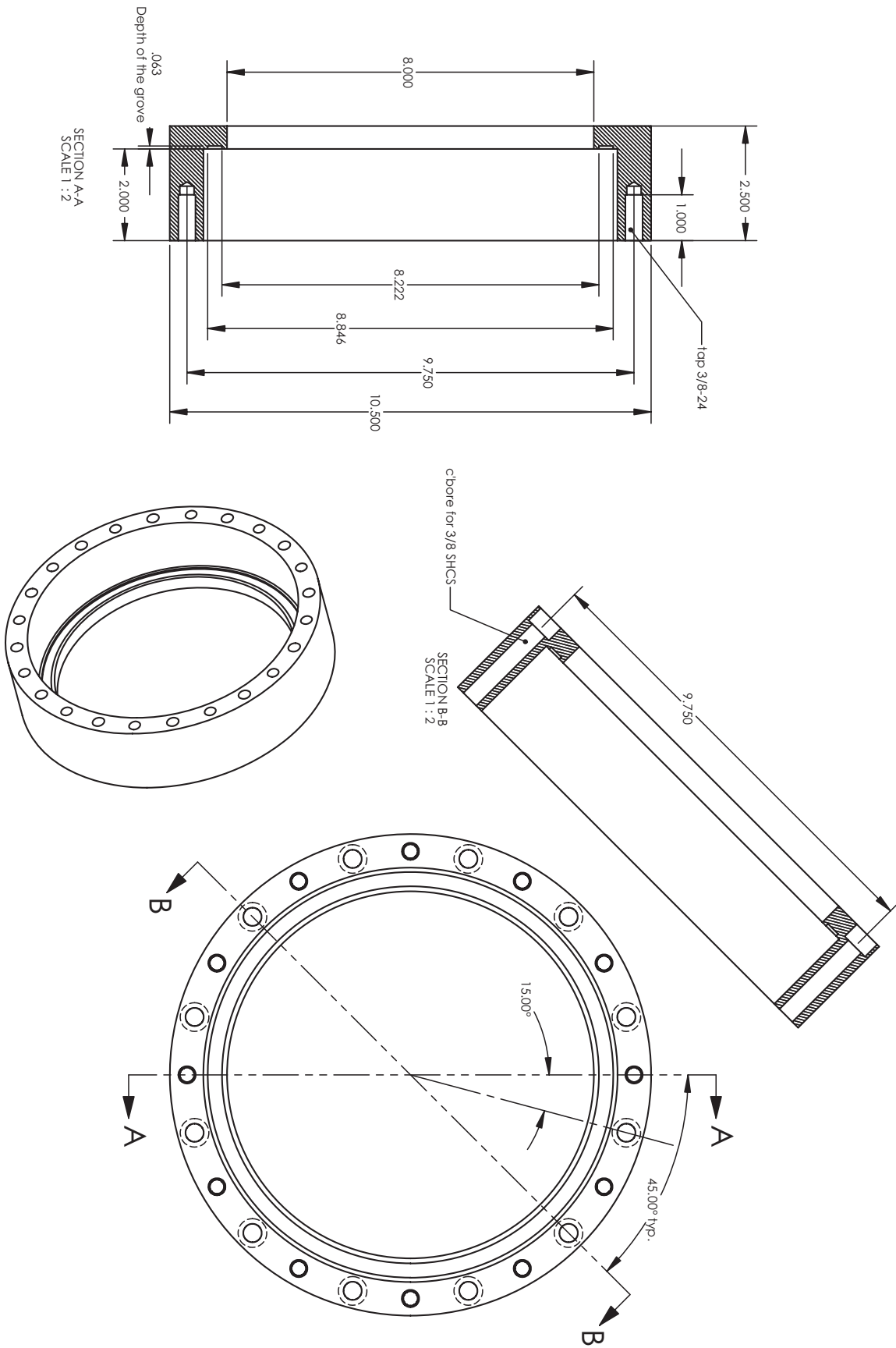


Figure C.4: Window housing (part 9) drawing.

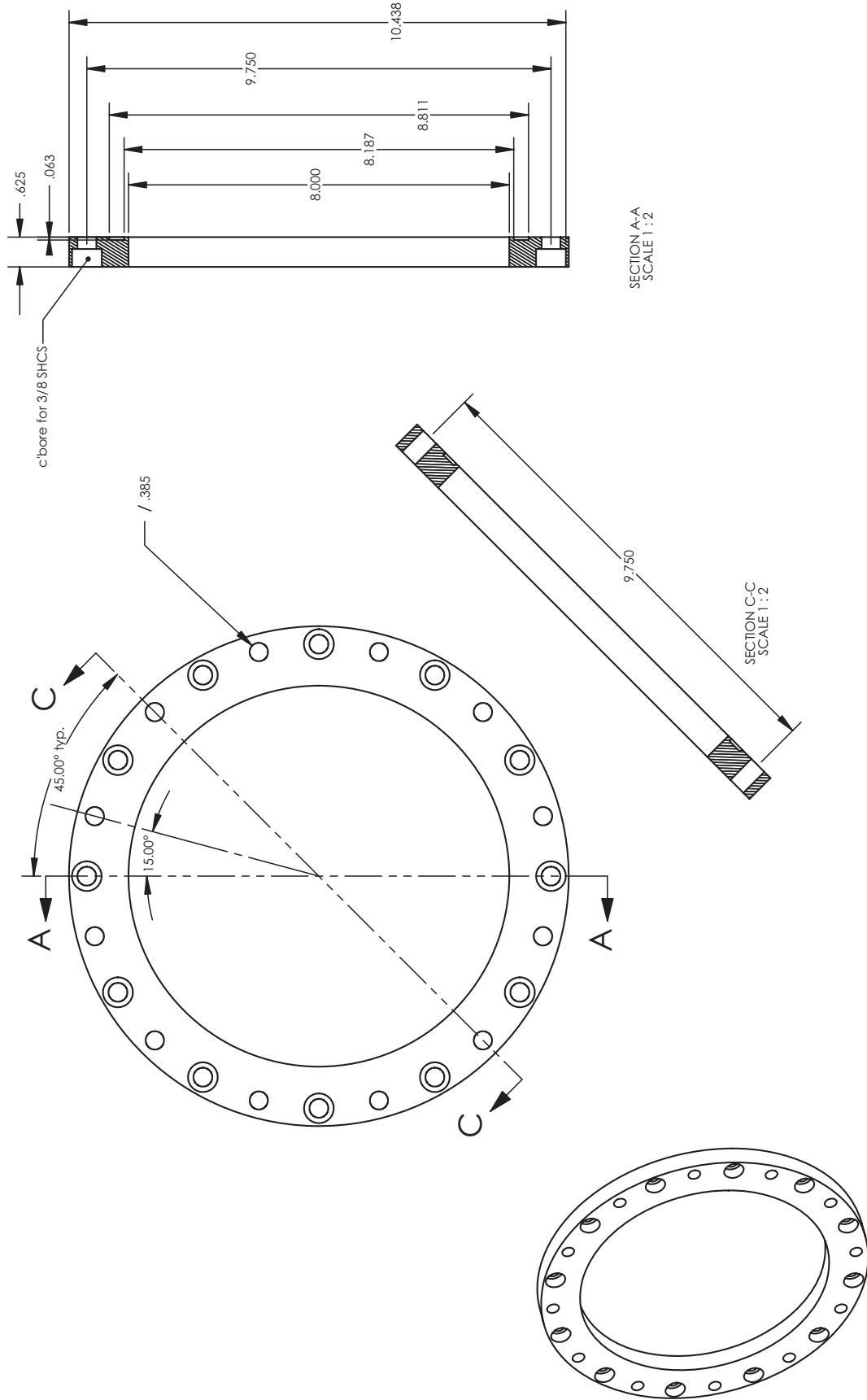


Figure C.5: Window clamp (part 10) drawing.

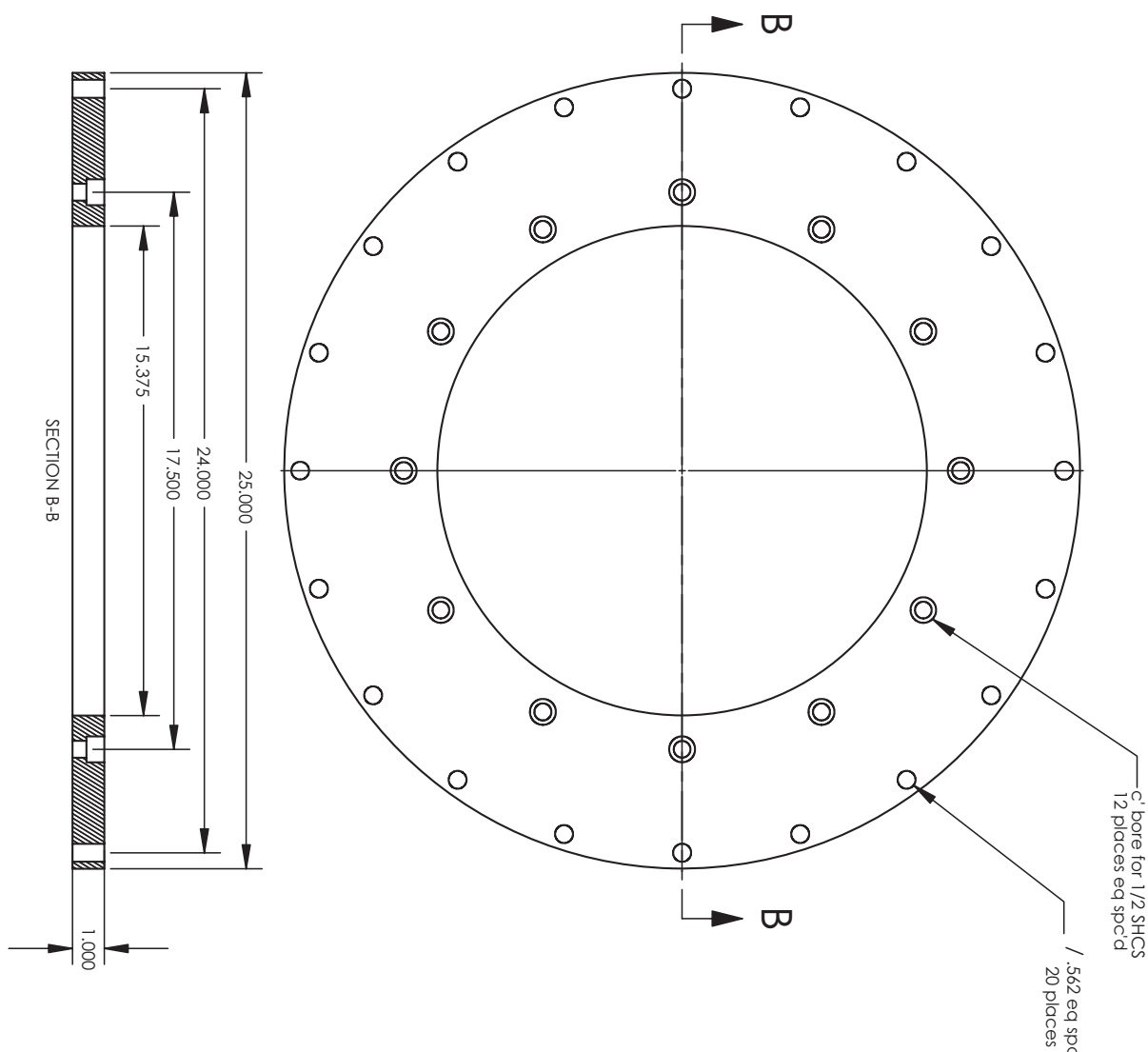
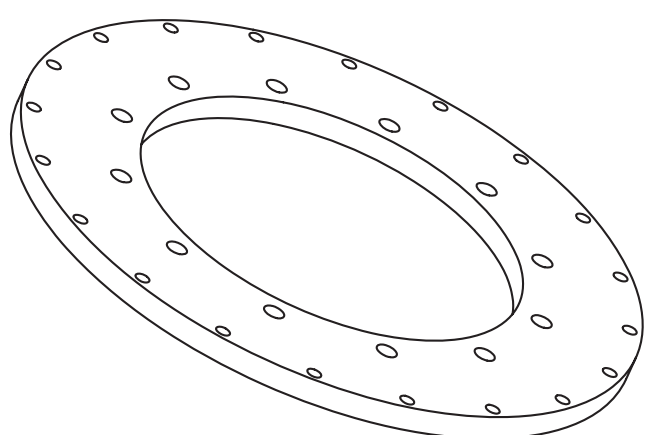


Figure C.6: Test section flange (part 11) drawing.



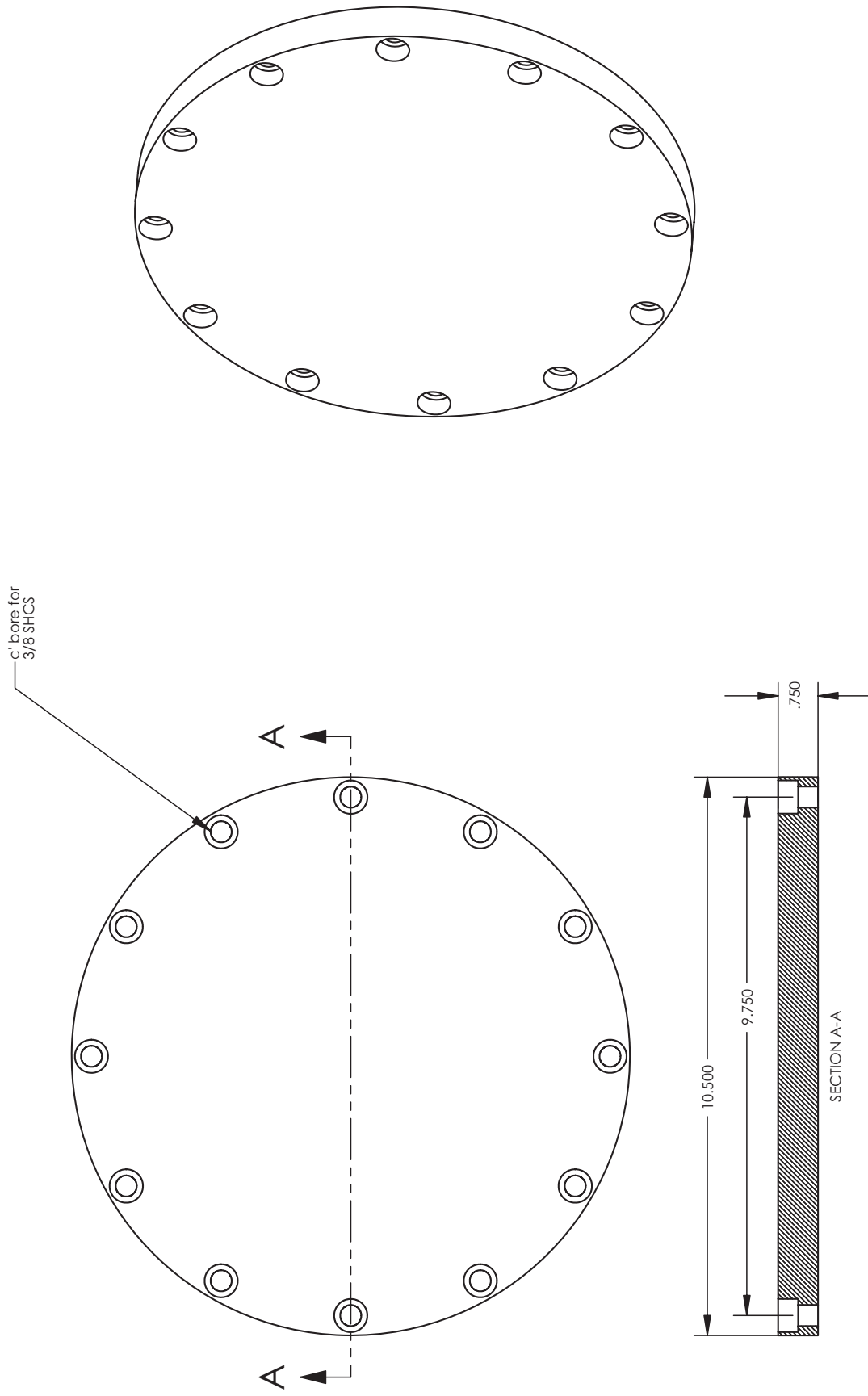


Figure C.7: Window blank (part 12) drawing.

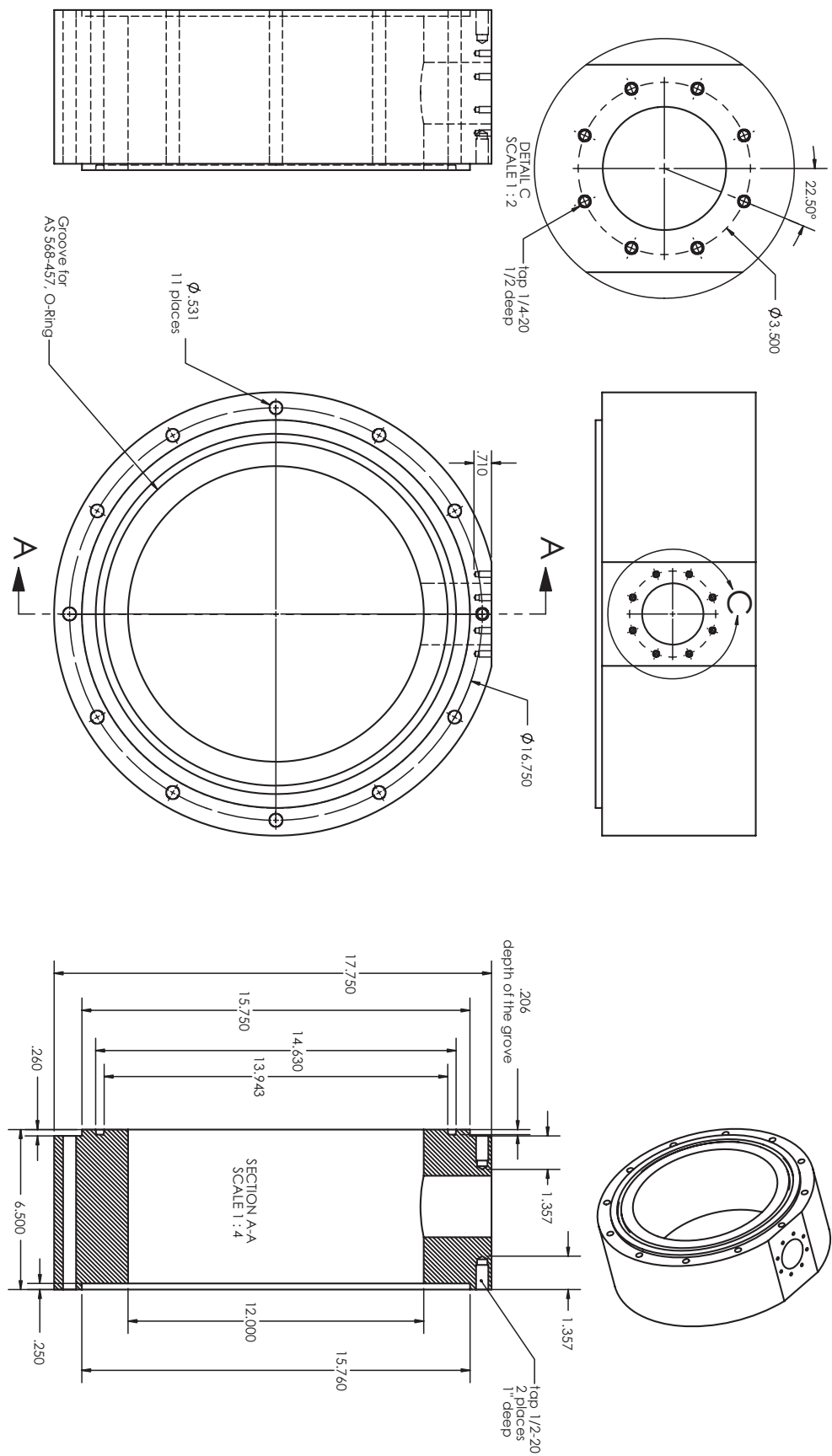


Figure C.8: Injector flange (part 14) drawing.

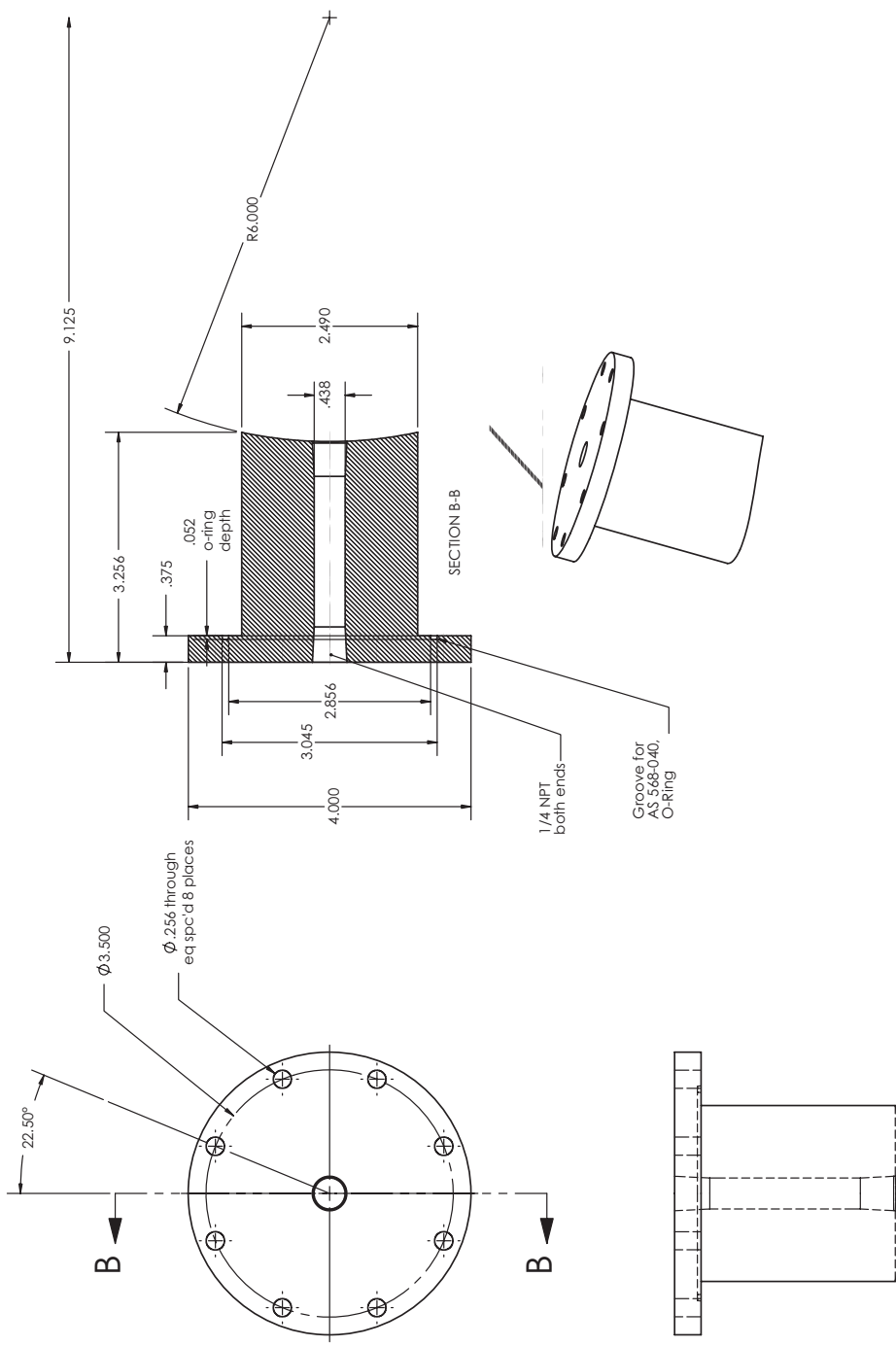


Figure C.9: Injector block (part 15) drawing.

Appendix D

Double Wedge Model

D.1 Adjustable Wedge Model

Table D.1: Primary components of the adjustable wedge model.

Part Number	Part Name	Quantity
1	Bearing Mount	2
3	Bearing Mount Cross Rib	2
5	Wedge Shaft	1
6	Window Cap	1
7	Motor-Gearbox Assembly	1
8	Top Gear Shaft	1
9	Motor Mount	1
10	Rocker	1
11	Moving Wedge	1
12	Rod End	2
13	Threaded Rod	1
15	Wedge Rod	1
16	Rocker Housing	1
17	Rocker Housing Lid	1

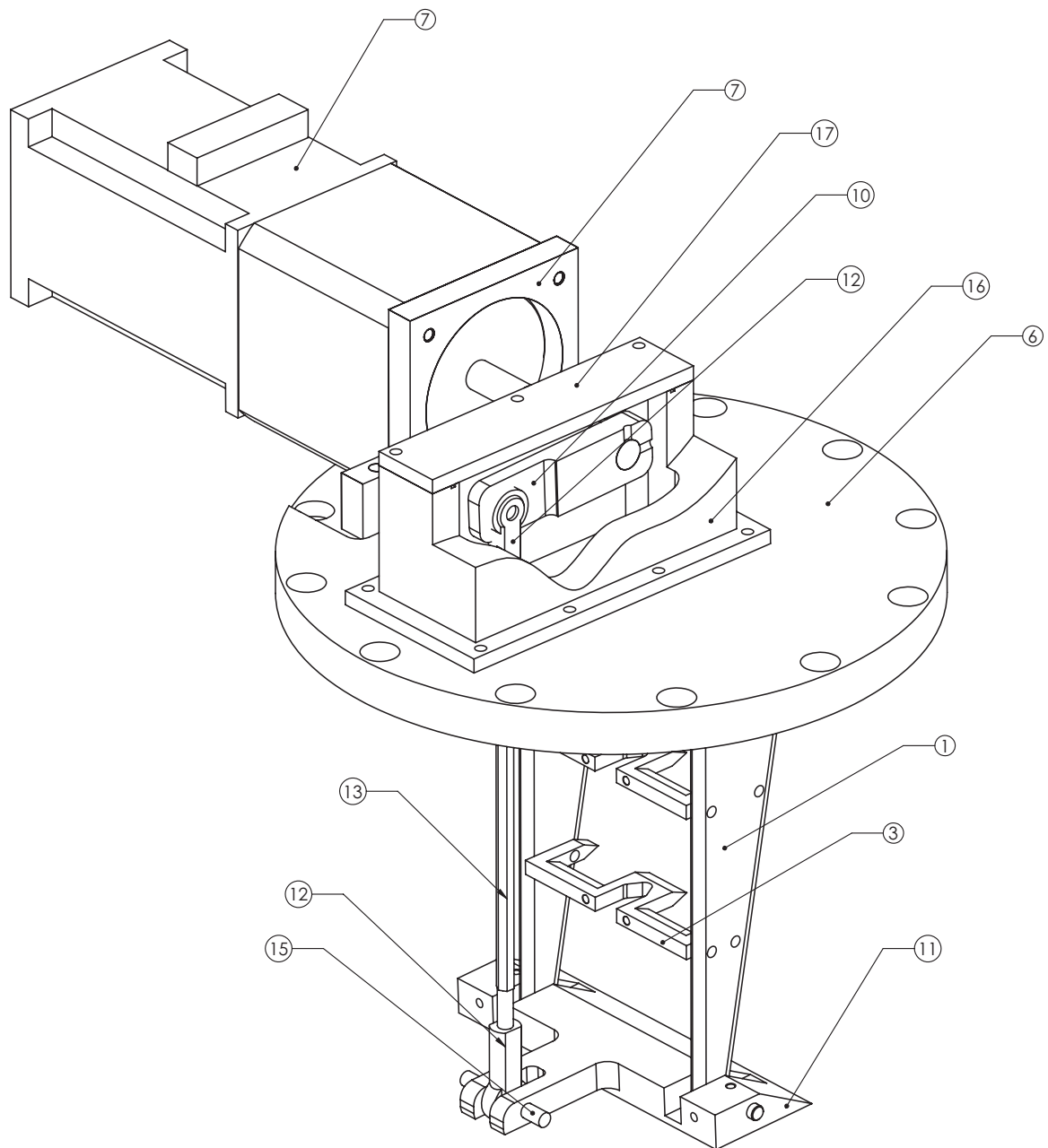
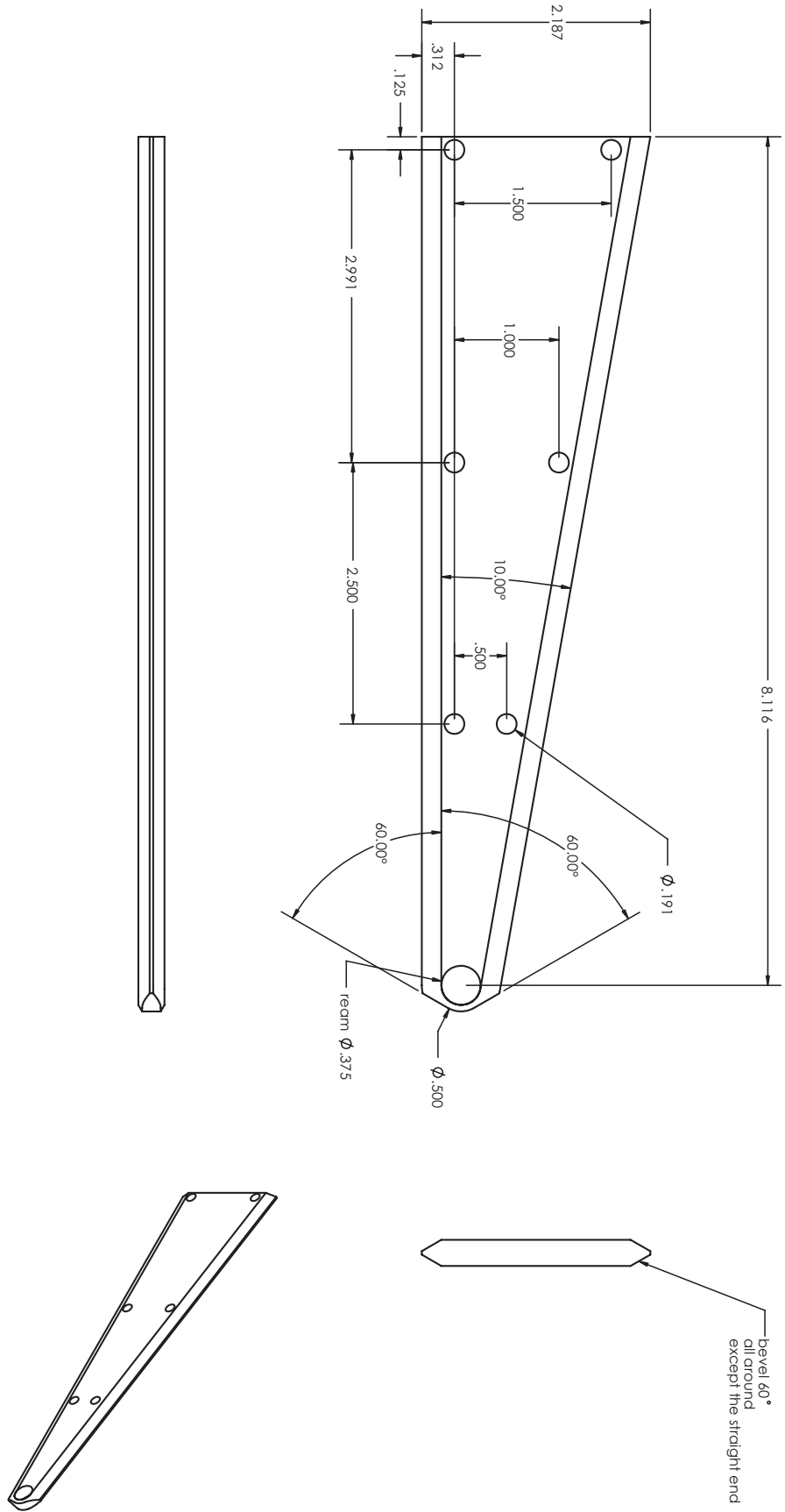


Figure D.1: Adjustable wedge model assembly drawing of the various primary components and their relationships to each other.



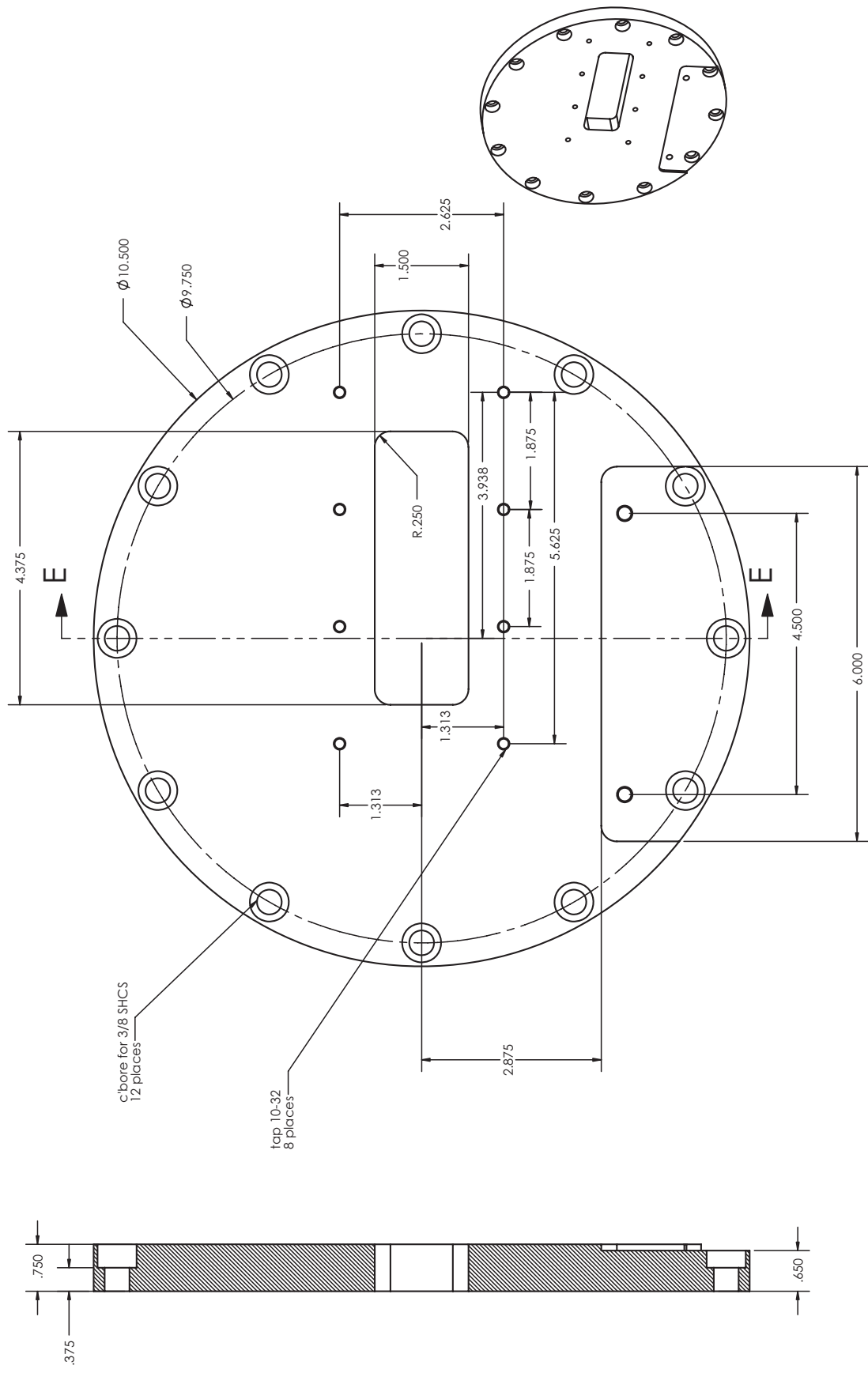


Figure D.3: Window cap (part 6) drawing.

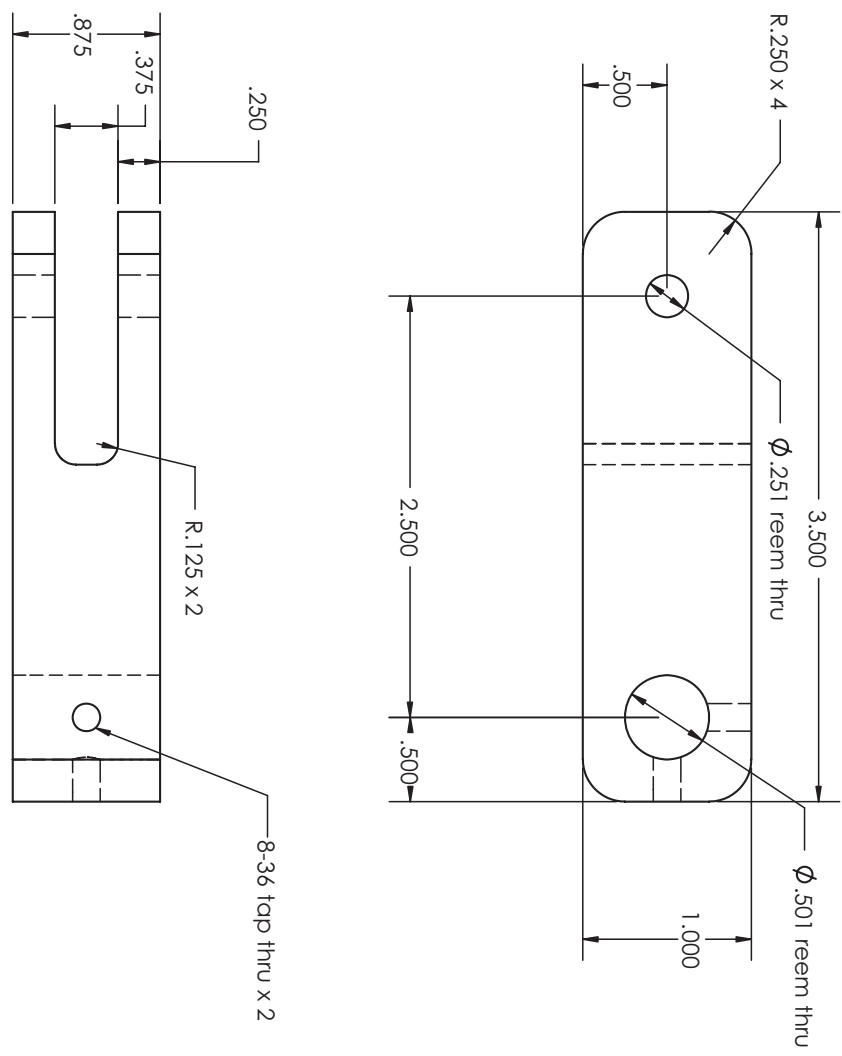
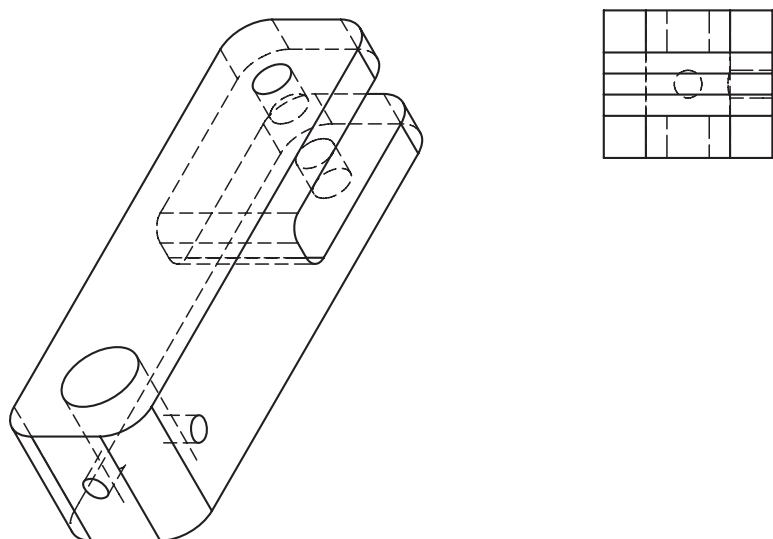


Figure D.4: Motor mount (part 9) drawing.



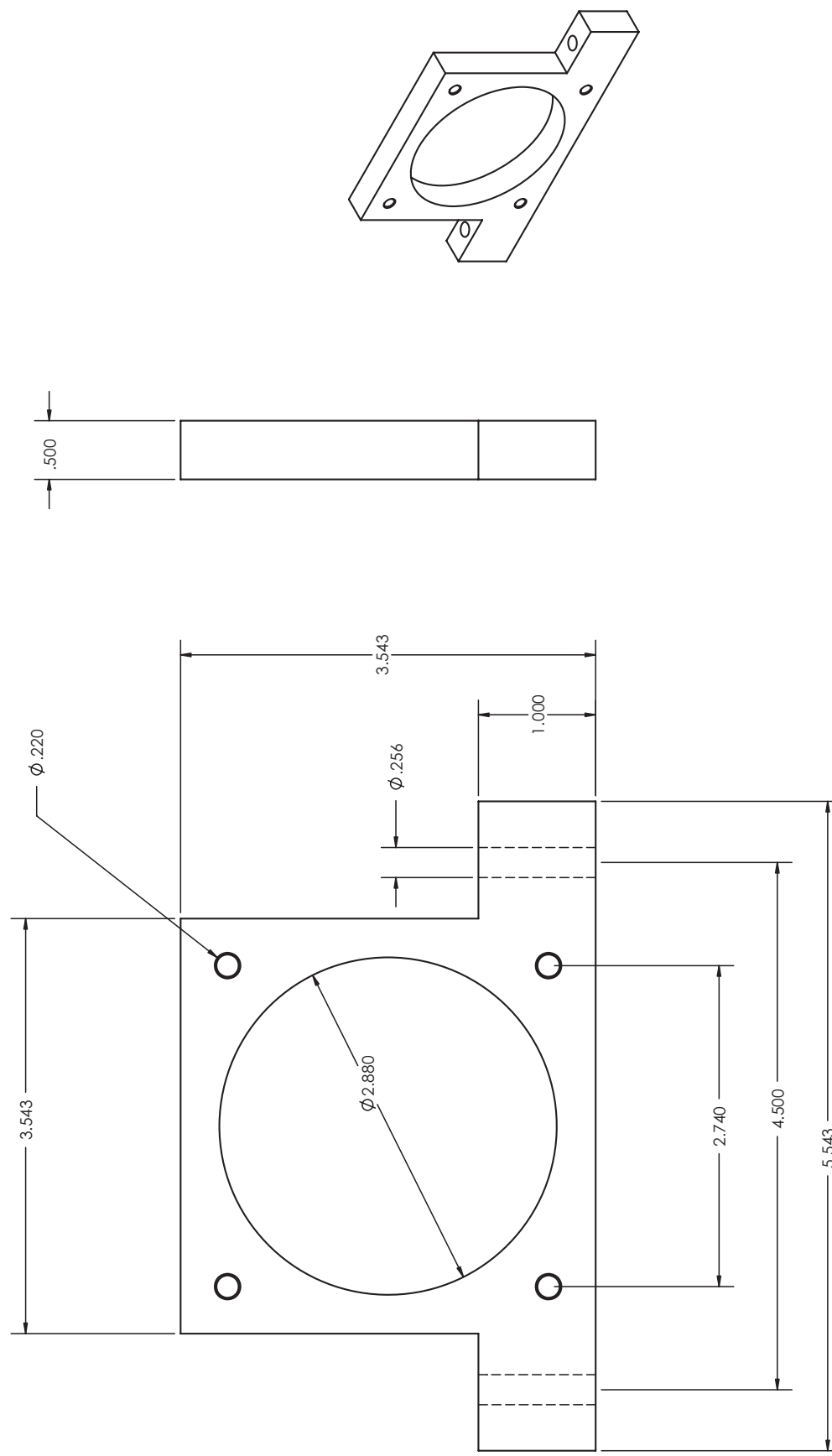


Figure D.5: Rocket (part 10) drawing.

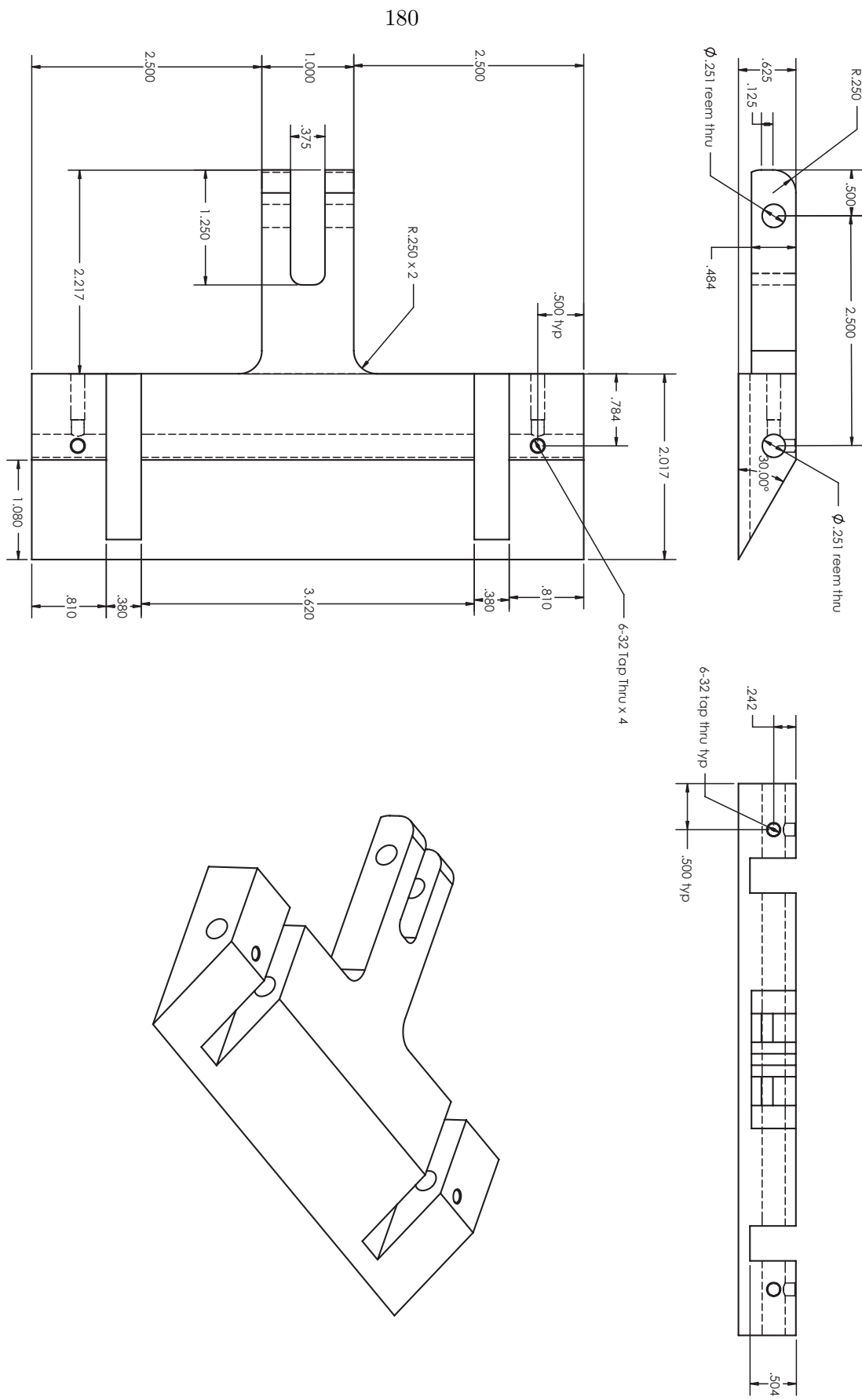


Figure D.6: Moving wedge (part 11) drawing.

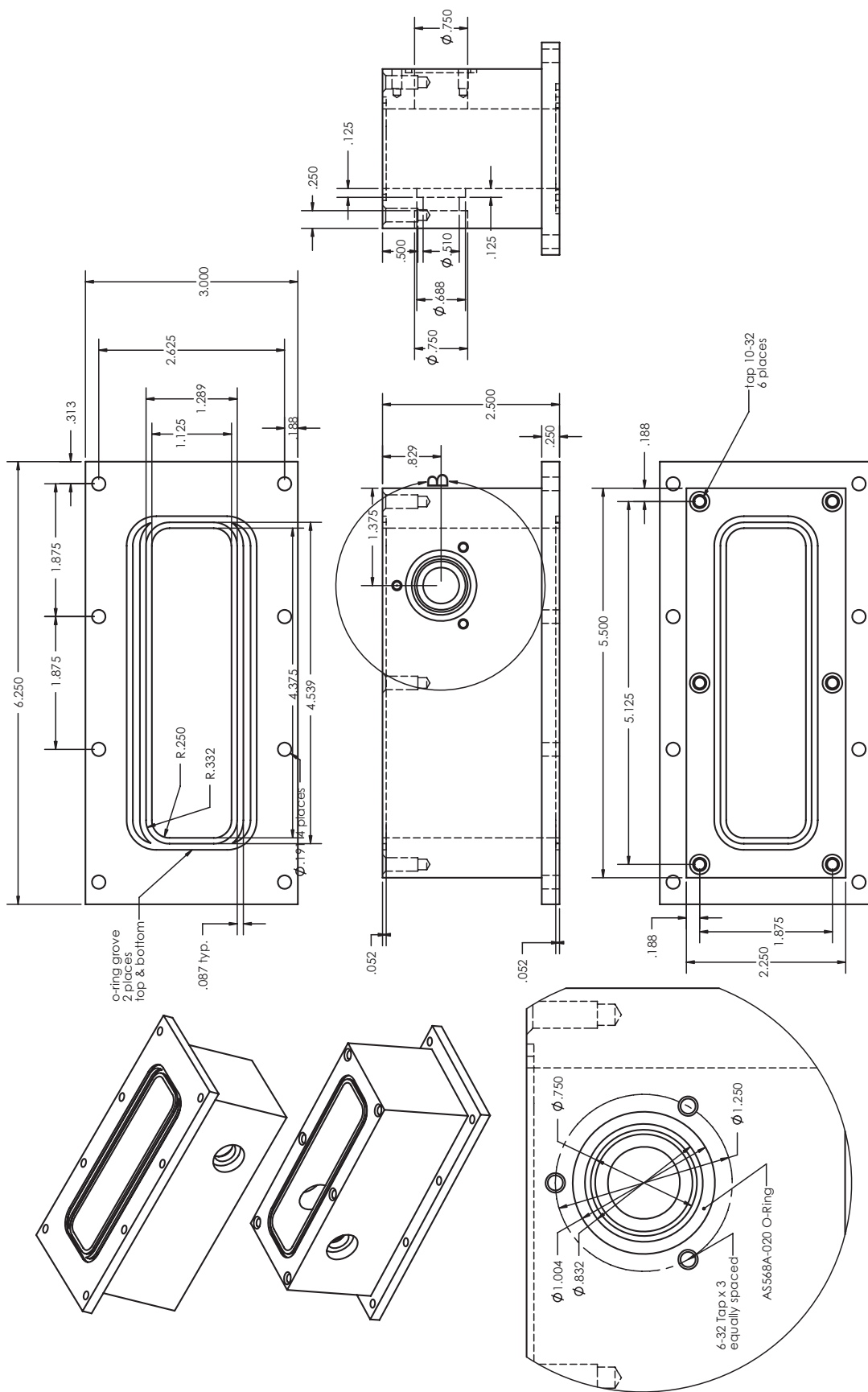


Figure D.7: Rocker housing (part 16) drawing.

182

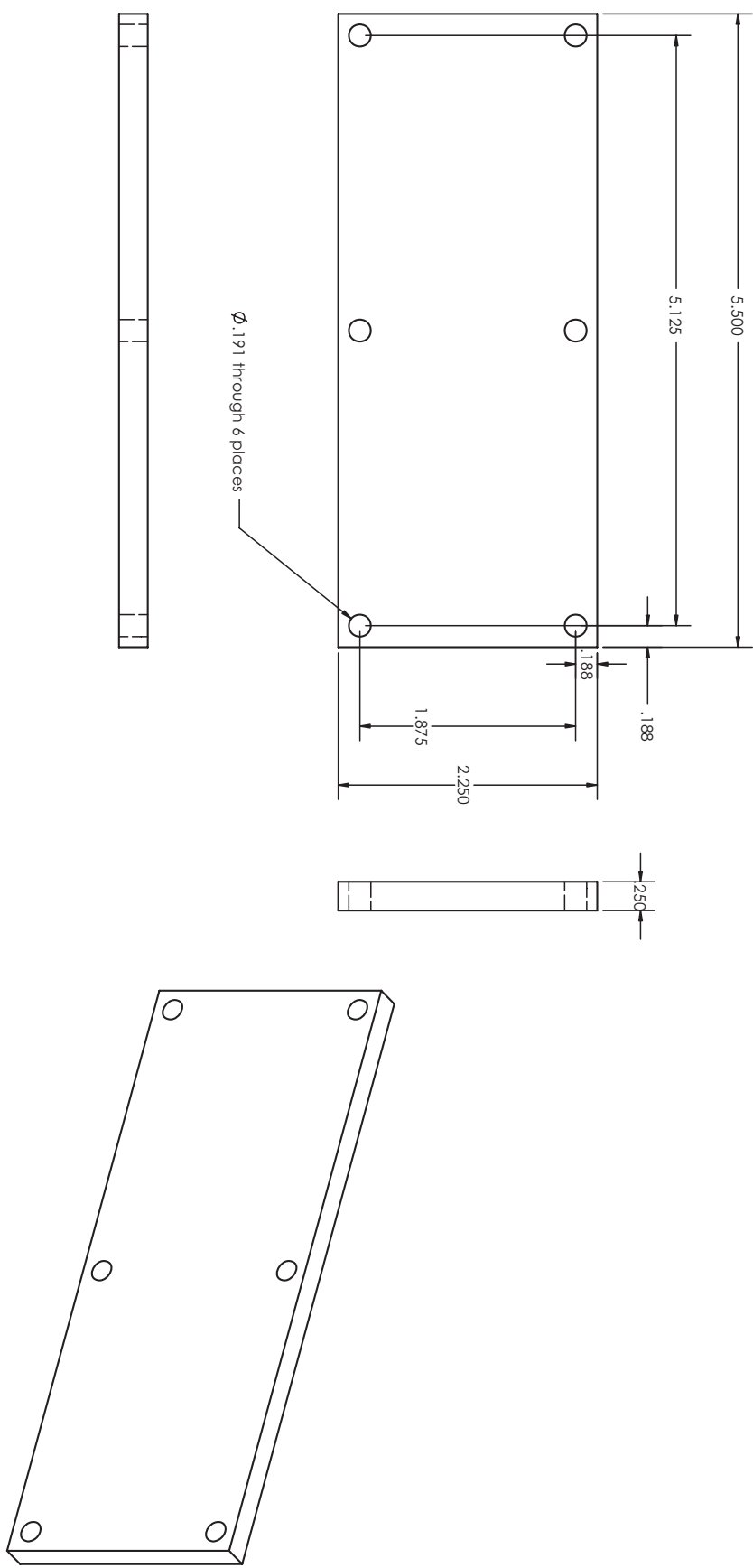


Figure D.8: Rocker housing lid (part 17) drawing.

D.2 Fixed Wedge Model

Table D.2: Primary components of the fixed wedge model.

Part Number	Part Name	Quantity
1	Fixed Wedge	1
2	Vertical Support	2
3	Horizontal Support	1
4	Window Cap	1

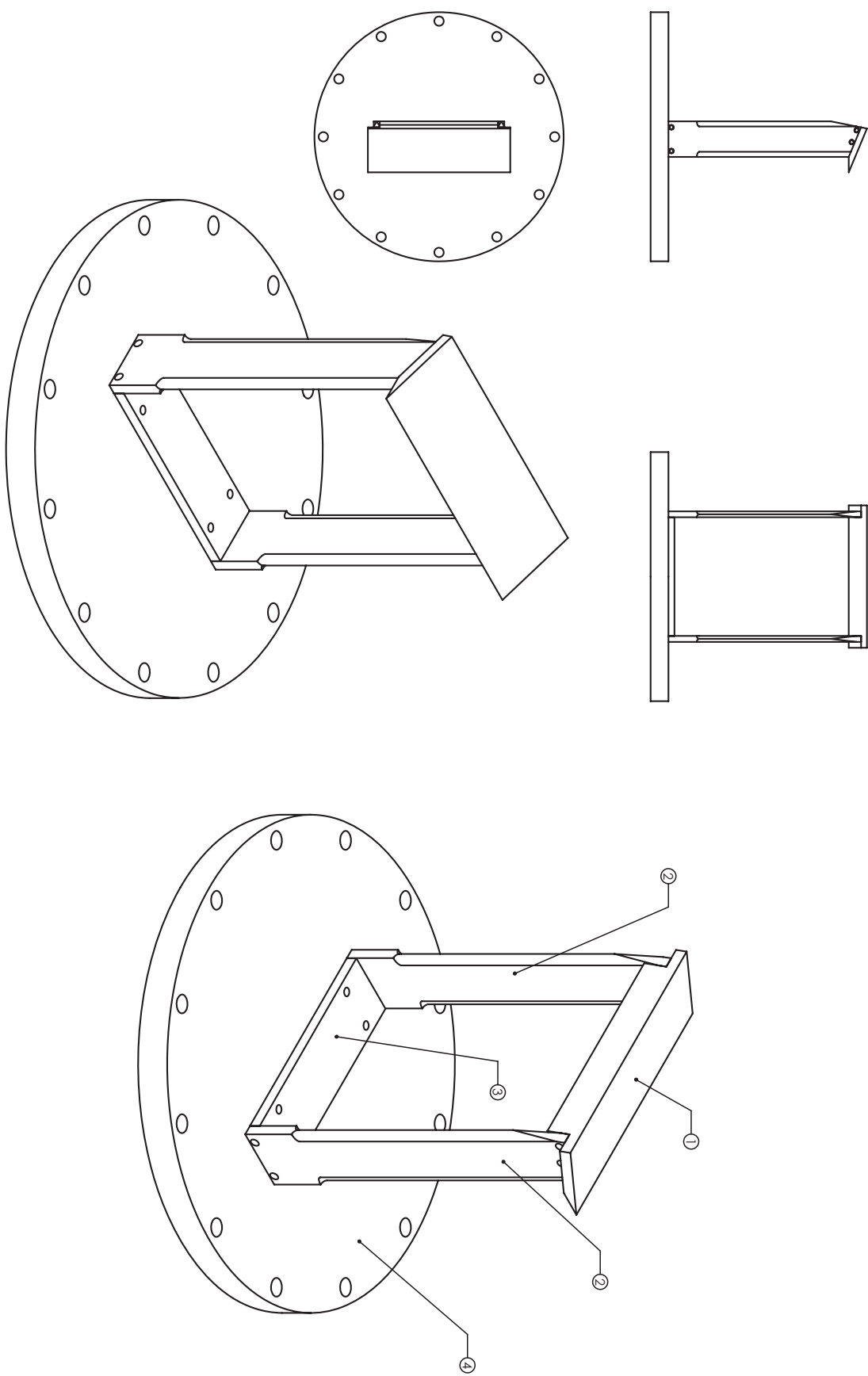


Figure D.9: Fixed wedge model assembly drawing of the various primary components and their relationships to each other.

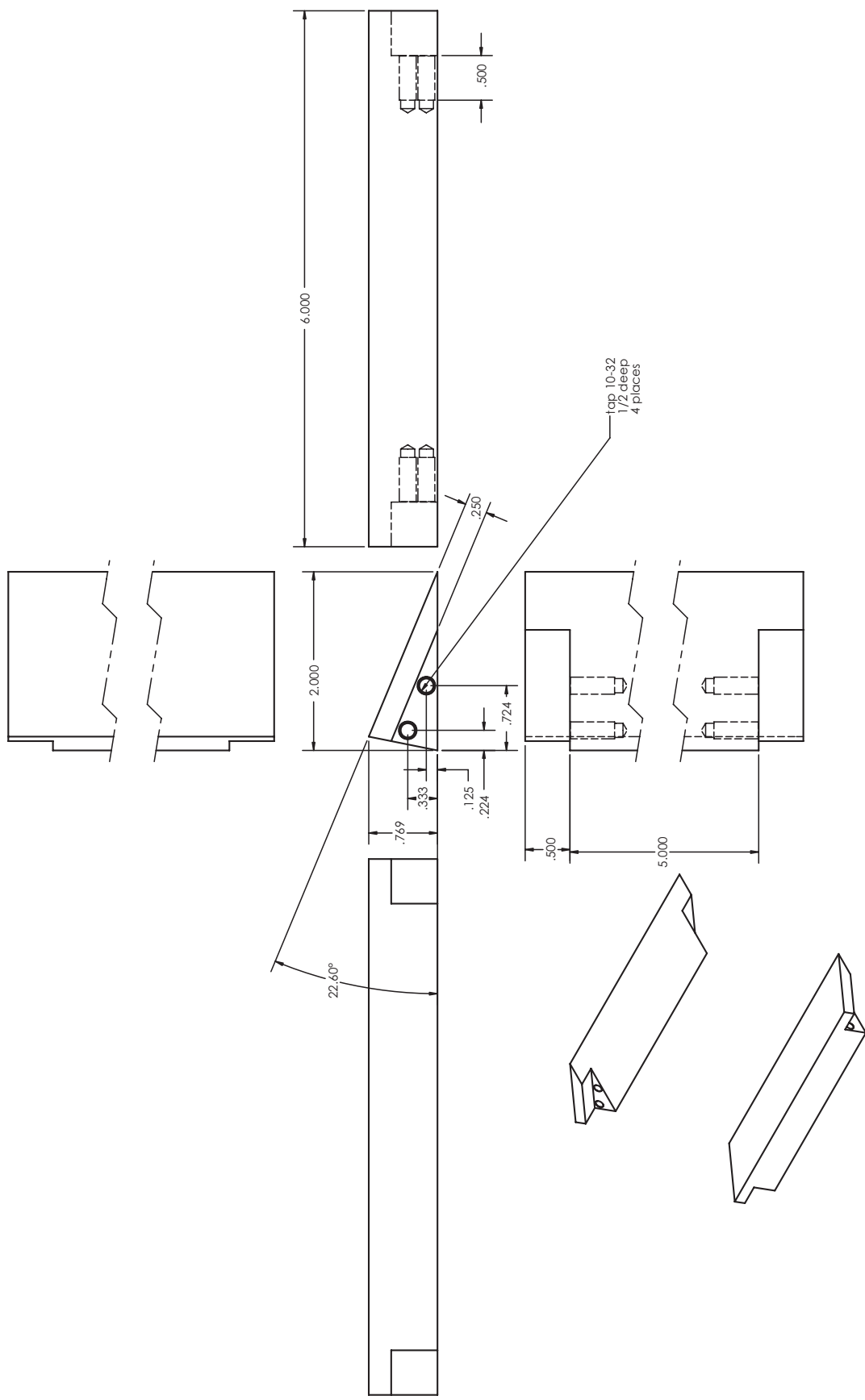


Figure D.10: Fixed wedge (part 1) drawing.

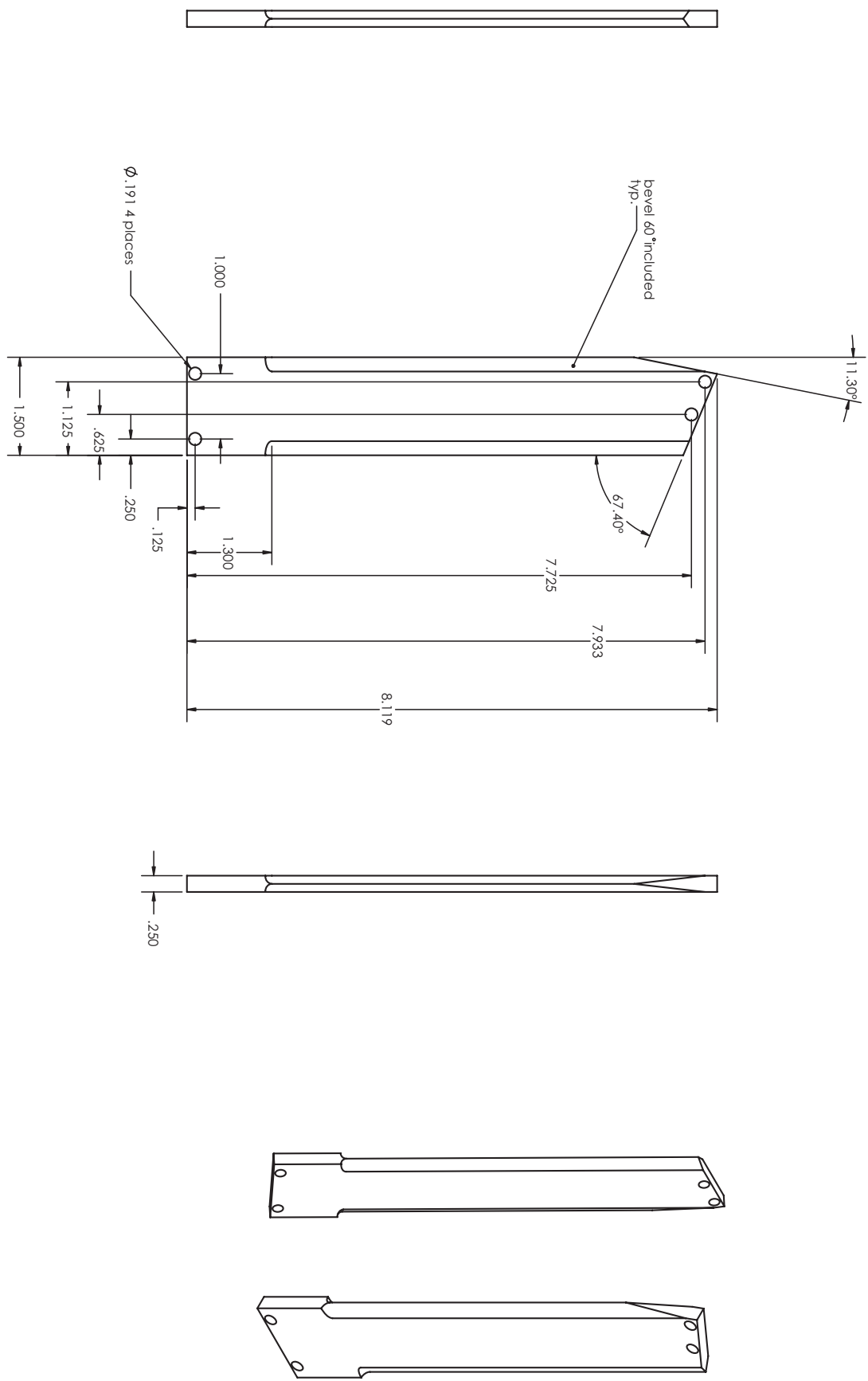


Figure D.11: Vertical support (part 2) drawing.

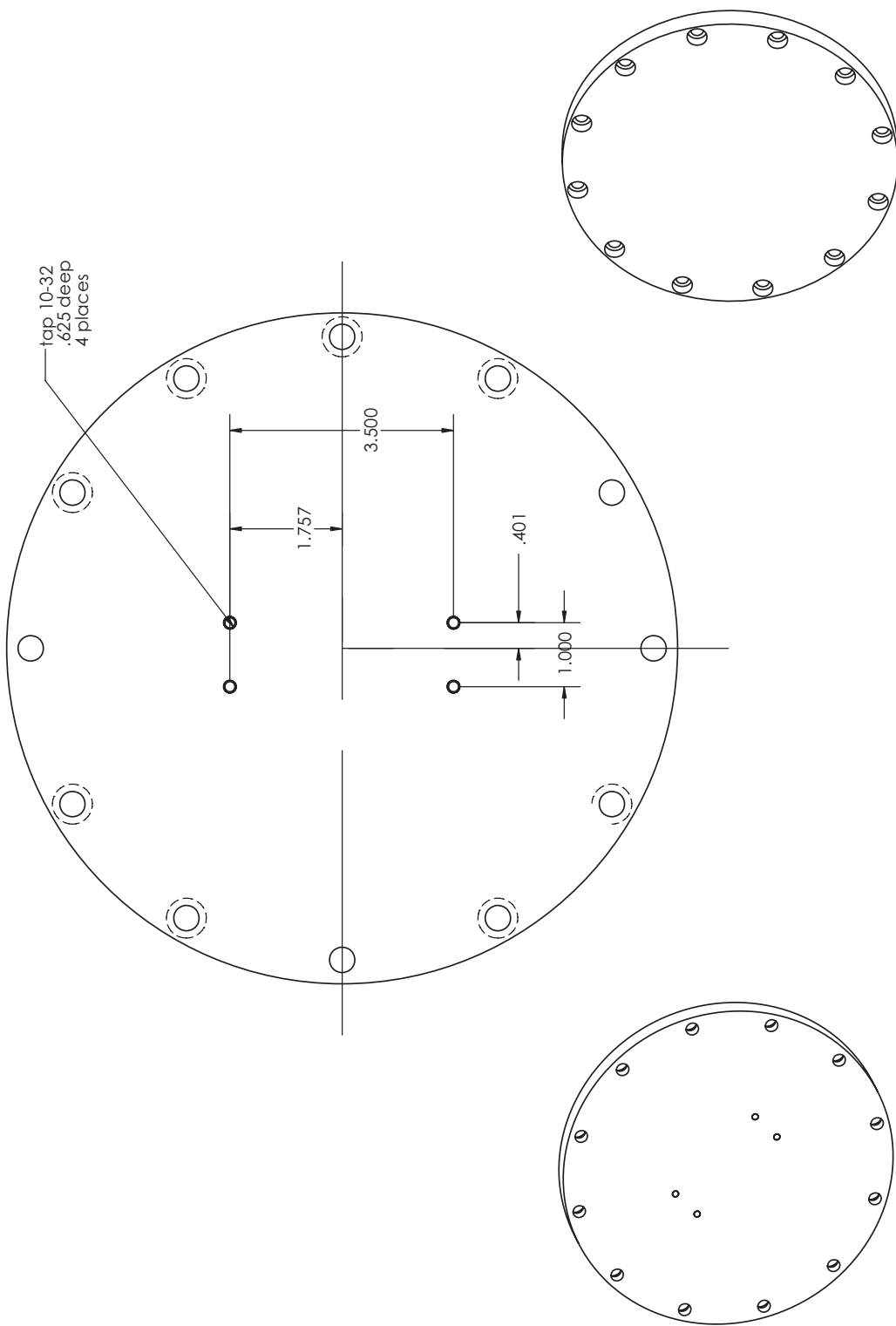
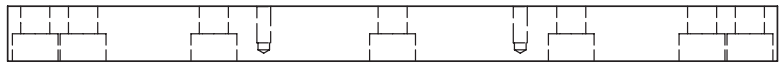


Figure D.12: Window cap (part 4) drawing.

Bibliography

- [1] John von Neumann. Oblique reflection of shocks. Technical report, Bureau of Ordnance, 1943.
- [2] L. F. Henderson and A. Lozzi. Experiments on transition of Mach reflection. *Journal of Fluid Mechanics*, 68:139–155, 1975.
- [3] H. G. Hornung and G. Kychakoff. Transition from regular to Mach reflexion of shock waves in relaxing gases. In B. Ahlborn, A. Herzberg, and D. Russell, editors, *Shock Tube and Shock Wave Research*, pages 297–302, Seattle, 1977. University of Washington Press.
- [4] H. G. Hornung, H. Oertel, and R. J. Sandeman. Transition to Mach reflection of shock-waves in steady and psuedo-steady flow with and without relaxation. *Journal of Fluid Mechanics*, 90:541–547, 1979.
- [5] L. F. Henderson and A. Lozzi. Further experiments on transition to Mach reflexion. *Journal of Fluid Mechanics*, 94:541–559, 1979.
- [6] H. G. Hornung and M. L. Robinson. Transition from regular to Mach reflection of shock-waves Part 2. The steady-flow criterion. *Journal of Fluid Mechanics*, 123:155–164, 1982.
- [7] D. J. Azevedo. *Analytic Prediction of Shock Patterns in a High-Speed, Wedge-Bounded Duct*. PhD thesis, State University of New York, 1989.
- [8] M. S. Ivanov, S. F. Gimelshein, and A. E. Beylich. Hysteresis effect in stationary reflection of shock-waves. *Physics of Fluids*, 7(4):685–687, 1995.
- [9] A. Chpoun, D. Passerel, H. Li, and G. Ben-Dor. Reconsideration of oblique shock wave reflections in steady flows. *Journal of Fluid Mechanics*, 7(4):686–687, 1995.

- [10] M. S. Ivanov, A. N. Kudryavtsev, S. B. Nikiforov, D. V. Khotyanovsky, and A. A. Pavlov. Experiments on shock wave reflection transition and hysteresis in low-noise wind tunnel. *Physics of Fluids*, 15(6):1807–1810, 2003.
- [11] N. Sudani, M. Sato, T. Karasawa, J. Noda, A. Tate, and M. Watanabe. Irregular effects on the transition from regular to Mach reflection of shock wave in wind tunnel flows. *Journal of Fluid Mechanics*, 459:167–185, 2002.
- [12] M. Ivanov, G. Klemenkov, A. Kudryavtsev, S. Nikiforov, A. Pavlov, V. Fomin, A. Kharitonov, D. Khotyanovsky, and H. G. Hornung. Experimental and numerical study of the transistion between regular and Mach reflections of shock waves in steady flows. In *The 21st International Symposium on Shock Waves*, 1997.
- [13] H. Yan, R. Adelgren, G. Elliott, D. Knight, and T. Beutner. Effect of energy addition on MR → RR transition. *Shock Waves*, 13:113–121, 2003.
- [14] Ames Research Staff. Equations, tables, and charts for compressible flow. Technical Report 1135, Ames Aeronautical Laboratory, 1953.
- [15] B. W. Skews and J. T. Ashworth. The physical nature of weak shock wave reflection. *Journal of Fluid Mechanics*, 2005.
- [16] A. M. Tesdall and J. K. Hunter. Self-similar solutions for weak shock reflection. *SIAM Journal of Applied Mathematics*, 2002.
- [17] C. J. Chapman. *High Speed Flow*. Cambridge University Press, Cambridge, 2000.
- [18] D. J. Azevedo and C. S. Liu. Engineering approach to the prediction of shock patterns in bounded high-speed flows. *AIAA Journal*, 31:83–90, 1993.
- [19] G. Ben-Dor. *Shock Wave Reflection Phenomena*. Springer-Verlag, New York, 1992.
- [20] H. Li and G. Ben-Dor. A parametric study of Mach reflection in steady flows. *Journal of Fluid Mechanics*, 341:101–125, 1997.
- [21] H. Li, M. Schotz, and G. Ben-Dor. Wave configuration of Mach reflection in steady flows: Analytical solution and dependence on downstream influences. In B. Sturtevant, J. E. Shepherd, and H. G. Hornung, editors, *International Symposium on Shock Waves*, volume 1, pages 393–398, Pasadena, CA, 1995.

- [22] M. Schotz, A. Levy, G. Ben-Dor, and O. Igra. Analytical prediction of the wave configuration size in steady flow Mach reflections. *Shock Waves*, 7:363–372, 1997.
- [23] A. Chpoun and E. Leclerc. Experimental investigation of the influence of downstream flow conditions on Mach stem height. *Shock Waves*, 9:269–271, 1999.
- [24] J. J. Quirk. Amrita - a computational facility (for CFD modelling). In *VKI 29th CFD Lecture Series, ISSN 0377-8312*, 1998.
- [25] N. F. Ponchaut, H. G. Hornung, D. I. Pullin, and C. A. Mouton. On imploding cylindrical and spherical shock waves in a perfect gas. *Journal of Fluid Mechanics*, 560:130–122, 2006.
- [26] J. Vuillon, D. Zeitoun, and G. Ben-Dor. Reconsideration of oblique shock wave reflection in steady flows. Part 2. Numerical investigation. *Journal of Fluid Mechanics*, 301:37–50, 1995.
- [27] R. Deiterding. AMROC-blockstructured adaptive mesh refinement in object-oriented C++. Available at <http://amroc.sourceforge.net>, 2003.
- [28] L. I. Sedov. *Similarity and Dimensional Methods in Mechanics*. Academic Press, 4th edition, 1959.
- [29] N. F. Ponchaut, F. Zhang, and J. H. S. Lee. Blast wave from the explosion of a reacting sphere. In *Combustion Institute/Canadian Section Spring Technical Meeting*, Waterloo, ON, 2006.
- [30] J. J. Korte. Aerodynamic design of axisymmetric hypersonic wind-tunnel nozzles using least-squares/parabolized Navier-Stokes procedure. *AIAA Journal of Spacecraft and Rockets*, 29(5):685–691, 1992.
- [31] J. J. Korte. A CFD-based aerodynamic design procedure for hypersonic wind-tunnel nozzles. In *AGARD 70th Fluid Dynamics Panel Meeting*, Torino, Italy, 1992.
- [32] J. J. Korte, A. Kumar, D. J. Singh, and J. A. White. CAN-DO - CFD-based aerodynamic nozzle design & optimization program for supersonic/ hypersonic wind tunnels. In *AIAA 17th Aerospace Ground Testing Conference*, Nashville, TN, 1992.

- [33] M. Y. El-Naggar, J. T. Klamo, M.-H. Tan, and H. G. Hornung. Experimental verification of the Mach-number field in a supersonic ludwieg tube. *AIAA Journal*, 42(8):1721–1724, 2004.